JAAVSO

Volume 50
Number 2
2022

The Journal of the American Association of Variable Star Observers

Visual and Near-Infrared Photometric Observations of Betelgeuse

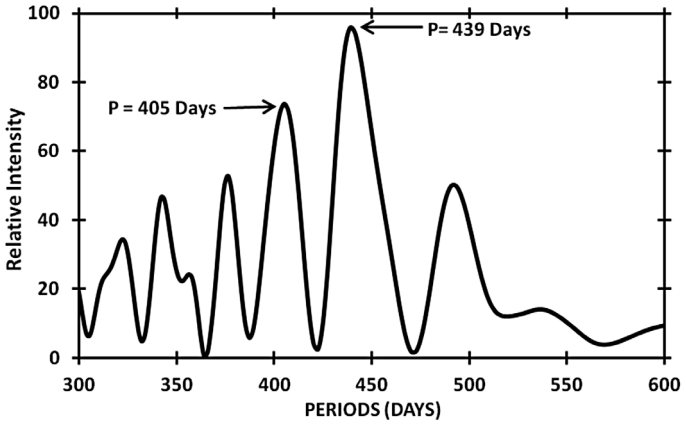

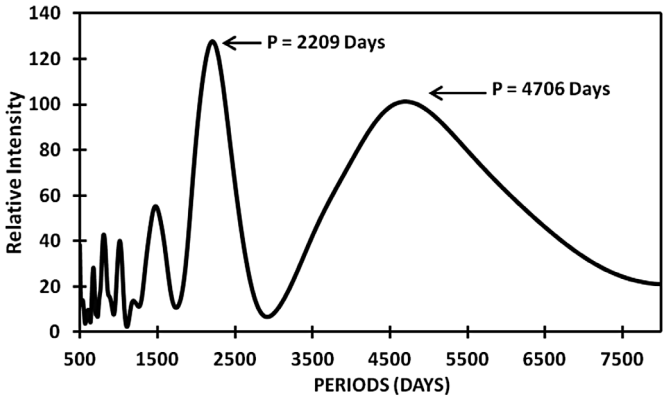

Short-tem (upper panel) and long-term (lower panel) PERANSO-generated periods using the V-band fitted observations. The dominant (higher relative intensity) and secondary (lower relative intensity) periods are indicated in days.

Also in this issue...

The American Association of Variable Star Observers
185 Alewife Brook Parkway, Suite 410, Cambridge, MA 02138, USA

The Journal of the American Association of Variable Star Observers

The Board of the American Association of Variable Star Observers 2021–2022

ISSN 0271-9053 (print)
ISSN 2380-3606 (online)

JAAVSO

The Journal of
The American Association
of Variable Star Observers

Volume 50
Number 2
2022

ISSN 0271-9053 (print)
ISSN 2380-3606 (online)

AAVSO
185 Alewife Brook Parkway,
Suite 410, Cambridge, MA 02138
USA

Publication Schedule

The Journal of the American Association of Variable Star Observers is published twice a year, June 15 (Number 1 of the volume) and December 15 (Number 2 of the volume). The submission window for inclusion in the next issue of JAAVSO closes six weeks before the publication date. A manuscript will be added to the table of contents for an issue when it has been fully accepted for publication upon successful completion of the referee process; these articles will be available online prior to the publication date. An author may not specify in which issue of JAAVSO a manuscript is to be published; accepted manuscripts will be published in the next available issue, except under extraordinary circumstances.

Page Charges

Page charges are waived for Members of the AAVSO. Publication of unsolicited manuscripts in JAAVSO requires a page charge of US $100/page for the final printed manuscript. Page charge waivers may be provided under certain circumstances.

Publication in *JAAVSO*

With the exception of abstracts of papers presented at AAVSO meetings, papers submitted to JAAVSO are peer-reviewed by individuals knowledgeable about the topic being discussed. We cannot guarantee that all submissions to JAAVSO will be published, but we encourage authors of all experience levels and in all fields related to variable star astronomy and the AAVSO to submit manuscripts. We especially encourage students and other mentees of researchers affiliated with the AAVSO to submit results of their completed research.

Subscriptions

Institutions and Libraries may subscribe to JAAVSO as part of the Complete Publications Package or as an individual subscription. Individuals may purchase printed copies of recent JAAVSO issues via Createspace. Paper copies of JAAVSO issues prior to volume 36 are available in limited quantities directly from AAVSO Headquarters; please contact the AAVSO for available issues.

Instructions for Submissions

The *Journal of the AAVSO* welcomes papers from all persons concerned with the study of variable stars and topics specifically related to variability. All manuscripts should be written in a style designed to provide clear expositions of the topic. Contributors are encouraged to submit digitized text in MS WORD, LATEX+POSTSCRIPT, or plain-text format. Manuscripts should be submitted through the JAAVSO submission portal (https://www.aavso.org/apps/jaavso/submit/) or may be mailed electronically to journal@aavso.org or submitted by postal mail to JAAVSO, 185 Alewife Brook Parkway, Suite 410, Cambridge, MA 02138, USA.

Manuscripts must be submitted according to the following guidelines, or they will be returned to the author for correction:

Manuscripts must be:
1) original, unpublished material;
2) written in English;
3) accompanied by an abstract of no more than 100 words.
4) not more than 2,500–3,000 words in length (10–12 pages double-spaced).

Figures for publication must:
1) be camera-ready or in a high-contrast, high-resolution, standard digitized image format;
2) have all coordinates labeled with division marks on all four sides;
3) be accompanied by a caption that clearly explains all symbols and significance, so that the reader can understand the figure without reference to the text.

Maximum published figure space is 4.5" by 7". When submitting original figures, be sure to allow for reduction in size by making all symbols, letters, and division marks sufficiently large.

Photographs and halftone images will be considered for publication if they directly illustrate the text.

Tables should be:
1) provided separate from the main body of the text;
2) numbered sequentially and referred to by Arabic number in the text, e.g., Table 1.

References:
1) References should relate directly to the text.
2) References should be keyed into the text with the author's last name and the year of publication, e.g., (Smith 1974; Jones 1974) or Smith (1974) and Jones (1974).
3) In the case of three or more joint authors, the text reference should be written as follows: (Smith et al. 1976).
4) All references must be listed at the end of the text in alphabetical order by the author's last name and the year of publication, according to the following format: Brown, J., and Green, E. B. 1974, *Astrophys. J.*, **200**, 765.
Thomas, K. 1982, *Phys. Rep.*, **33**, 96.
5) Abbreviations used in references should be based on recent issues of JAAVSO or the listing provided at the beginning of *Astronomy and Astrophysics Abstracts* (Springer-Verlag).

Miscellaneous:
1) Equations should be written on a separate line and given a sequential Arabic number in parentheses near the right-hand margin. Equations should be referred to in the text as, e.g., equation (1).
2) Magnitude will be assumed to be visual unless otherwise specified.
3) Manuscripts may be submitted to referees for review without obligation of publication.

Online Access

Articles published in JAAVSO, and information for authors and referees may be found online at: https://www.aavso.org/apps/jaavso/

The Journal of the American Association of Variable Star Observers
Volume 50, Number 2, 2022

Editorial

Variable Star Research

Table of Contents continued on next page

Solar

Variable Star Data

Research Update

Errata

Editorial

Self-Correction and Updating in Astronomical Papers

Nancy D. Morrison
Editor-in-Chief, *Journal of the AAVSO*

Department of Physics and Astronomy and Ritter Observatory, MS 113, The University of Toledo, 2801 W. Bancroft Street, Toledo, OH 43606; jaavso.editor@aavso.org

Received December 5, 2022

Published papers constitute the historical record of science, and we often think of them as fixed monuments to scientists' work. However, the record as a whole develops faster and faster as more and more new work is added. Now that most journal articles are not crystallized in print, one can imagine that it may even be possible for individual papers to evolve. After all, most projects are not ever truly finished. Sometimes, authors gather new information about a result that is not enough for a whole new paper but is suitable for a short update.

More seriously, scientific publications sometimes contain mistakes in data acquisition, reduction, or analysis. It's too bad to make a mistake, but the important thing is how its maker addresses it. Scientific journals carry out the task of maintaining the integrity of the record, in the face of those occasional errors, through retraction of articles and publication of errata.

Retraction concerns scientific errors that are serious enough to invalidate the conclusion of a paper. It can also concern ethical breaches such as plagiarism discovered after publication, in which case the Editor may initiate a retraction (Vishniac 2015). Recently, *JAAVSO* published its first retraction (Axelsen 2021). Author Axelsen is to be commended for the care with which he analyzed that error.

Errata sometimes bring to readers' attention major errors that alter an article's research conclusions. Or the error may be minor, affecting only the details or the clarity of a presentation. Errata are usually written by the author of the original paper, although the error may have been brought to the author's attention by someone else. Errata appear in *JAAVSO* at a rate of one or two per issue, comparable to other scientific journals.

Now what about updates to articles, which do not correct errors but simply add new information? The present volume introduces a "Research Update," a short article that, rather than correcting an error, incorporates new information that modifies or clarifies a research result. This type of submission is not typical in standard scientific journals; *JAAVSO* is fortunate in having the flexibility to publish such an item at low cost. The only other example of which I am aware is the *Research Notes of the American Astronomical Society* (*RNAAS*).[1] It accepts articles that build on results published in that journal or elsewhere.

Our new feature came about because author Ernst Pollmann asked to update his article with Philip Bennett (Pollmann and Bennett 2020) in order to resolve a discrepancy between periods derived from different features in the Hα profile of target star VV Cep. We are glad to provide this service.

Because this update involved no new methods or concepts but only additional data, it was not sent for peer review. The Editor will determine whether any future updates will be sent for peer review. In the case of errata, referees may be informed if significant errors are involved. Referees are always informed of retractions.

Because of the possibility that a journal article may be corrected or updated, you should check for a newer version of any article that is important for your research. Our staff has begun the practice of inserting a note at the end of the abstract of each updated or corrected article, with a link to the update or correction. Therefore, when checking an article in *JAAVSO*, always read the abstract page of the online version.

You can also find updates, errata, and retractions in the list of citations to our articles in NASA's Astrophysics Data System (ADS).[2] If an article has received a citation in the literature, the notation "cited:" and the number of citations appear in the results list from an ADS search, after the article's bibliographic code. But our articles' updates and corrections are not indexed in the ADS, nor do they appear in the ADS citation lists, until they appear in our complete, published issue.

JAAVSO encourages authors to submit retractions (in case they are unfortunately necessary), errata, and updates. Of course, new articles are welcome when significant new results require substantial treatment. Updates offered by researchers other than the author of an article can be considered, upon consultation with the original author. Our goals are that our published articles remain at the forefront of the field and our readers always have access to fresh information.

References

Axelsen, R. A. 2021, *J. Amer. Assoc. Var. Star Obs.*, **49**, 197.
Pollmann, E., and Bennett, P. 2020, *J. Amer. Assoc. Var. Star Obs.*, **48**, 118.
Vishniac, E. T. 2015, *Astrophys. J.*, **815**, 79.

[1] https://journals.aas.org/news/scope-of-research-notes-of-the-american-astronomical-society/
[2] https://ui.adsabs.harvard.edu

B,V Observations and Analyses of the EW Stars NY Boötis and V508 Cygni

Andreas Beck
Schickhardtstraße 59, 71116 Gärtringen, Germany; Andreas.Beck@HFT-Stuttgart.de

Laurent Corp
56 Avenue de Paris, 12000 Rodez, France; astro.laucorp@orange.fr

Gerard Samolyk
P.O. Box 20677, Greenfield, WI 53220; gsamolyk@wi.rr.com

Received March 4, 2021; revised August 6, 2021, February 23, June 27, 2022; accepted July 2, 2022

Abstract This paper describes the acquisition of CCD-derived photometric data from two eclipsing overcontact binaries, NY Boo and V508 Cyg. Astrophotography filters (blue and green) were used, but measurements were transformed to the Johnson-Cousins standard using the reference star fields in M67. Aside from producing period-folded light curves for both variable systems, new times-of-minimum were added to other literature values in order to update each ephemeris.

1. Introduction

NY Boo and V508 Cyg are eclipsing binaries of the W UMa type (EW), many of which are characterized by a high amplitude in their light curves and continuous changes of the light curve. Since the outer atmospheres of the two stars are in contact, in many cases orbital periods are less than 1 day. In addition, mass transfer between the two components and/or angular momentum loss can cause long-term changes in the orbital period. Both systems currently lack detailed studies of their light curves and orbital parameters. The measurements and analyses performed herein help close the knowledge gap for these poorly studied systems. Both stars, with maximal visual magnitudes of 11.97 for NY Boo and 12.50 for V508 Cyg, are within the light grasp of modestly sized telescopes of about 15 to 30 cm.

2. Observations

CCD photometry of the eclipsing variable stars NY Boo and V508 Cyg was performed using a 13-inch Newtonian telescope (f/4) connected to a Moravian g2-1603 CCD camera cooled at –15° C. The FOV was 35×25 arcmin^2 and the plate scale is 1.46×1.46 arcsec^2/pixel. To perform wideband photometry the Deep-Sky GWB and BWB filter set from the company Astronomik (Astronomik 2020) was used. The obtained images were corrected by twilight flats, bias, and darks using the software AstroArt 6 (MSB Software 1998–2022).

Measurements using these filters were transformed to Johnson B and V values, and were then uploaded to the AAVSO International Database, where they fit well with data from other observers.

Figure 1 shows the transmission curves of the wide-band filters used, compared to those of standard Johnson filters.

The observations were made on six nights between 24 August and 12 September 2020 for NY Boo, and on seven nights between 24 October and 18 November 2020 for V508 Cyg. The exposure time for every frame was 120 s; a filter change (BWB, GWB, BWB, …) was performed between each recording throughout each imaging session. Using the Julian Date, the astrometric coordinates, and the geographical coordinates of the observatory, the Heliocentric Julian Date (HJD) for center of exposures was calculated.

The photometric evaluations were performed with the help of self-written programs (jupyter notebooks) based on Photutils (Bradley 2020), a module package of Astropy (Astropy Collab. *et al.* 2013). To get the instrumental magnitudes an aperture radius of five pixels was chosen, which is about one-and-a-half to double the size of the full width half maximum (FWHM) of the stars. The transformation to Johnson V and B bandpass standards was achieved using measured coefficients of first-order calculated from the standard star field M67.

Subsequently, with the help of the American Association of Variable Star Observers (AAVSO) Photometric All-Sky Survey (APASS; Henden *et al*. 2009) suitable reference stars with constant brightness and where possible nearly the same color as the variable stars were selected. With these differential photometric analysis was performed. The coordinates and magnitudes of the comparison stars used were given by the APASS catalogue and are summarized in Table 1. In Table 1, the Name field gives the names of the variables and identifications for the comparison stars. The number following the first part of the comparison star name (e.g. C0, C1) is the record number from APASS.

Figure 2 shows the field of NY Boo (in center) and the selected reference stars C0, C1, and C2 as well as the check star (CS = C3). The field of V508 Cyg with selected reference stars is shown in Figure 3.

Dense star fields like that around V508 Cyg are usually best handled by point spread function (PSF) photometry, however, there are very few programs accessible to amateurs which feature this ability. Since care was taken to ensure that no other stars lie in the measurement aperture (5 pixels), in our case the aperture method was sufficient.

After choosing suitable comparison stars their relative fluxes were determined via Equation 1:

$$\varphi_{i,rel} = \frac{\varphi_i}{\frac{1}{K-1}\sum_{k \neq i}^{K} \varphi_k} \quad (1)$$

Table 1. Variable stars and selected comparison stars for NY Boo and V508 Cyg with data from APASS (Henden *et al.* 2009).

Stat	*R.A. (2000) (°)*	*Dec. (2000) (°)*	*B*	*e_B*	*V*	*e_V*	*B – V*	*e_B – V*
NY Boo	225.2900	48.8044	12.773	0.244	12.128	0.229	0.640	0.330
	225.4580	48.8040	13.206	0.028	12.484	0.019	0.723	0.034
	225.0118	48.8985	12.888	0.008	12.154	0.041	0.734	0.042
	225.0295	48.8232	12.934	0.025	12.202	0.039	0.733	0.046
	225.2930	48.8976	13.141	0.017	12.334	0.026	0.806	0.032
V508 Cyg	308.5249	46.8711	14.034	0.245	12.918	0.435	1.116	0.499
	308.5002	46.8247	12.401	0.103	11.745	0.053	0.656	0.116
	308.3520	46.8023	12.261	0.109	11.603	0.057	0.658	0.123
	308.3519	46.9300	12.512	0.132	11.797	0.045	0.715	0.140

Table 2. Time of minima (ToM - 2.459e6) and calculated periods P.

Star	*Filter*	*ToM-1*	*σ*	*ToM-2*	σ	*ToM-3*	*σ*	*P/d*
NY Boo	V	86.4135	5.E–04	97.3615	4.E–04	105.3685	5.E–04	0.32678 ± 2e–5
	B	86.4159	8.E–04	97.3607	9.E–04	105.3682	8.E–04	
V508 Cyg	V	147.3183	4.E–04	159.4043	6.E–04	172.2676	5.E–04	0.77967 ± 1e–5
	B	147.3200	8.E–04	159.4032	8.E–04	172.2685	6.E–04	

Table 3. NY Boo ToM, Error, Type of Minima as well as Cycle Number and O – C which are calculated using the following light elements: t_n = 2459105.1980, P_n = 0.3267912.

Min. HJD	*HJD err*	*Typ*	*Epoch*	*O – C*	*Reference*
2456021.9009	0.0014	I	–9435.0	–0.02191	Diethelm (2012)
2456065.3823	0.0016	I	–9302.0	–0.00374	Hubscher and Lehmann (2013)
2456737.6407	0.0002	I	–7245.0	0.04512	Hoňková *et al.* (2015)
2456742.5429	0.0025	I	–7230.0	0.04545	Hubscher and Lehmann (2015)
2456746.3993	0.0004	I	–7218.0	–0.01965	Juryšek *et al.* (2017)
2457561.4174	0.0006	I	–4724.0	–0.01885	Juryšek *et al.* (2017)
2457879.5185	0.0007	II	–3750.5	–0.04901	Pagel (2018)
2459062.3895	0.0003	I	–131.0	0.00116	Samolyk (2020)
2459086.4153	0.0006	II	–57.5	0.00781	this paper
2459097.3615	0.0006	I	–24.0	0.00650	this paper
2459105.3685	0.0005	II	0.5	0.00712	this paper

Table 4. Fit parameters for NY Boo with one-σ uncertainties.

Linear fit parameters / NY Boo	
a_0	$-(0.0 \pm 1.4) \times 10^{-2}$
a_1	$+(0.0 \pm 2.4) \times 10^{-6}$

where φ represents the counts in ADU, i is the index of the selected star, and K is the total number of comparison stars. The results normalized relative to 1 are depicted in Figure 4 for NY Boo and in Figure 5 for V508 Cyg. As necessary a constant offset has been added to individual comparison stars to help visually differentiate the curves.

As can be seen, the flux of all comparison stars remained constant for the duration of the imaging sessions. The outliers below n = 20 and above n = 200 in Figure 4 result from the influence of high cirrus clouds passing through. These as well as the corresponding measurements for NY Boo were eliminated from consideration if deviations above 3σ (standard deviation) occurred. Hereafter, we chose C3 to be the check star (CS). Figure 5 for V508 Cyg shows a constant output in brightness for the selected comparison stars. Again, all measurements above 3σ were rejected for further calculations.

For later discussions, the following plots (Figures 6 and 7) also show the air mass of the measurements. Values above air mass 2.0 were also used but since the target and comparison stars had similar colors (B–V) they were not expected to suffer severely from differential refraction and/or color extinction.

Since the bandpass filters are changed alternately after each recording, a Savitzky-Golay (Savitzky and Golay 1964) filter was applied to interpolate (dotted curves in Figure 8), and thus generated simultaneous values for BWB and GWB for the B,V transformations. The Savitzky-Golay filter is an optimized low-pass filter for data smoothing removing high frequency noise, preserving the shape of a curve.

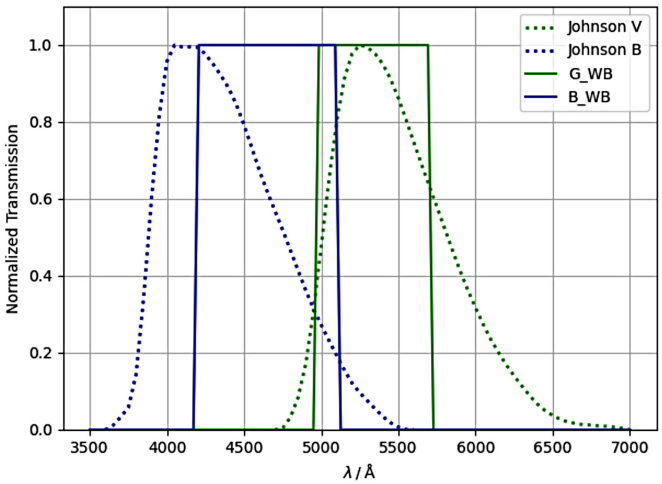

Figure 1. Normalized transmission curves of the used wide-band filters (G_{WB}, B_{WB}) and the corresponding Johnson filters.

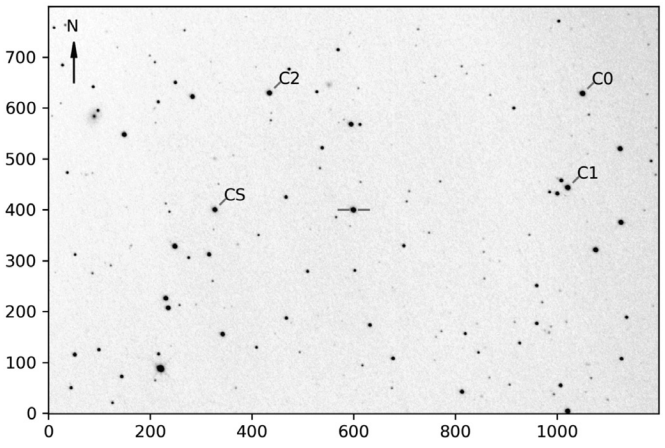

Figure 2. NY Boo with check (CS) and comparison stars (C0 to C2). The image field-of-view is 30 × 20 arcmin².

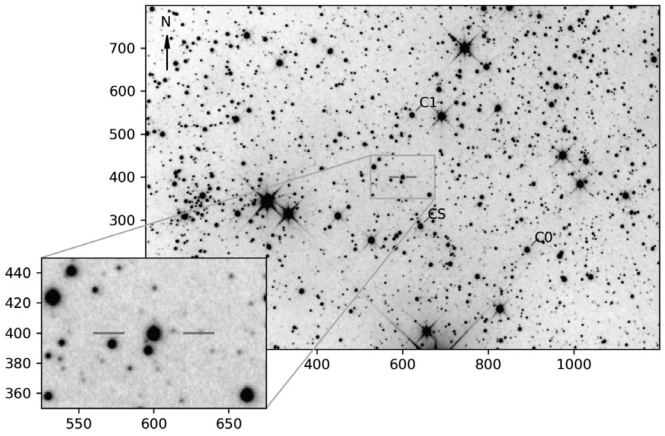

Figure 3. The image field for V508 Cyg with check (CS) and comparison stars (C0 and C2). In addition, the star-rich area around V508 has been enlarged. The FOV of the non-enlargement is 30 × 20 arcmin²; scale of inset: 3.7 × 2.5 arcmin².

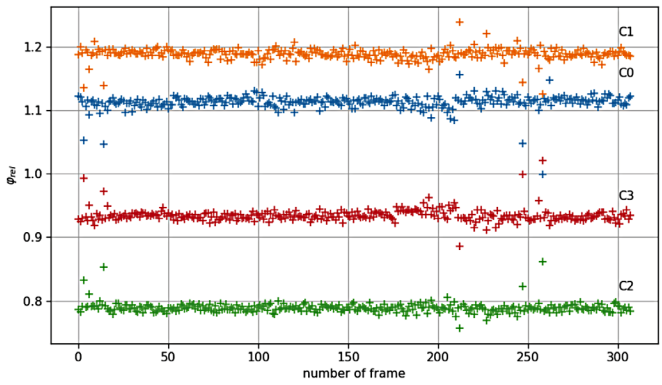

Figure 4. Relative flux for each comparison star used with NY Boo (filter = G_{WB}).

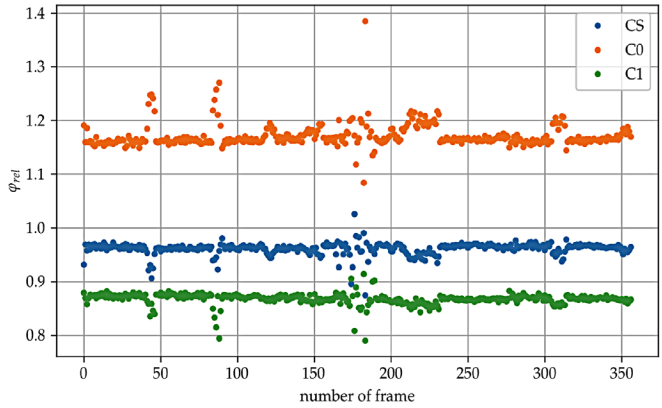

Figure 5. Relative flux for each comparison star used for V508 Cyg (filter = G_{WB}).

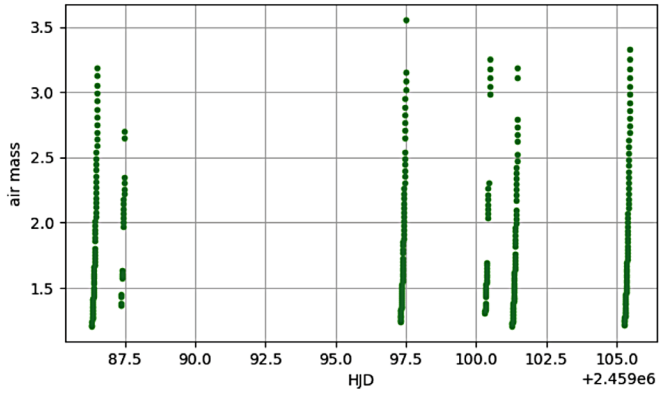

Figure 6. Air mass vs. HJD for NY Boo.

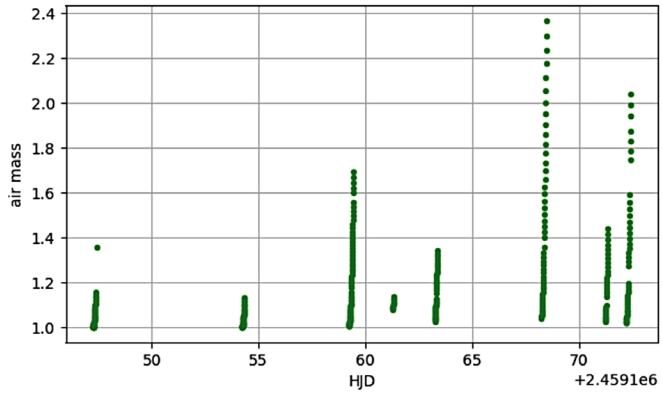

Figure 7. Air mass vs. HJD for V508 Cyg.

3. Times-of-Minima (ToM), Observed-minus-Calculated (O–C), and phase diagrams

3.1. ToM and O–C analysis

To determine the orbital period of the binaries, the times-of-minima (ToM) were calculated using all available data showing a minimum. To calculate each ToM value a slightly modified Kwee and Van Woerden method (Corp 2018) was used, whereby the light curve measurements around each minimum were smoothed with a Savitzky-Golay (SG) filter. The resulting curves were then mirrored at a point in time so that the descending and ascending branches lie above each other. To achieve this, a least square fit according to Equation 2 was performed:

$$\mathrm{Min}(t) = \left[\tfrac{1}{N}\,\Sigma_k\,(V(t - k\Delta t) - V(t + k\Delta t))\right]^{\frac{1}{2}} \qquad (2)$$

A typical result is given in Figure 9 for NY Boo.

Since no model is available at this time, the uncertainty of the ToM is determined by errors of the individual measurements and the symmetry of the curve. Figure 10 shows the curves mirrored at ToM and overlaid. The curve symmetry also determines the evaluation range for the determination of the minimum. As long as the deviations between both branches are smaller than the statistical error of the individual measurements of magnitudes, the curve is used for evaluation. In order to determine the uncertainty, the measurement points were varied within the limits of their uncertainty by means of Monte Carlo simulation and then the curve was evaluated. The scatter of the values obtained in this way was taken as the uncertainty of ToM. Because the timing is very accurate (about 1 to 2 s), its influence was neglected. With this method uncertainties in the range of 20 to 40 s (0.0002 to 0.0005 d) are obtained, depending on the course of the curves.
The same is depicted in Figures 11 and 12 for V508 Cyg.

Table 2 shows the results for both binaries. The periods P are determined using the following equations:

$$n = \mathrm{round}\left(\frac{ToM_2 - ToM_1}{P_{VSX}}\right) \qquad (3)$$

$$P = \left(\frac{ToM_2 - ToM_1}{n}\right) \qquad (4)$$

Thereby a first estimation based on the VSX data (Watson *et al.* 2014) was used (Equation 3). Afterwards Equation 4 yields the new value for the period. In addition the O–C values are calculated.

These updated orbital periods show small deviations from the original values reported by VSX for NY Boo (0.32679 d) and V508 Cyg (0.77966 d).

An O–C diagram is constructed by plotting observed ToM values minus those calculated from an ephemeris equation (y-axis) versus the corresponding epoch (x-axis). The resulting plot can be used to detect any change(s) in the orbital period of a binary star. In order to produce the necessary O–C diagrams, an ephemeris was updated using the ToM values for NY Boo (Table 3). With each new ephemeris, the old parameters (epoch t_0, period P_0) and under certain circumstances a third parameter c0 are used to calculate the observed minus calculated residuals. Depending on their behavior these are fitted using a linear or quadratic expression (see Equation 5). A straight-line relationship means the period has not changed over the defined epoch. Those O–C vs epoch plots best fit with a quadratic curve indicates a constant period change.

$$(O-C)_0 = \mathrm{ToM}(E) - (t_0 + P_0 \cdot E + c_0 \cdot E^2) = a_0 + a_1 \cdot E + a_2 \cdot E^2 \qquad (5)$$

To obtain new parameters (epoch t_n, period P_n, c_n), the O–C values have to fulfill the following condition (Equation 6):

$$(O-C)_0 = \mathrm{ToM}(E) - (t_n + P_n \cdot E + c_n \cdot E^2) = 0 \qquad (6)$$

After subtracting Equations 5 and 6 from each other and performing a coefficient comparison, the following new parameters are obtained:

$$\begin{aligned} t_n &= t_0 + a_0 \\ P_n &= P_0 + a_1 \\ c_n &= c_0 + a_2 \end{aligned} \qquad (7)$$

In addition, the fit provides the uncertainties of the parameters. Whether a linear or quadratic fit has to be used can be seen from the resulting preliminary O–C curve and the residuals of the fit.

By applying Equations 5 and 6 to historical and current ToM data new O–C values are achieved. In Figure 13 and Table 3 the results are depicted for NY Boo. Table 4 shows the corresponding fit parameters.

The updated ephemeris for NY Boo is:

$$\begin{aligned} &\mathrm{Min.(HJD)} = 2459105.1980 \pm 0.014 \\ &+ (0.32679122 \pm 0.0000024) \times E. \end{aligned} \qquad (8)$$

The situation is completely different with V508 Cyg. Only CCD data for the years 1992 to 2020 are used for the evaluation. Older photographic measurements do not fit very well. Due to the large scatter in data only the most recent data are used to calculate a linear ephemeris. The following plot (Figure 14) shows the data used and the linear fit.

A linear fit which can be used for the next few years yields the following ephemeris:

$$\begin{aligned} &\mathrm{Min.\ (HJD)} = 2459172.26816 \pm 0.00029 \\ &+ (0.7796603 \pm 0.0000001) \times E. \end{aligned} \qquad (9)$$

If the whole data set is considered a quadratic fit works best. All data used as well as the fit results are show in Figure 15.

The quadratic ephemeris is

$$\begin{aligned} &\mathrm{Min\,(HJD)} = 2459172.2629 \pm 0.0013 \\ &+ (0.7796610 \pm 0.0000045) \times E \\ &+ (1.63 \pm 0.29) \times 10^{-10} \times E^2 \end{aligned} \qquad (10)$$

The complete data set for V508 Cyg together with the references is given in Table 5.

Table 5. ToM, Error, Type of Minima as well as Epoch and O–C data for V508 Cyg.

Min HDJ	*HDJ err*	*Typ*	*Epoch*	*O – C*	*Reference*
2448834.7945	0.0005	I	–13259.0	0.0425	Goderya *et al.* (1995)
2448884.6923	0.0004	I	–13195.0	0.0420	Goderya *et al.* (1995)
2448887.8134	0.0006	I	–13191.0	0.0445	Goderya *et al.* (1995)
2448888.5912	0.0007	I	–13190.0	0.0426	Goderya *et al.* (1995)
2448889.7624	0.0001	II	–13188.5	0.0443	Goderya *et al.* (1995)
2448898.7279	0.0006	I	–13177.0	0.0437	Goderya *et al.* (1995)
2448916.6618	0.0004	I	–13154.0	0.0454	Goderya *et al.* (1995)
2448939.6589	0.0007	II	–13124.5	0.0425	Goderya *et al.* (1995)
2448834.7946	0.0003	I	–13259.0	0.0426	Goderya *et al.* (1995)
2448884.6924	0.0004	I	–13195.0	0.0421	Goderya *et al.* (1995)
2448887.8140	0.0001	I	–13191.0	0.0451	Goderya *et al.* (1995)
2448888.5999	0.0016	I	–13190.0	0.0513	Goderya *et al.* (1995)
2448889.7633	0.0013	II	–13188.5	0.0452	Goderya *et al.* (1995)
2448898.7281	0.0006	I	–13177.0	0.0439	Goderya *et al.* (1995)
2448916.6622	0.0005	I	–13154.0	0.0458	Goderya *et al.* (1995)
2448939.6591	0.0005	II	–13124.5	0.0427	Goderya *et al.* (1995)
2452802.4672	0.0027	I	–8170.0	0.0238	Hubscher *et al.* (2005)
2452834.4374	0.002	I	–8129.0	0.0279	Hubscher *et al.* (2005)
2452862.5056	0.0016	I	–8093.0	0.0284	Hubscher (2007)
2452864.4531	0.0011	II	–8090.5	0.0267	Hubscher *et al.* (2005)
2452867.5747	0.003	II	–8086.5	0.0297	Hubscher *et al.* (2005)
2452946.3186	0.0004	II	–7985.5	0.0279	Hubscher *et al.* (2005)
2453216.4645	0.0005	I	–7639.0	0.0215	Hubscher *et al.* (2005)
2453221.5264	0.0011	II	–7632.5	0.0156	Hubscher *et al.* (2005)
2453579.3945	0.0003	II	–7173.5	0.0196	Hubscher *et al.* (2006)
2453607.4575	0.0012	II	–7137.5	0.0148	Hubscher (2007)
2453612.5275	0.0009	I	–7131.0	0.0170	Hubscher *et al.* (2006)
2453621.4931	0.0008	II	–7119.5	0.0166	Hubscher *et al.* (2006)
2453637.4756	0.0013	I	–7099.0	0.0160	Hubscher *et al.* (2006)
2454073.3021	0.0002	I	–6540.0	0.0124	Hubscher and Walter (2007)
2455075.5525	0.0004	II	–5254.5	0.0095	Hubscher *et al.* (2010)
2455366.7537	0.0005	I	–4881.0	0.0075	Diethelm (2010)
2455817.3934	0.0001	I	–4303.0	0.0036	Hoňková *et al.* (2013)
2455838.4419	0.0003	I	–4276.0	0.0012	Hoňková *et al.* (2013)
2455838.4424	0.0002	I	–4276.0	0.0017	Hoňková *et al.* (2013)
2455838.4427	0.0006	I	–4276.0	0.0020	Hoňková *et al.* (2013)
2456169.4076	0.0004	II	–3851.5	0.0011	Hoňková *et al.* (2013)
2456169.4078	0.0002	II	–3851.5	0.0013	Hoňková *et al.* (2013)
2456169.4086	0.0004	II	–3851.5	0.0021	Hoňková *et al.* (2013)
2456461.3875	0.0006	I	–3477.0	–0.0017	Hoňková *et al.* (2015)
2456461.3897	0.0003	I	–3477.0	0.0005	Hoňková *et al.* (2015)
2456461.3902	0.0003	I	–3477.0	0.0010	Hoňková *et al.* (2015)
2456482.4406	0.0004	I	–3450.0	0.0005	Hoňková *et al.* (2015)
2456482.4406	0.0003	I	–3450.0	0.0005	Hoňková *et al.* (2015)
2456482.4407	0.0002	I	–3450.0	0.0006	Hoňková *et al.* (2015)
2456491.4064	0.0002	II	–3438.5	0.0002	Hoňková *et al.* (2015)
2456491.4070	0.0002	II	–3438.5	0.0008	Hoňková *et al.* (2015)
2456491.4072	0.0005	II	–3438.5	0.0010	Hoňková *et al.* (2015)
2456496.4725	0.0004	I	–3432.0	–0.0015	Hoňková *et al.* (2015)
2456496.4729	0.0002	I	–3432.0	–0.0011	Hoňková *et al.* (2015)
2456496.4734	0.0002	I	–3432.0	–0.0006	Hoňková *et al.* (2015)
2456500.3727	0.0004	I	–3427.0	0.0004	Hoňková *et al.* (2015)
2456500.3728	0.0005	I	–3427.0	0.0005	Hoňková *et al.* (2015)
2456500.3731	0.0006	I	–3427.0	0.0008	Hoňková *et al.* (2015)
2456501.5411	0.0003	II	–3425.5	–0.0006	Hoňková *et al.* (2015)
2456501.5415	0.0003	II	–3425.5	–0.0002	Hoňková *et al.* (2015)
2456501.5419	0.0003	II	–3425.5	0.0002	Hoňková *et al.* (2015)
2456542.4734	0.0002	I	–3373.0	–0.0005	Hoňková *et al.* (2015)
2456542.4735	0.0004	I	–3373.0	–0.0004	Hoňková *et al.* (2015)
2456542.4739	0.0002	I	–3373.0	0.0000	Hoňková *et al.* (2015)
2456569.3717	0.0002	II	–3338.5	–0.0005	Hoňková *et al.* (2015)
2456569.3720	0.0002	II	–3338.5	–0.0002	Hoňková *et al.* (2015)
2456569.3721	0.0003	II	–3338.5	–0.0001	Hoňková *et al.* (2015)
2456878.5074	0.0002	I	–2942.0	–0.0001	Hoňková *et al.* (2015)
2456878.5076	0.0002	I	–2942.0	0.0001	Hoňková *et al.* (2015)
2456878.5078	0.0004	I	–2942.0	0.0003	Hoňková *et al.* (2015)
2459147.3183	0.0004	I	–32.0	–0.0007	this paper
2459159.4043	0.0008	II	–16.5	0.0005	this paper
2459172.2676	0.0008	I	0.0	–0.0006	this paper
2459147.3200	0.0006	I	–32.0	0.0010	this paper
2459159.4032	0.0005	II	–16.5	–0.0006	this paper
2459172.2685	0.0006	I	0.0	0.0003	this paper

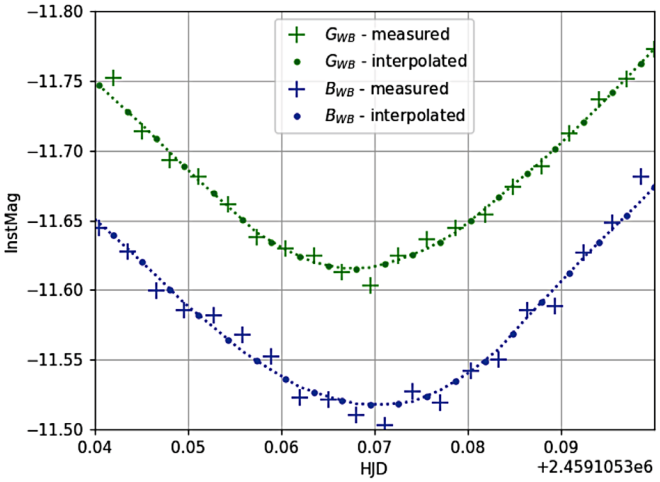

Figure 8. Example of an interpolation (dotted lines) for NY Boo (20-08-24) using a Savitzky-Golay filter (Savitzky and Golay 1964) to obtain simultaneous pairs of B_{WB}, G_{WB} data (instrumental magnitudes) for B, V transformations. Values for the B_{WB} bandpass are shifted by –0.20 mag to simplify comparison with the G_{WB} curve.

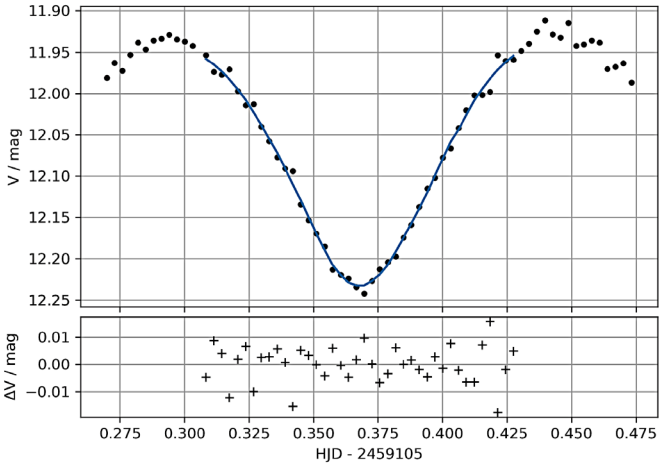

Figure 9. Upper: V-band measurements (•) of NY Boo and smoothed curve with SG filter (-); lower: the difference between both (+).

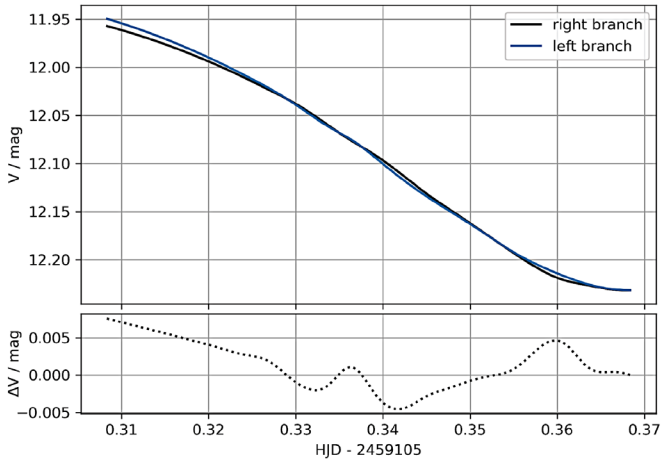

Figure 10. Upper: the interpolated right V branch of NY Boo corresponding to Figure 9, mirrored at t_{TOM} = 2459105.36843 ± 0.0005 to the left one; lower: the difference ΔV between both branches is plotted.

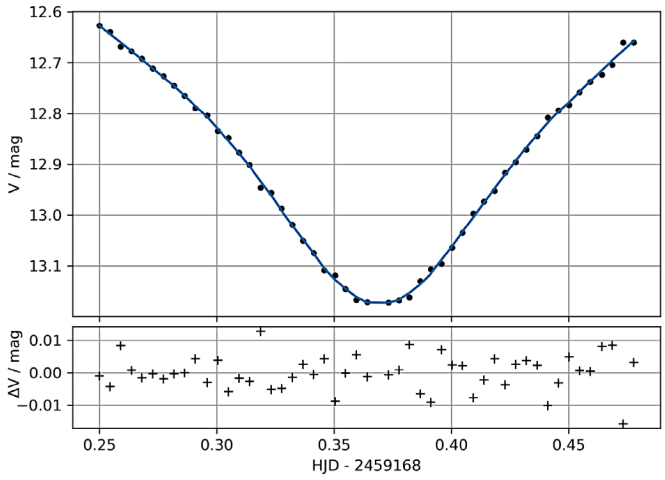

Figure 11. Upper: V band measurements (•) at V508 Cyg, smoothed curve (-); lower: the difference between both (+).

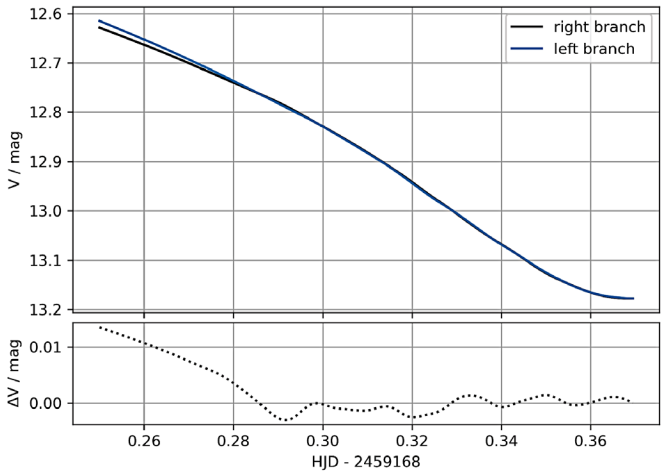

Figure 12. Upper: the right V branch of V508 Cyg (Figure 11), mirrored at tToM = 2459168.36956 ± 0.0003 to the left one; lower: the difference ΔV between the branches (Please note that in this case ΔV/mag ranges between 0.01 and some value around 0.005).

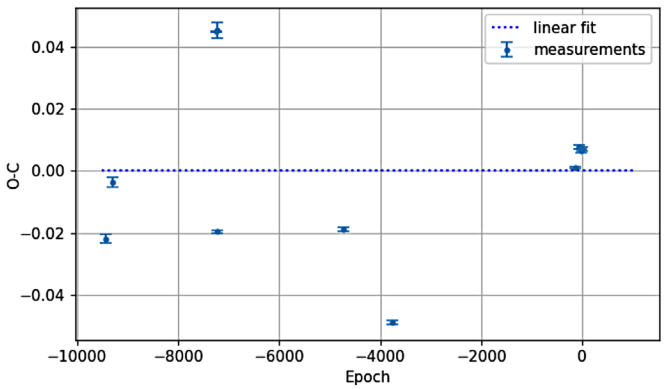

Figure 13. The best linear fit of the O–C data from NY Boo producing an intercept and a slope of 0.

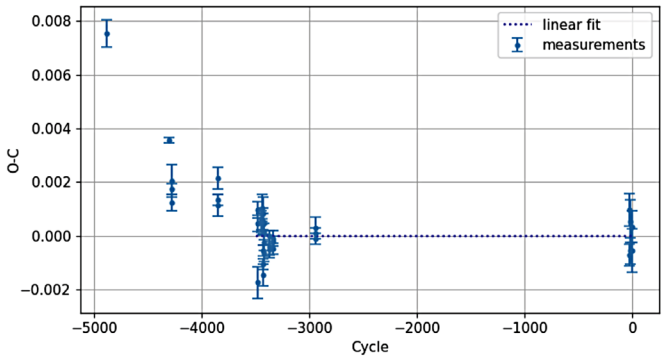

Figure 14. V508 Cyg O–C residuals for linear fit.

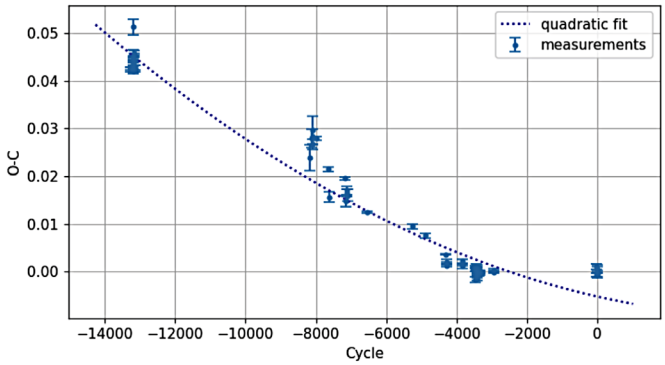

Figure 15. O–C data for V508 Cyg together with the quadratic fit curve ($a2 = (1.63 \pm 0.29) \times 10^{-10}$).

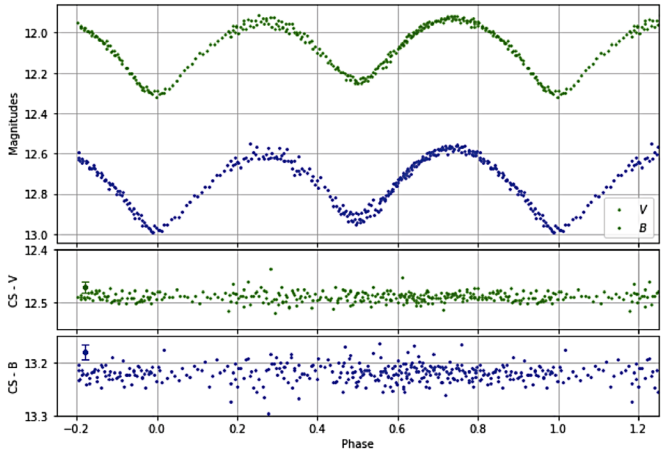

Figure 16. Phase diagram of period-folded (P = 0.326779) light curves for NY Boo in V and B. In addition the measurements of the check star (CS) are depicted below. The error bar, representing the standard deviation, is given within the subplots.

3. 2. Phase-analysis

With the help of the ToM values and the periods P obtained with Equation 4 the phase diagrams were calculated using the following equation:

$$\text{Phase} = \frac{\text{ToM}_1 - t}{P} - \text{integer}\left(\frac{\text{ToM}_1 - t}{P}\right) \qquad (11)$$

The results for NY Boo are shown in Figure 16.

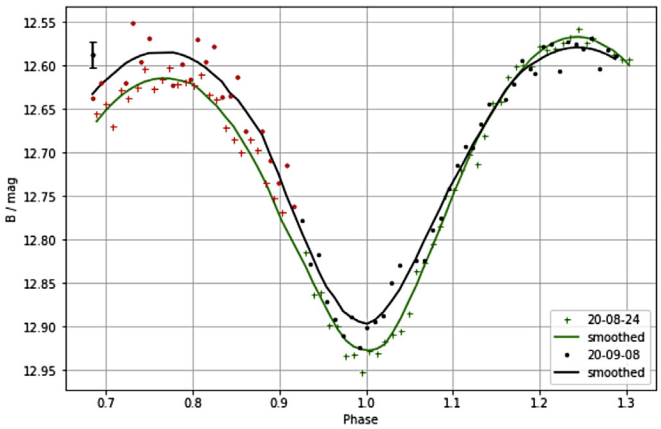

Figure 17. Phase diagram of two measurements series showing a systematic difference in B for NY Boo. The red symbols indicate air mass values larger than 2.

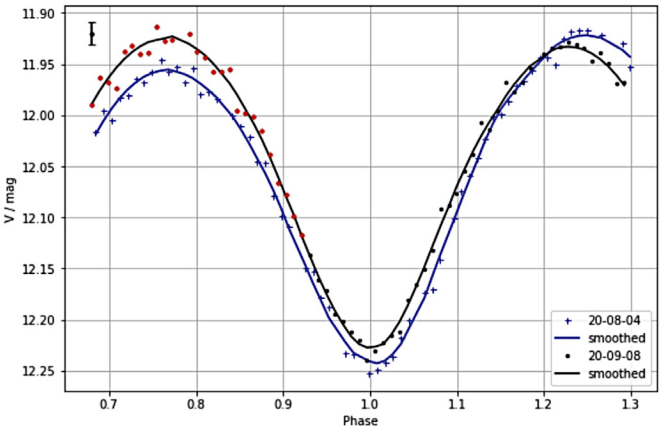

Figure 18. Phase diagram from two different dates showing a systematic difference in V for NY Boo. The red symbols indicate air mass values larger than 2.

The light curves show variations between 12.57 and 12.93 in B and between 11.93 and 12.25 in V, respectively. The difference between both filters remained constant throughout the light curves, suggesting that there is very little difference in effective temperature (T_{eff}). The color index B–V of NY Boo has a value of 0.66 ± 0.03. A primary minimum can clearly be seen (Phase = 0 and Phase = 1).

The standard deviations for the check star are in the range of 0.008 for the V filter and 0.012 for the B filter, respectively. The period-folded curves produced from data acquired between August 24, 2020, and September 12, 2020, exhibit much more scatter than would be expected. This may indicate that some event on NY Boo changed the light curve between these two relatively close dates. To investigate this further, two selected curves measured at different times (August 24, 2020, and September 8, 2020) were plotted with different symbols (Figures 17 and 18). In addition, the curves were smoothed with an SG filter. The curves clearly show a slight change of about 0.05 mag in both B and V.

On closer inspection it is noticeable that the maxima are not at the same height. The maximum difference in Figure 18 is about 0.05 mag on August 24, 2020.

To investigate whether the differences in the light curve from both dates are due to atmospheric or zeropoint effects, the behavior of the check star was analyzed in detail (see Figure 19). The difference between the mean values of the considered measurement periods are below 0.002. The standard deviations of the check star measurement at both periods are smaller than 0.01. No jumps or drift is noticeable. Considering also that the color difference between variable star and check star is only about 0.1—there should be minimal extinction effects—it can be assumed that the curves are related to varying stellar properties such as sun spots or an inhomogeneous rotating gas envelope.

To analyze color changes during darkening, the color index B-V was plotted versus phase in Figure 20. The plotted uncertainties result from the fluctuations within the two regions ($\varphi = 0$ to 0.5 and $\varphi = 0.5$ to 1). Due to the uncertainties, only small changes of $\Delta(B–V) = 0.04 \pm 0.02$ in the range 0 to 0.5 can be detected.

Figure 21 shows the same brightness investigations that were performed for the check star of V508 Cyg, which was also found to be very constant.

The phase diagram for V508 Cyg shown in Figure 22 was calculated in the same way as that for NY Boo. In contrast to NY Boo it shows no light curve anomalies. Here the maxima and minima are the same, making it impossible to visually determine which one is the primary minimum. Nonetheless, based on the linear ephemeris (Equation 8) the primary minimum (Min I) was predicted to occur on 2459147.3183, 24590147.3200, 2459172.2676, and 2459172.2685.

The light curve shows variations between 13.85 and 14.55 in B and between 12.50 and 13.18 in V, respectively. The color index B–V of this binary has a value of about 1.37 ± 0.05 (mean value during the measurement periods) and shows no variations within the uncertainties (see Figure 23).

4. Stellar properties

To accurately determine stellar temperatures, it is essential to take into account the influence of gas and dust in the galactic disk. Assuming a distance for NY Boo of D = (391) pc given in Bailer-Jones Gaia DR2 (Bailer-Jones 2015; Eur. Space Agency 2018), the interstellar extinction AV can be calculated using models A of Amôres and Lépine (2005) and A2 (Amôres and Lépine 2007). The latter takes into account the spiral structure of our galaxy. The resulting values are $A1_V = 0.10$ for the A model and $A2_V = 0.10$ for A2, respectively. In this case both models yield the same value. This allows the calculation of the color shift, i.e. reddening, using Equation 12 given in Amôres and Lépine (2005):

$$E(B-V) = \frac{A_V}{3.1} \qquad (12)$$

To obtain the intrinsic color Equation 13 was applied:

$$(B-V)_0 = (B-V) - E(B-V) \qquad (13)$$

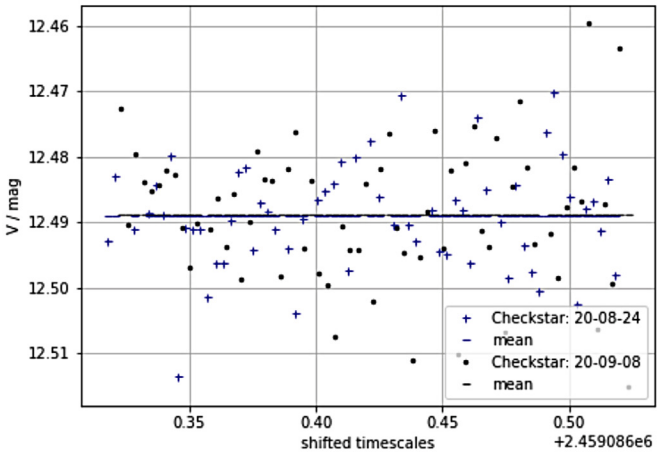

Figure 19. Brightness measurements of the check star for NY Boo on two different observation nights.

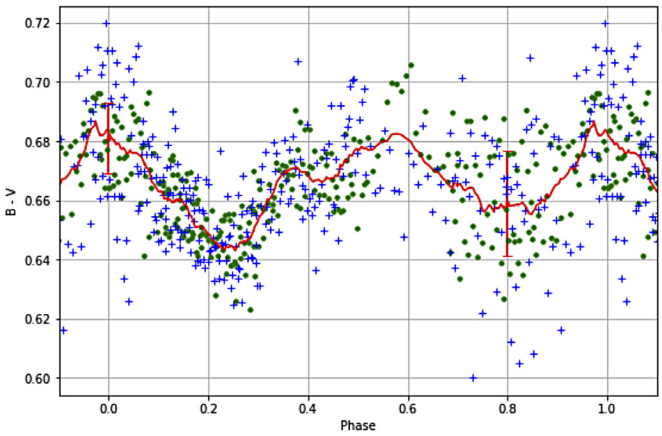

Figure 20. Moving average of (B–V) (red line) as well as B–V (blue +) and B–V (green •) of NY Boo.

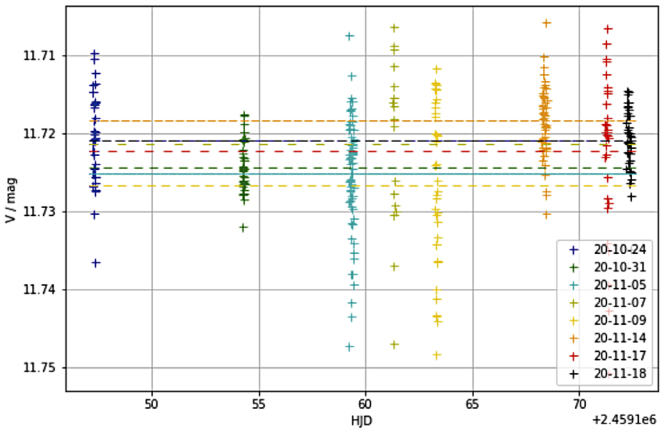

Figure 21. Brightness measurements of the check star for V508 Cyg for all observation nights.

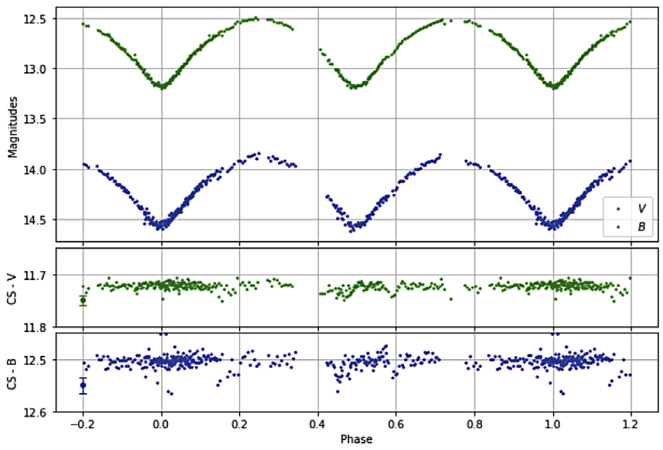

Figure 22. Phase diagram of period-folded light curves for V508 Cyg in V and B.

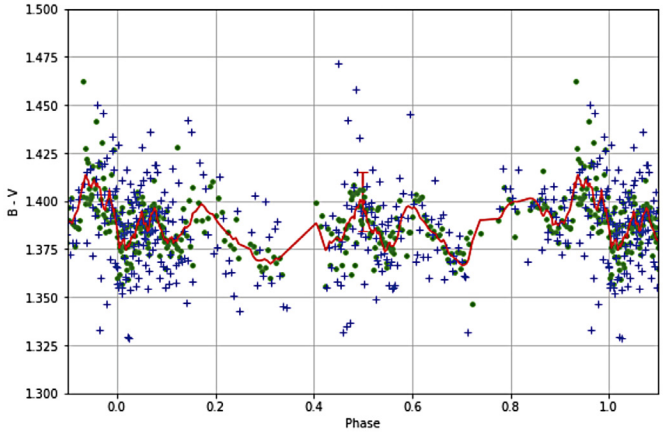

Figure 23. Moving average of (B–V) (red line) as well as B–V (blue +) and B–V (green •) for V508 Cyg.

To calculate the effective temperatures T_{eff} and the bolometric correction (BC) the polynomial approaches given by Flower (1996) and Torres (2010) were used. With the help of the distance modulus (Equation 14) and the bolometric correction (Equation 15) the values given in Table 5 were calculated.

$$M_v = V - A_V + 5 - 5\log\left(\frac{D}{pc}\right) \quad (14)$$

$$M_{bol} = M_V + BC \quad (15)$$

Besides the above equation for the determination of M_V via the distance modulus, there is, according to Rucinski and Duerbeck (1997), the possibility to determine the absolute magnitude of overcontact binary stars on the basis of their orbital period.

$$M_V(P) = -4.44\log(P) + 3.02\,(B-V)_0 + 0.12 \quad (16)$$

Equation 16 is valid for periods P = 0.2 to about 1.0 d. Our results calculated using this equation are denoted "This study" in Tables 6 and 7.

Table 6. A comparison of values for NY Boo reported in Gaia DR2 and those determined with our data for T_{eff}, BC, M_V, M_{bol}, L, and R.

	Gaia DR2	σ	*This Study*	σ
D/pc	391.8	–3.7/+3.8	346	7
A_V	—	—	0.098	0.001
(B–V)	—	—	0.66	0.01
$(B-V)_0$	—	—	0.63	0.01
T_{eff}/(K)	5668	–225/+162	5791	48
M_V	—	—	4.17	0.04
BC	—	—	–0.077	0.001
M_{bol}	—	—	4.01	0.09
$L/L_\odot$	1.76	0.03	1.54	0.06
$R/R_\odot$	1.37	–0.07/+0.12	1.23	0.03

Table 7. A comparison of values for V508 Cyg reported in Gaia DR2 and those determined with our data for T_{eff}, BC, M_V, M_{bol}, L, and R.

		Gaia DR2	σ	*This Study*	σ
D/pc		2892	–186/+212	447	53
$A1_V$		—	—	0.25	0.001
$A2_V$		—	—	1.49	0.28
(B–V)		—	—	1.37	0.05
$(B-V)_0$	$A1_V$	—	—	1.27	0.01
$(B-V)_0$	$A2_V$	—	—	0.89	0.10
T_{eff}/(K)		4597	–159/+421		
	$A1_V$			4333	83
	$A2_V$			5079	227
M_V	$A1_V$	—	—	4.49	0.15
	$A2_V$	—	—	3.28	0.31
BC	$A1_V$	—	—	–0.74	0.05
	$A2_V$	—	—	–0.27	0.09
M_{bol}	$A1_V$	—	—	5.23	0.16
	$A2_V$	—	—	3.56	0.32
$L/L_\odot$		102.3	–13.3/+13.3		
	$A1_V$	—	—	0.63	0.09
	$A2_V$	—	—	2.92	0.85
$R/R_\odot$	$A1_V$	15.95	–2.57/+1.16	1.40	0.11
	$A2_V$			2.21	0.38

To calculate the luminosity L and the radius R of one star of the investigated binaries with respect to our sun the following relations were used:

$$\frac{L}{L_\odot} = \frac{1}{2}\,10^{-0.4(M_{bol}-4.72)} \quad (17)$$

$$\frac{R}{R_\odot} = \left(\frac{1}{2}\,\frac{T_{eff,\odot}^4}{T_{eff}^4}\,10^{-0.4(M_{bol}-4.72)}\right)^{\frac{1}{2}} \quad (18)$$

In the following tables the results are given for both binaries, NY Boo (Table 6) and V508 Cyg (Table 7), respectively. The uncertainties of dependent variables were calculated using the appropriate rules for error propagation.

The same equations were applied to obtain the values for V508 Cyg. However, the position of V508 Cyg within a large nebulous region of Cygnus created a significant challenge to obtaining a realistic value for reddening, the intrinsic color $(B–V)_0$, and ultimately the effective temperature, size, and luminosity.

Looking at the results obtained from Gaia DR2, which are not adjusted for interstellar extinction, it should be fairly obvious that something is amiss with the reported distance to V508 Cyg. The calculated size (~16 $R_\odot$) and luminosity (~102 $L_\odot$) could only come from a giant star, a highly unlikely candidate for an overcontact binary with an orbital period less than 1 day.

Given the dusty region where V508 Cyg resides, results from the empirical relationship (Equation 16) described by Rucinski and Duerbeck (1997) may be biased due to significant extinction that is likely to be experienced with B and, to a lesser extent, V. Gettel *et al.* (2006) report an empirical relationship for distance (pc) where:

$$\log D = 0.2\ V_{max} - 0.18 \log (P) - 1.60\ (J - H) + 0.56. \quad (19)$$

At longer wavelengths (J and H), reduced extinction is expected. In this case the calculated distance is 447 ± 53 pc. This is nearly 6.5-fold shorter distance than that reported in Gaia DR2. This results in far less interstellar extinction with Model A (A_V = .250) but similar to the value obtained with Model A2 (A_V = 1.45), which accounts for the spiral structure of our galaxy. Whether we accept the distance results from applying Equations 14–16 or Equation 19, it is very obvious that V508 Cyg is much closer (6- to 8-fold) than that reported by Gaia DR2. Therefore the range in values reported for T_{eff}, A_V, M_V, M_{bol}, R, and L suffers from much greater variability than is suggested by the formal errors reported in Table 7. A high resolution uv-vis classification spectrum would be very helpful in trying to obtain a better estimate for the effective temperature of V508 Cyg.

5. Discussion and conclusions

5.1. NY Boo

Over a relatively short period of time between August 24 and Sept 12, 2020, light curves from this binary exhibited unexpected changes, namely, the position of both curves appeared to shift by nearly 0.05 mag. One explanation for this would be a very active photosphere due to large sunspots and a high X-ray activity. There is significant scatter around Max I (Figure 16) which could be explained by the O'Connell effect. Hot or cold starspots could also be caused by irregular mass transport or an inhomogeneous dust and gas envelope (O'Connell 1951; Davidge and Milone 1984). The nearly constant B–V color (Figure 20) indicates that both components have nearly the same effective temperature, estimated by our data to be 5791 ± 48 K. Distance data D = 392 (–3.73 / +3.80) pc derived from Gaia DR2 (Bailer-Jones 2015) are calculated from very accurate parallax measurements, the gold standard for this determination. Using the distance modulus (Equation 14), our determinations of V_{max} (11.97 ± 0.008), M_V (4.17 ± 0.04) from Equation 16, A_V (0.1), and intrinsic color ($(B–V)_0$ = 0.628 ± 0.014) indicated that NY Boo is 346 ±7 pc away from Earth. In the case of NY Boo our estimate is 13% less than the parallax-derived value. We calculate a bolometric magnitude of 4.25 ± 0.04 mag from our results. Thus, with Equations 17 and 18, a luminosity of 1.57 ± 0.01 $L_\odot$ and a radius of 1.24 ± 0.01 $R_\odot$ were determined, respectively. According to low resolution UV-vis spectra reported in LAMOST DR5 (Zhou *et al.* 2009), NY Boo is classified as a main sequence G3 star. To model the light curves properly using the Wilson-Devinney code (Terrell and Wilson 2005; Terrell 2022) further measurements will have to be made. Of particular importance since both stars exhibit partial eclipses, radial velocity determinations obtained by spectroscopy will be necessary to arrive at dependable solution for the mass ratio.

5.2. V508 Cyg

V508 Cyg is an interesting case in which the parallax-derived distance reported in Gaia DR2 and Gaia DR3 is probably very wrong. There are at least two lines of evidence that suggest this possibility. If we assume for the moment that V508 Cyg is 2892 pc distant, then in order for the apparent V magnitude to be approximately 12.5, it must be rather large (~16 $R_\odot$, Table 7) for a cool star to be this visible. Contact binaries can, in principle, consist of two evolved stars. Perhaps the best investigated example is V1309 Sco (see Stepień 2011), in which two subgiants formed a contact system before they merged, producing a so-called red nova. However, a contact binary consisting of two giants with radii of several solar radii would have an orbital period much longer than 0.78 d. Thus in the case of V508 Cyg there are contradictory data: a large distance to the star and a low temperature require correspondingly large component radii which cannot be accommodated by a tight orbit.

Secondly, there is nearly a hundred-fold difference in M_v (~ –1.30 mag, A2V) when calculated using Equation 14 when D = 2,892 pc, compared to M_v calculated (~ 3.28) using Equation 16 from Rucinski and Duerbeck (1997). Substituting M_v = 3.28 back into Equation 14 and solving for distance results in about 351 pc, a value far closer than that reported by Gaia. However, for the sake of comparison we adopted the value (447 ± 53 pc) derived from Equation 19 (Gettel *et al.* 2006), using longer wavelength (J and H) measurements that are likely to be less affected by interstellar extinction. Since estimates for interstellar extinction depended heavily on whether Model A (Amôres and Lépine 2005) or Model A2 (Amôres and Lépine 2007) is used, the corresponding calculations for M_V, BC, M_{bol}, T_{eff}, R, and L are reported in Table 7. Given the great uncertainty in all these determinations, much more data (classification spectra, radial velocities (RV), and complete multicolor light curves) will be needed to accurately describe V508 Cyg.

The O–C diagram predicts an increase (0.0132 sec/year) in the orbital period. This constant change in the orbital period can result from mass transfer, loss of angular motion, or a combination of both phenomena. In addition, the residuals from the quadratic fit (O–C vs epoch E) suggest there may be an underlying sinusoidal change in the orbital period. This could indicate the presence of a third gravitationally bound body,

although at this time there are not enough ToM values to arrive at a defensible value for orbital period (P3) of this body.

In addition, comparisons of Max I to Max II and Min I to Min II from each bandpass also show no clear differences. Here, there is no color change (B–V), which indicates that the effective temperatures of the partners are probably very close. V508 Cyg is located near the galactic plane where strong gas and dust accumulation lead to a strong color shift at shorter wavelengths like B. A comparison with other measurements (J and H passbands) suggests an effective temperature in the range of 4333 to 5079 K.

The distance to V508 Cyg reported in Gaia DR2 (2,892 pc) is highly suspect. In order for it to be detected this far away with a relatively small aperture telescope it would have to be a highly luminous K class giant. However, the established orbital period (0.779658 d) is simply too short for two stars that are 16 solar radii in size. Estimates using Equations 16 (Rucinski and Duerbeck 1997) and 19 (Gettel *et al.* 2006) suggest that the approximate distance is between 350 and 450 pc, thereby keeping this system on the main sequence. Nonetheless, a high resolution uv-vis classification spectrum will be necessary to confirm this assignment. Under any circumstances, V508 Cyg would be a worthy candidate for further study.

6. Acknowledgements

We acknowledge with thanks the variable star observations from the AAVSO International Database contributed by observers worldwide and used in this research. We acknowledge also the BRNO database for reporting their observations. This research made use of Astropy, a community-developed core Python package for Astronomy (Astropy Collaboration *et al.* 2013) and Photutils, an Astropy package for detection and photometry of astronomical sources (Bradley *et al.* 2020). This research has made use of the VizieR catalogue access tool, CDS, Strasbourg, France (DOI: 10.26093/cds/vizier). The original description of the VizieR service was published in Ochsenbein *et al.* (2000).

We thank the referee for the thorough review and a lot of helpful comments and suggestions.

References

Amôres, E. B., and Lépine, J. R. D., 2005, *Astron. J.*, **130**, 659.
Amôres, E. B., and Lépine, J. R. D., 2007, *Astron. J.*, **133**, 1519.
Astronomik. 2020, astronomical filters (https://www.astronomik.com/de/photographic-filters/deep-sky-rgb-colour-filters.html).
Astropy Collab., Robitaille, T. P., *et al.* 2013, *Astron. Astrophys.*, **558A**, 33.
Bailer-Jones, C. A. L. 2015, *Publ. Astron. Soc. Pacific*, **127**, 994.
Bradley, L. 2020, Photutils package (https://github.com/astropy/photutils/tree/1.0.1).
Corp, L. 2018, in *Proceedings for the 37th Annual Conference of the Society for Astronomical Sciences*, ed. B. Buchheim, Science, Society for Astronomical Sciences, Rancho Cucamonga, CA, 255.
Davidge, T. J., and Milone, E. F. 1984, *Astrophys. J., Suppl. Ser.*, **55**, 571.
Diethelm, R. 2010, *Inf. Bull. Var. Stars*, No. 5945, 1.
Diethelm, R. 2012, *Inf. Bull. Var. Stars*, No. 6029, 1.
European Space Agency. 2018, Gaia Data Release 2 (https://www.cosmos.esa.int/web/gaia/dr2).
Flower, P. J. 1996, *Astrophys. J.*, **469**, 355.
Gettel, S. J., Geske, M. T., and McKay, T. A. 2006, *Astron. J.*, **131**, 621.
Goderya, S. N., Leung, K. C., ands Schmidt, E. G. 1995, *Astron. J.*, **110**, 346.
Henden, A. A., Welch, D. L., Terrell, D., and Levine, S. E. 2009, *Bull. Amer. Astron. Soc.*, **41**, 669.
Hoňková, K., *et al.* 2013, *Open Eur. J. Var. Stars*, **160**, 1.
Hoňková, K., *et al.* 2015, *Open Eur. J. Var. Stars*, **168**, 1.
Hubscher, J. 2007, *Inf. Bull. Var. Stars*, No. 5802, 1.
Hubscher, J., and Lehmann, P. 2013, *Inf. Bull. Var. Stars*, No. 6070, 1.
Hubscher, J., and Lehmann, P. B. 2015, *Inf. Bull. Var. Stars*, No. 6149, 1.
Hubscher, J., Lehmann, P. B., Monninger, G., Steinbach, H.-M., and Walter, F. 2010, *Inf. Bull. Var. Stars*, No. 5941, 1.
Hubscher, J., Paschke, A., and Walter, F. 2005, *Inf. Bull. Var. Stars*, No. 5657, 1.
Hubscher, J., Paschke, A., and Walter, F. 2006, *Inf. Bull. Var. Stars*, No. 5731, 1.
Hubscher, J., and Walter, F. 2007, *Inf. Bull. Var. Stars*, No. 5761, 1.
Juryšek, J., et. al. 2017, *Open Eur. J. Var. Stars*, **179**, 1.
O'Connell, D. J. K. 1951, *Riverview Coll. Obs. Publ.*, **2**, 85.
Ochsenbein, F., Bauer, P., and Marcout, J. 2000, *Astron. Astrophys., Suppl. Ser.*, **143**, 23.
Pagel, L. 2018, *Inf. Bull. Var. Stars*, No. 6244, 1.
Rucinski, S. M., and Duerbeck, H. W. 1997, *Publ. Astron. Soc. Pacific*, **109**, 1340.
Samolyk, G. 2020, *J. Amer. Assoc. Var. Star Obs.*, **48**, 256.
Savitzky, A., and Golay, M. J. E. 1964, *Anal. Chem.*, **36**, 1627.
Stępień, K. 2011, *Astron. Astrophys.*, **531A**, 18.
Terrell, D. 2022, *Galaxies*, **10**, 8 (DOI: 10.3390/galaxies10010008).
Terrell, D., and and Wilson, R. E. 2005, *Astrophys. Space Sci.*, **296**, 221.
Torres, G. 2010, *Astron. J.*, **140**, 1158.
Watson, C., Henden, A. A., and Price, C. A. 2014, AAVSO International Variable Star Index VSX (Watson+, 2006–2014; https://www.aavso.org/vsx).
Zhou, A.-Y., Jiang, X.-J., Zhang, Y. P., and Wei, J.-Y. 2009, *Res. Astron. Astrophys.*, **9**, 349.

Three New Variable Stars Discovered in Cassiopeia during a Northern Sky Survey Session

Nello Ruocco
Osservatorio Astronomico "Nastro Verde" (C82), Sorrento, Italy; nello_ruocco@hotmail.com

Received August 1, 2021; revised June 15, 2022; accepted June 16, 2022

Abstract This paper describes the discovery of three new variable stars in Cassiopeia—UCAC4 749-017875, UCAC4 749-017890, and UCAC4 749-018171. They are a pulsating star and two eclipsing binary systems, respectively, discovered in 2015 and included in the AAVSO Variable Star Index, but only now published due to lack of time. I encourage all observers to observe these stars further in order to better characterize them.

1. Introduction

In this paper I present the results of the discovery of three new variable stars—UCAC4 749-017875, UCAC4 749-017890, and UCAC4 749-018171—made in November 2015 during a scheduled northern sky data-gathering session at the Astronomical Observatory "Nastro Verde" of Sorrento.

2. Instruments and methods

All the observations have been made using a Schmidt Cassegrain Telescope 0.25-m f/10 with focal reducer (f/6.3) and a CCD SBIG ST-8. All observations are unfiltered.

The search for new variable stars was carried out with the Muniwin software (Hroch 2014) and the differential photometry was done with Maxim DL (Diffraction Ltd. 2012). The light curve and the calculation of its main parameters were done with Peranso (Vanmunster 2013). The light curve and the calculation of its main parameters was done with Peranso. To calculate periods, I used CLEANest, which is a sophisticated algorithm of the Peranso period analysis software.

3. Results

Table 1 summarizes the main parameters for the three new variables. Each variable can easily be found in the AAVSO VSX database (Watson *et al.* 2014) through its identifier as it appears in the first column. In the table, Epoch means time of maximum brightness for pulsating stars and time of primary minimum for eclipsing binaries.

3.1. UCAC4 749-017875

UCAC4 749-017875 is a δ Scuti star with a period of 0.10229 day (2.455 h) and an amplitude of about 0.07 magnitude between 15.58 and 15.65 V. In Figure 1, the light curve is phased with the

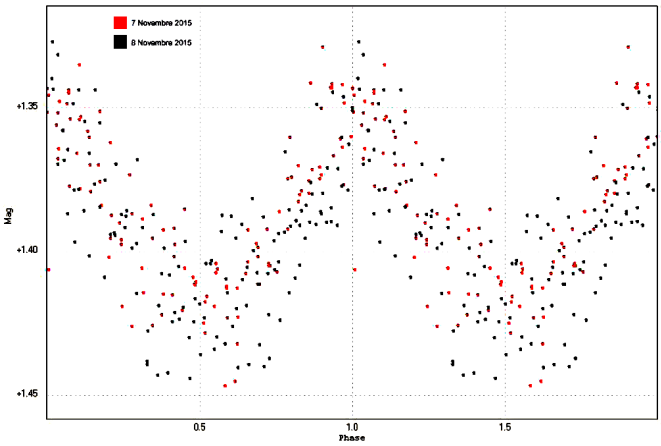

Figure 1. Unfiltered light curve of UCAC4 749-017875.

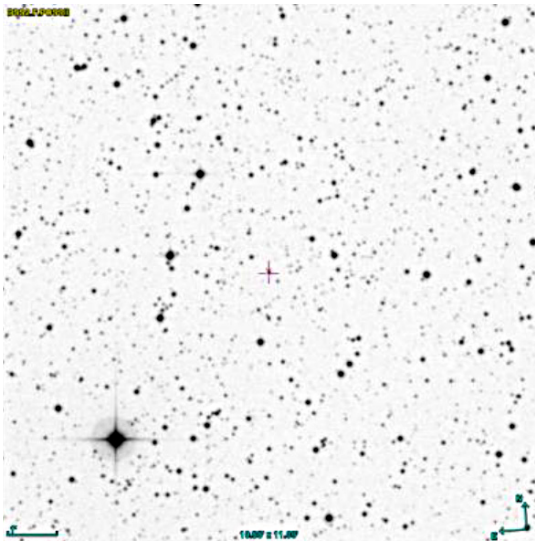

Figure 2. Field from Aladin for UCAC4 749-017875.

Table 1. Main information and results for the new variables discovered.

Star (VSC Identifier)	*R.A. (J2000) h m s*	*Dec. (J2000) ° ′ ″*	*Constellation*	*V*	*Period (day)*	*Epoch (HJD)*	*Type*
UCAC4 749-017875	01 47 46.44	+59 42 23.9	Cas	15.58–15.65	0.10229	2457334.4485 ± 0.001	DSCT
UCAC4 749-017890	01 47 50.63	+59 38 32.3	Cas	16.00-16.16	0.38600	2457330.3539 ± 0.001	EW
UCAC4 749-018171	01 49 20.46	+59 41 50.4	Cas	15.94-16.35	0.35507	2457329.503 ± 0.001	EW

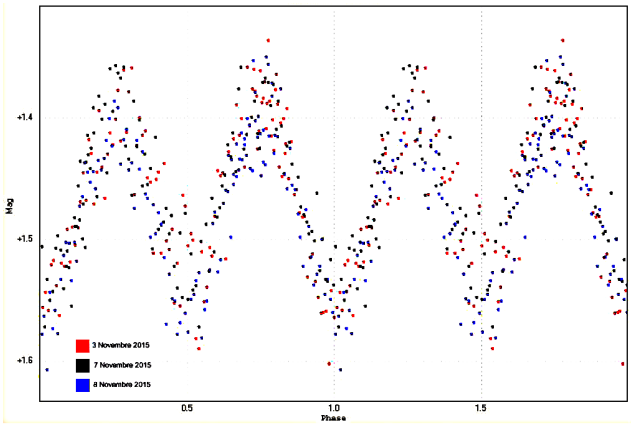

Figure 3. Unfiltered light curve of UCAC4 749-017890.

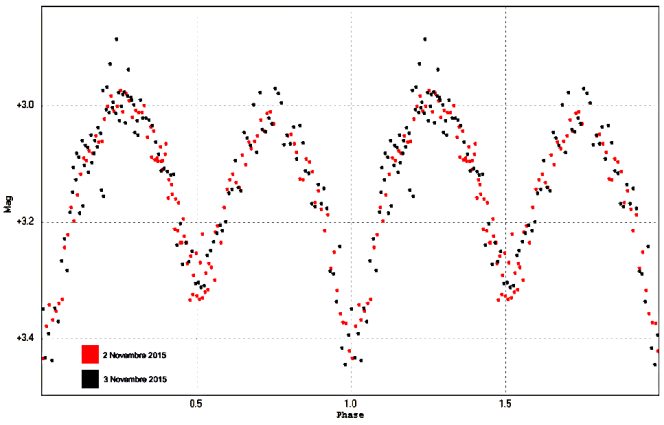

Figure 5. Unfiltered light curve of UCAC4 749-018171.

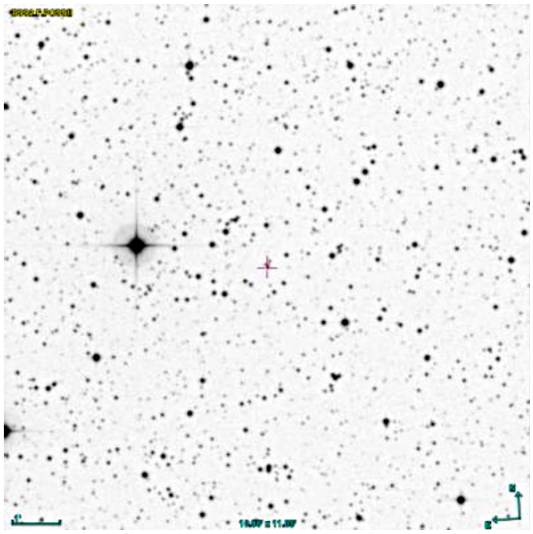

Figure 4. Field from Aladin for UCAC4 749-017890.

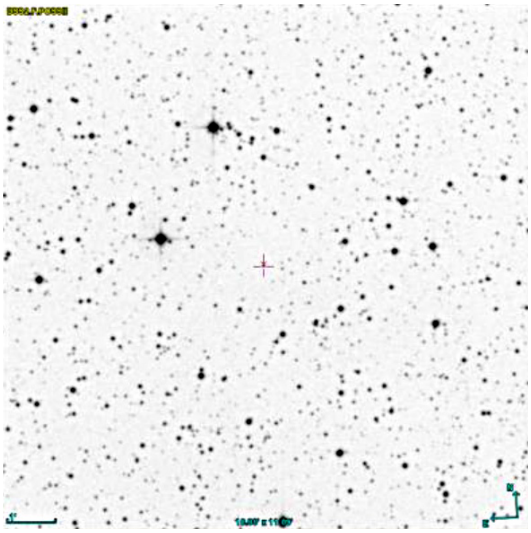

Figure 6. Field from Aladin for UCAC4 749-018171.

main period of the pulsator. Figure 2 shows the field from Aladin with the new variable star marked in the center with a cross.

3.2. UCAC4 749-017890

UCAC4 749-017890 is an EW eclipsing binary with a period of 0.38600 day (9.264 h) and an amplitude of about 0.16 magnitude between 16.00 and 16.16 V. In Figure 3, the light curve is phased with the main period of the binary. Figure 4 shows the field from Aladin with the new variable star in the center marked with a cross.

3.3. UCAC4 749-018171

UCAC4 749-018171 is an EW eclipsing binary with a period of 0.35507 day (8.522 h) and an amplitude of about 0.41 magnitude between 15.94 and 16.35 V. In Figure 5, the light curve is phased with the main period of the binary. Figure 6 shows the field from Aladin with the new variable star marked in the center with a cross.

4. Conclusion

Three new variable stars were found by myself in November 2015 during a scheduled northern sky data-gathering session at the Astronomical Observatory "Nastro Verde" of Sorrento. Each new variable star —UCAC4 749-017875, UCAC4 749-017890, and UCAC4 749-018171—can be found in the AAVSO VSX database (Watson *et al* 2014). Since only my observations were involved in the discovery, readers are encouraged to make observations needed to build an O–C graph to check if there have been changes in the parameters.

References

Diffraction Limited. 2012, MaxIm DL image processing software (http://www.cyanogen.com).

Hroch, F. 2014, Munipack (http://munipack.astronomy.cz/), Astrophysics Source Code Library, record ascl: 1402.006 (2014ascl.soft02006H)).

Vanmunster, T. 2013, Peranso v.2.50 light curve and period analysis software (http://www.cbabelgium.com/peranso).

Watson, C., Henden, A. A., and Price, C. A. 2014, AAVSO International Variable Star Index, VSX (Watson+, 2006–2017; http://www.aavso.org/vsx).

Five New Variable Stars Discovered during a Campaign to Determine the Rotation Period of Asteroids

Antonio Catapano
Luca D'Avino
Andrea Di Dato
Maurizio Mollica
Luigi Morrone
AstroCampania—Osservatorio Astronomico "Salvatore Di Giacomo" (L07), Agerola (Na), Italy

Alfonso Noschese
AstroCampania—Osservatorio Astronomico "Salvatore Di Giacomo" (L07), Agerola (Na), Italy, and Osservatorio Astronomico Elianto (K68), Pontecagnano (Sa), Italy

Nello Ruocco
AstroCampania—Osservatorio Astronomico "Salvatore Di Giacomo" (L07), Agerola (Na), Italy, and Osservatorio Astronomico "Nastro Verde" (C82), Sorrento (Na), Italy; nello_ruocco@hotmail.com

Antonio Vecchione
AstroCampania—Osservatorio Astronomico "Salvatore Di Giacomo" (L07), Agerola (Na), Italy

Received August 2, 2021; revised August 11, 2021; accepted August 11, 2022

Abstract This paper describes the discovery of five new variable stars, AC_V1– AC_V5—two binary systems and three pulsating stars—between 2017 and 2019. They have been included in the AAVSO Variable Star Index, but are being published now. We encourage all observers to further observe these stars so as to better characterize them. It might be interesting to make subsequent observations for constructing O–C diagrams as well as for modeling the binary systems.

1. Introduction

In this paper we describe the results of the discovery of five new variable stars, made between 2017 and 2019 during a scheduled northern sky survey to determine light curves of asteroids using the robotic telescope of the astronomical observatory "S. Di Giacomo" in Agerola, Italy. The stars have been named with the acronym AC (AstroCampania—the amateur astronomy club that manages Agerola's Observatory) followed by the progressive discovery number.

2. Instruments and methods

All the observations have been made remotely using the 0.5-m f/8 Ritchey-Chretien telescope and a FLI PL4240 CCD in Agerola and, only for the High Amplitude Delta Scuti (HADS) stars, the T25 iTelescope, a Planevawe CDK 431-mm with a FLI PL6303E CCD in New Mexico. The search for new variable stars was carried out with the Muniwin2 software (Hroch 2014) and the differential photometry was made with Maxim DL1 (Diffraction Limited 2012). The light curve and the calculation of its main parameters was made with Peranso3 (Vanmunster 2004–2021).

3. Results

Table 1 summarizes the main parameters for the five new variables. Each of them can be easily searched in the AAVSO VSX database (Watson *et al.* 2014) through their identifier as it appears in the first column. In the table, Epoch indicates the time of maximum brightness for pulsating stars and time of primary minimum for eclipsing binaries.

Table 1. Information and results for the new variables discovered.

Star (VSX identifier)	*R.A. (J2000) h m s*	*Dec. (J2000) ° ′ ″*	*Const.*	*V*	*Period (days)*	*Epoch (HJD)*	*Type*
AC_V1	17 30 53.42	–12 55 58.1	Ser	18.06–18.51	0.05797	2457921.4725	HADS
AC_V2	17 30 14.60	–12 56 26.0	Ser	15.7–16.11	0.134508	2457921.413	HADS
AC_V3	19 22 11.76	–17 03 10.0	Sgr	16.5–16.75	0.046238	2457929.4157	HADS
AC_V4	07 05 01.31	+20 27 26.7	Gem	15.79–16.30	0.376400	2458125.3333	EW
AC_V5	07 05 29.29	+20 22 54.7	Gem	17.93–18.37	0.262094	2458125.536	EW

3.1. AC_V1

AC_V1 is a HADS star with a period of 0.05797 d (83.48 m), an amplitude of about 0.45 magnitude, and a range between 18.06 and 18.51 V. In Figure 1, the light curve is phased with the main period of the pulsator. Figure 2 shows the field from the ALADIN interactive sky atlas (Bonnarel *et al.* 2000) with the new variable star in the center.

3.2. AC_V2

AC_V2 is a HADS star with a period of 0.134508 d (3.2282 h), an amplitude of about 0.41 magnitude, and a range between 15.7 and 16.11 V. In Figure 3, the light curve is phased with the main period of the pulsator. Figure 4 shows the field from the ALADIN interactive sky atlas (Bonnarel *et al.* 2000) with the new variable star in the center.

3.3. AC_V3

AC_V3 is a HADS star with a period of 0.046238 d (66.583 m), an amplitude of about 0.23 magnitude, and a range between 16.5 and 16.75 V. In Figure 5, the light curve is phased with the main period of the pulsator. Figure 6 shows the field from the ALADIN interactive sky atlas (Bonnarel *et al.* 2000) with the new variable star in the center.

3.4. AC_V4

AC_V4 is an EW star with a period of 0.376400 d (9.0336 h), an amplitude of about 0.51 magnitude, and a range between 15.79 and 16.30 V. In Figure 7, the light curve is phased with the main period of the binary. Red dots are our observations; black dots are ASAS-SN data. Figure 8 shows the field from the ALADIN interactive sky atlas (Bonnarel *et al.* 2000) with the new variable star in the center.

3.5. AC_V5

AC_V5 is an EW star with a period of 0.262094 d (6.2903 h), an amplitude of about 0.44 magnitude, and a range between 17.93 and 18.37 V. In Figure 9, the light curve is phased with the main period of the binary. Figure 10 shows the field from the ALADIN interactive sky atlas (Bonnarel *et al.* 2000) with the new variable star in the center.

4. Conclusion

Five new variable stars, AC_V1–AC_V5 (two binary systems and three pulsating stars), discovered between 2017 and 2019 have been included in the AAVSO Variable Star Index, and are now described here for the first time. We encourage all observers to further observe these stars so as to better characterize them. This work of discovery should only be the starting point from which to start in order to continue following these stars and their trend over time, perhaps by building periodic O–C diagrams and checking whether or not there are changes in the system.

References

Bonnarel, F., *et al.* 2000, *Astron. Astrophys., Suppl. Ser.*, **143**, 33 (https://aladin.u-strasbg.fr).

Diffraction Limited. 2012, MaxIm DL image processing software (http://www.cyanogen.com).

Hroch, F. 2014, Munipack (http://munipack.astronomy.cz/), Astrophysics Source Code Library, record ascl: 1402.006 (2014ascl.soft02006H).

Vanmunster, T. 2004-2021, Peranso v.2.50 light curve and period analysis software (https://www.cbabelgium.com/peranso).

Watson, C., Henden, A. A., and Price, C. A. 2014, AAVSO International Variable Star Index VSX (Watson+, 2006–2017; http://www.aavso.org/vsx).

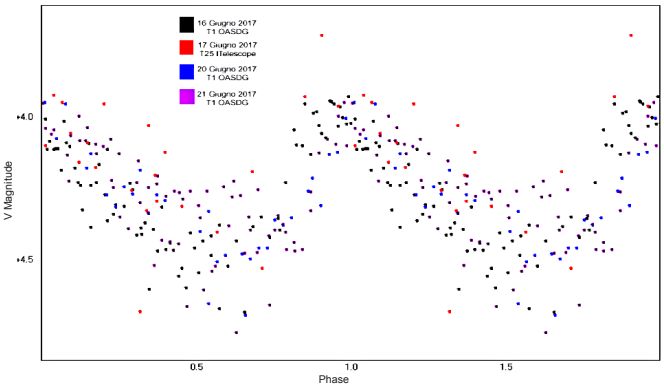

Figure 1. V light curve of AC_V1.

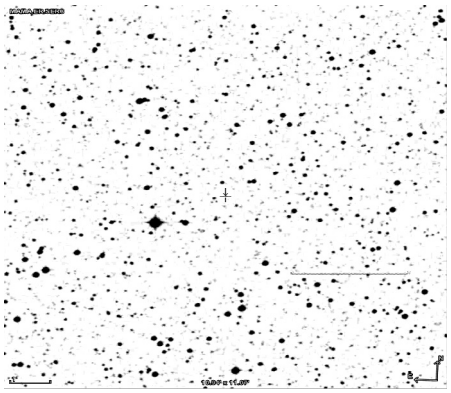

Figure 2. Field of AC_V1 from ALADIN (Bonnarel *et al.* 2000).

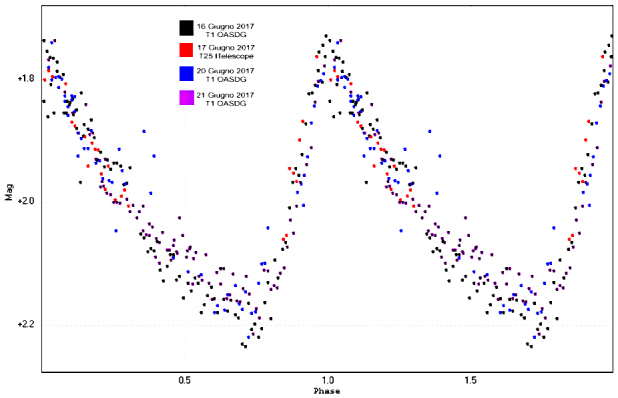

Figure 3. V light curve of AC_V2.

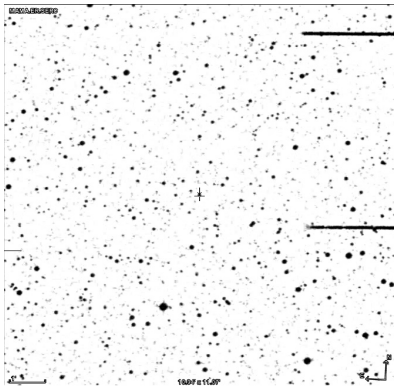

Figure 4. Field of AC_V2 from ALADIN (Bonnarel *et al.* 2000).

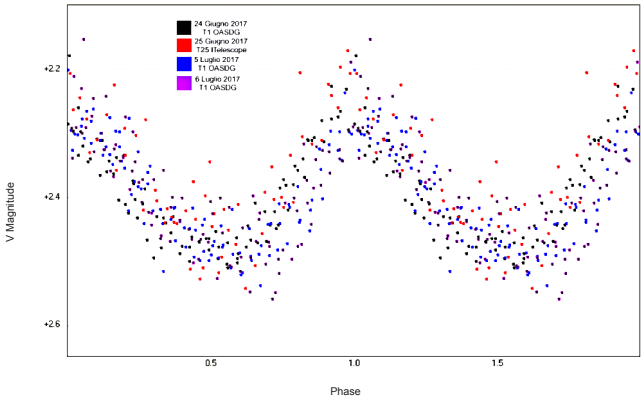

Figure 5. V light curve of AC_V3.

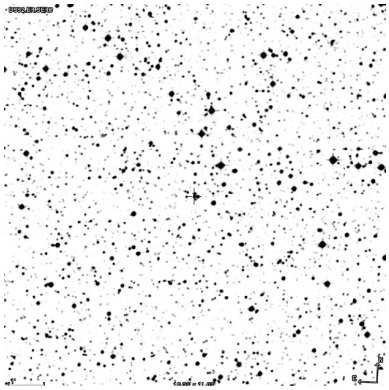

Figure 6. Field of AC_V3 from ALADIN (Bonnarel *et al.* 2000).

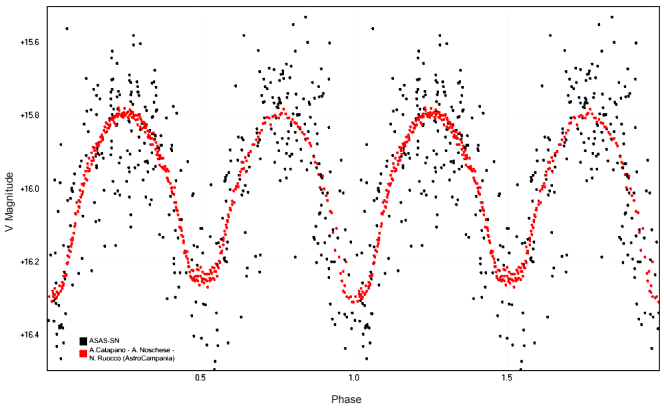

Figure 7. V light curve of AC_V4.

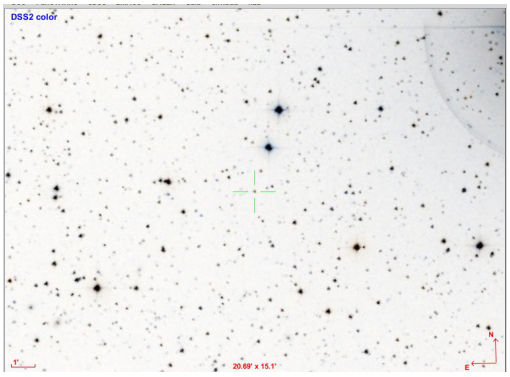

Figure 8. Field of AC_V4 from ALADIN (Bonnarel *et al.* 2000).

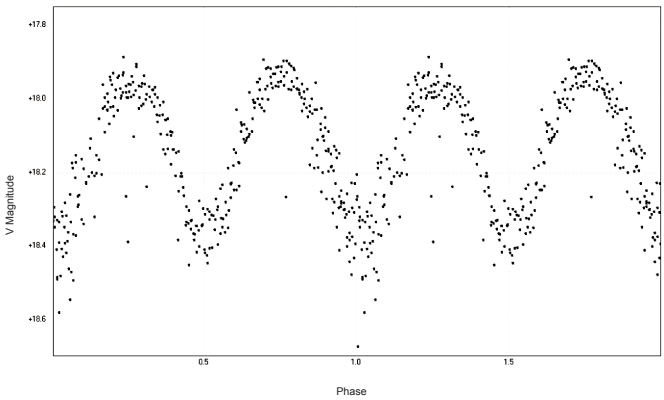

Figure 9. V light curve of AC_V5.

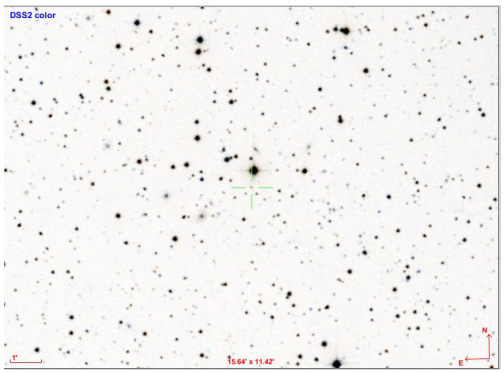

Figure 10. Field of AC_V5 from ALADIN (Bonnarel *et al.* 2000).

Toward the Confirmation of an Ultra-Short Period Hot Jupiter "Puffy Planet" with a Near Grazing Transit, TOI-2341.01

Darcy Wenn
Oscar Geerts
Derrick Liu
ELTHAM College of Education, 1660 Main Road, Research, VIC 3095, Australia; dtwenn@bigpond.com; oscargeerts@gmail.com; dliu40207@gmail.com

Michael Fitzgerald
Las Cumbres Observatory, 6740 Cortona Drive, Goleta, CA 93117; psyfitz@gmail.com

Saeed Salimpour
Max Planck Institute for Astronomy, Königstuhl 17, 69117 Heidelberg, Germany; IAU Office of Astronomy for Education, 69117 Heidelberg, Germany; Deakin University, 221 Burwood Hwy, Burwood, VIC 3125, Australia; astrophysics@saeedsalimpour.com

Andrew Yen
ELTHAM College of Education, 1660 Main Road, Research, VIC 3095, Australia; ayen@ELTHAMcollege.vic.edu.au

Received March 18, 2022; revised August 11, 2022; accepted September 7, 2022

Abstract This paper reports on ground-based observations of the candidate exoplanet TOI-2341.01 (TESS Object of Interest-2341.01), initially observed by the Transiting Exoplanet Survey Satellite (TESS). The analysis of data provides evidence for the increased likelihood that TOI-2341.01 is a Jupiter-sized gas giant with a radius of 86,409 km ± 6,011 km (R_{Jup} 1.209 ± R_{Jup} 0.084), orbiting the host star TOI-2341 at 0.0118 AU ± 0.00073 AU with a transit duration of 0.065 days ± 0.006 days (1.560 ± 0.144 hours or 93.6 minutes ± 7 minutes). TOI-2341.01 has an orbital period of 0.877640 days ± 0.000004 day (21.0634 hours ± 0.0002 hour) and has a mid-transit time of BJD_TDB 2459411.74201 ± 0.00010. Furthermore, a grazing criterion value of 0.99 ± 0.14 was calculated, determining that TOI-2341.01 is highly likely to be a near-grazing transit. It is also noted that estimated mass values were attained via the TESS Follow-up Observation Program, projecting TOI-2341.01's mass as 55.3 M_E (0.17 M_J) and thus possessing an estimated density of 122.28 kg/m^3 (0.12228 g/cm^3). This investigation has also cleared the field surrounding TOI-2341.01 out to 43 arcminutes of eclipsing binaries that could produce a false positive.

1. Introduction

Over recent decades, exoplanet detection has increased exponentially, owing to space-based missions such as Kepler (Borucki *et al.* 2010) and TESS (Ricker *et al.* 2015). Although many detection methods such as radial velocity, microlensing, direct imaging, and transit timing variations are employed to determine the planetary systems of other stars, these aforementioned space-based missions have permitted the mass employment of the transit method, allowing for rapid, repeatable, and increasingly numerous exoplanet detections. This detection method requires stars to be monitored for drops in flux caused by a planet transiting in front of the star. The dip in flux allows for the determination of the planet's radius, orbital period, and semi-major axis. Since the launch of NASA's now-retired Kepler mission and current TESS mission, a new set of planetary objects has been discovered, dubbed "hot Jupiters." These planets have similar physical properties to Jupiter but have lower densities, are often tidally locked (Mandushev *et al.* 2007) and have extremely short orbital periods (usually less than ten days) with low eccentricities (Wang *et al.* 2015). Since its launch, NASA's TESS satellite has detected over 5,908 exoplanets to date; however, only about 4% of those have been confirmed, leaving many candidates to be investigated.

Table 1. Summary of each light curve quality and the definition of the assigned designations.

Light Curve Quality	*Definition*
Good Light Curve	Light curves with a clear and complete drop in flux. The transit is easily visible and can be identified in residuals.
Poor Light Curve	Light curves clear and complete drops in flux but with undesirable properties such as minimal, unclear or noisy drops in flux despite otherwise favourable atmospheric conditions.
Partial Light Curve	Light curves cut off on either side of the transit due to atmospheric conditions such as cloud, rain, wind or light.
Technical Issues	Light curves that produced an error while being processed due to weather, image error, insufficient data or other anomalies.

Under this premise, the investigation of exoplanet candidate TOI-2341.01 (TOI-2341 b) commenced. This investigation aims to highlight this exoplanet candidate's properties and nature to understand this planetary body further and add to the ever-increasing catalogue of previously discovered hot Jupiter class exoplanets. Prior to this investigation, TOI-2341.01 was characterized by TESS and associated surveys to possess a semi-major axis relative to stellar radius ratio (a/R_s) of 4.641 ± 1.021

Table 2. Details of observations.

Light Curve Designation TOI2341.01	*Date of Observation (MM/DD/YYYY)*	*Telescope*	*Observatory*	*Filter*	*Exposure Time (seconds)*	*Detrending Parameter*	*Transit Quality*
ECB.1	08/26/2021	PlaneWave Instr. CDK 17"	ELTHAM College	Bessel B	180	0.967664421	Partial
ECIP.1	09/08/2021	PlaneWave Instr. CDK 17"	ELTHAM College	SDSS i'	240	0.997830786	Partial
ECL.1	09/16/2021	PlaneWave Instr. CDK 17"	ELTHAM College	Luminance	240	1.00163253	Good
ECL.2	09/23/2021	PlaneWave Instr. CDK 17"	ELTHAM College	Luminance	40	1.006906109	Good
ECL.3	09/25/2021	PlaneWave Instr. CDK 17"	ELTHAM College	Luminance	40	1.002733981	Technical error
ECL.4	09/26/2021	PlaneWave Instr. CDK 17"	ELTHAM College	Luminance	40	1.001186931	Poor
ECRP.1	09/01/2021	PlaneWave Instr. CDK 17"	ELTHAM College	SDSS r'	180	0.999270846	Partial
ECRP.2	08/19/2021	PlaneWave Instr. CDK 17"	ELTHAM College	SDSS r'	90	0.99475672	Partial
LCOB.1	10/04/2021	Meade LX200 16"	Cerro Tololo	Bessel B	90	1.006974028	Technical error
LCOB.2	09/05/2021	Meade LX200 16"	Cerro Tololo	Bessel B	300	1.02133523	Poor
LCOIP.1	09/24/2021	Meade LX200 16"	Siding Springs	SDSS i'	90	1.007174333	Good
LCOIP.2	09/02/2021	Meade LX200 16"	Siding Springs	SDSS i'	300	1.009928858	Partial
LCOIP.3	09/09/2021	Meade LX200 16"	Siding Springs	SDSS i'	300	1.00223799	Good
LCORP.1	09/05/2021	Meade LX200 16"	Cerro Tololo	SDSS r'	300	1.002108894	Poor
LCORP.2	10/04/2021	Meade LX200 16"	Cerro Tololo	SDSS r'	90	0.999053465	Good
LCOV.1	09/26/2021	Meade LX200 16"	Cerro Tololo	Bessel V	90	1.018566403	Good
LCOW.1	07/01/2021	Meade LX200 16"	Cerro Tololo	Pan-STARRS w	75	1.008050852	Partial
LCOW.2	07/17/2021	Meade LX200 16"	Cerro Tololo	Pan-STARRS w	75	1.014530207	Good
LCOW.3	07/16/2021	Meade LX200 16"	Cerro Tololo	Pan-STARRS w	75	1.025370914	Good
LCOW.4	09/24/2021	Meade LX200 16"	Siding Springs	Pan-STARRS w	40	1.006302628	Poor
LCOW.5	09/24/2021	Meade LX200 16"	Siding Springs	Pan-STARRS w	40	1.00176371	Partial
LCOW.6	09/23/2021	Meade LX200 16"	Siding Springs	Pan-STARRS w	40	1.00112731	Technical error
LCOZS.1	10/08/2021	Meade LX200 16"	Siding Springs	Pan-STARRS Zs	90	1.013713456	Good
LCOZS.2	09/09/2021	Meade LX200 16"	Siding Springs	Pan-STARRS Zs	300	1.004841398	Good

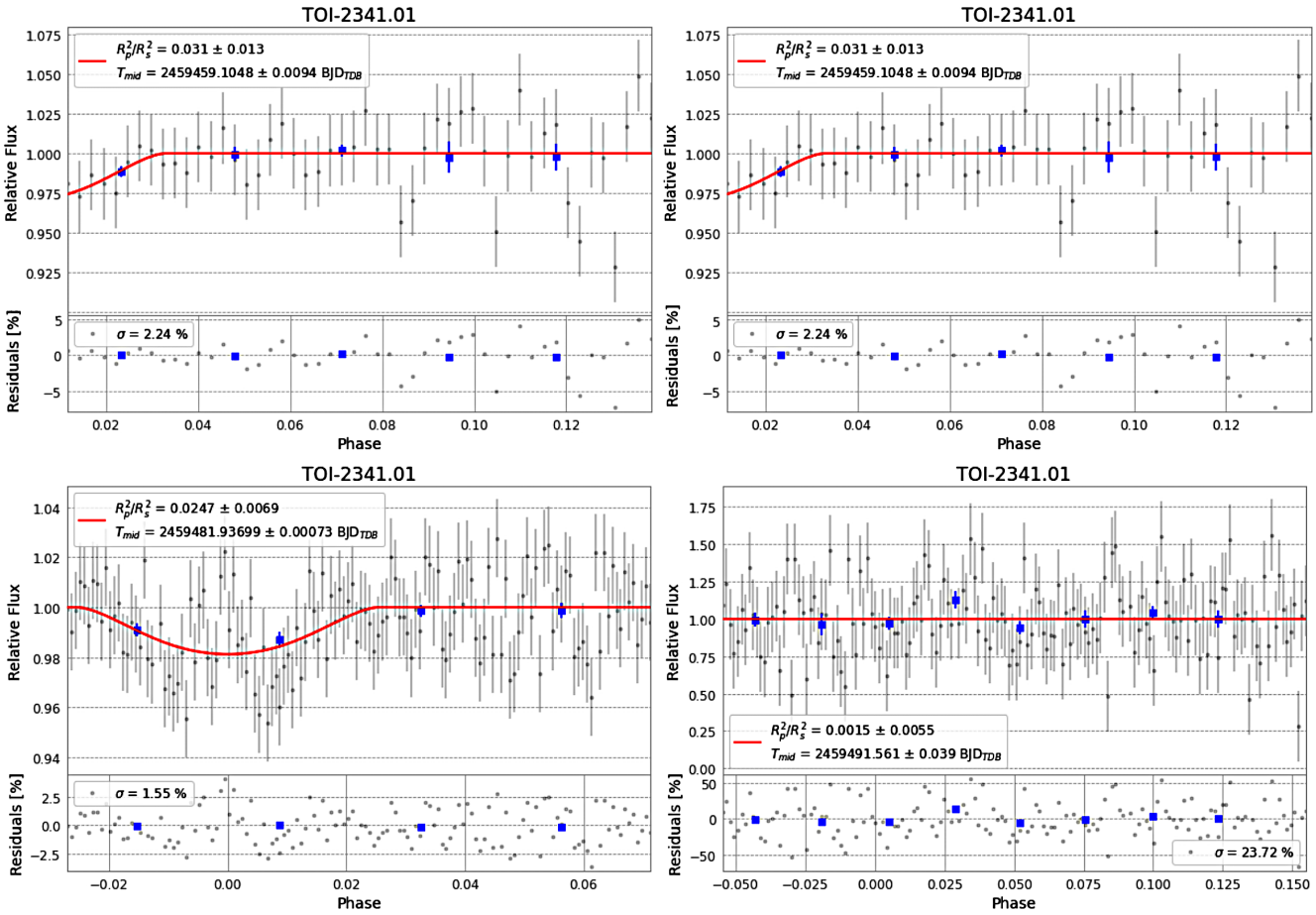

Figure 1. The top left panel is an example of a "Partial Light Curve," as a portion of the transit is missing from the graph. The top right panel is an example of a "Good Light Curve"; a clear and pronounced drop in stellar flux is shown. The bottom left panel is an example of a "Poor Light Curve," as noise drastically affects the transit plot and residuals. The bottom right panel is a "Technical Issue"; despite taking place in the transit window, no transit is shown.

and a ratio of planetary radius to the stellar radius (R_p/R_s) of 0.097 ± 0.008 (Montalto *et al.* 2020).

2. Observations

Observations of 24 transits of TOI-2341.01, collected between 1 July 2021 and 4 October 2021, were analyzed. These observations were conducted at the ELTHAM College Observatory utilizing a PlaneWave Instruments CDK 17-inch (0.43-m) telescope equipped with an SBIG STX-16803 CCD camera giving a field of view of 43.12 × 43.12 arcminutes, and on the Las Cumbres Observatory (LCO) Network (Brown *et al.* 2013), utilizing the Meade LX200 16-inch (0.4-m) telescopes equipped with SBIG STL-6303 CCD cameras giving a field of view of 29.2 × 19.5 arcminutes. All data were captured from the ELTHAM College Observatory in Victoria, Australia, the Siding Springs Observatory in New South Wales, Australia, and the Cerro Tololo Inter-American Observatory in Chile's Coquimbo Region. The observations on the LCO network were scheduled using ExoRequest (Sarva *et al.* 2020; Salimpour *et al.* 2021).

3. Data quality

To attain satisfactory data for the production of a light curve, several environmental factors must be considered, such as lack of cloud cover, accurate telescopic tracking, a minimal field of view (FOV) drift, and good seeing (sharp images due to still stratospheric and mesospheric conditions). Seeing significantly affected many of the later transits collected for this investigation due to TOI-2341.01's right ascension (R.A.) and thus low altitude in the southern sky during the observing campaign. Out of 24 transits in this study, 10 were "good transits." Each transit was given a designation denoting its quality, as explained in Table 1. A breakdown of the results from processing each transit is shown in Table 2, including the date of observation, the telescope and observatory utilized, filter, exposure time, and a column to indicate transit quality. Examples for each designation are shown in Figure 1. All light curves are shown in Appendix A.

4. Data reduction and light curve production

For photometric evaluation of the data, PSFEx (Point Spread Function Extractor; Bertin 2011) photometry, produced by the OSS (Our Solar Siblings) pipeline (Fitzgerald 2018), was analyzed through the Python script Astrosource (Fitzgerald *et al.* 2021), which used ensemble photometry to produce a series of output files and plots containing the variability in flux seen from TOI-2341 during the transit period. Astrosource also created a list of calibration stars for utilization in the production of a transit curve. Comma Separated Value (.csv) output files measuring the barycentric dynamical time (BJD_TDB), orbital phase, and flux produced by Astrosource were subsequently input into the EXOTIC (EXOplanet Transit Interpretation Code) pipeline (Zellem *et al.* 2020). The selected comparison stars are listed in Table 3 and shown in Figure 2, and were set to be close to the target, not too close to other stars in the field, and sufficiently bright. These comparison stars were used as an ensemble by Astrosource to extract the exoplanet light curves.

Table 3. Comparison stars selected by Astrosource.

Letter Designation	*Star Name*
B	TYC 8790-2326245
C	HD 194254
D	UCAC2 8922690
E	AAVSO 035-3704842
F	AAVSO 035-2326245
G	UCAC3 74-468439

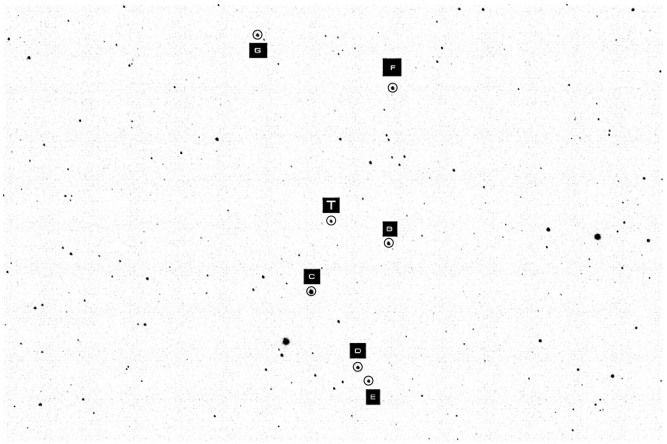

Figure 2. An image of the target star, TOI-2341 (label T), and the comparison stars (listed in Table 3) that were automatically selected by Astrosource.

The EXOTIC software was run via Python 3.10 across versions 1.0 through 1.10. The parameters of TOI-2341.01 provided from the NASA Exoplanet Archive (NEA), details of the imaging session, and the telescope utilized for each session were entered into JavaScript Object Notation (.json) files, which were utilized by the EXOTIC pipeline.

EXOTIC was then used to perform an MCMC (Markov-Chain Monte Carlo) fitting routine to fit an exoplanet transit model to the reduced light curve, as shown in Figure 3. EXOTIC also reports from this fit the scatter in the residuals, the mid-transit time (T_{mid}), transit depth $(R_p/R_s)^2$, the ratio of planetary radius to the stellar radius (R_p/R_s), semi-major axis relative to the stellar radius (a/R_s), air mass, and transit duration (T_{dur}) throughout the observation window.

Furthermore, EXOTIC detrends data pertaining to the production of a light curve by fitting to the function defined in Equation 1, where c is the coefficient to which the data are fitted, and airmass is the actual air mass value for that respective dataset as determined by EXOTIC and telescope data.

$$f = e(c \times \text{airmass}) \quad (1)$$

Detrending values for each transit are listed as part of Table 2.

4.1. EXOTIC data and analysis

Astrosource and EXOTIC's reduction processes produced 24 new light curves of TOI-2341.01, shown in Appendix A. Each light curve shows the measured normalized flux over the transit period, with some datasets comprising larger portions of the orbital phase than others. Error bars are also included for each plot point during transit and non-transit periods.

Table 4. Parameters produced by EXOTIC reduction.

Planetary Parameters	*Value*	*SEM*	*Error (%)*
Ratio of planet to stellar radius (R_p/R_s)	0.20033	± 0.01393	6.96
Transit depth (R_p/R_s)	4.191	± 0.528	12.61
Semi major axis/stellar radius (a/R_s)	4.1079	± 0.2542	6.19
Scatter in the residuals of the lightcurve fit	1.757	± 0.312	17.77
Transit duration	0.065	± 0.006	9.26

The resulting plot shows relative flux over phase, and a trendline of the light curve is overlaid. Residuals are also stated under the primary graph, and $(R_p/R_s)^2$ (transit depth) and the Tmid (transit midpoint) are shown overlaid on the primary graph. EXOTIC also outputs planetary parameters in the format of a .txt file, stating the (R_p/R_s), (a/R_s), transit depth $(R_p/R_s)^2$, and transit duration (T_{dur}).

To assess the reliability of planetary parameters while using a complete dataset, an "outlier clipping" algorithm was performed. This algorithm compares a given parameter across all inputted transits and eliminates all values that deviate substantially from the mean. In particular, all values with a distance greater than twice the standard deviation from the mean are discarded. It is noteworthy to mention the recursive nature of this algorithm; if a value is clipped, the standard deviation is recalculated, and the algorithm resets until no clips are recorded. Following the removal of outliers, the mean and standard error are calculated and are respectively displayed as planetary parameter ± error.

The planetary parameters seen in Table 4 are outputted from this algorithm making use of data derived from all ten "good" transits. The algorithm did not clip any values from any of the transits inputted, indicating a high degree of data consistency across the "good" transits.

In some instances, the values presented in this investigation deviate compared to previous literature (Montalto *et al.* 2020). The transit depth has been determined to have increased from prior literature from 1.205% ± 0.003% to 4.191% ± 0.529%. The semi-major axis over stellar radius (a/Rs) has decreased relative to previous literature from 4.64 ± 1.02 to a value of 4.108 ± 0.254.

The Transit Duration (days) of TOI-2341.01 has increased from 0.019 ± 0.055 to 0.065 ± 0.006, approximately three times the value published by the NASA Exoplanet Archive. The increase in Tdur likely results from how EXOTIC measures transit duration. However, this value is precise and accurate. A gradual sloping transit occurs between phases –0.04 and +0.04; this may be attributed to the near grazing nature of TOI-2341.01's transit. The 0.08 phase between these points is equivalent to the calculated transit duration and can be observed in Figure 3.

The planet-to-stellar radius (R_p/R_s) ratio is noted to have increased from 0.097 ± 0.008 to 0.200 ± 0.014. This investigation has determined that TOI-2341.01 has a radius of roughly 20.03% ± 0.19% of its host star, TOI-2341, as determined by the aforementioned (R_p/R_s) value. TOI-2341 is likely to be an M-type main-sequence star. This classification is based on TOI-2341's radius of 0.62 $R_\odot$ ± 0.02 $R_\odot$, an effective temperature of 3495 K ± 157 K, and a measured magnitude of 12.722 ± 0.008

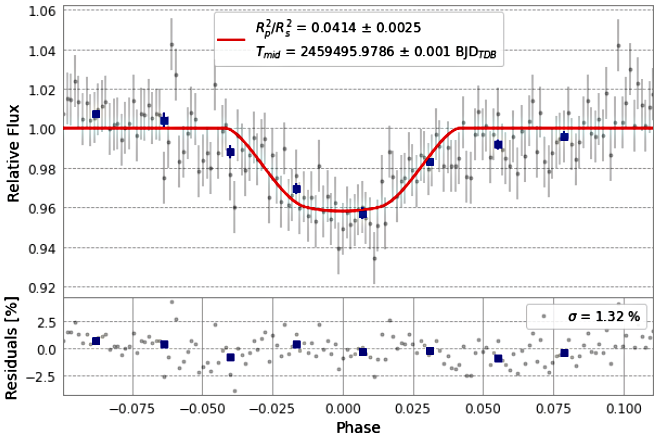

Figure 3. A light curve produced from an imaging session conducted on the Las Cumbres Observatory Network using a ZS filter (Effective central wavelength 870 nm, Full Width at Half Maximum 104 nm). Here a clear drop in relative flux is demonstrated, outlining the transit of TOI-2341.01.

utilizing TESS's detector bandpass of 600–1000 nm centered on the Cousins I band with a wavelength of 786.5 nm (Barclay 2022) . The luminosity of TOI-2341.01 was calculated to be 0.0514 ± 0.006, as given by the Stefan-Boltzmann equation for luminosity seen in Equation 2. Furthermore, the TESS Follow-up Observation Program (TFOP) lists an estimated mass for TOI-2341 as 0.6 $M_\odot$. These characteristics match with known properties of M-type stars, and values for calculation were provided by available literature of TOI-2341 from the NASA Exoplanet Archive and Montalto *et al.* (2020).

$$L = 4\pi R^2 \cdot \sigma T^4 \quad (2)$$

The Stefan-Boltzmann Law (Equation 2): In this equation, σ is the Stefan-Boltzmann Constant where $\sigma = 5.67^{-8}$ $(W/(m^2 \times K^4))$.

From the R_p/R_s value stated above, the planetary radius of TOI-2341.01 can be determined. The value for R_s was used from the NASA Exoplanet Archive, 0.62 ± 0.02 $R_\odot$. The formula for calculating planetary radius (r_{km}) is shown in Equation 3.

$$r_{km} = R_s \cdot (R_p / R_s) \pm SEM \quad (3)$$

Just as the planetary radius of an exoplanet can be calculated utilizing R_p/R_s, the semi-major axis of an exoplanet can be determined from the EXOTIC output a/R_s. The larger the semi-major axis, the longer the orbital and transit periods, which is how EXOTIC calculates this parameter when calculating an individual light curve. The equation utilized is shown in Equation 4.

$$d_{AU} = \frac{R_s \cdot (a / R_S)}{1.496 \cdot 10^8 \text{ km}} \cdot 1AU \pm \frac{SEM}{1.496 \cdot 10^8 \text{ km}} \cdot 1AU \quad (4)$$

Equations 3 and 4 and their respective SEM (standard error to the mean) calculations were performed for each "good transit" dataset, leading to an average value from 10 data points in combination with the SEM. These results are reported in AU and km to align with the prior literature; however, comparison values are also stated. The planetary radius of TOI-2341.01 is

calculated to be approximately 86,409 km ± 6011 km, or 1.209 ± 0.084 R_{Jup}. The semi-major axis of TOI-2341.01 was calculated to be approximately 0.0118 AU ± 0.0007 AU. Directly related to the semi-major axis, the transit duration of TOI-2341.01 was determined by EXOTIC to be 0.065 day ± 0.006 day (1.560 ± 0.144 hours or 93.6 ± 8.6 minutes). The calculated radius value falls outside the uncertainty values presented within the NASA Exoplanet Archive and prior literature (Montalto *et al.* 2020). In this investigation, it has been calculated that TOI-2341.01 is approximately 63% larger than previously calculated, a difference of 4.95 Earth radii. However, we conclude that this increase in radius over previous calculations is likely to be closer to the true value due to the increased number of recorded transits, the near grazing nature of the TOI-2341.01 light curve, and the quality of the light curves used in the production of these parameters.

4.2. The ephemeris data and analysis

As part of EXOTIC's reduction process, a text file (.txt) of planetary parameters is produced. These .txt files include T_{mid} (mid-transit time) values for the reduced transit. To provide updated orbital period and Tmid values as part of this investigation, Tmid values from all 10 "good transits" were collated into a .csv file alongside the respective standard error to the mean values (SEM). The .csv file was accompanied by a JSON file containing the calculated parameters for TOI-2341.01 produced by EXOTIC. Following the production of both files, the .csv file was fed through an ephemeris fitter (Pearson 2019) that collated each Tmid value from the available transits and produced a revised transit midpoint and orbital period for TOI-2341.01. These values are noted in Table 5. A plot is also produced (Figure 4), revealing the deviation between each recorded mid-transit time from each observation and the predicted mid-transit time derived from the ephemeris fitter's new transit midpointvalue. Below that plot, a residuals plot is shown, demonstrating the deviation of each recorded mid-transit time from the calculated transit midpoint value in minutes. It is noted that the values presented are confirmed as precise due to the repeated observation of TOI-2341.01 over multiple months.

It is also noted as part of this investigation that a test run of the ephemeris fitter was performed that included all 24 transits in the production of an updated ephemeris for TOI-2341.01. This test resulted in very similar values for orbital period and transit midpoint, with slightly greater error values produced that overall did not deviate from the dataset provided in this publication. It was ultimately decided to use the "good transits" only to maintain consistency with the planetary parameters for TOI-2341.01 calculated using only that portion of the dataset.

4.3. The near grazing nature of TOI-2341.01

It can also be stated, based on the nature of the transit plots produced by EXOTIC, that it is a possibility that TOI-2341.01 is a near grazing transit. In a traditional grazing transit, such as WASP-67b (Mancini *et al.* 2014), the second and third contact points where the planetary body has entirely passed in front of the stellar disk are missing from the transit light curve. In essence, a grazing transit is where the planet skims or only partially occludes the stellar disk, leading to a "v-shaped" or

Table 5. Revised orbital period and transit midpoint values calculated via the ephemeris fitter and their respective errors.

Parameter	*Value*	*SEM*
Orbital period (days)	0.877638	± 0.000004
Transit midpoint (BJD_TDB)	2459411.742011	± 0.000131

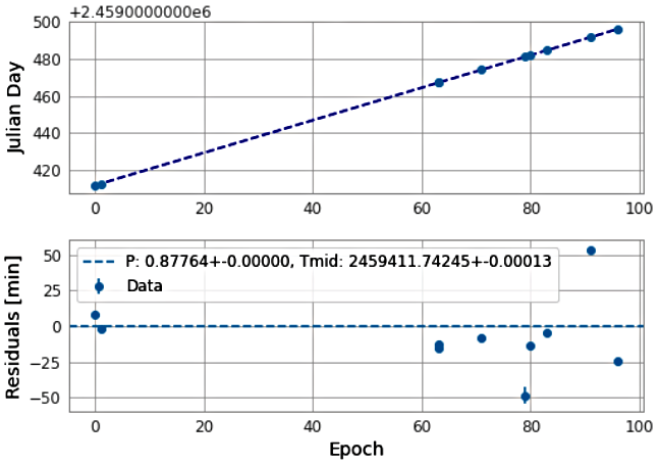

Figure 4. A plot of the deviation between each recorded mid-transit time from each observation and the predicted mid-transit time derived from the ephemeris fitter's new transit midpoint value.

shallow light curve instead of a standard, flat-bottomed light curve. As shown in Figure 5, TOI-2341.01 exhibits similar characteristics to HAT-P-14b (Torres *et al.* 2010), a grazing transit, in contrast to another Hot Jupiter, HAT-P-32b (Hartman *et al.* 2011), which is a regular transit. Furthermore, TOI-2341.01 is listed in prior literature as a v-shaped, potentially grazing transit with an orbital inclination of 78.93° ± 2.02° (Montalto *et al.* 2020). As 0° represents the planet passing directly between Earth and the relevant star, and 90° represents an "edge-on" orbit relative to Earth, it is noted that 78.93° is an extremely high orbital inclination and therefore likely to only partially occlude TOI-2341. The grazing criterion can be calculated to determine whether a planet is a grazing transit (Lillo-Box *et al.* 2015). To calculate the grazing criterion, one must calculate the impact parameter (b) using Equation 5.

$$b = \frac{a \cos i}{R_*} \quad (5)$$

Solving for a in ratio $a/R_s = 4.1079$ results in a value of a = 2.53523. The value a is defined as the semi-major axis of TOI-2341.01. Using Equation 5, the value of b is calculated to be 0.79 ± 0.14. Therefore, when calculating the grazing criterion, the ratio $R_p/R_s = 0.2003 \pm 0.0139$ and the impact parameter b = 0.79 ± 0.14 suggest that TOI-2341.01 is likely to be a near grazing transit. For a transit to be grazing, a value of > 1 must be calculated using Equation 6.

$$b + R_p / R_S > 1 \quad (6)$$

For TOI-2341.01, a value of 0.99 ± 0.14 is calculated, creating an upper value of 1.13 and a lower value of 0.85 for the grazing criterion. As the calculated grazing criterion for TOI-2341.01 is 0.99 ± 0.14, and a grazing transit is considered any value > 1,

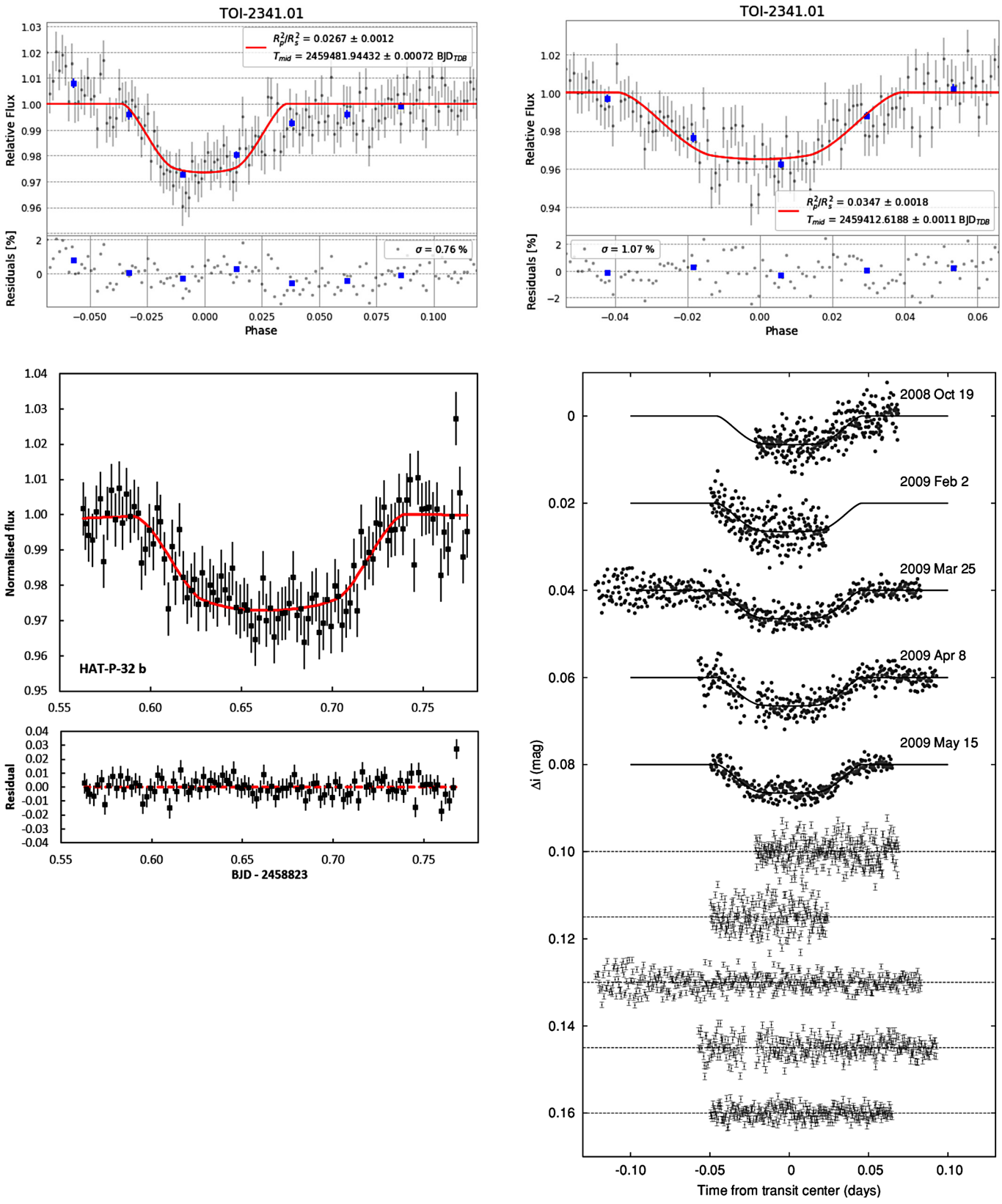

Figure 5. Examples of TOI-2341.01 transit plots during this investigation (top row) compared to HAT-P-14b (Torres *et al.* 2010) (right) and HAT-P-32b (Fowler *et al.* 2021) (bottom left). Note the similarities between HAT-P-14b's and TOI-2341.01's near grazing transit. The similarity is demonstrated in trend lines and flux plots that follow a smoother curve that does not define a transit bottom clearly. Compared to HAT-P-32b's complete occlusion and flat-bottomed transit, the flux plots and a sharper transit curve are demonstrated.

TOI-2341.01 is likely a near grazing transit. Therefore, it is similar to near-grazing transits like that of HAT-P-14b, which has a grazing criterion of 0.968 ±0.022.

The categorization of TOI-2341.01 as a near grazing transit is also concluded from the light curves produced. Traditional light curves will show a significant, rapid drop in stellar flux during the transit period, with a steep and equal curve in the final minutes of the transit period. For near-grazing or grazing transits, an observed transit and its subsequent light curves will show shallow, slow drops in stellar flux that are evidence of a grazing nature of a planet. Examples of the difference between a standard and near grazing transit light curve plot, including a comparison to TOI-2341.01, are shown in Figure 5.

4.4. The estimated mass of TOI-2341.01

While radial velocity measurements have not been recorded for TOI-2341.01 as of the writing of this publication, estimated mass measurements for TOI-2341 and TOI-2341.01 have been published on the TESS Follow-up Observing Program (TFOP) website. These estimations are provided in Table 6 (Massachusetts Institute of Technology (MIT) 2021).

It can therefore be stated for the purposes of this investigation that TOI-2341's assumed mass is 0.6 $M_{\odot}$ and TOI-2341.01's assumed mass is 55.3 M_E. It is important to note that these mass values are estimates based on available data supplied by TESS on the NASA Exoplanet Archive, TFOP (MIT 2021), and prior studies (Montalto *et al.* 2020). While these mass values cannot be used as substitutes for confirmed mass parameters determined through radial velocity measurements, these values have been checked for accuracy as visualised below.

Equation 7, Kepler's Third Law, can be utilized to calculate the orbital period of a planetary body, in this case TOI-2341.01.

$$T^2 = \frac{4\pi^2}{G \times (M_1 + M_2)} \times r^2 \quad (7)$$

In Kepler's Third Law, T is the orbital period in minutes, G is the gravitational constant (6.6743×10^{-11} m^3 kg^{-1} s^{-2}), M is the mass of an object in solar masses, and r is the radius of the satellite's orbit in astronomical units. If the calculation of an orbital period utilizing Kepler's Third Law and values provided from both this investigation and mass values from TFOP (MIT 2021) aligns with the calculated ephemerides as part of this investigation, then these mass estimates can be used to bolster this investigation's conclusion that TOI-2341.01 is indeed likely to be a strong planet candidate. Substituting the values into Equation 7 the formula looks as follows:

$$T^2 = \frac{4\pi^2}{(6.6743 \times 10^{-11}) \times (0.6 + (1.166051 \times 10^{-4})} \times 0.0118^2 \quad (8)$$

Solving for T, a value of 1272.57 minutes, just 8.76 minutes greater than the 1263.80-minute orbital period determined by the ephemeris fitter as part of this investigation. As the value established by Kepler's Third Law is 0.00688% greater than the value calculated by the fitter, the team has deemed these estimate mass values notable and in line with new values calculated in this investigation, giving greater plausibility to the likelihood of TOI-2341.01 being a strong planetary candidate. However, it should be stated again that these mass values are estimates provided by TFOP and should not be used over values provided by radial velocity measurements. Radial velocity measurements of TOI-2341.01 should be calculated in follow-up studies of this star system as outlined in section 8.

Table 6. Estimates of the mass of TOI-2341 and TOI-2341.01 provided by the Massachusetts Institute of Technology's TESS Follow-up Observation Program.

Stellar Body	*Estimated Mass ($M_{\odot}$)*	*Estimated Mass (M_J)*	*Estimated Mass (M_E)*
TOI-2341	0.6	628	333030
TOI-2341.01	1.66051×10^{-4}	0.173	55.3

4.5. Estimates of a low density "Puffy Planet"

Utilizing mass measurements from TFOP (MIT 2021) and radius measurements determined by EXOTIC, it is possible to estimate the density of TOI-2341.01 by determining the mass and volume of the planet. TFOP has listed TOI-2341.01's mass as 55.03 M_E, which is equivalent to 3.302516×10^{26} kg. This investigation has determined TOI-2341.01's radius to be 86,409.140 km ± 6011.210 km. Converting to meters, the new values are 86,409,140 m ± 60,1121 × 10^6 m. The volume of TOI-2341.01 can be determined with Equation 9:

$$\frac{4}{3} \times \pi \times 86409140^3 \quad (9)$$

This formula provides a value for TOI-2341.01's internal volume of 2.7025122×10^{24} m^3. By dividing the mass of TOI-2341.01 in kilograms by the volume in cubic meters as demonstrated in Equation 10, an estimate density value can be attained.

$$\frac{3.304728 \cdot 10^{26}}{2.7025122 \cdot 10^{24}} = 122.2835 \text{ kg/m}^3 \quad (10)$$

The calculated density estimates of 122.2835 kg/m^3 or 0.12228 g/cm^3 places TOI-2341.01 in the low mass, high radius range of hot Jupiter class exoplanets, also known as "Puffy Planets." While it is important to reiterate that these density and mass values are again estimates and should be followed up with prior study as detailed in section 8, these values add weight toward TOI-2341.01's likelihood of remaining a strong planetary candidate.

5. Blended eclipsing binaries and candidate legitimacy

A common false positive among TESS planet candidates is the presence of a "blended eclipsing binary" (EB). A blended EB occurs when another star and an orbiting planet or secondary star as part of a binary system exists close to the star being observed, in this case, TOI-2341, causing an erroneous signal similar to a planetary transit. Due to disparity in transit depth as a result of noise within the light curves collected by this investigation, a chromaticity check was undertaken to identify major deviations from a mean transit depth that could indicate a blended EB.

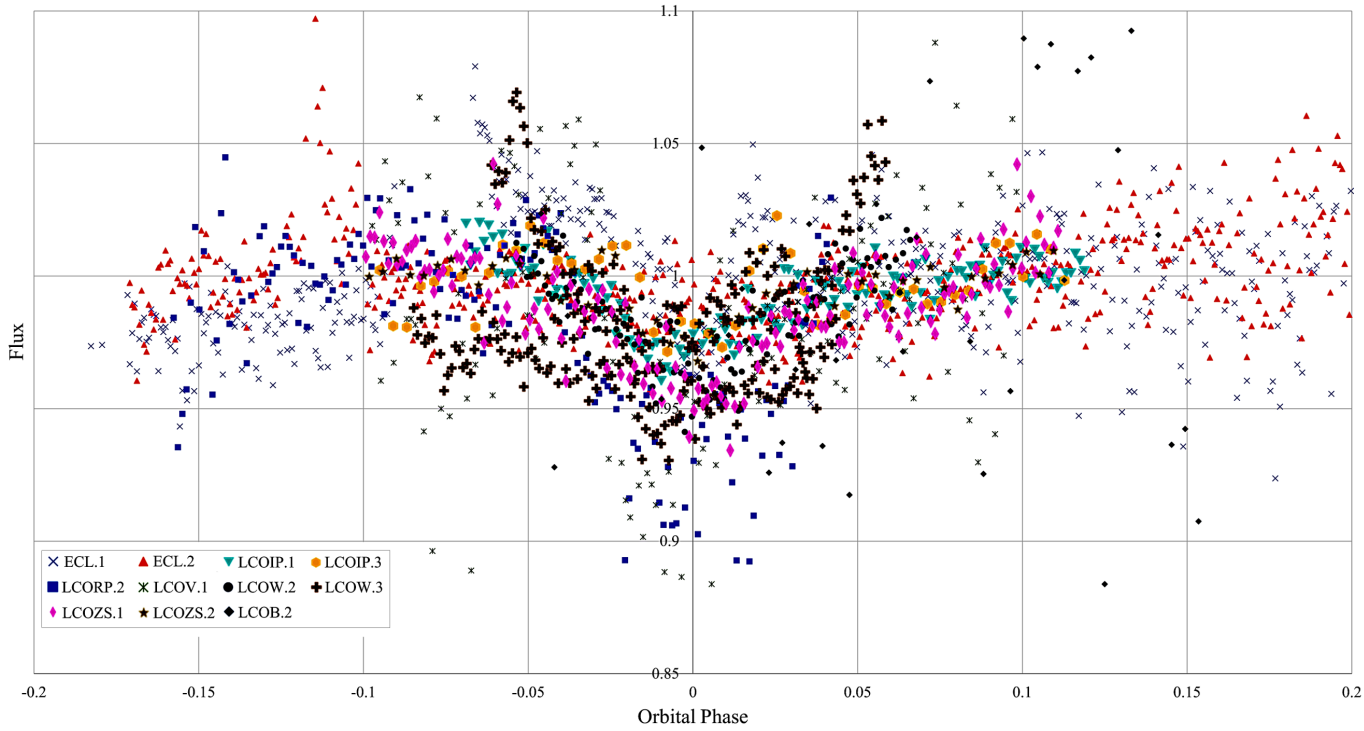

Figure 6. A visual demonstration of all ten "good transits" overlaid with "poor transit" TOI2341.01LCOB.2 to demonstrate deviation from the mean transit depth of 4.191 ± 0.529.

Blended EBs are also responsible for false "grazing-transit" detections, hence it was necessary to provide evidence to clear the observed field around TOI-2341 of blended and regular EBs. Table 7 presents recorded transit depths compared to the observed passbands of all ten "good transits" within this investigation, and one "poor" transit to cover the blue passband. Transit Depth 1 in Table 7 denotes the first light curve of that passband, and Transit Depth 2 is the second where applicable.

Figure 6 demonstrates the relationship between the ten "good transits" as well as a "poor" B Filter transit, TOI2341.01LCOB.2. Each transit does not significantly deviate from the mean transit depth of 4.191 ± 0.529 excluding the V and R passbands, of which there was only one recorded "good transit" and hence is the likely causation of its deviation.

Utilizing results provided by Table 7 and Figure 6, it can be stated that there is no correlation between different passbands and differing transit depths due to the high uncertainty values inclusive of the same passband across multiple transits. Therefore, it is likely differing transit depths across passbands can be attributed to noise caused by weather, equipment, or anomalies presented by the potential near grazing nature of TOI-2341.01 as illustrated in section 4.3.

Further evidence to clear the field of the TOI-2341 system of blended EBs can be found in prior literature where it is stated that TOI-2341.01 has an inclination of 78.93° ± 2.02° (Montalto *et al.* 2020), further backed by section 4.3 where TOI-2341.01's grazing criterion is calculated to be 0.99 ± 0.14, pushing the likelihood of TOI-2341.01's near grazing nature to an increased chance.

Another common feature of blended EB's is an erroneous second dip in flux caused by two orbiting stars in a binary pair. As shown in Figure 7 (Montalto *et al.* 2020), there are no recorded secondary dips in flux from TOI-2341 between phase –0.4 and 0.4, potentially ruling out the presence of a blended EB along the light curve, or at the least drastically reducing its probability.

Table 7. Passbands and transit depths of "good transits."

Filter	*Transit Depth 1 (%)*	*Transit Depth 2 (%)*
IP	2.67 ± 0.12	5.73 ± 0.54
R	6.21 ± 0.0057	N/A
V	5.93 ± 0.36	N/A
B	6.23 ± 3.73	6.06 ± 3.47
UV	4.14 ± 0.25	3.69 ± 0.78
Luminance	5.81 ± 0.56	1.27 ± 0.11
Clear	3.47 ± 0.18	2.99 ± 0.21

Greater evidence can be presented for the absence of blended and eclipsing binaries by the estimated mass and density values provided by a combination of TFOP (MIT 2021) and prerequisite values calculated as part of this investigation. The mass of TOI-2341.01 is estimated to be 55.3 M_E (0.1739 M_J) and its density is projected to be 122.2835 kg/m^3 or 0.12228 g/cm^3. While mass and density values are estimates and should be treated as such due to the uncertainty and extrapolation of information in the datasets from which they were attained, both values match planetary parameters calculated through this investigation with postulates such as Kepler's Third Law, and therefore can be treated with a degree of accuracy great enough to use as evidence toward the legitimacy of this planet candidate.

This investigation combined with prior literature (Montalto *et al.* 2020; MIT 2021) provides evidence towards the elimination of the blended EB hypothesis as an explanation for difference in transit depth and the v-shaped nature of the light curves collected within this study. However, as reiterated, despite mass and density estimated a conclusive statement cannot be

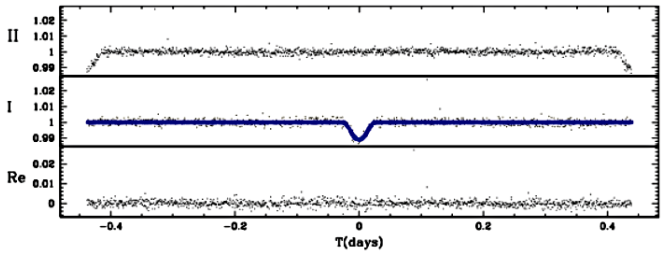

Figure 7. A transit recorded as part of a prior literature study (Montalto *et al.* 2020) shows the absence of a secondary dip common amongst blended EBs that provides greater evidence towards TOI-2341.01 existence as a hot Jupiter.

Table 8. All calculated planetary parameters for TOI-2341.01.

Planetary Parameters	*Values*	*SEM*	*Error (%)*
TOI-2341.01 radius (km)	86409	± 6011	6.957
TOI-2341.01 radius (R_E)	13.548	± 0.942	6.957
TOI-2341.01 radius (R_J)	1.209	± 0.084	6.957
Semi-major axis (KM)	1770692	± 109614	6.190
Semi-major axis (AU)	0.0118	± 0.0007	6.190
Transit duration (min)	93.6	± 8.6	9.259
Transit duration (h)	1.56	± 0.14	9.259
Transit duration (days)	0.065	± 0.006	9.259
Transit depth	4.191	± 0.529	12.614
Orbital period (days)	0.877640	± 0.000008	8.8×10^{-4}
Orbital period (h)	21.0634	± 0.0001	8.8×10^{-4}
Orbital period (min)	1263.8043	± 0.0011	8.8×10^{-4}
Mid-transit time (BJD_TDB)	2459411.742011	± 0.000131	1.0×10^{-8}
Grazing criterion	0.99	± 0.14	14.14
Planet mass (M_E) (estimate-TFOP)	55.3	N/a	n/a
Planet mass (M_J) (estimate-TFOP)	0.1739503	N/a	n/a
Planet density (kg/m^3) (estimate)	122.2835	N/a	n/a
Planet density (g/cm^3) (estimate)	0.12228	N/a	n/a

made as part of this paper due to the absence of radial velocity measurements, and hence true mass values for TOI-2341.01 and TOI-2341. Further investigations as detailed in section 8 should focus on the collection of radial velocity measurements to conclusively determine the nature of this planet candidate.

However, it can be stated with certainty that this investigation clears the field of view observed by both telescopes utilized in the imaging process of eclipsing binaries, as no false positive transits or erroneous dips have been recorded within the phase of TOI-2341.01's orbit studied during this investigation. Field-of-view measurements for both telescopes can be obtained in section 2. It can also be stated that the agreement between projected mass values and the data collected in this investigation lends significant weight toward the legitimacy of this planet candidate.

6. Results

In summary, Table 8 contains all calculated planetary and orbital parameters for TOI-2341.01 as part of this investigation. These are derived from the EXOTIC output values found in Table 4 and the ephemeris fitter output values found in Table 5. High error-values presented within transit duration can be explained by the near grazing nature of TOI-2341.01, which reduces EXOTIC's ability to determine a transit duration accurately. However, this transit duration can be visually confirmed via analysis of Figure 3, where 93 minutes is equivalent to the period of phase between –0.04 and +0.04 on the plot. Estimated values for planetary mass and density have also been provided in this table, however, it is notable that these estimates should be treated as such and do not substitute for further studies into the true mass value of this candidate planet described in section 8.

7. Conclusion

This paper presents 24 new light curves of TOI-2341.01 from observations conducted at the ELTHAM College, Cerro Tololo, and Siding Springs Observatories. These 24 new light curves and subsequent checks for the existence of nearby eclipsing binaries support the possibility of TOI-2341.01's existence as a planetary body first identified by NASA's TESS satellite. Furthermore, utilization of EXOTIC (Zellem *et al.* 2020) produced planetary parameters that were reduced via the process of standard deviation for TOI-2341.01. This investigation determined that TOI-2341.01 has a radius of 86,409 km ± 6011 km, or 1.209 R_{Jup} ± 0.084 R_{Jup}, and a semi-major axis 0.0118 AU ± 0.0007 AU, or 1,763,246 ± 58302 km. TOI-2341.01 has a revised transit depth of 4.191% ± 0.529%, with a transit duration of 0.065 ± 0.006 day (1.56 ± 0.14 hours or 93.6 ± 8.6 minutes). A revised orbital period for TOI-2341.01 was calculated to be 0.8776386 ± 0.0000042 day. The mid-transit point was revised and calculated as BJD_TDB 2459411.742011 ± 0.000131. These updated parameters demonstrate that TOI-2341.01 is larger and orbiting closer to TOI-2341 than stated in previous literature (Montalto *et al.* 2020). Furthermore, the calculated grazing criterion value of 0.99 ± 0.14 indicates that TOI-2341.01 is likely a near-grazing transit. It is also of note that estimate mass values were attained via the TESS Follow-up Observation Program that listed TOI-2341.01's mass as 55.3 M_E (0.173 M_J) (MIT 2021), and thus an estimate of planetary density, combining the mass values provided by TFOP and radius and volume values calculated in this survey, was calculated to be 122.28 kg/m^3 ± 0.12228 g/cm^3. The host star TOI-2341 is likely an M-type main-sequence star, based on TOI 2341's radius of 0.62 $R_\odot$ ± 0.02 $R_\odot$, effective temperature of 3495 K ± 157 K, a measured magnitude of 12.722 ± 0.008 in the Cousins I band (Barclay 2022) and has a calculated luminosity of 0.051 ± 0.006 given by the Stefan-Boltzmann equation (Equation 2). Furthermore, the TESS Follow-up Observation Program (TFOP) lists an estimated mass for TOI-2341 as 0.6 $M_\odot$. It can be stated that given available data collected as part of this investigation, there is significant credibility to the conclusion of TOI-2341.01's existence as a planetary body rather than a false positive. In this event TOI-2341.01 would fit the classification of a hot Jupiter or more specifically a "puffy planet." This study has determined that the field of view captured by telescopes utilized in this investigation is clear of eclipsing binaries. However, further work is required to determine TOI-2341.01's true nature, most prominently in the collection of radial velocity measurements detailed in section 8. Investigations of this kind would rule out the possibility of an eclipsing binary and add further evidence to support the existence of this candidate planet.

8. Future work

There is a strong case for continued study of the TOI-2341 system utilizing larger telescopes to obtain radial velocity measurements. While mass values have been provided by the TESS Follow-up Observation Program, these values are estimates calculated utilizing available TESS data and are not substitutes for actual values, thus they should be treated as projections. Data on the radial velocity of TOI-2341.01 and TOI-2341 would allow for the calculation of true masses for both bodies in the system, either concluding or refuting TOI-2341.01's existence as a planetary body with a much greater degree of certainty.

Future investigations into the nature of TOI-2341.01 should also conduct more transit observations, narrowing down parameters provided in both prior literatures and this paper to gain a greater insight into the TOI-2341 system as a whole. Given uncertainties presented as part of this study, follow up observations are a necessity to produce quality light curves of this exoplanet.

9. Acknowledgements

Thank you to Kalée Tock, who not only provided her insight during various discussions regarding the nature of TOI-2341.01 but also provided the programs required for the production of updated and revised mid-transit times.

Thank you to Pat Boyce for his discussion and insight into the production of this paper throughout the investigation process, allowing the team to approach the investigation process from a new perspective.

Thank you to Kyle Pearson for his assistance with issues that arose during the use of the EXOTIC software and his continued support with EXOTIC and data reduction throughout the production process. Furthermore, the utilization of his ephemeris fitter allowed for calculating an orbital period and transit midpoints that would otherwise not be possible.

Thank you to Rob Zellem for his incredible assistance with EXOTIC and the conclusions of this paper. Without his help this paper would not be possible. An additional thank you for his production and maintenance of the EXOTIC software and thank you to the EXOTIC team.

This investigation would not be possible without the NASA Exoplanet Archive, owned and operated by the California Institute of Technology in collaboration with the National Aeronautics and Space Administration under the Exoplanet Exploration Program.

Furthermore, this publication uses the EXOTIC data reduction software produced by Exoplanet Watch, a citizen science project owned and operated by NASA's Jet Propulsion Laboratory. Also utilized was the program AstroSource, made to pre-reduce data for the production of light curves under investigation conditions.

References

Barclay, T. 2022, "Characteristics of the TESS space telescope," NASA High Energy Astrophysics Science Archive Research Center (HEASARC; https://heasarc.gsfc.nasa.gov/docs/tess/the-tess-space-telescope.html).

Bertin, E. 2011, in *Astronomical Data Analysis Software and Systems XX*, eds. I. N. Evans, A. Accomazzi, D. J. Mink, A. H. Rots, ASP Conf. Ser. 442, Astronomical Society of the Pacific, San Francisco, 435.

Borucki, W. J., *et al.* 2010, *Science*, **327**, 977 (doi: 10.1126/science.1185402).

Brown, T. M., *et al.* 2013, *Publ. Astron. Soc. Pacific*, **125**, 1031.

Fitzgerald, M. T. 2018, *Robotic Telesc., Student Res. Education Proc.*, **1**, 343 (doi: 10.32374/rtsre.2017.033).

Fitzgerald, M., Gomez, E., Salimpour, S., Singleton, J., and Wibowo, R. 2021, *J. Open Source Software*, **6**, 2641 (doi: 10.21105/joss.02641).

Fowler, M. J. F., Sienkiewicz, F. F., Zellem, R. T., and Dussault, M. E. 2021, *J. British Astron. Assoc.*, **131**, 359 (arXiv:2007.13381).

Hartman, J. D., *et al.* 2011, *Astrophys. J.*, **742** (doi: 10.1088/0004-637X/742/1/59).

Lillo-Box, J., Barrado, D., Santos, N. C., Mancini, L., Figueira, P., Ciceri, S., and Henning, Th. 2015, *Astron. Astrophys.*, **577A**, 105 (doi.org/10.1051/0004-6361/201425428).

Mancini, L., *et al.* 2014, *Astron. Astrophys.*, **568A**, 127 (doi: 10.1051/0004-6361/201424106).

Mandushev, G., *et al.* 2007, *Astrophys. J.*, **667**, L195 (doi: 10.1086/522115).

Massachusetts Institute of Technology. 2021, TESS Followup Observation Program, TOIs accessed 2021-11-11 (https://tess.mit.edu/wp-content/uploads/RVvaluesByESM_onlyPCs_rankedESM.txt).

Montalto, M., *et al.* 2020, *Mon. Not. Roy. Astron. Soc.*, **498**, 1726 (doi: 10.1093/mnras/staa2438).

Pearson, K. A. 2019, *Astron. J.*, **158**, 243 (doi: 10.3847/1538-3881/ab4e1c).

Ricker, George R., *et al.* 2015, *J. Astron. Telesc. Instrum. Syst.*, **1**, 014003 (doi: 10.1117/1.JATIS.1.1.014003).

Salimpour, S., Fitzgerald, M., and Demmert, H. 2021, *Astron. Theory, Obs. Methods*, **2**, 45 (doi: 10.32374/atom.2020.2.6).

Sarva, J., Freed, R., Fitzgerald, M. T., and Salimpour, S. 2020, *Astron. Theory, Obs. Methods*, **1**, 34.

Torres, G., *et al.* 2010, *Astrophys. J.*, **715**, 458 (doi: 10.1088/0004-637X/715/1/458).

Wang, J., Fischer, D. A., Horch, . P., and Huang, X. 2015, *Astrophys. J.*, **799**, 229 (doi: 10.1088/0004-637X/799/2/229).

Zellem, Robert T., *et al.* 2020, *Publ. Astron. Soc. Pacific*, **132**, 054401 (doi: 10.1088/1538-3873/ab7ee7).

Appendix A: Light curves of TOI-2341.01 reduced by EXOTIC.

The appendix is a complete collection of all transits observed as part of this investigation into the nature of TOI-2341.01. Light curve designations are listed below their respective plot, and further details are attributed to their designations in Table 2.

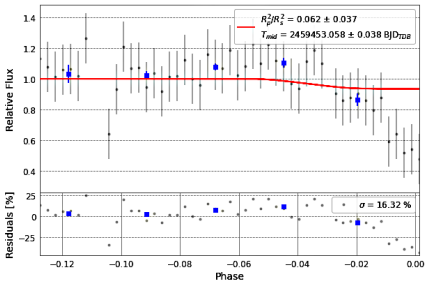

TOI2341.01ECB.1

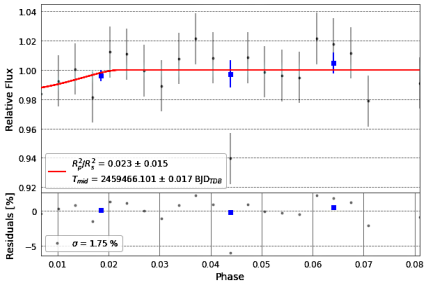

TOI2341.01ECIP.1

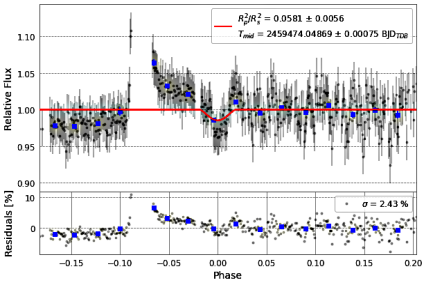

TOI2341.01ECL.1

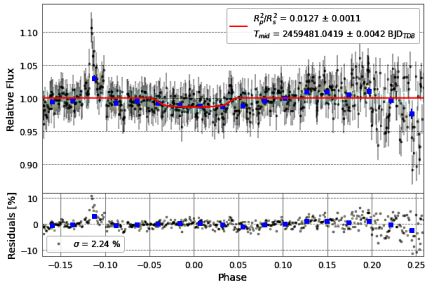

TOI2341.01ECL.2

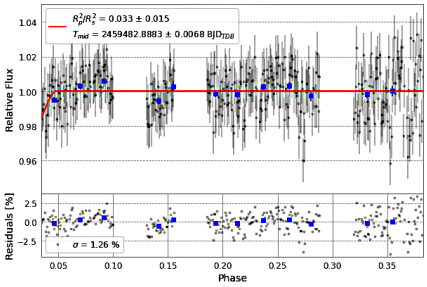

TOI2341.01ECL.3

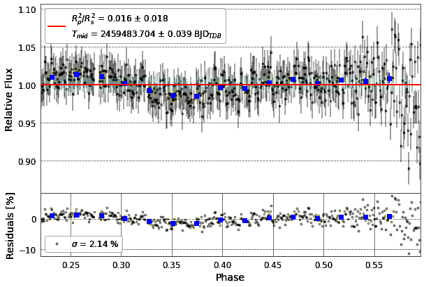

TOI2341.01ECL.4

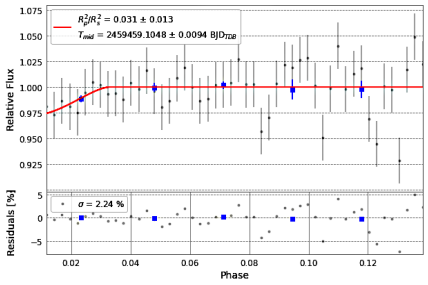

TOI2341.01ECRP.1

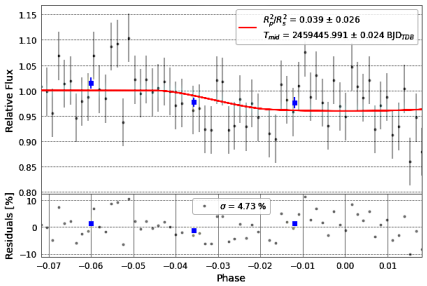

TOI2341.01ECRP.2

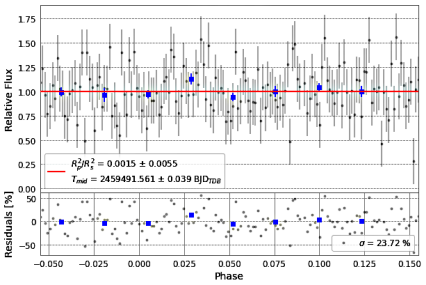

TOI2341.01LCOB.1

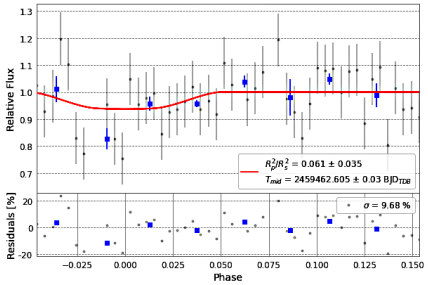

TOI2341.01LCOB.2

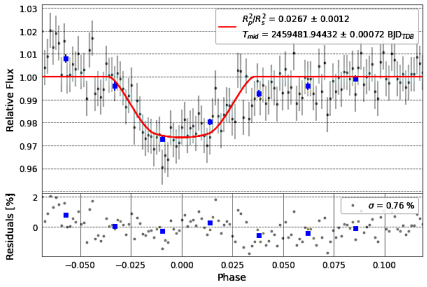

TOI2341.01LCOIP.1

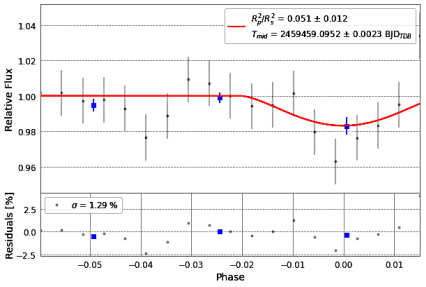

TOI2341.01LCOIP.2

Appendix A: Light curves of TOI-2341.01 reduced by EXOTIC (cont.).

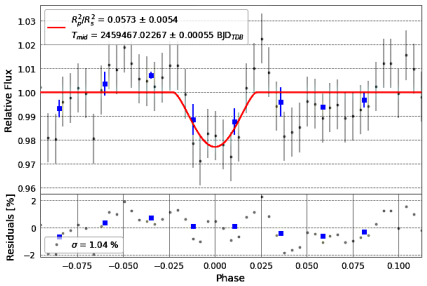

TOI2341.01LCOIP.3

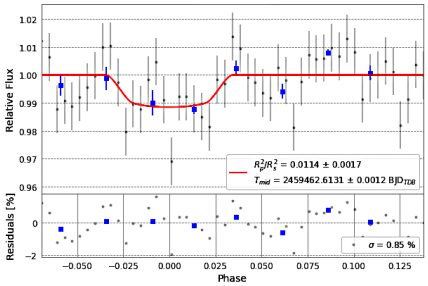

TOI2341.01LCORP.1

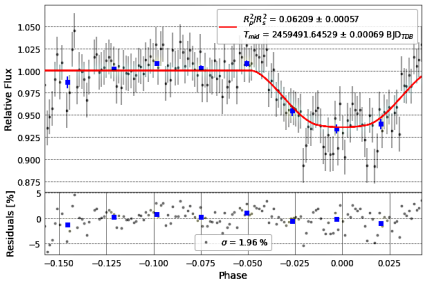

TOI2341.01LCORP.2

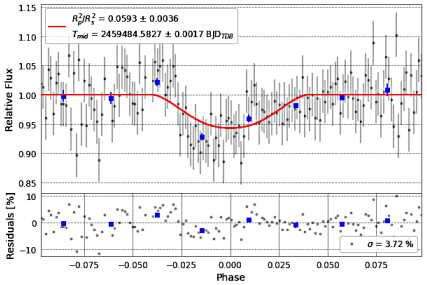

TOI2341.01LCOV.1

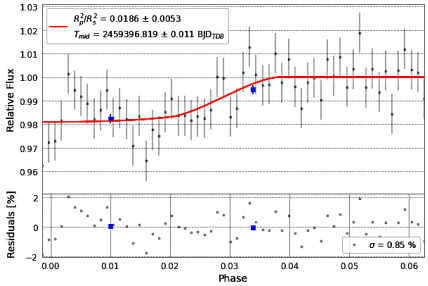

TOI2341.01LCOW.1

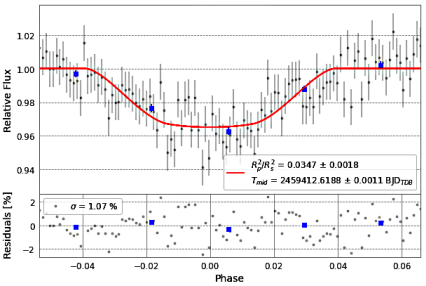

TOI2341.01LCOW.2

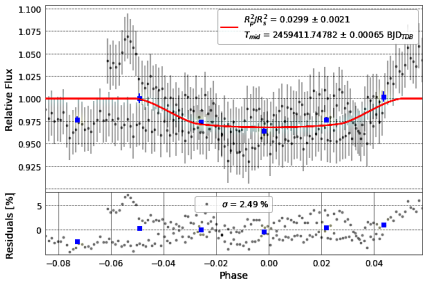

TOI2341.01LCOW.3

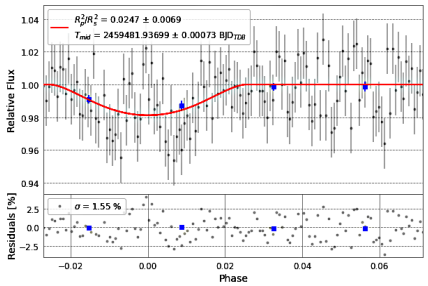

TOI2341.01LCOW.4

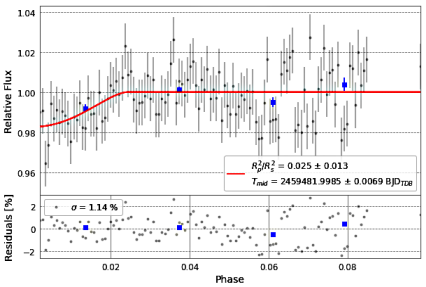

TOI2341.01LCOW.5

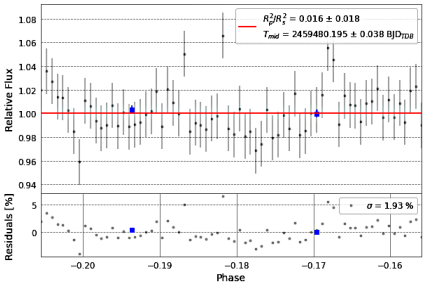

TOI2341.01LCOW.6

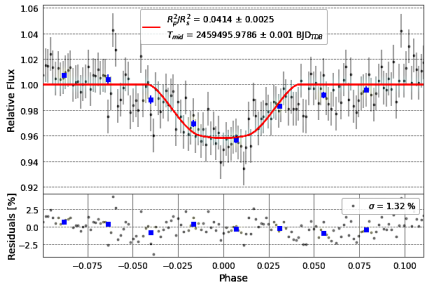

TOI2341.01LCOZS.1

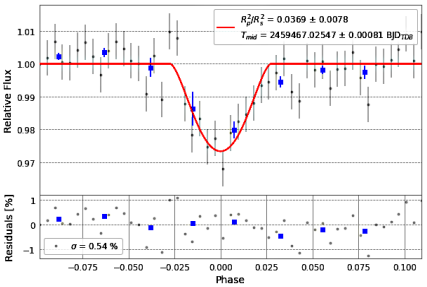

TOI2341.01LCOZS.2

CCD Photometry, Period Study, and Light Curve Modeling of the Overcontact Binary Systems NSVS 5374825 and GR Piscium

Kevin B. Alton
UnderOak Observatory, 70 Summit Avenue, Cedar Knolls, NJ 07927; kbalton@optonline.net

Received May 4, 2022; revised June 30, 2022; accepted July 5, 2022

Abstract During this study precise time-series multi-bandpass (B, V, and I_c) light curve (LC) data for NSVS 5374825 (2018–2019) and GR Psc (2019) were acquired at Desert Blooms Observatory (DBO). Both targets produced new times of minimum which were used along with other eclipse timings mined from the SuperWASP survey and the literature to update their corresponding ephemerides. Preliminary evidence suggests a secular decrease in the orbital period of GR Psc between 2004 and 2019, while during the same time span NSVS 5374825 experienced an increase in its orbital period. Roche modeling to produce synthetic fits to the observed LC data was accomplished using the Wilson-Devinney code. Since each system exhibits a total eclipse, a reliable value for the mass ratio (q) could be determined leading in turn to initial estimates for the physical and geometric elements of both variable systems. Absolute determinations will still require radial velocity and high resolution spectral classification studies.

1. Introduction

CCD-derived photometric data for NSVS 5374825 (GSC 3111-0679) were first acquired from the ROTSE-I survey between 1999–2000 (Akerlof *et al.* 2000; Woźniak *et al.* 2004; Gettel *et al.* 2006) and later from the Catalina Sky (Drake *et al.* 2014), SuperWASP (Butters *et al.* 2010), and ASAS-SN (Jayasinghe *et al.* 2018) surveys. Its classification as a W UMa variable was assigned according to Hoffman *et al.* (2009). No other times of minimum (ToM) have been found in the literature; this paper marks the first detailed period analysis and multi-color Roche model assessment of light curves (LCs) for NSVS 5374825. In a similar fashion the variability of GR Psc (GSC 1747-0967) was initially observed (Martignoni 2006) from data acquired during the ROTSE-1 Survey (1999–2000). Later on (2005–2013) sparsely-sampled light curve data were collected during the Catalina Sky Survey, ASAS (Pojmański 2005), SuperWASP (Butters *et al.* 2010), and ASAS-SN (Jayasinghe *et al.* 2018) surveys. Michaels (2020) published a detailed investigation on GR Psc which coincidently included photometric data (B,V, g', r') acquired during nearly the same time period (October–November 2019) as the study herein. With one notable exception, the results from both studies were very similar.

2. Observations and data reduction

Precise time-series photometric observations were acquired at Desert Blooms Observatory (DBO, USA: 31.941 N, 110.257 W) using two different CCD cameras. In 2018, NSVS 5374825 images were obtained with an SBIG STT-1603ME CCD camera mounted at the Cassegrain focus of a 0.4-m Schmidt-Cassegrain telescope. This combination (f/6.8) produced an image scale of 1.36 arcsec/pixel (bin = 2 × 2) and a field-of-view (FOV) of 11.5' × 17.2'. In 2019 all photometric data were generated using a QSI 683 wsg-8 CCD camera mounted on the same optical tube assembly. This focal-reduced (f/7.2) instrument produced an image scale of 0.76 arcsec/pixel (bin = 2 × 2) and a field-of-view (FOV) of 15.9 × 21.1 arcmin. In both cases the CCD cameras were equipped with photometric B, V, and I_c filters manufactured to match the Johnson-Cousins Bessell specification. Image (science, darks, and flats) acquisition software (TheSkyX Pro Edition 10.5.0; Software Bisque 2019) controlled the main and off-axis guide cameras. Computer clock time was updated immediately prior to each session. Dark subtraction, flat correction, and registration of all images collected at DBO were performed with AIP4Win v2.4.1 (Berry and Burnell 2005). Instrumental readings were reduced to catalog-based magnitudes using the APASS star fields (Henden *et al.* 2009, 2010, 2011; Smith *et al.* 2011) built into MPO Canopus v10.7.1.3 (Minor Planet Obs. 2010). In order to minimize any potential error due to differential refraction and color extinction, only data from images taken above 30° altitude (airmass <2.0) were included. All photometric data acquired from NSVS 5374825 and GR Psc at DBO can be retrieved from the AAVSO International Database (Kafka 2021; observer code "AKV").

Uncertainty in comparison star measurements made in the same FOV with NSVS 5374825 or GR Psc typically stayed within ± 0.007 mag for V- and I_c- and ± 0.010 mag for B-passbands. The identity, J2000 coordinates, and color indices (B–V) for these stars are provided in Table 1. AAVSO finder charts for NSVS 5374825 (Figure 1) and GR Psc (Figure 2) are centered around each target along with its corresponding ensemble (1–5) of comparison stars.

3. Results and discussion

Results and detailed discussion about the determination of linear and quadratic ephemerides are provided in this section. Thereafter, the multi-source approach for estimating the effective temperatures for NSVS 5374825 and GR Psc along with Roche-lobe modeling results with the W-D code are examined. Finally, preliminary estimates for mass ($M_\odot$) and radius ($R_\odot$), along with corresponding calculations for luminosity ($L_\odot$), surface gravity (log (g)), semi-major axis ($R_\odot$), and bolometric magnitude (M_{bol}), are derived.

Table 1. Astrometric coordinates (J2000), V-mags and color indices (B - V) for NSVS 5374825, GR Psc, and their corresponding five comparison stars used in this photometric study.

Star	*R.A.* *h m s*	*Dec.* ° ′ ″	*V-mag*[a]	*(B−V)*[a]
NSVS 5374825	18 10 33.53	+42 16 23.1	13.228	0.586
GSC 3111-1428	18 10 18.31	+42 15 49.2	13.227	0.796
GSC 3110-1324	18 09 18.73	+42 13 21.1	12.836	0.857
GSC 3110-1053	18 09 37.61	+42 12 55.1	14.084	0.559
GSC 3111-1679	18 10 06.28	+42 09 32.7	14.094	0.553
GSC 3111-1650	18 10 14.35	+42 12 22.9	14.048	0.460
GR Psc	01 09 31.89	+22 39 19.8	11.296	0.444
GSC 1747-0927	01 06 38.53	+22 46 22.8	11.355	1.117
GSC 1747-0179	01 09 15.13	+22 44 17.4	12.109	0.603
GSC 1747-0517	01 10 21.93	+22 51 59.1	10.916	0.502
GSC 1747-0623	01 10 18.66	+22 38 02.6	12.469	0.663
GSC 1747-0841	01 10 20.39	+22 37 24.9	13.172	0.593

[a] *V-mag and (B−V) for comparison stars derived from APASS database described by Henden* et al. *(2009, 2010, 2011) and Smith* et al. *(2011).*

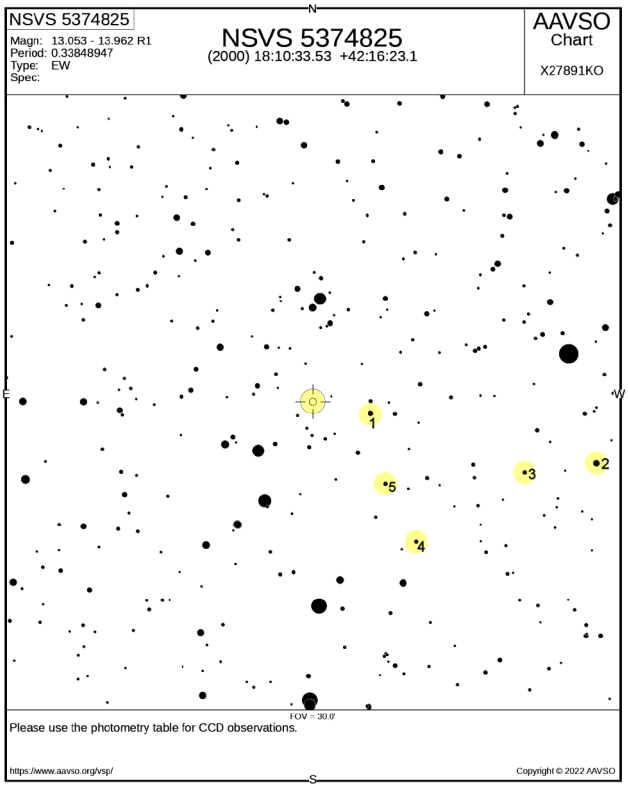

Figure 1. Finder chart for NSVS 5374825 (center) also showing the comparison stars (1–5) used for aperture-derived ensemble photometry.

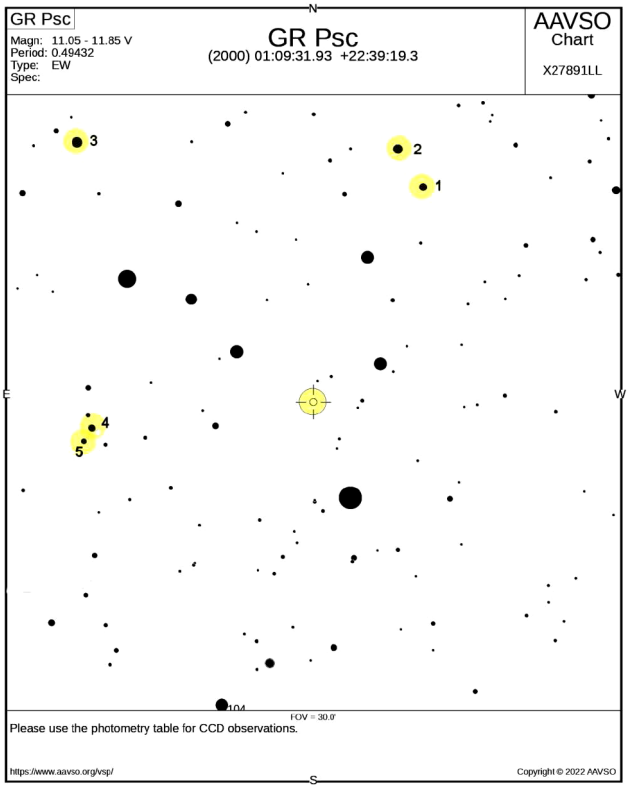

Figure 2. Finder chart for GR Psc (center) also showing the comparison stars (1–5) used for aperture-derived ensemble photometry.

3.1. Photometry and ephemerides

ToM values and associated errors from data acquired at DBO were calculated according to Andrych and Andronov (2019) and Andrych *et al.* (2020) using the program MAVKA (https://uavso.org.ua/mavka/). Simulation of extrema (Min I and Min II) was automatically optimized by finding the most precise degree (α) and best fit algebraic polynomial expression. A "wall-supported line" (WSL) algorithm (Andrych *et al.* 2017) provided the best fit, as the eclipse passes through totality, resulting in a flattened bottom. Long-term or secular changes in orbital period can sometimes be revealed by plotting the difference between the observed eclipse times and those predicted by a reference epoch against cycle number. These residuals (ETD) vs. epoch were fit using scaled Levenberg-Marquardt algorithms (QtiPlot ~0.9.9–rc9; https://www.qtiplot.com/). The results from these analyses are separately discussed for each binary system in the subsections below. NSVS 5374825 and GR Psc were also imaged during the SuperWASP survey (Butters *et al.* 2010), which provided a rich source of photometric data taken (30-s exposures) at modest cadence that repeats every 9 to 12 min. In some cases (NSVS 5374825, n = 80; GR Psc, n = 36) SuperWASP measurements taken between 2004 and 2008 were amenable to extrema estimation using MAVKA.

3.1.1. NSVS 5374825

A total of 584 photometric values in B-, 589 in V-, and 571 in I_c-passbands were acquired at DBO from NSVS 5374825 between 19 May 2018 and 27 May 2019. Included in these determinations were nine new times of minimum (ToM) acquired during this study which are summarized in Table 2. Period-folded LCs from the Catalina Sky and ASAS-SN surveys were used to interpolate a mid-point time during Min I and Min II. These two results, along with other eighty ToM values estimated from the SuperWASP survey from 2004 through 2008, were used to determine whether any secular changes in the orbital period could be detected from the eclipse timing residuals.

Inspection of the ETD residuals vs. epoch plot (Figure 3) reveals a parabolic relationship. ToM values acquired between 2017 and 2019 were used to determine a near-term linear ephemeris:

Table 2. Sample table of NSVS 5374825 times-of-minimum (16 May 2004–27 May 2019), cycle number and eclipse timing difference (ETD) between observed and predicted times derived from the updated linear ephemeris (Equation 1).

HJD = 2400000+	*HJD Error*	*Cycle No.*	*ETD*	*Ref.*
53141.6420	0.0002	–16216.5	0.0315	1
53142.6588	0.0007	–16213.5	0.0328	1
53143.6711	0.0003	–16210.5	0.0296	1
54621.5160	0.0003	–11844.5	0.0179	1
54623.5476	0.0002	–11838.5	0.0185	1
54624.5629	0.0006	–11835.5	0.0183	1

References in sample: (1) SuperWASP (Butters et al. 2010); Full table available at: ftp://ftp.aavso.org/public/datasets/3831-Alton-NSVS_5374825.txt. All references relevant to the full table that appears on the AAVSO ftp site are included in the References section of this article. All references are given in the full table.

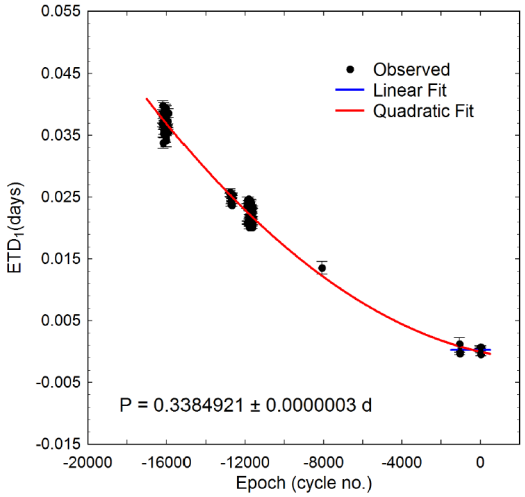

Figure 3. The upwardly directed quadratic fit (Equation 2) to the ETD vs. epoch data is shown with a solid red line and suggests the orbital period of NSVS 5374825 is increasing with time. The linear ephemeris (Equation 1) was determined from near-term data acquired between 2017 and 2019 (solid blue line). ToM measurement uncertainty is defined by the error bars.

Table 3. Sample table of GR Psc times-of-minimum (13 July 2004–20 Nov 2019), cycle number and eclipse timing difference (ETD) between observed and predicted times derived from the updated linear ephemeris (Equation 3).

HJD = 2400000+	*HJD Error*	*Cycle No.*	*ETD*	*Ref.*
53199.6707	0.0003	–11344.5	–0.0082	1
53200.6585	0.0004	–11342.5	–0.0090	1
53201.6472	0.0004	–11340.5	–0.0089	1
54020.4896	0.0003	–9684	–0.0057	1
54021.4782	0.0005	–9682	–0.0058	1
54022.4674	0.0003	–9680	–0.0052	1

[a] Outlier value not included in period analyses; nr = not reported ("a" and "nr" not shown in this sample).
References in sample: (1) SuperWASP (Butters et al. 2010); Full table available at: ftp://ftp.aavso.org/public/datasets/3831-Alton-GR_Psc.txt. All references relevant to the full table that appears on the AAVSO ftp site are included in the References section of this article. All references are given in the full table.

$$\text{Min. I (HJD)} = 2458630.76818(3) + 0.3384921(3)\,E. \quad (1)$$

The difference between the observed eclipse times and those predicted by the linear ephemeris (Equation 1) against epoch (cycle number) was best fit by a quadratic relationship (Equation 2) where:

$$ETD = -2.2799 \cdot 10^{-4} - 2.8854 \cdot 10^{-7} E + 9.9473 \cdot 10^{-11} E^2. \quad (2)$$

Since the coefficient of the quadratic term (Q) is positive, this result would suggest that the orbital period has been increasing at a constant rate ($dP/dt = 2Q/P$) of 0.0185 ± 0.0011 s · y^{-1}. This rate is similar to many other overcontact systems reported in the literature (Latković *et al.* 2021). Period change over time that can be described by a parabolic expression is often attributed to mass transfer or by angular momentum loss (AML) due to magnetic stellar wind (Qian 2001, 2003; Li *et al.* 2019). Ideally, when AML dominates, the net effect is a decreasing orbital period. If conservative mass transfer from the more massive to its less massive secondary star prevails, then the orbital period can also decrease. Separation increases when conservative mass transfer from the less massive to its more massive binary cohort takes place or spherically symmetric mass loss from either body (e.g. a wind but not magnetized) occurs. In mixed situations (e.g. mass transfer from less massive star, together with AML) the orbit evolution depends on which process dominates. Since the orbital period is not a constant, then linear ephemerides need to be regularly updated.

3.1.2. GR Psc

A total of 733 photometric values in B-, 690 in V-, and 703 in I_c-passbands were acquired from GR Psc between October 19, 2019, and November 15, 2019. Included in these determinations were seven new ToM values acquired at DBO which are provided in Table 3. Twenty-one ToM estimates from the literature, along with thirty-six ToM values determined from the SuperWASP survey from 2004 through 2008, were used to determine whether any secular changes in the orbital period could be detected from the eclipse timing residuals. An updated linear ephemeris (Equation 3) based on near term ETD values (2012–2019) was derived as follows:

$$\text{Min. I (HJD)} = 2458807.47917(7) + 0.4943189(1)\,E. \quad (3)$$

These data are shown as a blue horizontal line in Figure 4. Nevertheless, since the orbital period appears to be decreasing at a constant rate, ephemerides for GR Psc will need to be updated on a regular basis.

Plotting the difference between the observed eclipse times and those predicted by the linear ephemeris against epoch (Figure 4) uncovered what appears to be a quadratic relationship (Equation 4) where:

$$ETD = -6.5912 \cdot 10^{-5} - 3.8752 \cdot 10^{-7} E - 9.8507 \cdot 10^{-11} E^2. \quad (4)$$

In this case the ETD residuals vs. epoch can be best described by an expression with a negative quadratic coefficient ($-9.8507 \cdot 10^{-11}$), suggesting that the orbital period has been slowly decreasing

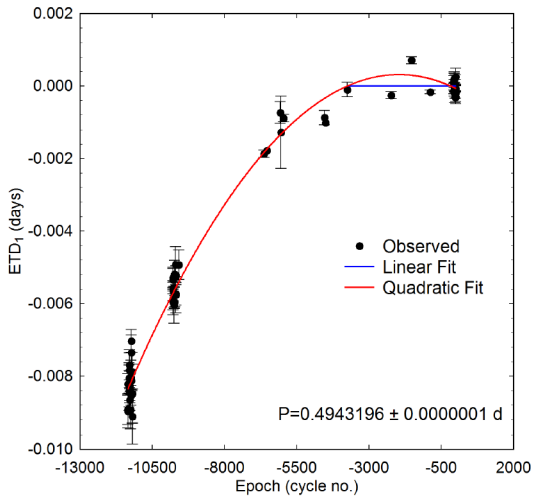

Figure 4. The downwardly directed quadratic fit to the ETD vs. epoch data (Equation 4) is shown with a solid red line and suggests the orbital period of GR Psc is decreasing with time. The linear ephemeris (Equation 3) (solid blue line) is determined from near-term data acquired between 2014 and 2019. Measurement uncertainty is defined by the error bars when available.

over time at the rate of $-0.0126\,(6)\,s\cdot y^{-1}$. Michaels (2020) reported a more rapid orbital period change rate ($-0.021\,s\cdot y^{-1}$). These differences are largely attributed to the inclusion of additional ToM values from the SuperWASP survey as well as those acquired at DBO. Nonetheless, both values are consistent with many other overcontact systems reported in the literature (Latković *et al.* 2021).

3.2. Effective temperature estimation

Throughout this paper the primary star is defined as the more massive member of each binary system. No medium-to-high resolution classification spectra were found in the literature for either variable. Therefore, the effective temperature (T_{eff1}) of each primary star has been estimated using color index (B–V) data acquired at DBO and others determined from astrometric (USNO-A2.0, USNO-B1.0, and UCAC4) and photometric (2MASS and APASS) surveys. These were transformed as necessary to (B–V)[1,2]. Interstellar extinction (A_V) was calculated ($E(B-V)\times 3.1$) using the reddening value (E(B–V)) estimated from Galactic dust map models reported by Schlafly and Finkbeiner (2011).

The intrinsic color ($(B-V)_0$) for NSVS 5374825 that was calculated from measurements made at DBO and those acquired from three other sources are listed in Table 4. Additional temperature values were mined from the Gaia DR2[3] (Gaia Collaboration *et al.* 2016, 2018), LAMOST DR5[4], and TESS[5] websites. The median T_{eff} and median absolute deviation values derived from all sources indicate a primary star with an effective temperature (5400 ± 173 K) that probably ranges in spectral class between G7V and K1V. These values represent a fairly broad range of temperatures (840 K) in which uncertainty of the mean (5550) approaches ±400 K. The potential impact on parameter estimates from Roche modeling with the WD code is addressed in section 3.4.

Similarly, dereddened color indices ($(B-V)_0$) for GR Psc gathered from different sources are listed in Table 5. The median value (6700 ± 200 K) adopted for Roche modeling corresponds to a primary star that likely ranges in spectral class between F1V and F5V.

3.3. Modeling approach with Wilson-Devinney code

Roche modeling of LC data from NSVS 5374825 (Figure 5) and GR Psc (Figure 6) was accomplished using the programs

Table 4. Derivation of the primary star effective temperature (Teff1) of NSVS 5374825 based upon temperature estimates from multiple sources.

	APASS	*USNO-A2.0*	*2MASS*	*Present Study*	*Gaia DR2*[a]	*LAMOST DR5*[b]	*TESS*[c]	*Houdashelt* et al. *(2000)*
$(B-V)_0$[d]	0.540	0.844	0.744	0.551	—	—	—	—
T_{eff}[e] (K)	6100	5180	5464	6045	5260^{+188}_{-246}	5322 (29)	5299 (231)	5733 (263)
Spectral Class[f]	F8V-F9V	K0V-K1V	G8V-G9V	F8V-F9V	K0V-K1V	G9V-K0V	G9V-K0V	G2V-G3V

[a] *Gaia Collab. (2016, 2018).* [b] *Zhao* et al. *(2012); Wang* et al. *(2019).* [c] *https://exofop.ipac.caltech.edu/tess/ .* [d] *Intrinsic $(B-V)_0$ determined using reddening value $E(B-V) = 0.0459 \pm 0.0019$; T_{eff1} interpolated from Pecaut and Mamajek (2013).* [e] *Median of all T_{eff1} values (5400 ± 173 K) adopted for LC modeling which most likely corresponds to a G7V-K1V main sequence star.* [f] *Spectral class range estimated from Pecaut and Mamajek (2013).*

Table 5. Derivation of the primary star eective temperature (Teff1) of GR Psc based upon temperature estimates from multiple sources.

	APASS	*USNO-A2.0*	*2MASS*	*Present Study*	*Terrell* et al. *(2012)*	*Gaia DR2*[a]	*TESS*[b]	*Houdashelt* et al. *(2000)*
$(B-V)_0$[c]	0.404	0.469	0.374	0.423	0.365	—	—	—
T_{eff1}[d] (K)	6669	6396	6812	6586	6861	6909^{+285}_{-232}	6790 (361)	6570 (200)
Spectral Class[e]	F3V-F4V	F5V-F6V	F1V-F2V	F1V-F2V	F1V-F2V	F1V-F2V	F2V-F3V	F4V-F5V

[a] *Gaia Collab. (2016, 2018).* [b] *https://exofop.ipac.caltech.edu/tess/ .* [c] *Intrinsic $(B-V)_0$ determined using reddening value $E(B-V) = 0.0392 \pm 0.0005$; T_{eff1} interpolated from Pecaut and Mamajek (2013).* [d] *Median of all T_{eff1} values (6700 ± 200 K) adopted for LC modeling which most likely corresponds to a F1V-F5V main sequence star.* [e] *Spectral class range estimated from Pecaut and Mamajek (2013).*

[1] http://www.aerith.net/astro/color_conversion.html
[2] http://brucegary.net/dummies/method0.html
[3] http://vizier.u-strasbg.fr/viz-bin/VizieR?-source=I/345/gaia2
[4] http://dr5.lamost.org/search [5] https://exofop.ipac.caltech.edu/tess/

PHOEBE 0.31a (Prša and Zwitter 2005) and WDwint56a (Nelson 2009). Both feature a user friendly GUI interface to the Wilson-Devinney WD2003 code (Wilson and Devinney 1971; Wilson 1979; 1990). WDwint56a makes use of Kurucz's atmosphere models (Kurucz 2002), which are integrated over BVR_cI_c optical passbands. In both cases, the selected model was Mode 3 for an overcontact binary. Other modes (detached and semi-detached) were explored but never approached the goodness of fit achieved with Mode 3. Since the internal energy transfer to the surface of both variable systems is driven by convective (T_{eff1} <7500 K) rather than radiative processes, the bolometric albedo ($A_{1,2}$ = 0.5) was assigned according to Ruciński (1969) while the gravity darkening coefficient ($g_{1,2}$ = 0.32) was adopted from Lucy (1967). Logarithmic limb darkening coefficients (x_1, x_2, y_1, y_2) were interpolated (Van Hamme 1993) following each change in the effective temperature (T_{eff2}) of the secondary star during model fit optimization using differential corrections (DC). All but the temperature of the more massive star (T_{eff1}), $A_{1,2}$, and $g_{1,2}$ were allowed to vary during DC iterations. In general, the best fits for T_{eff2}, i, q, and Roche potentials ($\Omega_1 = \Omega_2$) were collectively refined (method of multiple subsets) by DC using the multicolor LC data. LCs from NSVS 5374825 (Figure 5) and GR Psc (Figure 6) do not exhibit significant asymmetry during quadrature (Max I ≅ Max II), which is often called the O'Connell effect (O'Connell 1951). As such, no spot was invoked to improve LC simulations for either variable. Third-light contribution (l_3) during DC optimization did not lead to any value significantly different from zero with either binary system. A detailed discussion of the determined mass ratio and derived masses follows in subsequent sections.

3.4. Modeling results with Wilson-Devinney code

It is generally not possible to determine unambiguously the mass ratio or total mass of an eclipsing binary system without spectroscopic radial velocity (RV) data. Standard errors reported in Tables 6 and 7 are computed from the DC covariance matrix and only reflect the model fit to the observations which assume exact values for any fixed parameter. These formal errors are generally regarded as unrealistically small considering the estimated uncertainties associated with the mean adopted T_{eff1} values along with basic assumptions about $A_{1,2}$, $g_{1,2}$, and the influence of spots added to the WD model. Normally, values for T_{eff1}, $A_{1,2}$, and $g_{1,2}$ are fixed with no error during modeling with the WD code. When T_{eff1} is varied by as much as ±10%, investigations with other OCBs including A- (Alton 2019; Alton *et al.* 2020) and W-subtypes (Alton and Nelson 2018) have shown that uncertainty estimates for i, q, or $\Omega_{1,2}$ were not appreciably (<2.5%) affected. Assuming that the actual T_{eff1} value falls within ±10% of the adopted values used for WD modeling (a reasonable expectation based on T_{eff1} data provided in Tables 4 and 5), then uncertainty estimates for i, q, or $\Omega_{1,2}$ would likely not exceed this amount.

The fill-out parameter (f) which corresponds to the outer surface shared by each star was calculated according to Equation 5 (Kallrath and Milone 1999; Bradstreet 2005) where:

$$f = (\Omega_{inner} - \Omega_{1,2}) / (\Omega_{inner} - \Omega_{outer}), \quad (5)$$

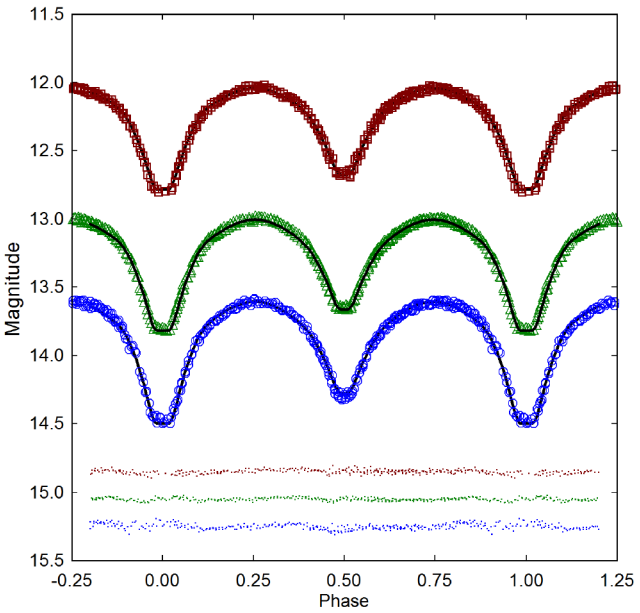

Figure 5. Folded CCD light curves for NSVS 5374825 produced from photometric data obtained between May 15, 2019, and May 27, 2019. The top (I_c), middle (V), and bottom curves (B) shown above were reduced to APASS-based catalog magnitudes using MPO Canopus. In this case, the Roche model (solid black lines) assumed a W-type overcontact binary with no spots; residuals from the model fits are offset at the bottom of the plot to keep the values on scale.

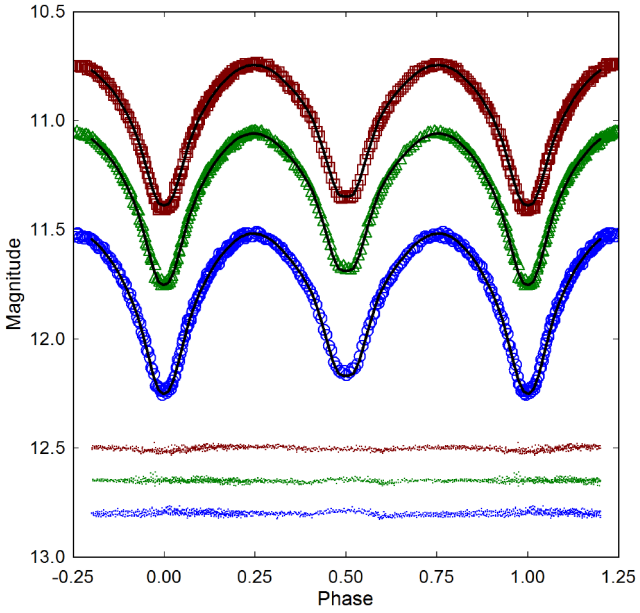

Figure 6. Folded CCD light curves for GR Psc produced from photometric data obtained between October 19, 2019, and November 15, 2019. The top (I_c), middle (V) and bottom curve (B) shown above were reduced to APASS-based catalog magnitudes using MPO Canopus. In this case, the Roche model (solid black lines) assumed an A-type overcontact binary with no spots; residuals from the model fits are offset at the bottom of the plot to keep the values on scale.

Ω_{outer} is the outer critical Roche equipotential, Ω_{inner} is the value for the inner critical Roche equipotential, and $\Omega = \Omega_{1,2}$ denotes the common envelope surface potential for the binary system. In both cases the systems are considered overcontact since 0 < f < 1.

3.4.1. NSVS 5374825

Only photometric data (BVI_c) acquired during 2019 were modeled using the Wilson-Devinney code (Figure 5). Derived

LC parameters and geometric elements are summarized in Table 6. In the case of NSVS 5374825 the flattened bottom at Min I (Figure 7) is indicative of a total eclipse, thereby suggesting that this system is a W-subtype overcontact binary system (Binnendijk 1970). Consequently, WD modeling proceeded under this assumption. With totality, degeneracy between the radii and inclination is broken (Terrell and Wilson 2005; Terrell 2022) such that a mass ratio can be determined with very small (<1%) relative error (Liu 2021). The Roche model for NSVS 5374825 did not require the addition of a spot or third light to improve the LC fits. Spatial images rendered (Figure 8) using Binary Maker 3 (BM3: Bradstreet and Steelman 2004) illustrate transit of the secondary across the primary face during Min II ($\varphi = 0.5$) and the shallow contact ($f = 0.11$) between each star.

3.4.2. GR Psc

The flattened bottom (Figure 7) observed during Min II is a diagnostic indicator for a total eclipse of the secondary star. It follows that the deepest minimum light (Min I) occurs when the smaller secondary transits the primary star (Figure 9). In this regard GR Psc behaves like an A-type overcontact binary and was therefore modeled accordingly. The Roche model for GR Psc did not require the addition of a spot or third light to improve the LC fits. LC parameters and geometric elements derived from the WD code are summarized in Table 7. Spatial renderings produced using BM3 (Figure 9) show (bottom) transit of the secondary during Min I ($\varphi = 0$) and the moderate contact ($f = 0.43$) between the two stars.

Except for a hot spot in the neck region of the primary star (Michaels 2020), a comparison of best fit results (Table 7) from both studies reveals very little difference in all other Roche model parameter estimates. Positioning a hot spot in the same region using data acquired at DBO during the same time period (2019) did not improve the fit in any bandpass (BVI_c). Perhaps the adopted higher effective temperature (6811 vs. 6700 K) and the different bandpasses (BVg'r' vs. BVI_c) account for this disparity.

3.5. Stellar parameters

Fundamental stellar parameters were estimated for both binary stars using results from the 2019 LC simulations. Importantly, without supporting RV data and classification spectra, these results should be considered preliminary and would be more accurately described as "relative" rather than "absolute."

3.5.1. NSVS 5374825

Calculations are described below for estimating the solar mass and size, semi-major axis, solar luminosity, bolometric V-mag, and surface gravity of each component (Table 8). Four empirically derived mass-period relationships (M-PR) for W UMa-binaries were used to estimate the primary star mass. The first M-PR was reported by Qian (2003), others followed from Gazeas and Stępień (2008), Gazeas (2009), and more recently Latković *et al.* (2021). According to Qian (2003), when the primary star is less than 1.35 $M_\odot$ or the system is W-type, its mass can be determined from:

Table 6. Lightcurve parameters evaluated by Roche modeling and the geometric elements derived for NSVS 5374825 assuming it is a W-type WUMa variable with no spots.

Parameter	*No spot*
T_{eff1} (K)[a]	5400 (173)
T_{eff2} (K)	5797 (186)
q (m_2 / m_1)	0.486 (1)
A[a]	0.5
g[a]	0.32
$\Omega_1 = \Omega_2$	2.816 (3)
i °	89.6 (4)
$L_1 / (L_1 + L_2)B$[b]	0.5535 (4)
$L_1 / (L_1 + L_2)V$	0.5811 (2)
$L_1 / (L_1 + L_2)I_c$	0.6029 (3)
r_1 (pole)	0.4222 (4)
r_1 (side)	0.4499 (5)
r_1 (back)	0.4800 (6)
r_2 (pole)	0.3033 (11)
r_2 (side)	0.3174 (13)
r_2 (back)	0.3537 (23)
Fill-out factor (%)	11
RMS (B)[c]	0.01317
RMS (V)[c]	0.00786
RMS (I_c)[c]	0.01048

All error estimates for T_{eff2}, q, $\Omega_{1,2}$, i, $r_{1,2}$, and L_1 from WDwint56A (Nelson 2009). [a] Fixed during DC. [b] L_1 and L_2 refer to scaled luminosities of the primary and secondary stars, respectively. [c] Monochromatic residual mean square error from observed values.

Table 7. Lightcurve parameters evaluated by Roche modeling and the geometric elements derived for GR Psc assuming it is an A-type W UMa variable with no spots.

Parameter	*This Study*	*Michaels 2020*
T_{eff1} (K)[a]	6700 (200)	6811
T_{eff2} (K)	6665 (199)	6760 (4)
q (m_2 / m_1)	0.432 (1)	0.431 (6)
A[a]	0.5	0.5
g[a]	0.32	0.32
$\Omega_1 = \Omega_2$	2.632 (1)	.619 (9)
i °	84.14 (11)	83.9 (3)
$A_S = T_S / T_{[star]}$[b]	—	1.06 (2)
Θ_S(spot co-latitude)[b]	—	98 (5)
φ_S (spot longitude)[b]	—	4 (2)
r_S (angular radius)[b]	—	19 (2)
$L_1 / (L_1 + L_2)B$[c]	0.6795 (1)	0.682 (10)
$L_1 / (L_1 + L_2)V$	0.6783 (1)	0.680 (10)
$L_1 / (L_1 + L_2)I_c$	0.6770 (1)	—
r_1 (pole)	0.4470 (2)	—
r_1 (side)	0.4817 (3)	0.4814 (8)
r_1 (back)	0.5178 (3)	—
r_2 (pole)	0.3103 (6)	—
r_2 (side)	0.3272 (7)	0.3452 (61)
r_2 (back)	0.3787 (16)	—
Fill-out factor (%)	43	47
RMS (B)[d]	0.00729	—
RMS (V)[d]	0.00562	—
RMS (I_c)[d]	0.00638	—

All error estimates for T_{eff2}, q, i, $\Omega_{1,2}$, A_S, Θ_S, φ_S, r_S, $r_{1,2}$, and L_1 from WDwint56A (Nelson 2009). [a] Fixed during DC. [b] Temperature factor (A_S); location (Θ_S, φ_S) and size (r_S) parameters in degrees. [c] L_1 and L_2 refer to scaled luminosities of the primary and secondary stars, respectively. [d] Monochromatic residual mean square fit from observed values.

$$M_1 = 0.391(59) + 1.96(17) \cdot P, \quad (6)$$

or alternatively when $M_1 > 1.35\,M_\odot$ or A-type then Equation 7:

$$M_1 = 0.761(150) + 1.82(28) \cdot P, \quad (7)$$

where P is the orbital period in days. Equation 6 leads to $M_1 = 1.05 \pm 0.08\,M_\odot$ for the primary.

The M-PR derived by Gazeas and Stępień (2008):

$$\log(M_1) = 0.755(59) \cdot \log(P) + 0.416(24), \quad (8)$$

corresponds to an OCB system where $M_1 = 1.15 \pm 0.10\,M_\odot$.

Gazeas (2009) reported another empirical relationship for the more massive (M_1) star of a contact binary such that:

$$\log(M_1) = 0.725(59) \cdot \log(P) - 0.076(32) \cdot \log(q) + 0.365(32). \quad (9)$$

from which $M_1 = 1.12 \pm 0.075\,M_\odot$.

Finally, Latković *et al.* (2021) conducted an exhaustive analysis from nearly 700 W UMa stars in which they established mass-period, radius-period, and luminosity-period relationships for the primary and secondary stars. Accordingly, the M-PR:

$$M_1 = (2.94 \pm 0.21 \cdot P) + (0.16 \pm 0.08). \quad (10)$$

leads to a primary star mass of $1.16 \pm 0.11\,M_\odot$. Using the photometric mass ratio ($q_{ptm} = 0.486 \pm 0.001$) derived from the LC model, the mean from these four values ($M_1 = 1.12 \pm 0.05\,M_\odot$) led to subsequent determinations of the secondary mass ($0.54 \pm 0.02\,M_\odot$) and total mass ($1.65 \pm 0.05\,M_\odot$).

The semi-major axis, $a(R_\odot) = 2.42 \pm 0.02$, was calculated from Newton's version of Kepler's third law where:

$$a^3 = (G \cdot P^2 (M_1 + M_2)) / (4\pi^2). \quad (11)$$

The effective radius of each Roche lobe (r_L) can be calculated over the entire range of mass ratios ($0 < q < \infty$) according to an expression derived by Eggleton (1983):

$$r_L = (0.49q^{2/3}) / (0.6q^{2/3} + \ln(1 + q^{1/3})), \quad (12)$$

from which values for r_1 (0.4425 ± 0.0003) and r_2 (0.3185 ± 0.0002) were determined for the primary and secondary stars, respectively. The radii in solar units for both binary components can be calculated such that $R_1 = a \cdot r_1 = 1.07 \pm 0.01\,R_\odot$ and $R_2 = a \cdot r_2 = 0.77 \pm 0.01\,R_\odot$.

Luminosity in solar units ($L_\odot$) for the primary (L_1) and secondary stars (L_2) was calculated from the well-known relationship derived from the Stefan-Boltzmann law where:

$$L_{1,2} = (R_{1,2} / R_\odot)^2 (T_{1,2} / T_\odot)^4. \quad (13)$$

Assuming that $T_{eff1} = 5400 \pm 173$ K, $T_{eff2} = 5797 \pm 186$ K, and $T_\odot = 5772$ K, then the stellar luminosities ($L_\odot$) for the primary and secondary are $L_1 = 0.88 \pm 0.11$ and $L_2 = 0.61 \pm 0.08$, respectively. The stellar mass and radius of the primary star closely matches that expected from a stand-alone late

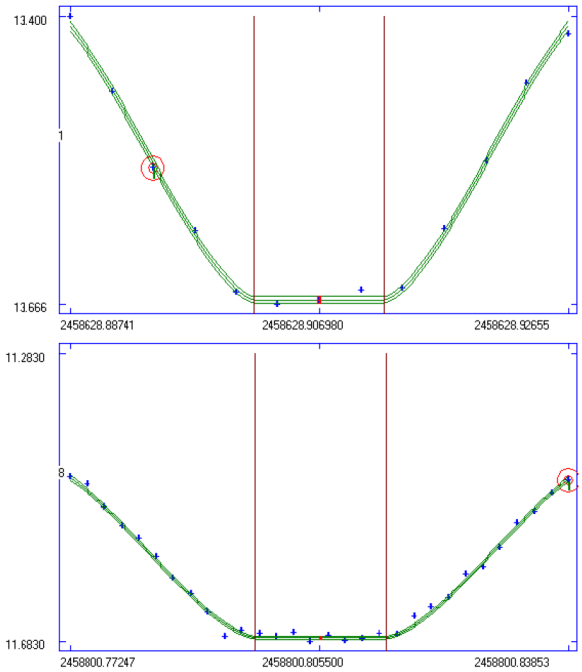

Figure 7. Total eclipse of NSVS 5374825 during Min I (top) and total eclipse of GR Psc during Min II (bottom) as determined using MAVKA. Mean eclipse duration for NSVS 5374825 was estimated to be 15.6 ± 0.8 min whereas the eclipse duration for GR Psc was longer (20.3 ± 0.4 min).

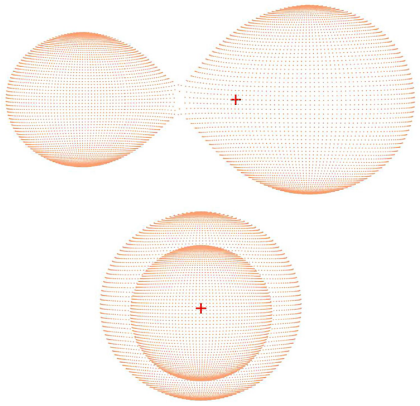

Figure 8. Spatial models of NSVS 5374825 illustrating (bottom) transit of the secondary star across the primary star face at Min II (φ = 0.5) and (top) the shallow contact (f = 0.1) between both stars.

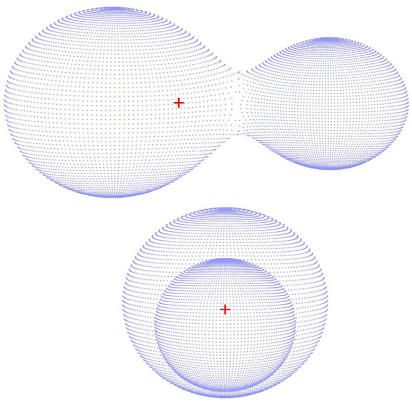

Figure 9. Spatial models of GR Psc showing (bottom) transit of the secondary star at Min I (φ = 0) and (top) the moderate contact (f = 0.43) between both stars.

Table 8. Preliminary stellar parameters for NSVS 5374825 using the mean photometric mass ratio ($q_{ptm} = m_2 / m_1$) from the Roche model fits of LC data (2019) and the estimated mass from four empirical Mass-Period relationships.

Parameter	*Primary*	*Secondary*
Mass ($M_\odot$)	1.12 ± 0.05	0.54 ± 0.02
Radius ($R_\odot$)	1.07 ± 0.01	0.77 ± 0.01
a ($R_\odot$)	2.42 ± 0.02	2.42 ± 0.02
Luminosity ($L_\odot$)	0.88 ± 0.11	0.61 ± 0.08
M_{bol}	4.89 ± 0.14	5.30 ± 0.14
Log (g)	4.43 ± 0.02	4.40 ± 0.02

Table 9. Preliminary stellar parameters for GR Psc using the mean photometric mass ratio ($q_{ptm} = m_2 / m_1$) from the Roche model fits (2019) and the estimated mass from four empirical Mass-Period relationships.

Parameter	*Primary*	*Secondary*
Mass ($M_\odot$)	1.57 ± 0.07	0.68 ± 0.03
Radius ($R_\odot$)	1.56 ± 0.02	1.07 ± 0.01
a ($R_\odot$)	3.45 ± 0.04	3.45 ± 0.04
Luminosity ($L_\odot$)	4.43 ± 0.54	2.02 ± 0.25
M_{bol}	3.13 ± 0.13	3.99 ± 0.13
Log (g)	4.25 ± 0.02	4.22 ± 0.02

G-type main sequence star. However, the secondary star in NSVS 5374825 is considerably more luminous (0.60 vs. 0.14 $L_\odot$) than a field star (K7V) with the same mass ($M_\odot = 0.53$) and a corresponding smaller size ($R_\odot \approx 0.56$).

Based on parallax data in Gaia EDR3 (Gaia Collaboration *et al.* 2021; Lindegren *et al.* 2021), this system can be found at a distance of 475.8 ± 2.9 pc. By comparison, a value derived using the distance modulus equation corrected for interstellar extinction ($A_V = 0.142 \pm 0.0059$) places NSVS 5374825 slightly farther (485.7 ± 36.6 pc) away but within measurement uncertainty. Other values derived herein and necessary to perform this calculation include $V_{max} = 13.01 \pm 0.01$ (Simbad V-mag = 13.03), bolometric correction (BC = –0.11) derived from Pecaut and Mamajek (2013), and the absolute V-magnitude ($M_V = 4.51 \pm 0.22$) from the combined luminosity (4.40 ± 0.22).

3.5.2. GR Psc

The same approach described above for NSVS 5374825 was used to estimate the primary star mass for GR Psc (Table 9) but this time for a putative F1V-F5V system ($T_{eff1} \sim 6700$ K). The mass-period empirical relationships (Equations 7–10) lead to a mean value of $1.57 \pm 0.07\ M_\odot$ for the primary star. This is similar to that expected from a single early F-type star. The secondary mass ($0.68 \pm 0.03\ M_\odot$) and total mass ($2.25 \pm 0.08\ M_\odot$) of GR Psc were derived from the mean photometric mass ratio (0.432 ± 0.001). If the secondary was a single main sequence star with a similar mass (early K-type) it would probably be much smaller ($R\odot \sim 0.75$), cooler ($T_{eff} \sim 4490$ K), and far less luminous ($L_\odot \sim 0.42$). The semi-major axis, $a(R_\odot) = 3.45 \pm 0.04$, was calculated from Equation 11 while the effective radius of each Roche lobe (r_L) was calculated according to Equation 12 from which values for r_1 (0.4530 ± 0.0001) and r_2 (0.3091 ± 0.0001) were determined for the primary and secondary stars, respectively. The radii in solar units for both binary components were calculated such that $R_1 = 1.56 \pm 0.02\ R_\odot$ and $R_2 = 1.07 \pm 0.01\ R_\odot$. Luminosity in solar units ($L_\odot$) for the primary (L_1) and secondary stars (L_2) was calculated according to Equation 13. Assuming that $T_{eff1} = 6700 \pm 200$ K, $T_{eff2} = 6665 \pm 199$ K, and $T_\odot = 5772$ K, then the stellar luminosities for the primary and secondary are $L_1 = 4.43 \pm 0.54$ and $L_2 = 2.02 \pm 0.25$, respectively. This study and the investigation by Michaels (2020) share very similar values for stellar mass, radius, and semi-major axis. Higher values for stellar luminosity and bolometric magnitude reported in Table 6 from Michaels (2020) are largely attributed to differences in the adopted T_{eff1} values (6811 vs. 6700 K).

This system is estimated to be 555.6 ± 10.3 pc away using the parallax-derived distances reported in Gaia EDR3 (Gaia Collaboration *et al.* 2021). A value independently derived from the distance modulus equation using data generated herein ($V_{max} = 11.06 \pm 0.01$ (Simbad $V_{mag} = 11.06$), $A_V = 0.224 \pm 0.005$, BC = –0.038 and $M_V = 2.76 \pm 0.14$) places GR Psc considerably closer (431.4 ± 29.2~pc).

4. Conclusions

New times of minimum were determined for both NSVS 5374825 and GR Psc based on precise time-series CCD-derived LC data acquired at DBO. These along with other published values and those extracted from the SuperWASP Survey (Butters *et al.* 2010) led to an updated linear ephemeris for each system. Potential changes in orbital period were assessed using differences between observed and predicted eclipse timings. A quadratic relationship was established between the residuals and epoch for both NSVS 5374825 and GR Psc. The orbital period for NSVS 5374825 appeared to be increasing ($0.0185 \cdot y^{-1}$) over a 15 year timespan (2004–2019) while GR Psc was slowly decreasing at a rate of $-0.0126\ s \cdot y^{-1}$. Both systems will require many more years of eclipse timing data to further substantiate any potential change(s) in orbital period. The adopted effective temperatures (T_{eff1}) for NSVS 5374825 (5400 ± 173 K) and GR Psc (6700 ± 200 K) most likely correspond to a G7V-K1V primary star for the former and an F1V-F5V primary for the latter. Both are overcontact systems which exhibit a total eclipse; therefore, the photometric mass ratios for NSVS 5374825 (q = 0.486) and GR Psc (q = 0.432) determined by Roche modeling should prove to be a reliable substitute for mass ratios derived from RV data. Nonetheless, spectroscopic studies (RV and classification spectra) will be required to unequivocally determine a mass ratio, total mass, and spectral class for both systems.

5. Acknowledgements

This research has made use of the SIMBAD database operated at Centre de Données astronomiques de Strasbourg, France. Time-of-minima data tabulated in the Variable Star Section of Czech Astronomical Society (B.R.N.O.) website proved invaluable to the assessment of potential secular changes in orbital period. In addition, the Northern Sky Variability Survey previously hosted by the Los Alamos National Laboratory, the All Sky Automated Survey Catalogue of Variable Stars (http://www.astrouw.edu.pl/asas/?page=acvs), the Catalina Sky

Survey (http://nesssi.cacr.caltech.edu\\/DataRelease/), and the ASAS-SN Variable Stars Database (https://asas-sn.osu.edu/variables) were mined for essential information. This work has made use of data from the European Space Agency (ESA) mission *Gaia* (https://www.cosmos.esa.int/gaia), processed by the *Gaia* Data Processing and Analysis Consortium (DPAC; https://www.cosmos.esa.int/web/gaia/dpac/consortium). Funding for the DPAC has been provided by national institutions, in particular the institutions participating in the *Gaia* Multilateral Agreement. This paper makes use of data from the first public release of the WASP data as provided by the WASP consortium and services at the NASA Exoplanet Archive, which is operated by the California Institute of Technology, under contract with the National Aeronautics and Space Administration under the Exoplanet Exploration Program. The use of public data from LAMOST is also acknowledged. Guoshoujing Telescope (the Large Sky Area Multi-Object Fiber Spectroscopic Telescope LAMOST) is a National Major Scientific Project built by the Chinese Academy of Sciences. Funding for the project has been provided by the National Development and Reform Commission. LAMOST is operated and managed by the National Astronomical Observatories, Chinese Academy of Sciences. Many thanks to the anonymous referee and Editor Morrison for valuable commentary and suggested changes to improve this paper.

References

Akerlof, C., *et al.* 2000, *Astron. J.*, **119**, 1901.
Alton, K. B. 2019, *J. Amer. Assoc. Var. Star Obs.*, **47**, 7.
Alton, K. B., and Nelson, R. H. 2018, *Mon. Not. Roy. Astron. Soc.*, **479**, 3197.
Alton, K. B., Nelson, R. H., and Stępień, K. 2020, *J. Astrophys. Astron.*, **41**, 26.
Andrych, K. D. 2017, *Odessa Astron. Publ.*, **30**, 57.
Andrych, K. D. and Andronov, I.L. 2019, *Open Eur. J. Var. Stars*, **197**, 65.
Andrych, K. D., Andronov, I. L., and Chinarova, L. L. 2020, *J. Phys. Studies*, **24**, 1902.
Banfi, M., *et al.* 2012, *Inf. Bull. Var. Stars*, No. 6033, 1.
Berry, R., and Burnell, J. 2005 *The Handbook of Astronomical Image Processing*, 2nd ed., Willmann-Bell, Richmond, VA.
Binnendijk, L. 1970, *Vistas Astron.*, **12**, 217.
Bradstreet, D. H. 2005, in *The Society for Astronomical Sciences 24th Annual Symposium on Telescope Science*, Society for Astronomical Sciences, Rancho Cucamonga, CA, 23.
Bradstreet, D. H., and Steelman, D. P. 2004, Binary Maker 3, Contact Software (http://www.binarymaker.com).
Butters, O. W., *et al.* 2010, *Astron. Astrophys.*, **520**, L10.
Diethelm, R. 2011, *Inf. Bull. Var. Stars*, No. 5960, 1.
Diethelm, R. 2012, *Inf. Bull. Var. Stars*, No. 6011, 1.
Drake, A. J., *et al.* 2014, *Astrophys. J., Suppl. Ser.*, **213**, 9.
Eggleton, P. P. 1983, *Astrophys. J.*, **268**, 368.
Gaia Collaboration, *et al.* 2016, *Astron. Astrophys.*, **595A**, 1.
Gaia Collaboration, *et al.* 2018, *Astron. Astrophys.*, **616A**, 1.
Gaia Collaboration, *et al.* 2021, *Astron. Astrophys.*, **649A**, 1.
Gazeas, K. D. 2009, *Commun. Asteroseismology*, **159**, 129.
Gazeas, K., and Stępień, K. 2008, *Mon. Not. Roy. Astron. Soc.*, **390**, 1577.
Gettel, S. J., Geske, M. T., and McKay, T. A. 2006, *Astron. J.*, **131**, 621.
Henden, A. A., Levine, S. E., Terrell, D., Smith, T. C., and Welch, D. L. 2011, *Bull. Amer. Astron. Soc.*, **43**.
Henden, A. A., Terrell, D., Welch, D., and Smith, T. C. 2010, *Bull. Amer. Astron. Soc.*, **42**, 515.
Henden, A. A., Welch, D. L., Terrell, D., and Levine, S. E. 2009, *Bull. Amer. Astron. Soc.*, **41**, 669.
Hoffman, D. I., Harrison, T. E., and McNamara, B. J. 2009, *Astron. J.*, **138**, 466.
Houdashelt, M. L., Bell, R. A., and Sweigart, A. V. 2000, *Astron. J.*, **119**, 1448.
Hubscher, J., and Lehmann, P. B. 2013, *Inf. Bull. Var. Stars*, No. 6070, 1.
Jayasinghe, T., *et al.* 2018, *Mon. Not. Roy. Astron. Soc.*, **477**, 3145.
Kafka, S. 2021, Observations from the AAVSO International Database (https://www.aavso.org/data-download).
Kallrath, J., and Milone, E. F. 1999, *Eclipsing Binary Stars: Modeling and Analysis*, Springer, New York.
Kurucz, R. L. 2002, *Baltic Astron.*, **11**, 101.
Latković, O., Čeki, A. and Lazarević, S. 2021, *Astrophys. J., Suppl. Ser.*, **254**, 10.
Li, K., *et al.* 2019, *Res. Astron. Astrophys.*, **19**, 147.
Lindegren, L., *et al.* 2021, *Astron. Astrophys.*, **649A**, 2.
Liu, L. 2021, *Publ. Astron. Soc. Pacific*, **133**, 084202.
Lucy, L. B. 1967, *Z. Astrophys.*, **65**, 89.
Martignoni, M. 2006, *Inf. Bull. Var. Stars*, No. 5700, 1.
Michaels, E. J. 2020, *J. Amer. Assoc. Var. Star Obs.*, **48**, 193.
Minor Planet Observer. 2010, MPO Software Suite (http://www.minorplanetobserver.com), BDW Publishing, Colorado Springs.
Nagai, K. 2012, *Bull. Var. Star Obs. League Japan*, No. 53, 1.
Nagai, K. 2014, *Bull. Var. Star Obs. League Japan*, No. 56, 1.
Nagai, K. 2020, *Bull. Var. Star Obs. League Japan*, No. 67, 1.
Nelson, R. H. 2009, WDwint56a: Astronomy Software by Bob Nelson (https://www.variablestarssouth.org/bob-nelson/).
O'Connell, D. J. K. 1951, *Publ. Riverview Coll. Obs.*, **2**, 85.
Özavcı, I., *et al.* 2019, *Open Eur. J. Var. Stars*, **203**, 1.
Pecaut, M. J,. and Mamajek, E. E. 2013, *Astrophys. J., Suppl. Ser.*, **208**, 9.
Pojmanski, G., Pilecki, B., and Szczygiel, D. 2005, *Acta Astron.*, **55**, 275.
Prša, A., and Zwitter, T. 2005, *Astrophys. J.*, **628**, 426.
Qian, S. 2001, *Mon. Not. Roy. Astron. Soc.*, **328**, 635.
Qian, S. 2003, *Mon. Not. Roy. Astron. Soc.*, **342**, 1260.
Ruciński, S. M. 1969, *Acta Astron.*, **19**, 245.
Samolyk, G. 2015, *J. Amer. Assoc. Var. Star Obs.*, **43**, 77.
Samolyk, G. 2017, *J. Amer. Assoc. Var. Star Obs.*, **45**, 121.
Samolyk, G. 2018, *J. Amer. Assoc. Var. Star Obs.*, **46**, 184.
Schlafly, E. F., and Finkbeiner, D. P. 2011, *Astrophys. J.*, **737**, 103.
Smith, T. C., Henden, A. A., and Starkey, D. R. 2011, in *The Society for Astronomical Sciences 30th Annual Symposium on Telescope Science*, Society for Astronomical Sciences, Rancho Cucamonga, CA, 121.

Software Bisque. 2019, The Sky X professional edition 10.5.0 (https://www.bisque.com).
Terrell, D. 2022, *Galaxies*, **10**, 8.
Terrell, D., Gross, J., and Cooney, W. R. 2012, *Astron. J.*, **143**, 99.
Terrell, D., and Wilson, R. E. 2005, *Astrophys. Space Sci.*, **296**, 221.
Van Hamme, W. 1993, *Astron. J.*, **106**, 2096.
Wang, R., *et al.* 2019, *Publ. Astron. Soc. Pacific*, **131**, 024505.
Wilson, R. E. 1979, *Astrophys. J.*, **234**, 1054.
Wilson, R. E. 1990, *Astrophys. J.*, **356**, 613.
Wilson, R. E. and Devinney, E.J. 1971, *Astrophys. J.*, **166**, 605.
Woźniak, P. R., *et al.* 2004, *Astron. J.*, **127**, 2436.
Zhao, G., Zhao, Y.-H., Chu, Y.-Q., Jing, Y.-P., and Deng, L.-C. 2012, *Res. Astron. Astrophys.*, **12**, 723.

Pulsating Red Giants in a Globular Cluster: ω Centauri

Julia V. E. Kim
John R. Percy
Department of Astronomy and Astrophysics, and Dunlap Institute for Astronomy and Astrophysics, University of Toronto, 50 St. George Street, Toronto ON M5S 3H4, Canada; juliaym.kim@mail.utoronto.ca; john.percy@utoronto.ca

Received May 26, 2022; revised June 6, 2022; accepted June 21, 2022

Abstract We have carried out light-curve and time-series analysis of a sample of 16 pulsating red giants (PRGs) in the globular cluster ω Cen, using observations from the ASAS-SN database, and the AAVSO software package VSTAR. Of the 16 stars, 1 was classified by ASAS-SN as Mira (M), 5 as semiregular (SR), and 10 as "long secondary period" (LSP), i.e. the dominant period was an LSP. We have determined pulsation periods (P) for all of them, secondary pulsation periods for 3, possible secondary pulsation periods for 4, and LSPs for 8. This confirms that LSPs are common in Population II stars. In the context of a recent model for LSPs, this implies that many Population II PRGs had planetary companions which accreted gas and dust to become brown dwarfs or low-mass stars, now enshrouded by dust. In this model, the LSP is the orbital period of the hypothetical companion. The amplitudes of the pulsation periods vary by up to a factor of 3.4 on a median time scale of 18 pulsation periods, for reasons unknown. The ratios of LSP/P cluster around 4 and 8, presumably depending on whether P is a fundamental mode or first overtone period. We have augmented our sample with a few stars from the literature to plot period-luminosity relations. Sequences for LSPs, fundamental, and first-overtone pulsation periods are visible. Our results show that the complex variability of the PRGs in ω Cen is similar to that of red giants in other stellar systems, and in the field. In Appendix A, we give results for a few red giants in NGC 6712, which we obtained as a prelude to the ω Cen project.

1. Introduction

Red giants vary in brightness in complex ways. They may pulsate in one or more radial modes, with variable pulsation amplitudes. About a third have a "long secondary period" (LSP), 5 to 10 times greater than the dominant pulsation period, and whose cause was uncertain until recently. The large convective cells in their outer layers and shock waves in their atmospheres may produce additional random variability. Soszyński *et al.* (2021) have made a strong case that LSPs are a result of binarity. The companion was initially a planet, which accreted matter from the red giant's strong stellar wind, and "grew" into a brown dwarf or low-mass star, which produces the observed LSP velocity variations. The now-dust-enshrouded companion eclipses the red giant, producing the LSP. At infrared wavelengths, the dust-enshrouded companion can be seen to be eclipsed by the red giant about half a cycle later.

It is therefore interesting to note that LSPs exist in red giants in globular clusters (GCs), which are among the oldest objects in our galaxy and which are metal-poor. Studies of the variability of red giants in 47 Tuc have been published by Lebzelter and Wood (2005) and Percy and Gupta (2021), among others. In this paper, we study the variability of red giants in ω Cen. We use data from the All-Sky Automated Survey for Supernovae (ASAS-SN). The data are publicly available at https://asas-sn.osu.edu/variables. Unfortunately, ASAS-SN cannot observe and measure stars in the dense cores of globular clusters, so only a small fraction of the red giants in the cluster can be studied. We have supplemented our results with some of those of Lebzelter and Wood (2016). Our datasets are somewhat longer than those of Lebzelter and Wood (2016) and, unlike those authors, we have identified more than one pulsation period in some of our stars, estimated the LSPs, and also studied their variable pulsation amplitudes.

The automated process which ASAS-SN uses to classify and to establish the main pulsation period is often poorly suited to the analysis of PRGs (Percy and Fenaux 2019). The data and the properties which ASAS-SN establish must, therefore, be confirmed by a visual inspection of the light curves and by a more quantitative analysis (Percy and Fenaux 2019) of, for instance, its Fourier spectrum and period-time contour plots.

In this paper, we perform a detailed analysis of ASAS-SN observations of PRGs in ω Cen, the largest known globular cluster in the Milky Way at a distance of 5,240 parsecs (pc) from the Earth. This is a rather complex cluster. It may have undergone more than one wave of star formation, and may even have initially been a dwarf galaxy.

The light curves of stars therein are inspected and studied for the purposes of establishing its type, its pulsation modes and periods, including LSPs, and any complexities such as amplitude variability; Fourier and wavelet analysis are then used to refine and provide more quantitative estimates of these initial observations. This project extends the work of Lebzelter and Wood (2016), who obtained nearly two years of photometric measurements of dozens of red giants in ω Cen. As many exhibited significant irregularities or multiperiodicities in their light curves, only a small proportion of their periods and LSPs could be established well (Lebzelter and Wood 2016).

In Appendix A, we give results for a few red giants in NGC 6712, which we obtained as a prelude to the ω Cen project.

2. Data and analysis

We analyzed a sample of 16 stars (Table 1) from the ASAS-SN variable star catalogue within 30 arcminutes of the center of ω Cen, and classified by ASAS-SN as Mira stars (if their visual range exceeded 2.5 magnitudes), red semiregular (SR) variables, or long secondary periods (LSP)—or more properly,

long-period variables with LSPs. The data can be found freely on-line (https://asas-sn.osu.edu/variables), reported to an error of 0.02 mag (Shappee *et al.* 2014; Jayasinghe *et al.* 2018; Jayasinghe *et al.* 2019).

With a careful inspection of the light curves, the variabilities of the main pulsation period and amplitude, as well as the LSP, could be clearly observed. The main pulsation period(s) could be also estimated to an accuracy of a few percent by measuring a few intervals between maxima and minima and averaging them together. To refine this primary analysis, the Fourier analysis and wavelet routines in the American Association of Variable Star Observers (AAVSO) time-series package, VSTAR, were used (Benn 2013). The rough estimates of the pulsation period(s) from the light curve enabled the authors to determine the important peak(s) in the Fourier spectrum. Without these estimates, such an identification would have been more difficult, as the low amplitudes and the complexity of the variability suppressed the peaks to values close to the noise level of 0.02 mag. With these periods established, wavelet analysis was then used to study the rate and range of the pulsation amplitude variability. Lastly, the wavelet contour diagram was examined to detect the presence of multiple pulsation period(s) as well as any mode switching which subsisted between them. Note that our time-series analysis yields the semi-amplitude, rather than the full amplitude or range.

For more information about the WWZ (weighted wavelet z-transform), see the VSTAR manual. For a detailed account, see Foster (1996).

3. Results

Table 1 lists the name, type, period PA, mean V and K magnitudes, and the distance d in parsecs of the star, all taken from the ASAS-SN website, as well as the primary pulsation period PP, the secondary pulsation period PS, the long secondary period LSP, and their respective semi-amplitudes, derived by the authors. The symbol "?", wherever it appears, denotes uncertainty in the value given or in the existence of a pulsation mode. The errors in the distances d are usually between 6 and 15 percent, whilst the errors in the amplitudes A are near 0.02 mag. The accuracy of the periods is limited by the finite length of the datasets, as well as by the complexity of the variability. The pulsation amplitudes are in almost every case variable, as has been found in many previous studies of pulsating red giants. The cause of the variable pulsation amplitudes is still unknown. The period in the ASAS-SN catalog is sometimes the pulsation period, sometimes the LSP, whichever is dominant. These results remind us that the variability of these stars is much more complex than can be expressed by a single average period and average amplitude.

Figure 1 shows the period-luminosity (PL) relations for all significant periods of the 16 stars in our sample as well as some of those studied by Lebzelter and Wood (2016). The K magnitudes are taken from the ASAS-SN website. The least-squares equations of the three sequences C', C, and D appearing in this figure are respectively given by

$$K_{mag,C'} = (-3.2 \pm 0.9) \log(P) + (13 \pm 2) \quad (1)$$

$$K_{mag,C} = (-3.5 \pm 0.3) \log(P) + (14.5 \pm 0.6) \quad (2)$$

$$K_{mag,D} = (-4 \pm 1) \log(P) + (17 \pm 3) \quad (3)$$

The general appearance of the figure is similar to that for other systems such as the LMC and SMC (Wood 2000; Soszyński *et al.* 2007), though our sample is much smaller than for those others. The ratios of LSP to P are, upon average, 6.5, but cluster around 4 and 8. Accordingly, the pulsation modes of stars in the sample must be primarily of the fundamental and first overtone, which respectively appear in the figure as sequences C and C'. The pulsation period ratios that we have found are also consistent with this conclusion.

The following are brief notes on individual stars in Table 1.

V826 Cen This is a *typical* star (Figure 2), which pulsates in two modes with periods of 89 and 51 days. As the ratio of these periods is 0.6, the star can be interpreted to be likely pulsating in the fundamental and first overtones (Xiong and Deng 2007). The presence, and superposition, of these two modes can be seen in its Fourier spectrum (Figure 3) and its wavelet contour diagram (Figure 4). An LSP of 542 days is also apparent in the

Table 1. Period Analysis of ASAS-SN Observations of PRGs in ω Centauri.

Name	*Type*	*PA (d)*	*(V)*	*K*	*d (pc)*	*PP (d)*	A_{PP}	*PS (d)*	A_{PS}	*LSP (d)*	A_{LSP}
V826 Cen	LSP	661	10.87	6.829	3841	89	0.01	51	0.01	542	0.02
J132630.11-472428.2	LSP	156	11.23	7.071	4580	148	0.06	—	—	>2000?	?
V825 Cen	M	233	12.24	5.942	3898	232	1.05	—	—	—	—
J132617.98-473003.2	SR	45	11.02	7.696	4758	43	0.04	—	—	—	—
J132558.72-473609.8	SR	83	12.03	8.143	4617	82	0.23	40?	0.06?	—	—
J132616.14-473057.5	SR	82	11.27	7.763	4008	82	0.08	?	?	—	—
J132508.28-472020.6	SR	62	11.62	7.801	5598	62	0.04	—	—	—	—
J132709.16-472340.6	LSP	297	11.09	7.844	5047	41?	0.01?	?	?	296	0.03
J132712.06-472947.3	LSP	272	11.08	8.710	4040	46	0.01	—	—	271	0.03
J132521.33-473655.3	LSP?	49	11.55	7.694	5040	48	0.05	—	—	650?	0.04?
J132634.87-373410.2	LSP	71	11.97	8.185	3958	62	0.03	35	0.03	383	0.03
J132552.30-475612.3	LSP	308	12.86	7.521	4600	34	0.03	25	0.03	310	0.06
J132521.33-473655.3	LSP	49	11.55	7.694	5040	48	0.05	—	—	310	0.06
J132606.97-472518.9	SR	40	11.38	7.816	5029	40	0.02	?	?	—	—
J132844.02-470856.3	LSP	383	13.12	8.497	6295	30?	0.02?	—	—	383	0.06
J132656.73-472054.6	LSP	316	11.45	7.839	5297	38	0.02	—	—	383	0.06

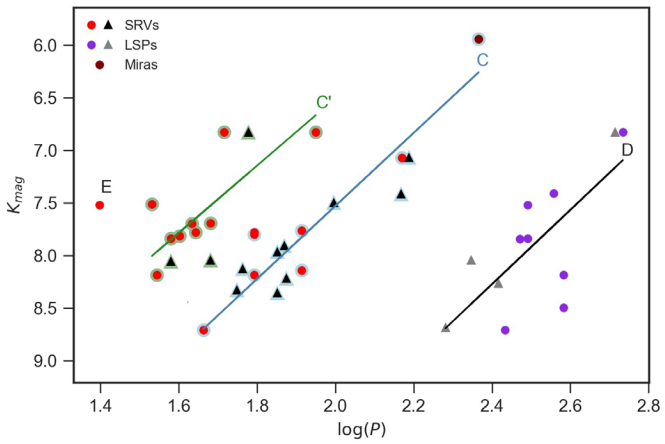

Figure 1. The period luminosity relations for red variables in ω Cen, where there is a point in the figure for each *significant* period found (that is, a point not marked by "?" in Table 1). The circular points are the measurements done by the authors; the triangular points are those found in Table 1 of "The Long Period variables in ω Centauri" by Lebzelter and Wood (2016). Sequences C', C, and D denote the sequences of first, fundamental, and LSP pulsators; the point E is perhaps the beginning of a sequence of second overtone pulsators. The points highlighted in blue and in orange are *considered* to belong to sequences C' and C, respectively, but there is some uncertainty in this classification. The least-squares equations of the sequences are given in Equations 1, 2, and 3 below.

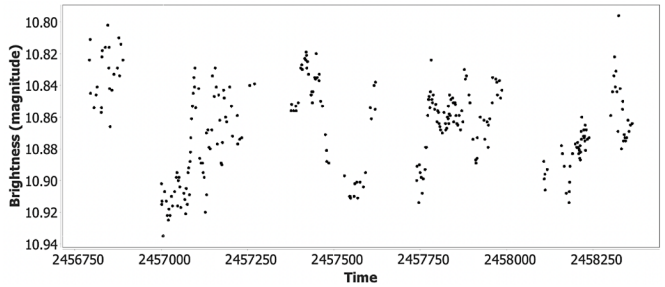

Figure 2. The V light curve of V826 Cen.

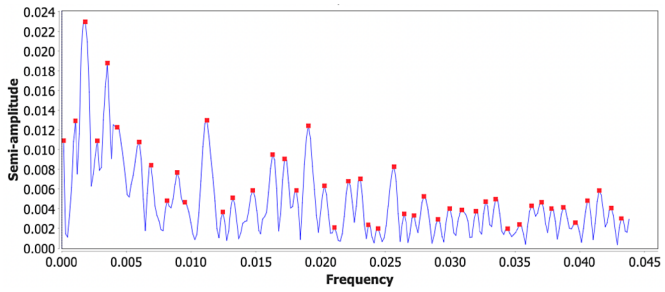

Figure 3. The Fourier spectrum of V826 Cen, in which is plotted the semi-amplitude against frequency (cycles/day). The two pulsation periods—51 days (0.01960 c/d) and 89 days (0.01123 c/d), the LSP—542 days (0.00185 c/d), and their aliases are visible. Its light curve is shown in Figure 2.

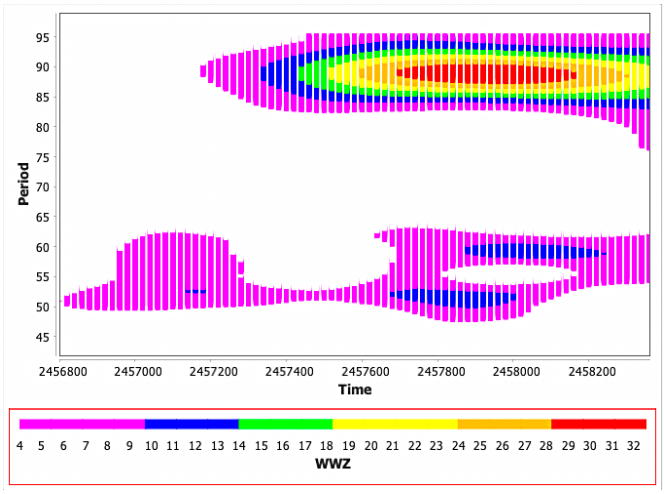

Figure 4. The wavelet contour diagram for V826 Cen, in which the period (d) is plotted against the Julian date, with WWZ amplitude in false color. It shows the presence of two pulsation modes with periods of about 50 and 90 days, each variable in amplitude. Its light curve is shown in Figure 2.

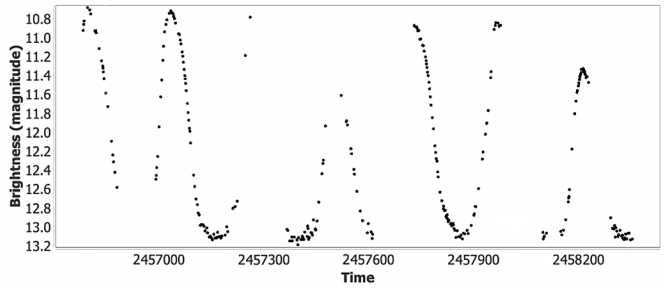

Figure 5. The V light curve of V825 Cen.

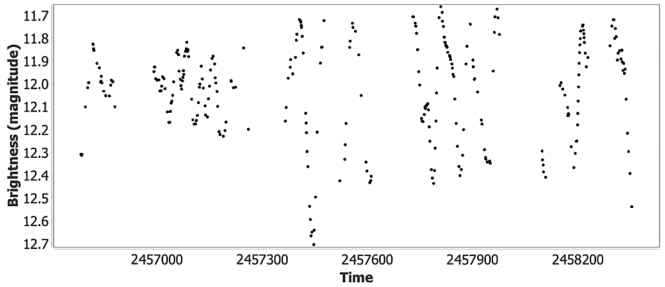

Figure 6. The V light curve of J132558.72-473609.8.

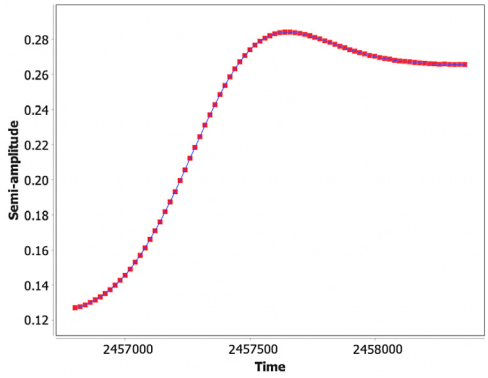

Figure 7. The variable pulsation semi-amplitude of J132558.72-473609.8, as determined by wavelet analysis. The amplitude doubles over a time interval of about 600 days. Its light curve is shown in Figure 6.

light curve and the Fourier spectrum of the star. Based on the distance of this star, as given in the ASAS-SN catalog, this star may possibly be a non-member, or the error in the distance may be large.

J132630.11-472428.2 The light curve shows a slow, linear ascent, perhaps owing to the presence of an LSP. The variations within are sawtooth, with momentary triangular blips that may arise from the presence of a shorter period mode of about 15 days, or from some non-pulsational process such as shock waves.

V825 Cen This is a Mira star with a period of 232 days (Figure 5). Though the maximum brightness varies from cycle to cycle, the minimum brightness remains constant, perhaps owing to the presence of a thirteenth-magnitude companion, observed in the same photometric aperture as the Mira star.

J132558.72-473609.8 The light curve is unusual, with a variable amplitude that doubles between the start of the second and third seasons (Figures 6 and 7). Like J132630.11-472428.2, the variations within are sawtooth, with momentary triangular blips arising perhaps from the presence of a shorter period mode of about 15 days. The light curve suggests the presence of two pulsation modes, with periods of 82 and 40 days, but as the amplitude of the latter is so small compared to the former and as it is less significant than several other peaks in the Fourier spectrum, the authors are not certain of its existence. It is also possible that it is a harmonic.

J132616.14-473057.5 There are three discordant points in the last season, owing presumably to instrumental effects. In the light curve and in the Fourier analysis, there is mild evidence of a shorter period mode of about 40 days superposed upon the primary mode of 82 days. It is also possible that this is a harmonic.

J132709.16-472340.6 The star pulsates with a period of 41 days in its first two seasons and has an LSP of 296 days. Though its period-time graph suggests that its period rises from 40 to 70 to 90 days, the semi-amplitudes of its peaks near 70 and 90 days in the Fourier spectrum are below the noise level and so make the authors uncertain of the existence of other pulsation modes.

J132552.30-475612.3 The star pulsates in two modes with periods of 34 and 25 days. As the ratio of these periods is 0.7, and as the first period falls upon sequence C' and the second upon the point labelled E in Figure 1, it is suspected that the star should be pulsating in its first and second overtones.

J132521.33-473655.3 There is a discordant point in the last season. Like J132630.11-472428.2 and J132558.72-473609.8, the variations within are sawtooth, with momentary triangular blips arising perhaps from the presence of a shorter period mode of about 25 days. The Fourier spectrum suggests the presence of an LSP with a period of 650 days, but the modulation of the mean V magnitude in the light curve is too slight to confirm this number to be reasonable.

J132606.97-472518.9 Observing the star to lie on sequence C' of Figure 1, the star can be deduced to be a first overtone pulsator with a steady pulsation period of about 40 days. Though the Fourier spectrum suggests the presence of a second pulsation period with a period of 63 days and a (small) semi-amplitude of 0.02, no evidence of it exists in the light curve or in the WWZ contour diagram.

J132844.02-470856.3 There are a few discordant points in the first three seasons. In its light curve and Fourier spectrum, there is evidence of a pulsation mode with low amplitude and with a period between 25 to 35 days.

J132656.73-472054.6 There are a few discordant points in the last season.

4. Discussion

Soszyński *et al.* (2007) have provided an explanation as to why the PL relations of the LSP are nearly parallel to those of the low-order radial pulsation modes. To account also for the *linearity* in the LSP PL relation, Soszyński *et al.* (2021) have proposed a mechanism of LSPs, in which a brown dwarf or low-mass star companion and its dusty cloud orbit the central PRG, eclipsing it once per orbit, with a period P_{LSP}. In this binary model, the ratio of the radius, R, of the central PRG to the orbital radius, A, of the companion can be presumed to be nearly constant for all stars in the cluster (but see discussion below), being given by

$$\frac{R}{A} \approx 0.24 Q_F^{-\frac{2}{3}} \left(\frac{P_F}{P_{LSP}} \right)^2 , \quad (4)$$

where Q_F and P_F are the pulsation constant and period of the fundamental mode, respectively (Soszyński *et al.* 2007). Supposing the stars to possess a mass $M \approx M_\odot$, an effective temperature satisfying $\log(T_e) \approx 3.6$ (Persson *et al.* 1980) and a luminosity satisfying $\log(L/L_\odot) \approx 3.0$ (Persson *et al.* 1980), then Xiong and Deng (2007) should suggest $Q_F \approx 10^{-1.1} \approx 0.08$ and, therefore, $A \approx 2R$. With Kepler's Third Law,

$$P_{LSP} = \frac{2\pi}{\sqrt{GM}} (R + A)^{\frac{3}{2}} \approx \frac{2^{\frac{5}{2}}\pi}{\sqrt{G}} \sqrt{\frac{R^3}{M}} . \quad (5)$$

The value, quoted above, for Q_F is based on non-adiabatic models in the linear approximation. This would not be appropriate for large-amplitude stars such as Miras. But almost all of the stars in our sample are small-amplitude pulsators, for which the linear approximation is appropriate.

With the Luminosity-Radius-Temperature Relation, $R = \sqrt{L/4\pi\sigma T_e^4}$, where σ is the Stefan-Boltzmann constant,

$$P_{LSP} \approx \frac{2\pi^{\frac{1}{4}}}{\sigma^{\frac{3}{4}} T_e^3 \sqrt{GM}} L^{\frac{3}{4}} . \quad (6)$$

Converting P_{LSP} into units of days, and taking the logarithm of both sides,

$$\mathrm{Log}(L) \approx \frac{4}{3} \log (P_{LSP,\,days}) + \frac{4}{3} \log \left(\frac{4300\, \sigma^{\frac{3}{4}} T_e^3 \sqrt{GM}}{\pi^{\frac{1}{4}}} \right) , \quad (7)$$

in which equation is it clear that the relation between log (L) and log (P_{LSP}) must be *linear*, consistent with the relation given by sequence D in Figure 1. The slope is consistent with the observed value in Figure 1.

It is interesting that LSPs obey a reasonably *tight* period-luminosity relation in Figure 1, and in corresponding figures in Wood (2000) and in Soszyński *et al.* (2007, 2021). In the context of Soszyński *et al.* (2021)'s explanation of the cause of LSPs,

the ratio of the radius A of the companion's orbit to the radius R of the star, which must be equal to or greater than 1, must, in fact, be relatively constant from star to star, as assumed above.

5. Conclusion

ω Cen is considered to be an anomalous globular cluster—massive, with multiple waves of star formation, and possibly even the core of a small galaxy that was absorbed by the Milky Way. Nevertheless, the complex variability of the red giants is similar to that in 47 Tuc (Percy and Gupta 2021), and other stellar systems, including the Milky Way. We identify period-luminosity relations for fundamental and first-overtone pulsators, and also for the LSPs in ω Cen. The pulsation amplitudes vary by a similar amount and on a similar time scale as those of the red giants in 47 Tuc. About half the stars show LSPs. Almost all the red giants in a sample of red giants in 47 Tuc did. About a third of red giants in other stellar systems do. It is possible that the incidence of LSPs in Population II stars is even greater than in Population I. The incidence of *companions* will be even higher still, since some companions' orbits will be seen flat-on, and will not produce LSPs. Studies of LSPs in other globular clusters would therefore be of interest.

The first author of this paper was an undergraduate astronomy and physics student. Projects of this kind are an excellent way for students to develop and integrate their science, math, and computing skills, motivated by (among other things) the knowledge that they are doing real science, with real data.

6. Acknowledgements

This paper made use of ASAS-SN photometric data. We wish to thank the ASAS-SN project team for their remarkable contribution to stellar astronomy, and for making the data freely available on-line, as well as the AAVSO for creating and making available the VStar time-series analysis package.

We also acknowledge and thank the University of Toronto Work-Study Program for financial support. The Dunlap Institute is funded through an endowment established by the David Dunlap Family and the University of Toronto.

References

Benn, D. 2013, VStar data analysis software (https://www.aavso.org/vstar-overview).
Foster, G. 1996, *Astron. J.*, **112**, 1709.
Jayasinghe, T., *et al.* 2018, *Mon. Not. Roy. Astron. Soc.*, **477**, 3145.
Jayasinghe, T., *et al.* 2019, *Mon. Not. Roy. Astron. Soc.*, **486**, 1907.
Lebzelter, T., and Wood, P. R. 2005, *Astron. Astrophys.*, **441**, 1117.
Lebzelter, T., and Wood, P. R. 2016, *Astron. Astrophys.*, **585**, A111.
Percy, J. R., and Fenaux, L. 2019, *J. Amer. Assoc. Var. Star Obs.*, **47**, 202.
Percy, J. R., and Gupta, P. 2021, *J. Amer. Assoc. Var. Star Obs.*, **49**, 209.
Persson, S. E., Frogel, J. A., Cohen, J. G., Aaronson, M., and Matthews, K. 1980, *Astrophys. J.*, **235**, 452.
Shappee, B. J., *et al.* 2014, *Astrophys. J.*, **788**, 48.
Soszyński, I., *et al.* 2007, *Acta Astron.*, **57**, 201.
Soszyński, I., *et al.* 2021, *Astrophys. J., Lett.*, **911**, L22.
Wood, P. R., 2000, *Publ. Astron. Soc. Australia*, **17**, 18.
Xiong, D. R., and Deng, L. 2007, *Mon. Not. Roy. Astron. Soc.*, **378**, 1270.

Appendix A: Period analysis of ASAS-SN observations of PRGs in NGC 6712

Table A1 lists properties concerning the period analysis of PRGs in the field of the NGC 6712 Cluster. We did not include them in Figure 1 because we wanted that figure to show stars with similar ages, distances, and compositions.

The following are brief notes on individual stars, which were analyzed as a prelude to the ω Cen project.

AP Sct Though the mean magnitude of the star remains roughly the same, the amplitude of its variability increases with time (Figure A1).

CH Sct, MR Sct The *shapes* of the light curves are very regular. From season to season, however, their brightnesses vary over a wide range of one to two visual magnitudes and also undergo a slow, linear ascent (Figure A2). We might therefore suspect the presence of an LSP whose period is larger than the time of observation (> 1,000 d).

NSV 11456 Owing perhaps to an LSP, the mean magnitude of the star alters from season to season, rising from the first to the second and falling from the second to the third.

NSV 11484 Any variability appears to be insignificant, being under the level of the noise. The light curve shows a slow, linear ascent, as the star brightens by 0.2 visual magnitude.

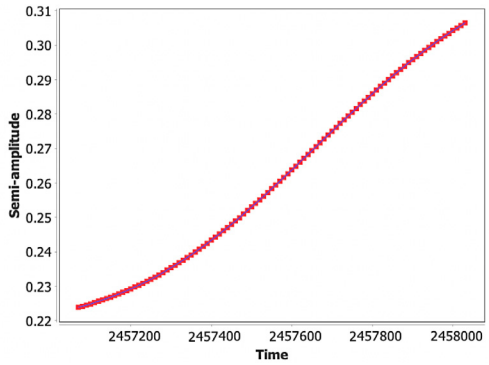

Figure A1. The variable pulsation semi-amplitude of AP Sct, as determined by wavelet analysis. The semi-amplitude undergoes a slow ascent.

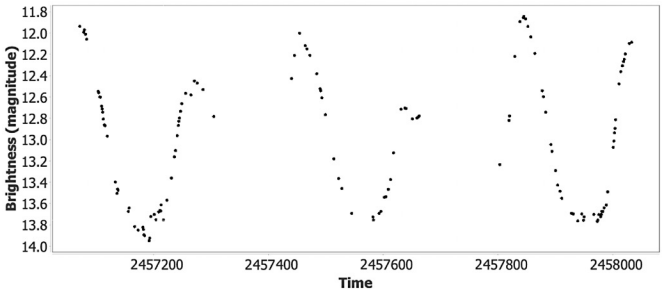

Figure A2. The V light curve of CH Sct.

Table A1. Period Analysis of ASAS-SN Observations of PRGs in NGC 6712.

Name	*Type*	*PA (d)*	*(V)*	*K*	*d (pc)*	*PP (d)*	A_{PP}	*PS (d)*	A_{PS}	*LSP (d)*	A_{LSP}
AP Sct	SR	112	12.45	8.15	6176	112	0.3	—	—	—	—
CH Sct	LSP?	192	13.01	8.126	5343	188	0.08	—	—	> 1000?	?
MR Sct	LSP?	117	12.77	8.274	5197	118	0.3	—	—	> 1000?	?
NSV 11456	LSP?	64	13.58	6.166	3402	64	0.08	—	—	> 1000?	?
NSV 11484	L	--	13.86	10.084	3550	--	--	—	—	--	--

Photometry and Transit Modeling of Exoplanet WASP-140b

Allen North
Department of Physical Science and Engineering, Harper College, 1200 W. Algonquin Road, Palatine, IL 60067; allen.north6@outlook.com

Timothy Banks
Department of Physical Science and Engineering, Harper College, 1200 W. Algonquin Road, Palatine, IL 60067, and Data Science, Nielsen, 200 W. Jackson, Chicago, IL 60606; tim.banks@nielsen.com

Received June 1, 2022; revised September 19, 2022; accepted September 20, 2022

Abstract Eleven transit light curves for the exoplanet WASP-140b were studied with the primary objective to investigate the possibility of transit timing variations (TTVs). Previously unstudied MicroObservatory and Las Cumbres Global Telescope Network photometry were analyzed using Markov Chain Monte Carlo techniques, including new observations collected by this study of a transit in December 2021. No evidence was found for TTVs. We used two transit models coupled with Bayesian optimization to explore the physical parameters of the system. The radius for WASP-140b was estimated to be $1.38^{+0.18}_{-0.17}$ Jupiter radii, with the planet orbiting its host star in 2.235987 ± 0.000008 days at an inclination of 85.75 ± 0.75 degrees. The derived parameters are in formal agreement with those in the exoplanet discovery paper of 2016, and somewhat larger than a recent independent study based on photometry by the TESS space telescope.

1. Introduction

An exoplanet is, in general, a planet orbiting a star other than our Sun. The first confirmed discoveries of exoplanets were made in the early 1990s, opening up a field that is rapidly expanding with several thousand confirmed exoplanets known today, giving us insight into different planetary systems to our own and introducing challenges to our understanding of how such systems form and evolve.

A variety of techniques are used to discover exoplanets. In this project, we concentrated on the transit methods that have been used to discover the most exoplanets to date—namely monitoring the brightness of the exoplanet system. Exoplanets are generally too close to their host stars to be seen as separate objects. The transit method tracks the brightness of the combined system (exoplanets and host star) with time, looking for changes caused such as when the planet passes in front of its star and blocks some light from reaching the Earth. The method tells us about the size of the planets and the angle at which they orbit about the host star relative to our line of sight.

In this paper we study transits for the exoplanet WASP-140b. This planet was discovered by Hellier *et al.* (2017), being 2.4 Jupiter masses and orbiting its V = 11.1 K0 host star (R.A. (J2000) $04^h\ 01^m\ 32.54^s$, Dec. (J2000) –20° 27' 03.9") once in roughly 2.24 days. Hellier *et al.* note a rotational modulation of the out of transit flux with an ~10.4-day cycle, which they attribute to magnetic activity of the host. They note that the transit is grazing, leading to a higher uncertainty in the estimate radius of the planet ($1.44^{+0.42}_{-0.18}$ Jupiter radii).

We apply the EXOTIC model (Zellem *et al.* 2020) to estimate basic parameters of the system such as time of mid-transit, planetary radius relative to the host star, and orbital radius. We compare and contrast these results with a simple transit model (Mandel and Agol 2002) we implemented with a Bayesian optimizer, as well as with literature results. We were particularly interested in seeing if there were deviations in the times of mid-transits compared to a fixed orbital period. The Transit Timing Variation (TTV) method is based on monitoring such changes in timing of transits. The presence of non-transiting planets (in the same system) can be inferred from TTV measurements. The gravitational interaction of these non-transiting planets will sometimes increase the orbital period of the transiting planet, and at other times decrease the period, depending on their relative positions, and so the mid-transit times will vary from a fixed, regular cycle.

2. Data and initial processing

The bulk of observations are 60-second, unfiltered exposures collected by a 6-inch aperture MicroObservatory (MObs; Sadler *et al.* 2001) telescope located at Mount Hopkins (latitude 31.675°, longitude –110.952°, 1,268 m altitude above sea level) in Arizona, using a KAF-1403 ME CCD camera with a pixel scale of 5.2" per pixel and 2 × 2 binning to reduce noise. These data were analyzed using EXOTIC, which is a PYTHON-based tool developed by JPL's "Exowatch" program for reducing exoplanet transit data. This software can run on a variety of operating systems as well as via Google's online "Colaboratory" tool.[1] Technical details on EXOTIC can be found in Zellem *et al.* (2020). Priors for Markov Chain Monte Carlo (MCMC) fitting by EXOTIC are automatically scraped from the NASA Exoplanet Archive (Akeson *et al.* 2013), while limb darkening parameters are generated by EXOFAST (Eastman *et al.* 2013). EXOTIC generates 1σ uncertainties based on the resulting posterior distributions.

Only dark images were available for the MObs observations, i.e., no flat field images were collected. The dark frames were collected at the beginning and end of each night of observation. As part of the analysis, EXOTIC applied the dark frames to

[1] For further details on this tool see: https://research.google.com/colaboratory/faq.html .

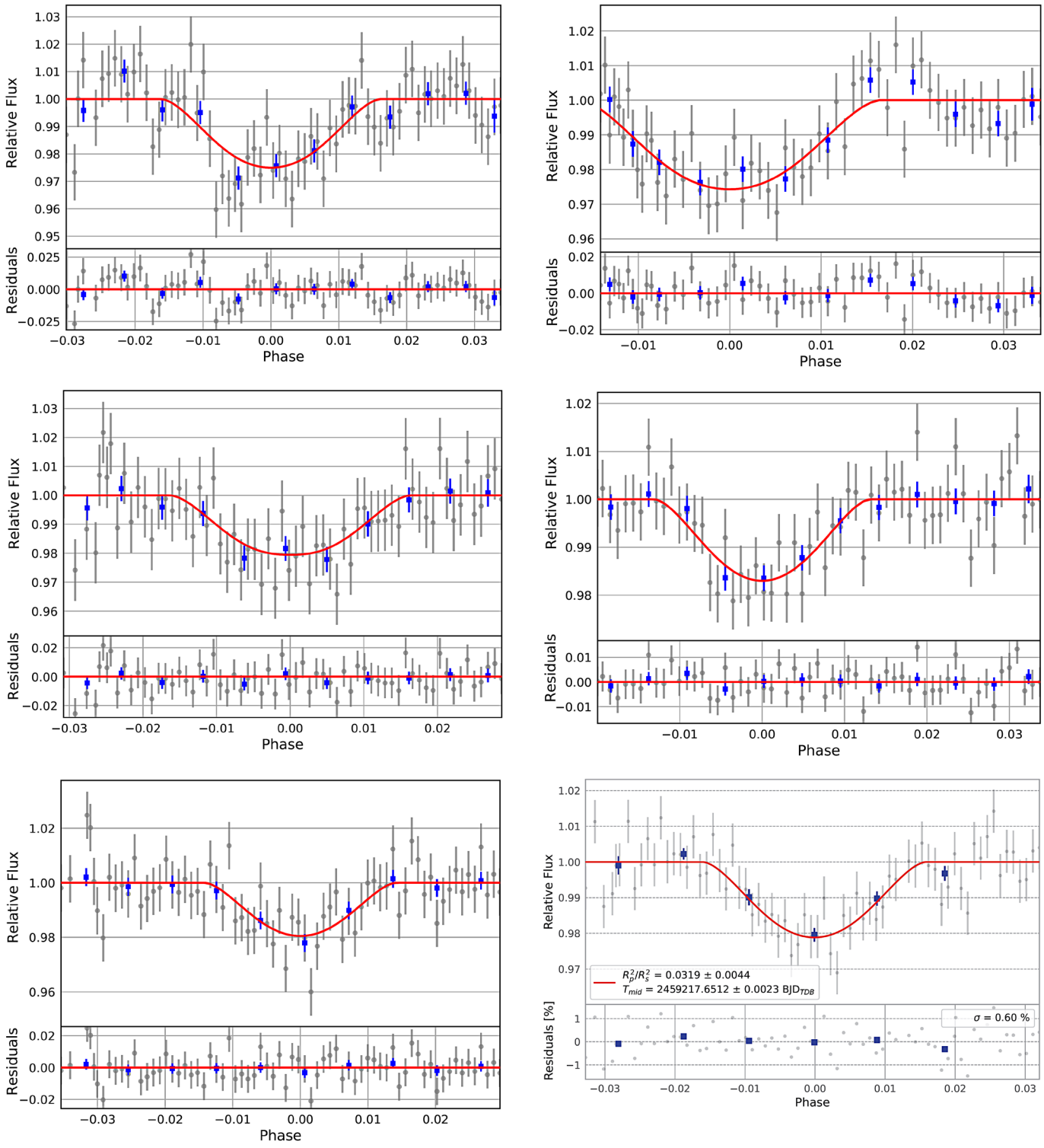

Figure 1: Selected WASP-140b transit data collected by the MicroObservatory and models. MicroObservatory observations have no filter. The red lines show the expected variation based on the best fitting exotic model for each transit. Not all transits are shown for reasons of space.

the science data, and then performed differential aperture photometry. For each transit, the analyst supplied EXOTIC a list of comparison stars. EXOTIC performed a stability assessment of this candidate list, choosing the most stable star as the final comparison star. Relatively poor pointing accuracy of the telescope and drift in tracking throughout a transit could lead to selection of different final comparison stars across the transits. However, typically EXOTIC selected stars 108 or 112 from the AAVSO comparison star sequence for WASP-140. We plate-solved science frames for each transit to ensure correct selection of the exoplanet host star, using astrometry.net, together with confirmation using charts prepared using the online AAVSO finding chart tool (VSP).

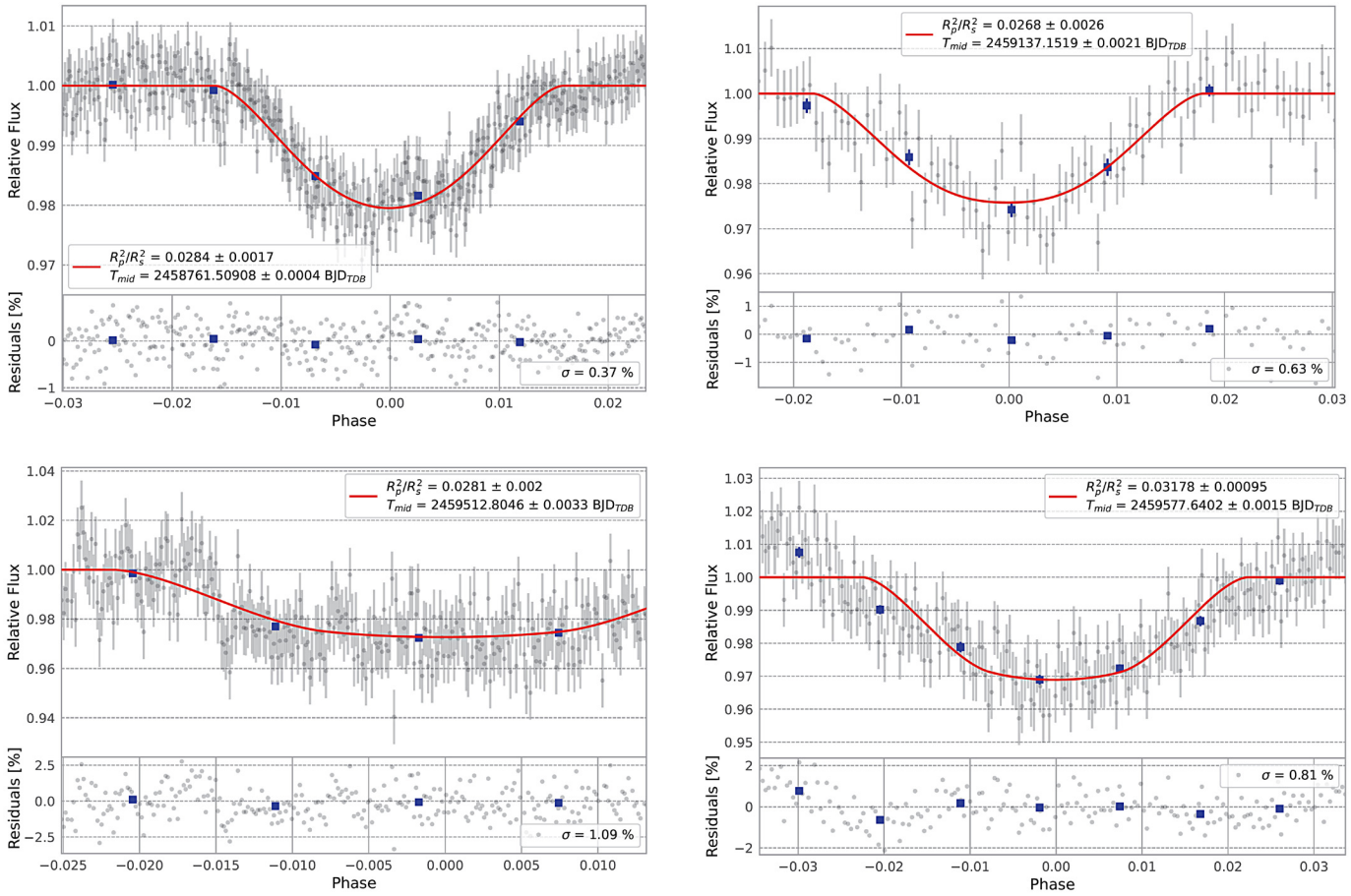

Figure 2: WASP-140b transit data collected using the LCO. The filters used for the LCO observations are indicated in the appropriate sub-figure captions.

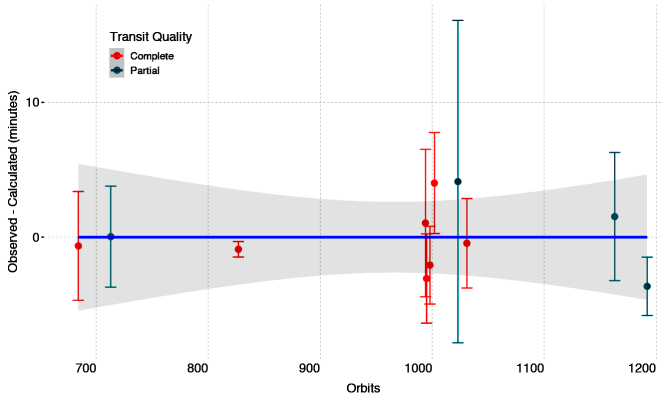

Figure 3. Residuals from linear regression fit of orbits versus mid-transit time for WASP-140b. A linear model was fitted to the residuals, with no statistically significant slope. The grey shaded zone is the 3-σ confidence interval for the regression. The blue line is the mean regression slope, which is not statistically different from zero at the 3-σ level. The error bars for the mid-transit timing estimates overlap with this, and with zero, indicating no statistically significant trends in the residuals. Transits were classified by eye into complete and incomplete transits, to see if data quality might obscure any trends (see Table 3). It does not.

3. Analysis

We analyzed 22 MObs attempts to observe transits of WASP-140b, dating from 12 October 2016 to 24 October 2021. Only 7 resulted in successful measurements of transits (see Figure 1 for charts of representative transits), a success rate of 32%. Clouds or incorrect pointing of the telescope accounted for the failed attempts. Table1 lists the key output from these fits using EXOTIC, namely the orbital semi-major axis a (relative to the stellar radius r_s), the planetary radius (r_p), and the time of mid-transit (in BJD). The observations and fitted parameter values from EXOTIC have been uploaded to the AAVSO exoplanet database, under the usercode BTSB.

We also made use of the Las Cumbres Observatory Global Telescope network (LCOGT; Brown *et al.* 2013), first using archival data of transits and also collecting r_p photometry on the night of 28 December 2021 using a telescope at the Cerro Tololo Inter-American Observatory. All the analyzed LCOGT data were collected using 0.4-meter telescopes equipped with CCDs. We processed all these data using EXOTIC, following flat fielding, dark subtraction, and bias correction via the LCO BANZAI system.[2] Model fits to the transits are shown in Figure 2 and final parameter estimates are given in Table 1. We did not upload the LCOGT archival data or the model fits based on these to the AAVSO Exoplanet Database, given that we did not collect the data and did not wish to "make claim" to them over the original investigators.

Table 1. *Fitted Parameters for WASP-140b from the* EXOTIC *modelling.*

Date	*Mid-transit*	a/r_s	r_s/a	r_p/r_s	*Quality*
18 Nov 2018	2458441.7633 ± 0.0028	7.69 ± 0.30	0.130 ± 0.005	0.1786 ± 0.0099	complete
22 Jan 2019	2458506.6080 ± 0.0026	7.63 ± 0.24	0.131 ± 0.004	0.179 ± 0.001	partial
11 Oct 2020	2459134.9220 ± 0.0038	7.51 ± 0.52	$0.133^{+0.010}_{-0.009}$	0.154 ± 0.024	complete
20 Oct 2020	2459143.8611 ± 0.0020	8.40 ± 0.26	0.119 ± 0.004	0.178 ± 0.015	complete
29 Oct 2020	2459152.8145 ± 0.0026	8.14 ± 0.33	0.123 ± 0.005	0.176 ± 0.016	complete
15 Dec 2020	2459199.7704 ± 0.0083	7.29 ± 0.64	$0.137^{+0.013}_{-0.011}$	0.119 ± 0.030	partial
02 Jan 2021	2459217.6512 ± 0.0023	7.70 ± 0.24	0.130 ± 0.004	0.179 ± 0.012	complete
04 Oct 2019	2458761.5091 ± 0.0004	7.631 ± 0.085	0.131 ± 0.001	0.1684 ± 0.005	complete
14 Oct 2020	2459137.1516 ± 0.0023	7.20 ± 0.23	$0.139^{+0.005}_{-0.004}$	0.1618 ± 0.0085	complete
24 Oct 2021	2459512.8046 ± 0.0033	6.56 ± 0.19	$0.152^{+0.005}_{-0.004}$	0.1678 ± 0.0059	partial
28 Dec 2021	2459577.6402 ± 0.0015	6.486 ± 0.035	0.154 ± 0.001	0.1783 ± 0.0027	partial

Note: Mid-transit times are given in Barycentric Julian Dates (Barycentric Dynamical Time), the orbital semi-major axis (a) in terms of the stellar radius (r_s), and the planetary radius (r_p) relative to the stellar radius. EXOTIC *outputs a/r_s, so a column giving the inverse is given for convenience when comparing with a later model and the literature. Uncertainties are 1σ. "Quality" is a subjective assessment by the authors of the quality of the light curve. Exposure times for the LCOGT observations were 16.5 seconds for 4 October 2019, 100 s for 14 October 2020, 16.8 s for 24 October 2021, and 60 seconds for 28 December 2021.*

3.1. Orbital period

The ephemeris of Hellier *et al.* (2017) was used to calculate the number of orbits made by Wasp-140b about its host star since their starting epoch. These were then regressed against the mid-transit times given in Table 1 using the "lm" function in R (R Core Team 2021), giving an orbital period of 2.2359870 ± 0.000008 days and an epoch of 2456912.349 ± 0.008. These are in good agreement with the values of Hellier *et al.* (2017): 2.2359835 ± 0.0000008 days for the orbit and 2456912.35105 ± 0.00015 for the epoch. Higher order polynomial fits did not result in additionally statistically significant parameters. Inspection of the residuals (see Figure 3) reveals no apparent variation in period. These results therefore do not indicate any significant transit timing variations (TTVs). As noted above, TTVs would indicate the presence of an additional planet in the WASP-104 system through its gravitational attraction periodically altering the orbital velocity of WASP-140b. This would have led to observed transits (of WASP-140b) being earlier or later than predicted by a linear ephemeris. Maciejewski (2022) also analyzed Transiting Exoplanet Survey Satellite (TESS; Ricker *et al.* 2015) data for the system searching unsuccessfully for TTVs, concluding that there were none currently detectable and so in agreement with the current study.

3.2. Transit models

While EXOTIC had already fitted the transits, we decided to build from "first principles" a simple transit model and couple this with optimization techniques in order both to make a comparison and to explore, including inclination as a free parameter. This was primarily a student project acting as an introduction to exoplanet research, so building our own model and coupling this with optimization was considered a good learning exercise. EXOTIC adopts its priors from the NASA Exoplanet Archive, hence it adopted the inclination from Hellier *et al.* (2017) as a fixed parameter. Given the glancing nature of this transit, fixing the inclination has a large effect on the derived parameter estimates. For optimization of our transit model, we used the Markov Chain Monte Carlo (MCMC) technique Hamilton Monte Carlo (HMC). MCMC allows construction of a Markov process such that the stationary distribution is the same as our target distribution, through the generation of a "chain" of random samples from the process. Through a sufficient number of samples, such a chain becomes close enough to the stationary distribution and therefore provides a good approximation to the target distribution. This is known as convergence of the MCMC chain (see Sinharay 2003), and allows exploration of the uncertainty in the parameter estimates—explaining our interest in this technique. We implemented HMC using the RSTAN implementation of STAN (Carpenter *et al.* 2017; STAN Development Team 2021) inside the statistical programming language R. Uniform priors were used, reflecting minimum previous knowledge of the parameters.

To build this model we used some key parameters of the exoplanet and its host star:

- a, r_s, and r_p were as defined above, with the radii being in terms of a;
- u = linear limb darkening coefficient (see below for an explanation of this parameter);
- i = orbital inclination (in degrees). Ninety degrees means that the orbital plane is in the line of sight from the Earth;
- offset = a parameter to adjust the reference point of phase axis;
- U = system brightness, used to adjust the reference point of flux axis. The out-of-transit flux should be approximately unity, i.e., the fluxes are normalized to the mean out-of-transit level.

We first consider that d is the center-to-center distance between the planet and the star. We can then calculate $z = d/r_*$, which denotes the normalized separation of the centers (of the exoplanet and its host star) and $p = r_p/r_*$, which is the ratio of the disk radii. This allows us to model a transit based on the equations in Mandel and Agol's (2002) paper. These specify that for a uniform source, the ratio of obscured to unobscured flux is $F^e(p, z) = 1 - \lambda^e(p, z)$, where:

[2] See https://github.com/LCOGT/banzai for further information on this data pipeline.

$$\lambda^{e}_{(p,z)} = \begin{cases} 0 & 1 + p < z \\ \frac{1}{\pi}\left[p^2 k_0 + k_1 - \sqrt{\frac{4z^2 - (1 + z^2 - p^2)^2}{4}}\right] & |1 - p| < z \leq 1 + p \\ p^2 & z \leq 1 - p \\ 1 & z \leq p - 1. \end{cases} \quad (1)$$

and $\kappa_1 = \cos^{-1}[(1 - p^2 + z^2) / 2z]$ and $k_0 = \cos^{-1}[(p^2 + z^2 - 1) / 2pz]$. This set of equations describes the flux of planetary systems in the following cases:

1. When the planetary disk does not obscure any portion of the stellar disk. There will be no dimming of the combined light, and so the normalized flux would be 1.
2. When the planetary disk is completely in front of the stellar disk. In the case of a uniformly bright stellar disk, the dimming will scale by the obscured area—which can be calculated by r_p^2 / r_s^2 (or p^2).
3. The boundary case when the planetary disk is moving onto or off the stellar disk.

The fourth case in Equation 1 corresponds to the unlikely case of when the planet is larger than (or equal to the same radius as) its host star.

Limb darkening refers to the phenomenon that the brightness of a star appears to decrease from the center to the edge, or limb, of the observed disk. This occurs because a stellar atmosphere increases in temperature with depth. At the center of a stellar disk an observer "sees" deeper and hotter layers that emit more light compared to at the limbs, where the upper and cooler layers are seen (which produce less light). The "small planet" approximation was used for the transit model, in that the limb darkening value corresponding to the center of the planetary disk projected onto the stellar disk was uniformly applied across the stellar area obscured by the planet. We implemented linear limb darkening for the model to adjust the obscured flux values, i.e., a limb darkening model with only a single term.

Only one of our data sets (LCOGT 04 October 2019) could be reliably fitted with this model, as it had a sufficient signal-to-noise ratio, a well-defined transit, and sufficient observations before and after the transit so that the out-of-transit flux levels were well constrained. Interestingly, we were not able to derive a determinate solution for the 04 October 2019 data set, which by eye appears to be a suitable transit. This would indicate that we have too many free parameters in the fit, a point we will come back to later in the paper. Table 2 presents results of this fitting and some example MObs fits. Clearly we were asking too much of the MObs data when we included inclination and limb darkening as free parameters, as we have physically unreasonable solutions for these data sets. EXOTIC is a better tool for these high noise data sets. The HCM fit to the LCOGT data is more reasonable.

3.3. Comparison with the literature

Hellier *et al.* (2017) estimated r_p / r_s as 0.166^{+0059}_{-0027}, $\cos i = 0.117^{+0013}_{-0009}$, and $r_s / a = 0.125^{+0030}_{-0022}$. These figures are in good agreement with the HMC model fit based on the LCOGT data bar for cos i, with the HCM model corresponding to an inclination of 85.07 ± 0.75 degrees compared to Hellier *et al.*'s value of $83.3^{+0.5}_{-0.8}$ degrees. This is within two standard deviations, though.

A comparison with the results from the EXOTIC model for the same data shows that the orbital radius from the HMC model is substantially larger (at ~9.2 times the stellar radius), as is the planetary radius (EXOTIC's 0.131 ± 0.001 r_s compared to 0.159 ± 0.013). The lack of agreement is puzzling, given that both Hellier *et al.* and EXOTIC both integrate the limb darkened fluxes obscured by the planetary disk, suggesting that the small planet approximation is not the primary cause of the difference.

Davoudi *et al.* (2020) used EXOFAST (Eastman *et al.* 2013) to model a clear filter 01 January 2017 transit data set of the system, finding the planet's radius to be 1.1990 ± 0.0735 that of Jupiter, which is smaller than Hellier *et al.* (2017)'s estimate of $1.44^{+0.42}_{-0.18}$ R_J and this paper's of $1.38^{+0.18}_{-0.17}$ R_J (although within the error ranges). No inclination or orbital radius data were supplied by Davoudi *et al.*, so a comparison is not possible.

Alexoudi (2022) applied the EMCEE Bayesian sampler (Foreman-Mackey *et al.* 2013) to analyze 28 transits from 3 sectors (Sector 4 from 18 October 2018 to 15 November 2018, sector 5 from 15 November 2018 to 11 December 2018, and

Table 2: MCMC results.

Date	r_p/r_s	r_s/a	*u*	*cos i*	*σ*	*Observatory*
04 October 2019	0.159 ± 0.013	0.109 ± 0.007	0.48 ± 0.23	0.086 ± 0.013	0.0036 ± 0.0001	LCOGT
11 October 2020	0.35 ± 0.23	0.14 ± 0.04	0.55 ± 0.30	0.16 ± 0.07	0.010 ± 0.001	MObs
20 October 2020	0.32 ± 0.22	0.10 ± 0.02	0.53 ± 0.28	0.11 ± 0.05	0.0058 ± 0.0005	MObs
02 January 2021	0.33 ± 0.20	0.11 ± 0.02	0.58 ± 0.28	0.11 ± 0.05	0.0063 ± 0.0005	MObs

Note: Only one of the LCOGT data sets gave a reliable solution. Results of three of the better MObs transits are shown, to demonstrate the lower confidence in the estimated parameter estimates for such data sets (together with an implausibly large "planet"). Uncertainties are 1σ. "Date" is the night of observation.

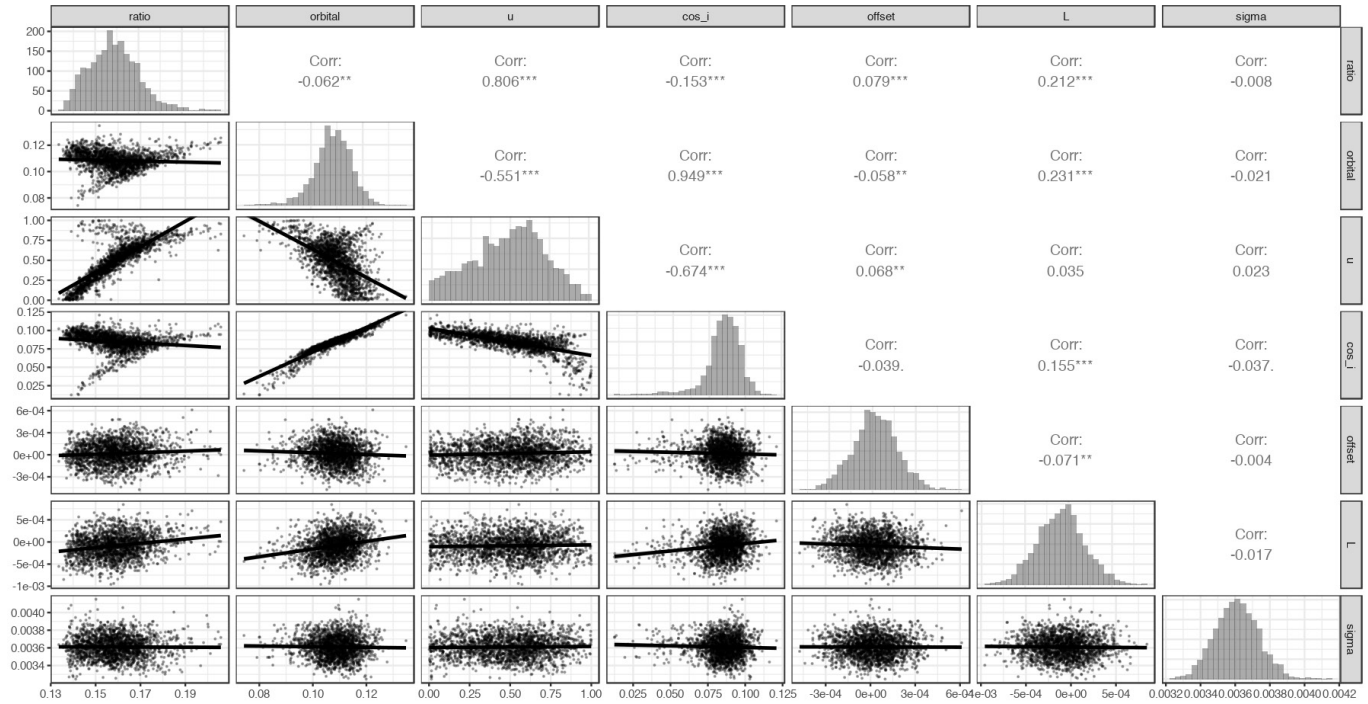

Figure 4. Example MCMC results for the 4 October 2019 transit of WASP-140b. This represents 4,000 steps in the Markov chain, including the initial steps known as "burn-in." These steps are excluded from the final results, and are considered a result of starting the optimization in a lower probability set of parameters, leading to movement to the global minimum. Actual runs included 40,000 steps, which unfortunately "overloaded" the plotting software and are therefore not included here. "Ratio" is the ratio of the planetary radius to the stellar one, "orbital" is the ratio of stellar radius to the orbital semi-major axis, "u" is the linear limb darkening co-efficient, "cos i" is the cosine of the inclination, "offset" an adjustment in phase, "L" an adjustment in flux, and "sigma" an estimate of the white noise in the data. The chart provides the distributions of each of these parameters on its diagonal as bar charts, correlations between the variables are given in the upper right, and scatter plots crossing each of the parameters in turn are given in the lower left. Each point in a scatter plot represents a step in the Markov chain. The bold lines are linear regressions to the data, corresponding to the correlation results.

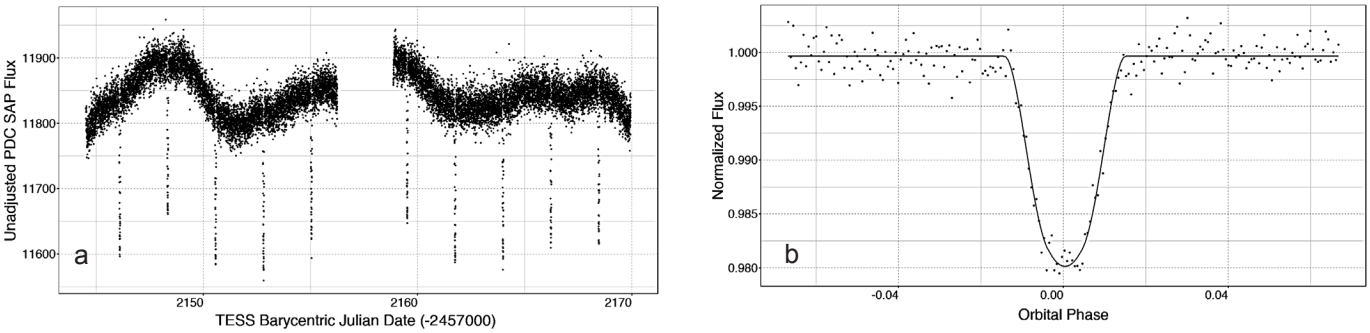

Figure 5. The figure on the left (a) shows the non-normalized Pre-search Data Conditioning Simple Aperture Photometry (PDC_SAP) generated by the TESS team, which has had removed longstanding systematic trends and so provides better data quality than the simple aperture photometry (also available from MAST). Remaining variability is clearly visible, showing these changes are on timescales comparable to that between transits. Hellier *et al.* (2017) noted residual variation at a 5–9 milli-magnitude amplitude. This range is consistent with the observed remaining variability. The figure on the right (b) shows one of these transits plus the optimal model generated by the HMC code. This transit is the second from the left in the data following the break in the middle of Figure 5a.

sector 31 from 21 October 2020 to 19 November 2020.) of data collected by the TESS space telescope. Alexoudi derived an inclination of 84.30 ± 0.06 degrees, $r_s/a = 0.1166 \pm 0.0008$, and $r_p/r_s = 0.1464 \pm 0.0010$. These values are similar to those of the current paper and Hellier *et al.* (2017), but not within formal uncertainties. Alexoudi noted the differences with Hellier *et al.*, commenting that these could be due to the higher accuracy of the TESS data. As a check, we downloaded two-minute cadence TESS data from MAST (see Figure 5a) and applied the HMC model to a transit (centered on TBJD 2459161.75; see Figure 5b). We found $rs/a = 0.109 \pm 0.008$, $rp/rs = 0.163 \pm 0.016$, and $\cos i = 0.089 \pm 0.016$ (~84.87°). The linear limb darkening coefficient was poorly constrained (0.48 ± 0.29). Our model resulted in a larger planetary radius than Alexoudi's, and very close to those derived from the LCOGT data.

3.4. Recommendations

Problems with the other data sets included the lack of sufficient pre-transit data, which prevented reliable estimates (e.g., the 14 October 2020 data set), while variations in the out-

of-transit flux levels prevented a reliable fit to the 28 December 2021 data set. The increased noise of the MObs data compared to LCOGT data also led to less accurate parameter estimates, especially for ratio of the planetary to stellar radii. It would be interesting to see if additional data processing, such as collection and use of flat fields, would help improve the quality of these data sets.

For transit fittings of this system, we recommend that the pre- and post-transit observations be roughly as long as the actual transit time period, particularly since the host star appears to be active (changing in flux levels) on a short time scale. For instance, the pre-transit flux levels appear to be greater than post-transit for the 28 December 2021 data set, and are a complication for a simple model such as ours.

A further complication is the use of the small planet approximation for a high inclination orbit such as that for WASP-140b; in later projects we intend to apply a graduated limb darkening adjustment to the obscured flux. There is a clear correlation between u with r_p/r_s and rs/a (see Figure 4), so locking u to a value based on theory could lead to a tighter confidence interval for these two parameters. The parameter u can also be seen to be poorly defined in Figure 4. This suggests that it could be better to set it to a value using theory and include u as a fixed (rather than a free) parameter. See Banks and Budding (1990) for further discussion of the information content of data and the question of over-parameterization. Finally, WASP-140b transits close to the stellar limb where the gradient will be strongest in the limb darkening, further supporting the conclusion above.

The signal-to-noise ratio is clearly important for transit fitting, affecting the accuracy of the MObs fits by our model. Observations with the LCOGT (similar to those presented here) appear to have sufficient "information content" to support the HMC model, providing sufficient data about the shoulders of the eclipse are collected for accurate estimation of the out-of-transit flux level.

4. Summary

This paper presented MCMC modeling of transits of WASP-140b, collected using robotic telescopes of the MObs and LCOGT. These data included a transit in December 2021 collected by the authors. We coded a fitting function based on the equations of Mandel and Agol (2002) and coupled this with Bayesian optimization. Together with the EXOTIC analysis program, two MCMC-based optimization models have been applied to these transits, deriving estimates for the times of mid-transit as well as physical parameters of the system. Inspection of the mid-transit times revealed a linear period with no statistical evidence from the data of transit time variations, i.e., no evidence for the gravitational influence of a non-transit planet on the orbit of WASP-140b.

Results from the two analysis programs (EXOTIC and HMC) were in good agreement, indicating the radius for WASP-140b to be $1.38^{+0.18}_{-0.17}$ Jupiter radii, with the planet orbiting its host star in 2.235987 ± 0.000008 days at an inclination of 85.75 ± 0.75 degrees. The derived parameters are in formal agreement with the discovery paper of Hellier *et al.* (2017), and somewhat larger than a recent independent study based on photometry by the TESS space telescope (Alexoudi 2022).

We were probably too ambitious in our selection of an exoplanet with a high inclination orbit about a host star itself with rapidly changing flux levels (to apply a high parameter model such as the HMC model), but that is part of the learning process. Application of techniques such as Gaussian Processes to model out the host star variations would be a good next step, which would allow combining multiple transits which could be binned together to increase the signal-to-noise ratio and strengthen the information content of the data. We also plan to use our HMC model on more simple systems, such as Kepler-1 (see, e.g., Ng *et al.* (2021) who applied the Mandel and Agol (2002) models, MCMC, and Gaussian Processes to Kepler space telescope data of Kepler-1b and other systems), which do not have such active host stars and orbits with inclinations closer to 90 degrees, where the model's deficiencies will be less and the correlation between limb darkening and inclination less confounding. Having made these comments, we still recommend that programming a simple model such as Mandel and Agol (2002) and coupling this with an optimizer is a useful learning exercise, and makes for a useful student project. Our points are rather to choose a more quiet system than the one we did, and to either implement improved handling of limb darkening for highly tilted systems or to choose an exoplanet with an orbit closer to 90° inclination as well as being somewhat smaller relative to its host star (so that the small planet approximation is more valid). If investigation of TTVs is the primary goal of the project, then EXOTIC is an excellent tool for such work.

5. Acknowledgements

This publication makes use of the EXOTIC data reduction package from Exoplanet Watch, a citizen science project managed by NASA's Jet Propulsion Laboratory (JPL) on behalf of NASA's Universe of Learning and which is supported by NASA under award number NNX16AC65A to the Space Telescope Science Institute. We are grateful for observing time on the Las Cumbres Observatory Global Telescope (LCOGT) Network, and to Rachel Zimmerman Brachman (JPL) for making available this opportunity. We thank the LCOGT for making available archival data. We also thank the The Center for Astrophysics | Harvard & Smithsonian for the MicroObservatory data kindly made available by Frank Sienkiewicz. This research has made use of the NASA Exoplanet Archive, which is operated by the California Institute of Technology, under contract with the National Aeronautics and Space Administration under the Exoplanet Exploration Program. We thank the University of Queensland for collaboration software. This paper includes data collected by the TESS mission and obtained from the MAST data archive at the Space Telescope Science Institute (STScI). STScI is operated by the Association of Universities for Research in Astronomy, Inc., under NASA contract NAS 5-26555. We thank the anonymous referee for their comments and guidance which improved the paper.

References

Akeson, R. L., *et al.* 2013, *Publ. Astron. Soc. Pacific*, **125**, 989.

Alexoudi, X. 2022, *Astron. Nachr.*, **343**, e24012 (DOI: 10.1002/asna.20224012).

Banks, T., and Budding, E. 1990, *Astrophys. Space Sci.*, **167**, 221.

Brown, T., *et al.* 2013, *Publ. Astron. Soc. Pacific*, **125**, 1031.

Carpenter, B., *et al.* 2017, *J. Statistical Softwar*e, **76**, 1 (DOI: 10.18637/jss.v076.i01).

Davoudi, F., *et al.* 2020, arXiv:2006.01591 (DOI: 10.48550/arXiv.2006.01591).

Eastman, J., Gaudi, B. S., and Agol, E. 2013, *Publ. Astron. Soc. Pacific*, **125**, 83.

Foreman-Mackey, D., Hogg, D. W., Lang, D., and Goodman, J. 2013, *Publ. Astron. Soc. Pacific*, **125**, 306 (DOI: 10.1086/670067).

Hellier C., *et al.* 2017, *Mon. Not. Roy. Astron. Soc.*, **465**, 3693 (DOI:10.1093/mnras/stw3005).

Maciejewski, G. 2022, *Acta Astron.*, **72**, 1 (arXiv:2202.11990).

Mandel, K., and Agol, E. 2002, *Astrophys. J.*, **580**, 171.

Ng, S.-Y., Jiadi, Z., Püsküllü, C., Banks, T., Budding, E., and Rhodes, M. D. 2021, *J. Astrophys. Astron.*, **42**, 110 (DOI: 10.1007/s12036-021-09779-3).

R Core Team. 2021, R: A Language and Environment for Statistical Computing, R Foundation for Statistical Computing, Vienna, Austria (https://www.R-project.org).

Ricker, G. R., et. 2015, *J. Astron. Telesc. Instrum. Syst.*, **1**, id. 014003 (DOI: 10.1117/1.JATIS.1.1.014003).

Sadler, P. M., Gould, R. R., Leiker, P. S., and Antonucci, P. R. A. 2001, *J. Sci. Education Technol.*, **10**, 39 (DOI: 10.1023/A:1016668526933).

Sinharay, S. 2003, "Assessing Convergence of the Markov Chain Monte Carlo Algorithms: A Review," MCMC, ETS Res. Rep. Ser. (DOI: 10.1002/j.2333-8504.2003.tb01899.x).

Stan Development Team. 2021, RStan: the R interface to Stan (http://mc-stan.org/).

Zellem, R. T., *et al.* 2020, *Publ. Astron. Soc. Pacific*, **132**, 054401 (DOI: 10.1088/1538-3873/ab7ee7).

An Examination of ATO J031.2309+52.9923, a δ Scuti Variable from the ATLAS Survey

Eric G. Hintz
Jarrod L. Hansen
Denise C. Stephens
Benjamin J. Derieg
Department of Physics and Astronomy, Brigham Young University, N283 ESC, Provo, UT 84602; hintz@byu.edu

Received June 1, 2022; revised July 29, 2022; accepted July 29, 2022

Abstract As part of our variable star follow-up program we have examined a number of stars from the ATLAS (Asteroid Terrestrial-impact Last Alert System) survey. The first of these, ATO J031.2309+52.9923, was reported with a period of 0.069705 d. Our revised period is 0.06970555 d, but we find an additional period of 0.074 d. We also report a suspected period change of $(1/P)\,dP/dT = -340 \times 10^{-8}\,yr^{-1}$. In addition to the primary period, we find two additional closely spaced periods of 0.07380 d and 0.07338 d, with a period ratio of $P_1/P_2 = 0.945$. The period ratio and change would indicate that this object is a δ Scuti variable with non-radial pulsations. We find that this target fits into the medium amplitude group of δ Scuti variables such as AN Lyncis.

1. Introduction

There are a large number of surveys that generate light curves, such as ATLAS (Asteroid Terrestrial-impact Last Alert System), which is looking for asteroids which could potentially hit the Earth. There is also ASAS-SN, which is looking for supernova events. Then there are systems like TESS that are looking for transiting planets. Finally, we are near the advent of LSST. In all these cases light curves of short period pulsating stars are generated. However, in many cases the cadence is not ideal for objects such as δ Scuti variables, with the TESS 2-minute cadence observations being an obvious exception.

As part of our campus observing program we selected a number of potential δ Scuti stars to examine at a higher cadence. We started with the ATLAS database of potential variables (Heinze *et al.* 2018). We selected objects from their lists of PULSE and MPUL objects for more detailed follow-up studies. One of the first targets selected was one we label as ATLAS 30 from our own internal numbering system. This target is designated ATO J031.2309+52.9923 in the ATLAS survey and had an estimated period of 0.069705 d. It is located at R.A. (2000) $02^h\ 04^m\ 55.4^s$, Dec. (2000) +52° 59' 32.6". This object is also found in the ASAS-SN (Shappee *et al.* 2014; Kochanek *et al.* 2017) archive (ASASSN-V J020455.45+525932.6), where it is listed as a High Amplitude δ Scuti (HADS) with a period of 0.0697056 d. In the TESS archives the target is TIC 250510098. From the 2MASS (02045542+5259325) and AllWISE (J020455.43+525932.5) surveys we find (Cutri *et al.* 2003, 2014):

J = 11.409 ± 0.025,
H = 11.273 ± 0.023,
K = 11.221 ± 0.022,
W1 = 11.186 ± 0.023,
W2 = 11.204 ± 0.021,
W3 = 11.193 ± 0.165,
W4 = 9.1.

From the Gaia EDR3 release (Bailer-Jones *et al.* 2021) we have a distance of 1,004 pc. Given galactic coordinates of l = 133.9849° and b = –8.2951°, this puts ATLAS 30 within the disk. From a Gaia DR2 reduction of surface temperatures Bai *et al.* (2019) we deduce a temperature for ATLAS 30 of 7430 ± 214 K. In the *TESS Input Catalogue* 34 (Stassun *et al.* 2019) they report a number of values: a temperature of 7728 ± 08 K, log g = 4.01 ± 0.10, [M/H] = –0.34 ± 0.02, and $M = 1.82\,M_\odot$. All these values point to ATLAS 30 being a late A dwarf, which is in line with a δ Scuti designation. The metal content is a bit surprising given the star's location in the disk.

Since ATLAS 30 is potentially a new δ Scuti variable we examined some basic information on the varieties of δ Scuti that exist. In Breger and Pamyatnykh (1998) they discuss the period changes seen in three groups of δ Scuti variables, Pop. I radial pulsators, Pop. I non-radial pulsators, and Pop. II radial pulsators. For all the radial pulsators they find changes in $(1/P)\,dP/dt$ to be in about the $\pm 10 \times 10^{-8}\,yr^{-1}$ range. For the non-radial pulsators they list changes 10x greater. For example, XX Pyx has a period change value for the primary period of $340 \times 10^{-8}\,yr^{-1}$ 41 (Handler *et al.* 1998) and $-110 \times 10^{-8}\,yr^{-1}$ for 4 CVn (Breger 1990). In addition, Breger and Pamyatnykh (1998) provide the first and second period for a number of radial and non-radial pulsators. For two radial pulsators they found $P_1/P_2 = 1.302$ for AI Vel and $P_1/P_2 = 1.279$ for SX Phe. From Handler *et al.* (1998) we find $P_1/P_2 = 0.929$ for XX Pyx.

In this paper we will present an O–C period determination for this potential new δ Scuti, along with a potential period change. A Fourier decomposition of the light curve will also be reported, and examined in each of the various seasons to provide all significant frequencies in the data.

2. Photometric data

2.1. Robotic observations

Beginning in 2019 we secured data on ATLAS 30 using a group of robotic telescopes mounted on the observation deck of the Eyring Science Center at Brigham Young University.

Table 1. Telescope and CCD specifications.

Telescope	*CCD*	*Pixel Size (μm)*	*Plate Scale ("/pixel)*	*Nights*	*Years*
TPO 12"	FLI ML8300	5.4	0.46	5	2021–2022
Vixen VMC200L	FLI ML3200	6.8	0.72	59	2019–2021
Vixen VMC200L	FLI ML8300	5.4	0.57	9	2022
Takahashi Mewlon-250	FLI ML8300	5.4	0.37	21	2019

Table 2. Comparison star values.

Star No.	*Name*	*R.A. (2000) h m s*	*Dec. (2000) ° ′ ″*	*B*	*V*
1	TYC 3685-1001-2	02 05 01.1	+53 00 05.6	12.06	11.47
2	TYC 3685-489-1	02 05 07.6	+52 59 43.0	11.90	11.53
3	TYC 3685-2151-1	02 05 32.8	+53 06 12.8	13.72	12.05
4	TYC 3685-2252-1	02 05 48.2	+53 06 27.2	12.79	12.01
5	TYC 3685-2211-1	02 04 57.0	+53 06 02.4	12.86	12.18
6	TYC 3685-225-1	02 05 08.0	+52 54 52.1	12.52	12.12

The overall facility is known as the Orson Pratt Observatory. This facility is located at an elevation of 1,430.4 m with moderately dark skies. We used three telescopes to secure data on 94 nights. The telescope configurations are given in Table 1, along with the number of nights for each configuration. For all but three nights of observing, the data were obtained through a Johnson V filter. The remaining three nights were taken with a Johnson B filter. All observations were reduced using standard IRAF procedures.

Each night's data were then processed through AstroImageJ (Collins *et al.* 2017) to generate light curves, using comparison stars to provide calibrated magnitudes. The area around our target star is shown in Figure 1 with the comparison stars marked. Information on the comparison stars is gathered in Table 2. None of the comparison stars are flagged as potentially variable in any survey and after a careful check we find no significant variations. We do note that there is a faint star to the East of ATLAS 30, however given our aperture choice we do not feel this star ever contributed light to our measurements. A sample of one of the longer nights of data is shown in Figure 2.

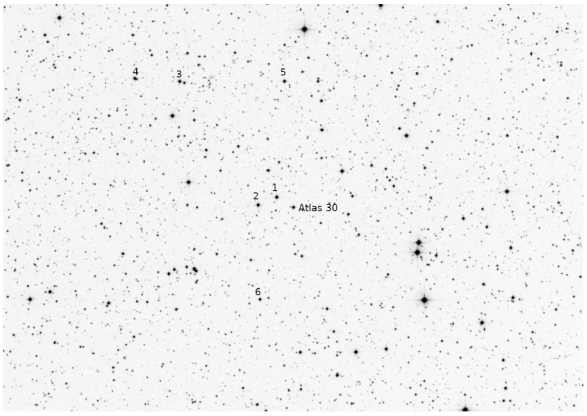

Figure 1. Field of ATO J031.2309+52.9923 (labeled ATLAS 30) with comparison stars labeled. North (up), east (left). Field of view is 31.6' × 23.7' at 0.57 arcsec/pixel.

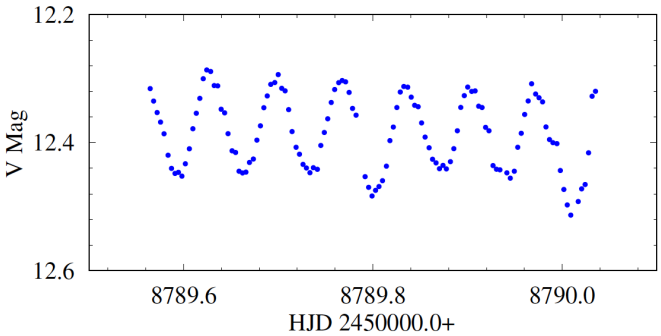

Figure 2. A long night of data from JD 2458789.

2.2. Archival photometry

In addition to our own data we gathered observations from three main archives. First we downloaded all the data from the ATLAS program (Heinze *et al.* 2018) using the NASA MAST archive. These observations are in two filters, c (140 observations) and o (154 observations). Those are effectively cyan and orange filters that cannot be directly matched to our data sets. We then did a search for the last 3,000 days within the ASAS-SN archive (Shappee *et al.* 2014; Kochanek *et al.* 2017). Data from AS-SN can be either in V (571 observations) or g (1315 observations). In this case we can add the V observations directly to our data set. Finally we downloaded the data from the TESS archive. These data come from a fairly wide filter centered roughly in the I band. From here we gathered 993 observations.

Table 4. Frequency content of ATO J031.2309+52.9923 from TESS data.

	Frequency c d^{-1}	*Amplitude mag.*	*Phase*	*S/N*
f_1	14.34546(7)	0.0452(1)	0.4869(5)	253
f_2	13.5498(7)	0.0048(1)	0.886(4)	27
$2f_1$	28.693(1)	0.0022(1)	0.925(9)	16
f_3	13.629(1)	0.0021(1)	0.72(1)	12

Table 3. Times of maximum light for ATO J031.2309+52.9923.

Cycle	*HJD 2450000.0+*	*O–C*	*Filter*
0	8522.65095	–0.00232	V
1	8522.71969	–0.00328	V
57	8526.62671	0.00023	B
57	8526.62481	–0.00167	V
58	8526.69606	–0.00013	B
229	8538.61579	–0.00005	V
230	8538.68528	–0.00026	V
272	8541.61370	0.00052	V
273	8541.68287	–0.00001	V
273	8541.68231	–0.00057	B
459	8554.65007	0.00195	V
2873	8722.91750	0.00018	V
2888	8723.96282	–0.00008	V

Note: Table 3 is published in its entirety in the machine-readable format. A portion is shown here for guidance regarding its form and content. Full table available at: ftp://ftp.aavso.org/public/datasets/3838-Hintz-atoj031.txt.

3. Analysis

3.1. Times of maximum light

The first stage of the analysis was to obtain times of maximum light from all light curves with sufficient coverage. This was done using using Peranso (Paunzen and Vanmunster 2016). We used a third order fit to each maximum and then obtained the time of maximum from the fit. We determined 176 times of maximum light, 173 in the V filter and 3 in the B filter. All these times are gathered in Table 3. Using only the times for the V filter we determined an ephemeris of:

$$HJD_{max} = 2458522.65327(23) + 0.069705552(28)E \quad (1)$$

The errors included are for the last two digits of both the period and starting epoch. Using this equation we determined calculated times of maximum light and O–C values for each maximum. These are also gathered into Table 3. In Figure 3 we show the O–C diagram for ATLAS 30. Since there appeared to be a slight bowing to the curve we determined a second order fit as given in:

$$HJD_{max} = 2458522.65217(41) + 0.06970593(12)E - 2.24(70) \times 10^{-11}E^2 \quad (2)$$

This is right at the edge of a 3σ detection for a period change. Continued coverage of this object would be needed to determine if the period change is real. Using the standard method of reporting period change we found $(1/P)(dP/dt) = -340 \times 10^{-8}\,yr^{-1}$. This is similar to the value found for XX Pyx by Handler *et al.* (1998), although it is negative. As mentioned earlier, a detailed discussion of period changes in δ Scuti variables can be found in Breger and Pamyatnykh (1998). If the detected period change is real it would indicate that ATLAS 30 is likely a non-radial pulsator.

Another interesting result from the O–C analysis has to do with patterns in the residuals. On a number of nights in November 2019 we found 5 to 7 maxima per night. This allowed us to examine cycle-to-cycle changes in the O–C values and the shapes of the light curves. As seen in Figure 4, there appears to be a potential periodic change in the O–C values. Using O–C data over 25 days from this time period, we used Peranso and found a frequency at $f_b = 0.794\,c\,d^{-1}$ that phased these O–C values. There was also a nearby peak at $f_a = 0.719\,c\,d^{-1}$, as shown in Figure 5. The lower panel in Figure 5 shows the phased O–C values using the f_b value. These values will be discussed further in the next section.

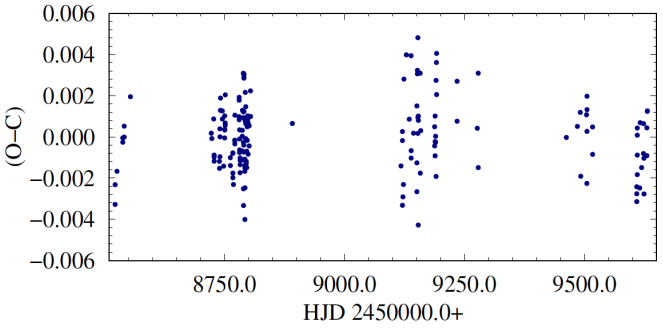

Figure 3. O–C Diagram from 174 times of maximum light from 2019 to 2022.

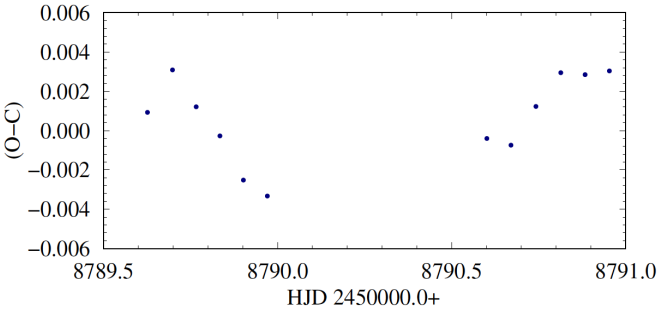

Figure 4. O–C Diagram for two consecutive nights in November 2019.

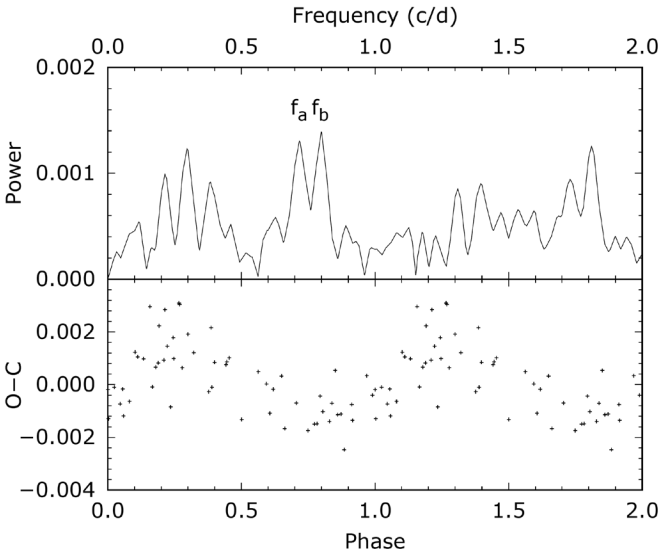

Figure 5. The upper panel is the power spectrum of the O–C values from November of 2019. The lower panel shows the phased O–C values for a frequency of 0.794 c d^{-1}.

3.2. Fourier decomposition

To begin our Fourier analysis we sorted long runs of data into sets based on gaps in the data. This allows for an examination of period and amplitude changes over time and reduces some aliasing. To perform our initial decomposition we used Period04 (Lenz and Breger 2005). From the TESS data we found a solution with frequencies as reported in Table 4. The S/N for the four reported frequencies are well above the cut-off suggested by Lenz and Breger (2005), but no other frequencies reach this level. We note that the filter system for TESS is a fairly wide filter centered near the traditional I filter. The one concern with the TESS data is the low Nyquist frequency of 24.0028 c/d. In Figure 5 we show the power spectrum for the original data set and with the first frequency removed. In the top graph we can see the primary frequency at 14.345 c d^{-1}, but we see another at 33.661 c d^{-1}. That is mirrored around the Nyquist frequency.

The value for $2f_1$ is a little above the Nyquist frequency, so there is some concern. In the lower panel of Figure 6 we see f_2 and $2f_1$. We also see the mirrored frequencies. For typical HADS, which have a fast rise that needs to be fit with a number of harmonics of the primary frequency, we would have more issues with this mirroring effect. However, given that ATLAS 30 has a more symmetric curve, the low Nyquist frequency doesn't have as much of an impact.

To further examine the frequency content of ATLAS 30 we split our own data set into two groups, one before JD2459000 and one after. This provided a much higher Nyquist frequency of approximately 135 c d^{-1}. For the data set before JD2459000 we found the power spectrum shown in Figure 7. This shows the typical power spectrum from a single location, without the mirroring effect. To confirm our frequency content we used the CLEANest method (Foster 1995) found in Persano. The same four frequencies were recovered. Although we don't find significant frequencies at f_1–f_2 and f_1–f_3 in the Fourier analysis, we note that these values of 0.795 and 0.716 are the same as the values found for the changes in O–C values. Therefore any sinusoidal changes seen in the O–C values are related to the beating of two frequencies, not from an orbital motion. We also note a period ratio of $P_1/P_2 = 0.945$ from our frequency solution.

When running a Period04 solution on the various data sets we found a different number of the primary frequencies listed above. For both the cyan and orange data sets from ATLAS we only recovered the primary frequency. This is also true of an analysis of the ASAS-SN g filter data. For the ASAS-SN V filter data we found f_1 and $2f_1$, but not the additional frequencies. From our largest seasonal data sample from 2019 we recovered the first three frequencies.

Using the four frequencies from Table 4 we examined various subsets of data from all sources. A primary focus here was on the V$ filter data from ASAS-SN and our observations. We find that the amplitude of the primary frequency has slowly increased over time from about 0.145 to 0.155 (see Figure 8). Knowing this slight change allows us to compare the amplitude in different spectral ranges for the same epoch. The ATLAS c filter has broad coverage from 420 nm to 650 nm and has an amplitude similar to the V filter at a common time. The ATLAS o filter covers a range of the Sloan r and i together. At JD 2457600

Table 4. Frequency content of ATO J031.2309+52.9923 from TESS data.

	Frequency c d^{-1}	*Amplitude* mag.	*Phase*	*S/N*
f_1	14.34546(7)	0.0452(1)	0.4869(5)	253
f_2	13.5498(7)	0.0048(1)	0.886(4)	27
$2f_1$	28.693(1)	0.0022(1)	0.925(9)	16
f_3	13.629(1)	0.0021(1)	0.72(1)	12

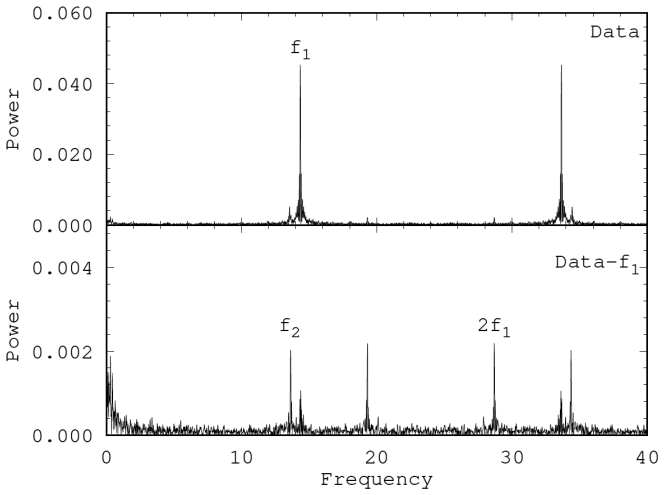

Figure 6. Fourier Spectrum from TESS data from Period04.

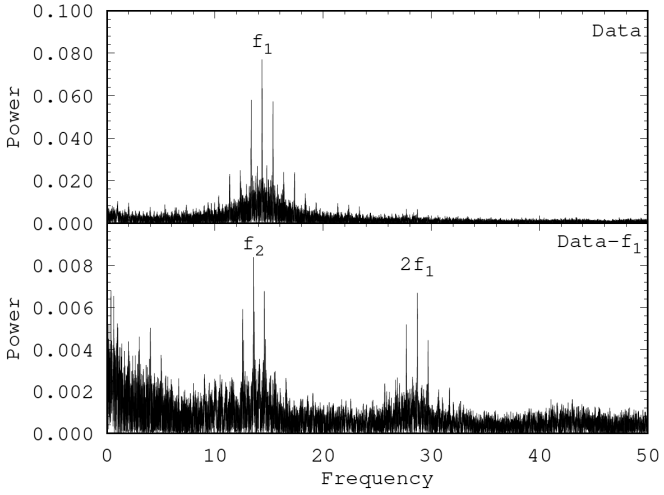

Figure 7. Fourier Spectrum from BYU data prior to JD2459000 from Period04.

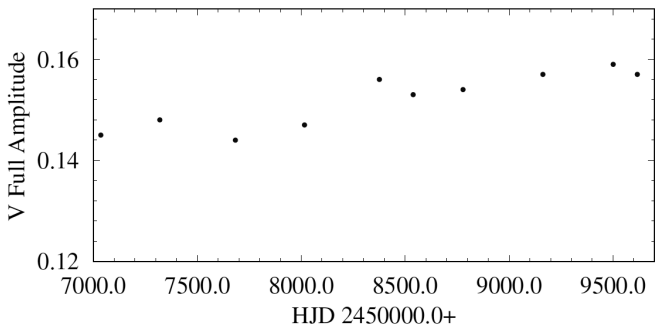

Figure 8. Full amplitude of the primary frequency as a function of time.

we find an amplitude of 0.144 in the V filter compared to 0.121 in the ATLAS o filter. At JD2458800 we have a V amplitude of 0.154 and a TESS amplitude of 0.091. Finally, we compare the ASAS-SN g observations with an amplitude of 0.173 to the V amplitude of 0.157. In all cases the bluer filter shows the higher amplitude that is normal for pulsating variable stars.

4. Conclusion

After an analysis of ATLAS 30 (ATO J031.2309+52.9923) we find that it is a non-radial δ Scuti variable with a fundamental frequency of f= 14.34546 c d^{-1}, or a period of 0.069705552 d. In addition, there is some evidence that this star is experiencing a period change of $(1/P)(dP/dt) = -340 \times 10^{-8}$ yr^{-1}. This is similar to values found for non-radial δ Scuti variables from previous publications. However, the detection of a period change is right at the 3σ level and will need to be confirmed by additional observations. A second period is also found at 0.073801 d. This gives a period ratio of $P_1/P_2 = 0.945$, which is similar to that found by Handler *et al.* (1998) for XX Pyx, which is a non-radial pulsator. Radial pulsators tend to have period ratios greater than 1.

An examination of all available data sets shows that the ATLAS data were able to accurately determine the primary frequency, but didn't recover the additional frequencies reported here. Therefore, those data alone could not fully characterize the object. The case was the same for g data from the ASAS-SN program. While the V data did recover the first harmonic ($2f_1$), they did not recover the two additional frequencies. Our high density data and the consistent data from TESS both recovered four clear frequencies.

We find that while the ASAS-SN program has labeled this star as a high amplitude δ Scuti, it really doesn't fit that characterization. The average amplitude in the V filter of 0.150 is below the general cut-off for HADS and the light curve shape isn't typical. The object also doesn't fall into the LADS category with amplitudes below 0.1. This object is typical of the in-between group of objects that have medium amplitudes such as AN Lyncis (Rodriguez *et al.* 1997; Zhou *et al.* 2017). Perhaps the best description is a medium amplitude δ Scuti, as it is called by Rodriguez *et al.* (1997).

5. Acknowledgements

We acknowledge the Brigham Young University, Department of Physics and Astronomy for their continued support of our research efforts. We wish to thank Maureen Hintz for her editorial help. We acknowledge a grant from the Theodore H. Dunham Fund for Astrophysical Research which has been used to help equip the BYU campus observatory. This research was also supported in part by NASA through the American Astronomical Society's Small Research Grant Program.

This publication makes use of data products from the Wide-field Infrared Survey Explorer, which is a joint project of the University of California, Los Angeles, and the Jet Propulsion Laboratory/California Institute of Technology, funded by the National Aeronautics and Space Administration. This publication makes use of data products from the Wide-field Infrared Survey Explorer, which is a joint project of the University of California, Los Angeles, and the Jet Propulsion Laboratory/California Institute of Technology, funded by the National Aeronautics and Space Administration. This publication makes use of data products from the Two Micron All Sky Survey, which is a joint project of the University of Massachusetts and the Infrared Processing and Analysis Center/California Institute of Technology, funded by the National Aeronautics and Space Administration and the National Science Foundation.

Facilities: TESS,MAST,BYU:0.2m,BYU:0.3m

References

Bai, Y., Liu, J., Bai, Z., Wang, S., and Fan, D. 2019, *Astron. J.*, **158**, 93.

Bailer-Jones, C. A. L., Rybizki, J., Fouesneau, M., Demleitner, M., and Andrae, R. 2021, *Astron. J.*, **161**, 147.

Breger, M. 1990, *Astron. Astrophys.*, **240**, 308.

Breger, M. and Pamyatnykh, A. A. 1998, *Astron. Astrophys.*, **332**, 958.

Collins, K. A., Kielkopf, J. F., Stassun, K. G., and Hessman, F. V. 2017, *Astron. J.*, **153**, 77.

Cutri, R. M., *et al.* 2003, VizieR Online Data Catalog: 2MASS All-Sky Catalog of Point Sources (2003yCat.2246....0C).

Cutri, R. M., *et al.* 2014, VizieR Online Data Catalog: AllWISE Data Release (2014yCat.2328....0C).

Foster, G. 1995, *Astron. J.*, **109**, 1889.

Handler, G., Pamyatnykh, A. A., Zima, W., Sullivan, D. J., Audard, N., and Nitta, A. 1998, *Mon. Not. Roy. Astron. Soc.*, **295**, 377.

Heinze, A. N., *et al.* 2018, *Astron. J.*, **156**, 241.

Kochanek, C. S., *et al.* 2017, *Publ. Astron. Soc. Pacific*, **129**, 104502.

Lenz, P., and Breger, M. 2005, *Commun. Asteroseismology*, **146**, 53.

Paunzen, E., and Vanmunster, T. 2016, *Astron. Nachr.*, **337**, 239.

Rodriguez, E., Gonzalez-Bedolla, S. F., Rolland, A., Costa, V., and Lopez de Coca, P. 1997, *Astron. Astrophys.*, **324**, 959.

Shappee, B. J., *et al.* 2014, *Astrophys. J.*, **788**, 48.

Stassun, K. G., *et al.* 2019, *Astron. J.*, **158**, 138.

Zhou, A.-Y., *et al.* 2017, arXiv:1710.03944.

A Photometric Study of the Eclipsing Binary BO Leporis

Edward J. Michaels
Waffelow Creek Observatory, 10780 FM 1878, Nacogdoches, TX 75961; astroed@ejmj.net

Received June 7, 2022; revised June 27, 2022; accepted June 27, 2022

Abstract Multi-band photometric observations of the Algol-type binary BO Lep are presented. The visual light curve displays a 1.7-magnitude deep primary eclipse and a shallow 0.2-magnitude secondary eclipse. Photometric light curve solutions were obtained using the Wilson-Devinney program which describe a semidetached configuration with a mass ratio of $M_2/M_1 = 0.510$, an inclination of i = 86.7°, and a temperature difference of $\Delta T = 2042$ K between the F2 and K3 component stars. The filling factor for the primary star is 72% and 99% for the secondary. A small asymmetry in the light curves was modeled with a cool spot located on the secondary star. New linear and quadratic ephemerides were computed, giving an orbital period of 0.80625824 d that is decreasing at a rate of -1.55×10^{-7} d yr^{-1}.

1. Introduction

The variability of BO Lep (GSC 05352-00074, TYC 5352-74-1) was first seen in sky patrol plates taken at the Bamberg Southern Station (Strohmeier 1967). More recent surveys have also identified the changing light of this star. These include the Northern Sky Variability Survey (NSVS), the All-Sky Automated Survey (ASAS), and the Catalina Sky Surveys (CSS) (Woźniak *et al.* 2004; Pojmański 2002; Drake *et al.* 2014). BO Lep was included in a catalog (compiled from CSS data) of northern eclipsing binaries with Algol-type light curves (Papageorgiou *et al.* 2018). This catalog gives an orbital period of 0.8062561 d and an eclipse amplitude of 1.405 magnitude. Using machine-learning algorithms Papageorgiou *et al.* (2018) classified each cataloged EA-type eclipsing binary as detached (D) or semidetached (SD). Of the 4,050 stars in the catalog (their Table 1), 4% received an uncertain classification (D/SD). BO Lep was in this group.

Eclipsing binary stars provide a means for determining fundamental stellar properties if accurate measurements are available. In this paper a photometric study of BO Lep is presented using precision high cadence observations. The observations and data reduction methods are presented in section 2. A period analysis is presented in section 3. Analysis of the light curves using the Wilson-Devinney model is presented in section 4. Discussion of the results is presented in section 5, and conclusions are presented in section 6.

2. Photometric observations

Photometric observations were acquired at the Waffelow Creek Observatory, Nacogdoches, Texas, using a 0.36-m Ritchey-Chrétien robotic telescope and a SBIG-STXL camera with a cooled KAF-6303E CCD (−20° C, 9-µm pixels). This data was collected on 17 nights in November and December 2021 and January 2022. Images were obtained in four passbands each night: Johnson V and Sloan g', r', and i'. The observation dates and number of images acquired are shown in the observation log (Table 1). The images were calibrated using bias, dark, and flat frames. MIRA software (Mirametrics 2015) was used for image calibration and the ensemble differential aperture photometry of the light images. The locations of the comparison and check stars are shown in Figure 1, and Table 2 gives their coordinates and standard magnitudes. The first comparison star in Table 2 (C1, GSC 05352-00056) is located only 19.4" to the SE of BO Lep and is approximately the same brightness. Each night, the seeing profile of these two stars was checked to verify that there was no blending of light in the sky and target annuli. It is interesting to note that the proper motion of these two stars is nearly the same in both R.A. and Dec. (EDR3 data; Gaia Collaboration *et al.* 2021). Gaia parallaxes

Table 1. Observation log.

Filter	*Dates*	*No. Nights*	*No. Images*
V, g', r', i'	2021 Nov 4–7	4	966
V, g', r', i'	2021 Nov 11–15	5	1217
V, g', r', i'	2021 Nov 22, 23, 29, 30	4	875
V, g', r', i'	2021 Dec 11, 12	2	478
V, g', r', i'	2022 Jan 16, 17	2	496

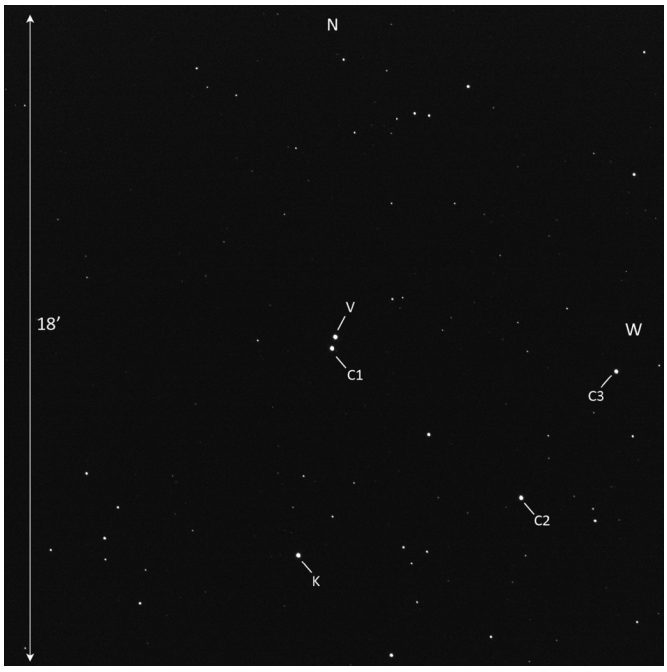

Figure 1. Finder chart for BO Lep (V), comparison (C1, C2, and C3) stars, and check (K) stars.

Table 2. APASS comparison and check star magnitudes.

Star	R. A. (2000) h	Dec. (2000) °	V	g′	r′	i′
BO Lep	5.880978	–11.05331	—	—	—	—
GSC 05352-00056 (C1)	5.881077	–11.05811	11.551	11.992	11.420	11.241
GSC 05352-00007 (C2)	5.875297	–11.12670	11.710	12.040	11.590	11.412
GSC 05325-00042 (C3)	5.882182	–11.15182	11.639	11.969	11.511	11.329
GSC 05325-00062 (K)	5.893910	–11.18185	11.541	11.848	11.378	11.292
Standard deviation of K-star magnitudes			± 0.006	± 0.007	± 0.006	± 0.006

Table 3. Average light-curve properties.

	Min I Mag.	Min II Mag.	Δ Mag. Min II – Min I	Max I Mag.	Max II Mag.	Δ Mag. Max II – Max I	Mag. Range Max II – Min I
V	12.954 ± 0.003	11.475 ± 0.005	1.479 ± 0.006	11.246 ± 0.003	11.250 ± 0.002	0.003 ± 0.004	1.705 ± 0.004
g'	13.420 ± 0.002	11.730 ± 0.001	1.689 ± 0.003	11.524 ± 0.001	11.527 ± 0.003	0.003 ± 0.003	1.893 ± 0.004
r'	12.715 ± 0.003	11.436 ± 0.003	1.279 ± 0.004	11.177 ± 0.002	11.181 ± 0.003	0.005 ± 0.004	1.533 ± 0.004
i'	12.409 ± 0.002	11.350 ± 0.003	1.059 ± 0.003	11.048 ± 0.002	11.055 ± 0.003	0.007 ± 0.003	1.354 ± 0.004

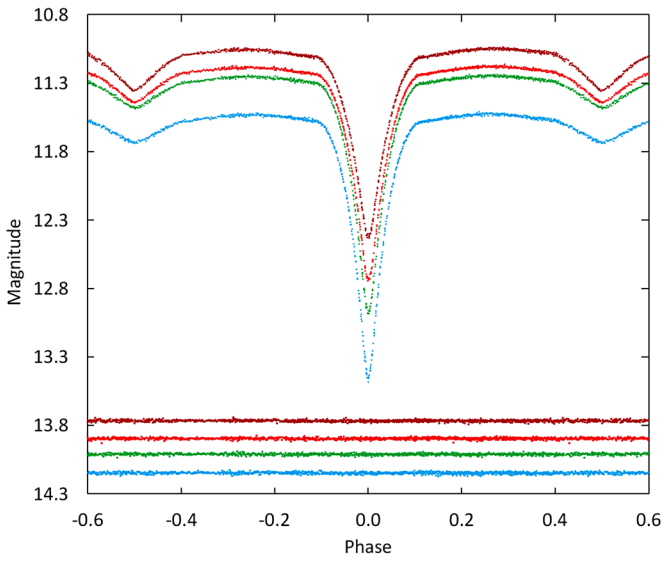

Figure 2. The folded CCD light curves in standard magnitudes. From top to bottom the passbands are i', r', V, and g'. In the same order, the bottom curves are the check-star magnitudes with offsets of +2.5, +2.5, +2.3, and +2.5 magnitudes, respectively. Error bars were omitted from the plotted points for clarity.

Table 4. Times of minima and O – C residuals.

Method	Epoch HJD 2400000+	Error	Cycle No.	O – C	Reference
ccd	51534.7138	0.0008	–2313.0	–0.00172	1
ccd	51535.1138	0.0032	–2312.5	–0.00494	1
ccd	52067.6529	0.0018	–1652.0	0.00150	1
ccd	52068.0543	0.0021	–1651.5	–0.00029	1
ccd	52810.2156	0.0011	–731.0	0.00147	1
ccd	52810.6169	0.0016	–730.5	–0.00034	1
ccd	53399.5880	—	0.0	0.00000	2
ccd	53624.5390	0.0018	279.0	0.00529	1
ccd	* 53624.9272	0.0051	279.5	–0.00966	1
ccd	54343.7170	0.0014	1171.0	0.00206	1
ccd	* 54344.1134	0.0171	1171.5	–0.00471	1
ccd	54538.0225	—	1412.0	–0.00041	3
ccd	54863.7504	0.0001	1816.0	–0.00031	4
ccd	54884.7161	0.0006	1842.0	0.00272	1
ccd	* 54885.1012	0.0168	1842.5	–0.01536	1
ccd	55528.9207	0.0004	2641.0	0.00796	5
ccd	55958.6515	0.0007	3174.0	0.00378	6
ccd	56265.8354	0.0005	3555.0	0.00377	7
ccd	56658.4813	0.0004	4042.0	0.00253	1
ccd	59523.9169	0.0001	7596.0	0.00075	8
ccd	59532.7858	0.0001	7607.0	0.00083	8
ccd	59548.9110	0.0001	7627.0	0.00086	8
ccd	59561.8112	0.0001	7643.0	0.00098	8
ccd	59597.6910	0.0006	7687.5	0.00231	8

** Outliers not used in the period analysis. References: (1) Zasche* et al. *(2014); (2) Watson* et al. *(2014); (3) Papageorgiou* et al. *(2018); (4) Diethelm (2009); (5) Diethelm (2011); (6) Diethelm (2012); (7) Diethelm (2013); (8) this paper.*

indicate BO Lep is 104 pc closer (Bailer-Jones *et al.* 2021), thus the pair is an optical double. The standard magnitudes of the comparison stars were taken from the AAVSO Photometric All-Sky Survey database (APASS; Henden *et al.* 2015). The instrumental magnitudes were converted to standard magnitudes using the APASS comparison star magnitudes. The Heliocentric Julian Date (HJD) of each observation was converted to orbital phase (φ) using the following epoch and orbital period: T_0 = 2459597.2866 and P = 0.80625424 d. Figure 2 shows the folded light curves plotted from orbital phase −0.6 to 0.6, with negative phase defined as (φ − 1). The error of a single observation ranged from 5 to 10 mmag. The check star magnitudes were plotted and inspected each night, but no significant variability was found (see bottom of Figure 2). The light curve properties for each passband are given in Table 3 (Min I, Min II, Max I, Max II, Δm). The observations can be accessed from the AAVSO International Database (Kafka 2017).

3. Period analysis and ephemerides

New times of minima were calculated from the observations using the Kwee and van Woerden (1956) method. The Heliocentric Julian Dates (HJD) of these minima are reported in Table 4, along with an additional 19 minima times found in the literature. The initial linear ephemeris for this period study was taken from Diethelm (2009) and is given by:

$$\text{HJD Min I} = 245399.588 + 0.806257\ E. \quad (1)$$

The differences between the observed and predicted minima times using this ephemeris are tabulated in the O − C column of Table 4. Before computing new ephemerides, the following three outliers were removed from the data set: cycles 279.5, 1171.5, and 1842.5. A least-squares solution of the Equation 1 residuals gives the following new linear ephemeris:

$$\text{HJD Min I} = 2453399.5890\ (2) + 0.80625721\ (4)\ E. \quad (2)$$

The top panel of Figure 3 shows the residuals (dots) calculated from Equation 1, with the dashed line the linear best-fit of Equation 2. The coefficient of determination from this regression, R^2 = 0.080, is quite low, indicating this ephemeris may not be reliable in predicting future primary eclipses. The orbital period may be undergoing a long-term linear period change, which is most often attributed to mass transfer or angular momentum loss due to magnetic braking. A second least-squares solution of the Equation 1 residuals gives the following quadratic ephemeris:

$$\text{HJD Min I} = 2453399.5896\,(1) + 0.80625824\,(6)\,E - 1.7\,(1)\times 10^{-10}\,E^2. \quad (3)$$

The coefficient of determination from this regression is considerably higher compared to the linear fit, with a value of R^2 = 0.518. The middle panel of Figure 3 shows the O − C residuals (dots) from Equation 1 and the quadratic ephemeris fit from Equation 3 (dashed line). The bottom panel of Figure 3 displays the residuals from the quadratic fit. The negative quadradic coefficient of Equation 3 indicates the orbital period is slowly decreasing. The rate of period change was calculated using the following equation:

$$dP/dt = (2Q/P)\cdot 365.24. \quad (4)$$

The orbital period is decreasing at a rate of $-1.55\,(9)\times 10^{-7}$ d yr^{-1}[7], or about 1.34 seconds per century.

4. Light curve analysis

4.1. Color, temperature, spectral type, and absolute magnitude

There are no spectroscopic measurements available for this binary, therefore an estimate of the primary star's effective temperature was determined from the photometric color data. For measuring color change and Roche modeling, the large number of photometric observations were binned in both phase and magnitude. This resulted in 125 normal points for each color with a phase width of 0.008. The phases and magnitudes of the observations in each bin were averaged. For color index, the binned r' magnitudes were then subtracted from the linearly interpolated g' magnitudes. The binned points of the r' light curve and the (g' − r') color index are shown in Figure 4 (bottom panel). The large difference in eclipse depths indicates the primary and secondary stars have very different temperatures. Over one orbital period, these temperature differences cause the large color change seen in Figure 4. The color index ranged from (g' − r') = 0.699 ± 0.003 at primary minimum to (g' − r') = 0.293 ± 0.004 at secondary minimum. Even though the eclipses are not quite total, a reasonable estimate for the primary star's effective temperature can be found by using the observed color at secondary eclipse (φ = 0.5). At this orbital phase the secondary star's contribution to the total system light is at a minimum. The color excess for this system is E(g' − r') = 0.11 ± 0.06 and E(B − V) = 0.097 ± 0.05. These values were determined from dust maps based on Pan-STARRS1 and 2MASS photometry and Gaia parallaxes (Green *et al.* 2018). Subtracting the color excess from the observed color at secondary eclipse gives the primary star's approximate intrinsic color, $(g' - r')_0$ = 0.18 ± 0.06. The effective temperature and spectral type for this color are T_{eff} = 6848 ± 187 K and F2, respectively (Pecaut and Mamajek 2013). This effective temperature is in good agreement with a value determined using Gaia EDR3 data, T_{eff} = 6781 ± 105 K (Anders *et al.* 2022). The absolute visual magnitude at quadrature (φ = 0.25), M_v = 3.1 ± 0.3, was calculated using the Gaia distance (d = 367 ± 42 pc) and the apparent visual magnitude corrected for extinction (m_v = 10.9 ± 0.2) (Bailer-Jones *et al.* 2021; Gaia Collaboration *et al.* 2016, 2018).

4.2. Synthetic light-curve modeling

For light curve modeling, 125 normal points were created from observations in the V, g', r', and i' passbands (see section 4.1). On average each normal point was formed from eight observations. The normal points were converted from magnitudes to relative flux for light curve modeling. Preliminary fits to each light curve were obtained using the Binary Maker 3.0 program (BM3; Bradstreet and Steelman 2002). The effective temperature of the primary star was fixed at 6848 K and

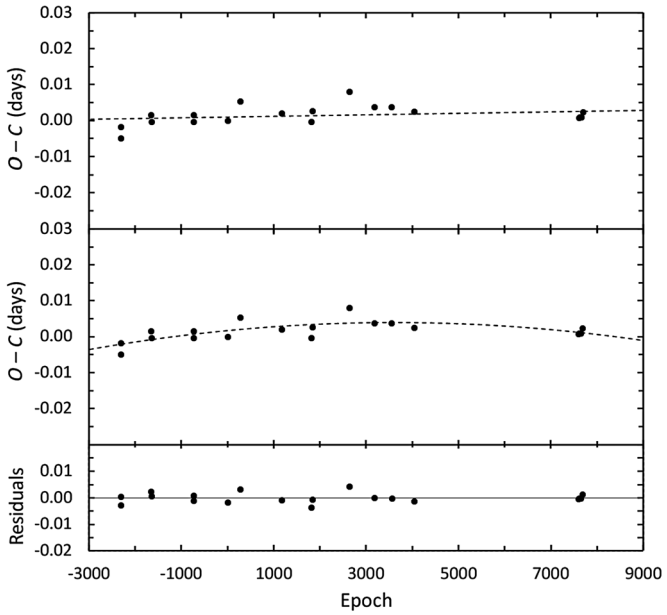

Figure 3. The top panel shows the O – C residuals (dots) from Equation 1 with the dashed line the linear best–fit of Equation 2. The middle panel shows the quadratic best–fit of Equation 3 (dashed line) to the Equation 1 residuals. The bottom panel shows the residuals from the quadratic fit.

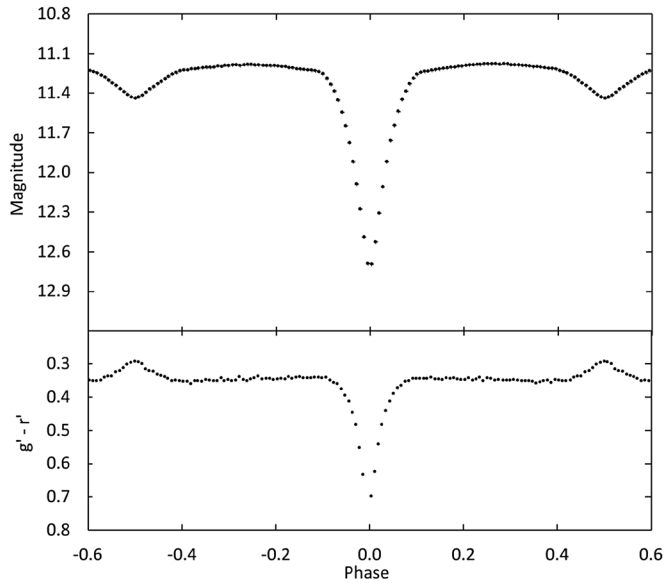

Figure 4. Light curve of the binned Sloan r' passband observations in standard magnitudes (top panel). The observations were binned with a phase width of 0.008. The errors for each binned point are approximately the size of the plotted points. The (g' – r') colors were calculated by subtracting the linearly interpolated binned g' and r' magnitudes.

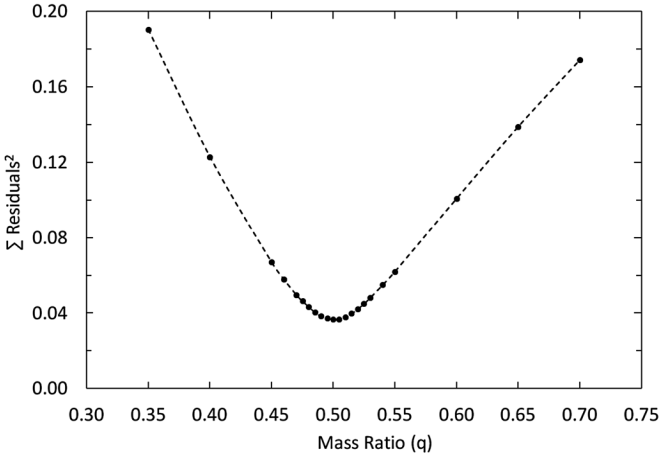

Figure 5. Results of the q-search showing the relation between the sum of the residuals squared and the mass ratio q.

Table 5. Results derived from light-curve modeling.

Parameter	*Mode-2: No Spots*	*Mode-2: Spot*	*Mode-5: Spot*
i (°)	86.57 ± 0.12	86.70 ± 0.08	86.58 ± 0.09
T_1 (K)	[1]6848	[1]6848	[1]6848
T_2 (K)	4801 ± 29	4806 ± 22	4809 ± 20
Ω_1	3.803 ± 0.020	3.752 ± 0.015	3.806 ± 0.018
Ω_2	2.904 ± 0.006	2.906 ± 0.016	[2]2.876
$q(M_2 / M_1)$	0.511 ± 0.002	0.510 ± 0.005	0.500 ± 0.005
$L_1/(L_1+L_2)$ (V)	0.841 ± 0.006	0.845 ± 0.005	0.838 ± 0.005
$L_1/(L_1+L_2)$ (g')	0.871 ± 0.006	0.877 ± 0.005	0.868 ± 0.005
$L_1/(L_1+L_2)$ (r')	0.810 ± 0.007	0.815 ± 0.006	0.807 ± 0.005
$L_1/(L_1+L_2)$ (i')	0.773 ± 0.007	0.777 ± 0.006	0.770 ± 0.006
r_1 side	0.323 ± 0.002	0.318 ± 0.001	0.315 ± 0.001
r_2 side	0.309 ± 0.002	0.311 ± 0.005	0.313 ± 0.001
x_1 (V)	0.62 ± 0.05	0.68 ± 0.03	0.63 ± 0.03
x_1 (g')	0.77 ± 0.05	0.81 ± 0.03	0.79 ± 0.03
x_1 (r')	0.41 ± 0.06	0.47 ± 0.04	0.42 ± 0.04
x_1 (i')	0.13 ± 0.07	0.19 ± 0.05	0.12 ± 0.05
x_2 (V)	0.84 ± 0.08	0.89 ± 0.06	0.84 ± 0.06
x_2 (g')	0.88 ± 0.10	0.96 ± 0.08	0.88 ± 0.07
x_2 (r')	0.69 ± 0.06	0.74 ± 0.05	0.69 ± 0.05
x_2 (i')	0.41 ± 0.07	0.45 ± 0.06	0.41 ± 0.06
Residuals	0.00021	0.00018	0.00019
Star 2		*Cool Spot*	*Cool Spot*
colatitude (°)	—	79 ± 13	79 ± 13
longitude (°)	—	330 ± 4	329 ± 4
spot radius (°)	—	12 ± 4	12 ± 4
temp. factor	—	0.85 ± 0.11	0.86 ± 0.11

Note: The errors in the stellar parameters result from the least–squares fit to the model. The actual uncertainties are considerably larger. The subscripts 1 and 2 refer to the star being eclipsed at primary and secondary minimum, respectively. [1] Assumed. [2] Calculated.

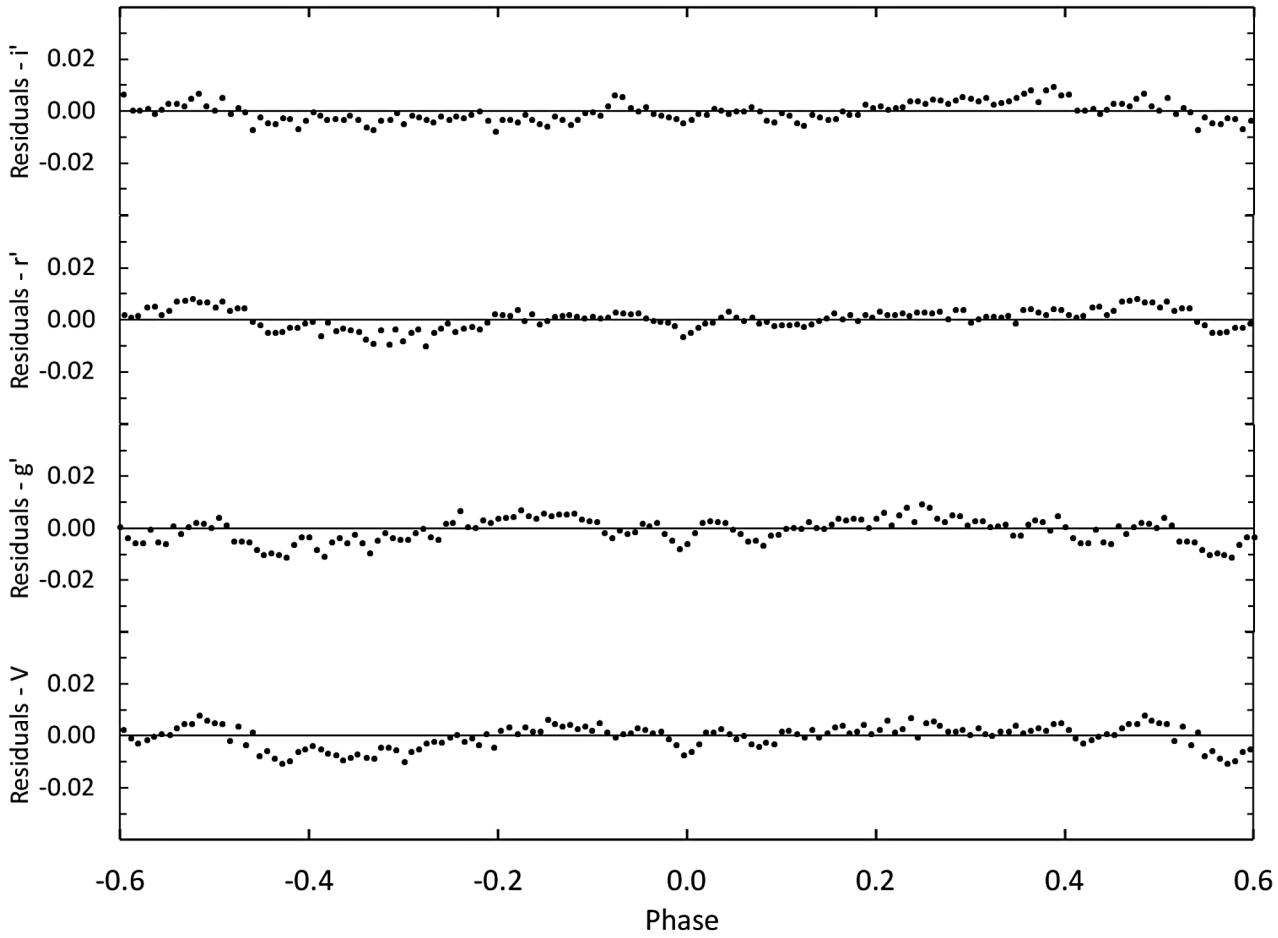

Figure 6. The residuals for the best-fit Mode-2 WD spotless model. Error bars are omitted from the points for clarity.

standard convective parameters were used for gravity darkening and bolometric albedo. Linear limb darkening coefficients were taken from van Hamme's (1993) tabular values. The other parameters—inclination, mass ratio, potentials, and secondary star temperature—were adjusted in sequence until a good fit was obtained between the synthetic light curves and the observations for each passband. The parameters resulting from each light curve fit were averaged. These averages were used as the initial input parameters for the computation of a simultaneous 4-color light curve solution using the 2015 version of the Wilson-Devinney (WD) program (Wilson and Devinney 1971; van Hamme and Wilson 1998).

The observed light curves display a deep partial primary eclipse, a shallow secondary minimum, and small changes in light outside of the eclipses (see Figure 2). This light curve morphology is characteristic of an Algol-type eclipsing binary. The components are often in a detached configuration with spherical or slightly elliptical components, but some are semidetached with one star filling its Roche lobe. Since the configuration of this system is unknown, the WD program was configured to Mode-2 for detached binaries. For modeling, the Kurucz (2002) stellar atmosphere radiation formulas were utilized, and the primary star's effective temperature was fixed at T_1 = 6848 K (see section 4.1). The subscripts 1 and 2 refer to the hotter and cooler components, respectively. Since both component temperatures are less than 7500 K, the internal energy transfer to the surface is due to convection rather than radiative transfer. Gravity brightening and bolometric albedo were therefore set to their standard convective values for modeling, $g_1 = g_2 = 0.32$ (Lucy 1968) and $A_1 = A_2 = 0.5$ (Ruciński 1969), respectively. The adjustable parameters include the inclination (i), mass ratio ($q = M_2/M_1$), potentials (Ω_1, Ω_2), secondary star effective temperature (T_2), band-specific luminosities for each wavelength (L), linear limb-darkening coefficients (x1, x2), and third light (l). The mass ratio cannot be determined directly, since radial velocity measurements are not available for this system. A reliable q value can also be obtained from a photometric solution, but only if the eclipses are total (Wilson 1978; Terrell and Wilson 2005). Since the eclipses are partial, a q-search was necessary to find the most likely mass ratio. A series of WD solutions were completed with each using a fixed mass ratio that ranged from 0.35 to 0.70. The relation between the $\Sigma Residuals^2$ and the q values is shown in Figure 5. The minimum residual value was located at q = 0.502. This value was used as the starting mass ratio for subsequent solution iterations where the mass ratio was an adjustable parameter. The final Mode-2 solution parameters are shown in column 2 of Table 5. The residuals from this solution (see Figure 6) show a small loss of light in each color between orbital phase 0.5 and 0.8. This type of asymmetry is often attributed to spotting in the photospheres of low mass stars. To fit the asymmetry, several spot configurations were modeled with BM3.

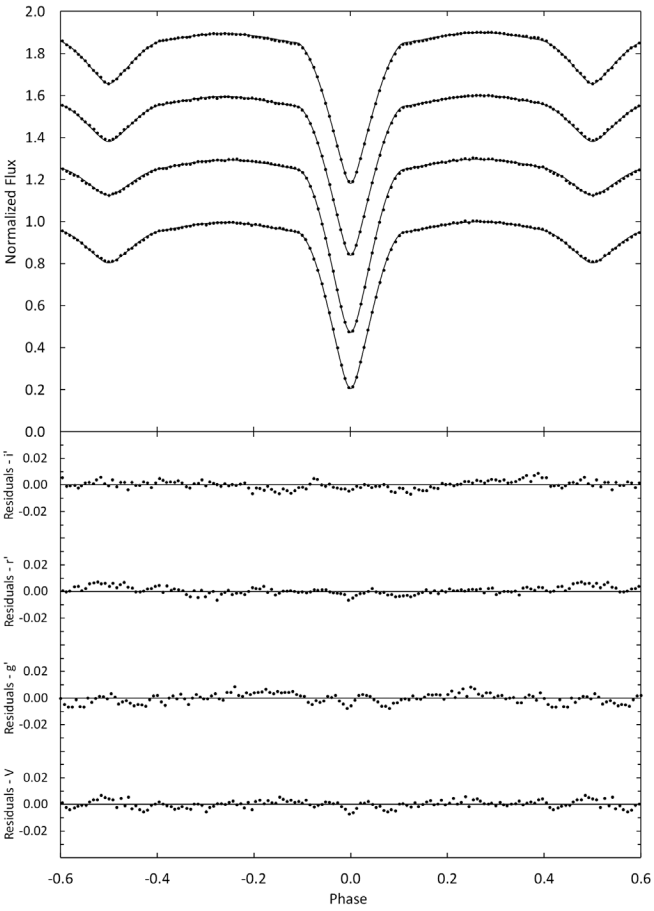

Figure 7. Comparison between the WD spotted best-fit model (solid curve) and the observed normalized flux curve. From top to bottom, the passbands are i', r', g', and V. Each light curve is offset by 0.30 for this combined plot. The residuals are shown in the bottom panel. Error bars are omitted from the points for clarity.

Table 6. Provisional absolute parameters.

Parameter	*Symbol*	*Value*
Stellar masses	M_1 ($M_\odot$)	1.47 ± 0.04
	M_2 ($M_\odot$)	0.73 ± 0.02
Semi–major axis	a ($R_\odot$)	4.74 ± 0.03
Mean stellar radii	R_1 ($R_\odot$)	1.49 ± 0.01
	R_2 ($R_\odot$)	1.51 ± 0.03
Bolometric magnitude	$M_{bol,1}$	3.1 ± 0.1
	$M_{bol,2}$	4.6 ± 0.2
Stellar luminosity	L_1 ($L_\odot$)	4.4 ± 0.4
	L_2 ($L_\odot$)	1.1 ± 0.2
Absolute visual magnitude	$M_{V,1}$	3.2 ± 0.1
	$M_{V,2}$	5.2 ± 0.2
Surface gravity	log g_1 (cgs)	4.26 ± 0.01
	log g_2 (cgs)	3.95 ± 0.01

Note: The calculated values in this table are provisional. Radial velocity observations are necessary for direct determination of M_1, M_2, and a.

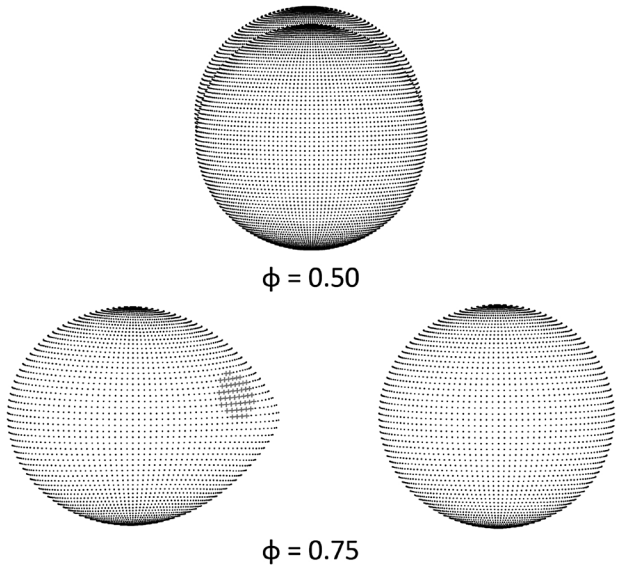

Figure 8. Roche lobe surfaces of the best–fit WD spot model showing spot locations. The orbital phase is shown below each diagram.

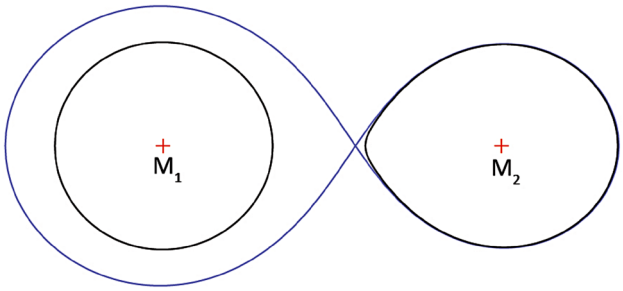

Figure 9. Roche configuration of BO Lep in the orbital plane. The blue line denotes the critical lobe and the black lines the potential surfaces of the two stars for the Mode-2 detached solution.

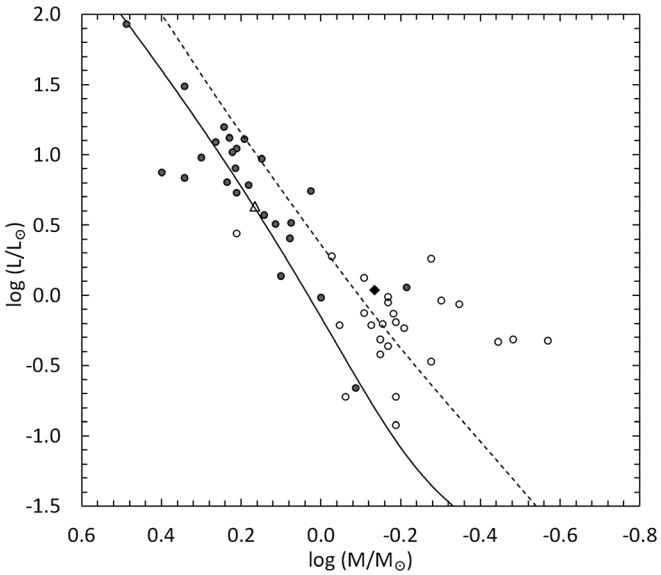

Figure 10. Positions of both components of BO Lep on the Mass-Luminosity diagram of 25 semidetached NCB binaries with well-determined parameters. Filled circles are the primary stars and open circles the secondary stars. The triangle and the diamond are the primary and the secondary of BO Lep, respectively. Solid and dotted lines refer to ZAMS and TAMS, respectively (Tout *et al.* 1996).

The spot parameters, latitude, longitude, spot size and temperature factor were adjusted until the asymmetry was minimalized. The best-fit spot parameters were then incorporated into a new Mode-2 WD model. The final solution parameters for the WD spot model are shown in column 3 of Table 5.

The Mode-2 solutions resulted in a semidetached configuration with the cooler less massive secondary star nearly filling its Roche lobe. A final solution was therefore attempted with the WD program set to Mode-5. This mode is often used for semidetached Algol systems. The secondary star's potential (Ω_2) is not adjustable in this mode since it is constrained to exactly fill its Roche lobe during solution iterations. The best-fit final parameters for this solution are shown in column 4 of Table 5. The two sets of solution parameters (Mode-2 and Mode-5) are mostly the same within the margin of errors. The only exceptions are small differences in Ω_2 and q, which is not unexpected given the constraint placed on the secondary component's potential in Mode-5. Figure 7 displays the normalized light curves overlaid by the synthetic Mode-5 solution curves (solid line), with the residuals in the bottom panel. The residuals were reduced by 10% compared to the spotless model. A graphical representation of the spotted model is shown in Figure 8. It should be noted that throughout the solution process, the third-light corrections were negligibly small and often negative. This result likely rules out a bright third body in the system but does not eliminate the possibility for a low luminosity red or brown dwarf star.

5. Discussion

Spectroscopic observations are not available for the direct determination of the orbital and stellar parameters, but provisional values can be estimated using the photometric solution's mass ratio and the mass of one component of the binary. The primary components of Algol systems are typically main sequence stars whose masses can be estimated from their spectral type. Using the primary star's effective temperature, a provisional mass of $M_1 = 1.47 \pm 0.04\ M_\odot$ was interpolated from Table 5 of Pecaut and Mamajek (2013). Combining this mass with the mass ratio gives a secondary mass of $M_2 = 0.73 \pm 0.02\ M_\odot$. Applying Kepler's Third Law gives a distance of $4.74 \pm 0.03\ R_\odot$ between the mass centers of the two stars. The bolometric magnitudes and luminosities were calculated using the solar values $T_{eff\odot} = 5771.8 \pm 0.7$ K and $M_{bol\odot} = 4.74$. The bolometric corrections, $BC_{V1} = -0.004$ for the primary star and $BC_{V1} = -0.390$ for the secondary, were interpolated from Table 5 of Pecaut and Mamajek (2013). The absolute visual magnitudes were computed using these bolometric corrections. All the provisional stellar parameters are collected in Table 6. A distance of 377 ± 70 pc was derived based on this system's visual luminosity, the apparent magnitude, and interstellar extinction ($A_V = 0.30 \pm 0.16$). This is consistent with the distance determined from the Gaia parallax (367-pc).

The observed light curves and the photometric solution indicate BO Lep is a semidetached binary where the less massive secondary star fills (or nearly fills) its Roche lobe while the primary star is inside its lobe. The filling factor measures how close the stars are to filling their respective Roche lobes. The filling factor of the primary star is defined as $f_1 = R_1 / R_L$, where R_1 is the radius of the primary and R_L is the volume radius of the Roche lobe calculated using Eggleton's (1983) formula,

$$\frac{R_L}{a} = \frac{0.49q^{\frac{2}{3}}}{0.6q^{\frac{2}{3}} + \ln\left(1 + q^{\frac{1}{3}}\right)}, \quad (5)$$

where a is the distance separating the mass centers and q the mass ratio. Using the Mode-2 solution radii, the filling factor for the primary star is 72%. The secondary filling factor, 99%, was calculated using a similar equation for R_L/a. Figure 9 shows the Roche surfaces with the nearly filled secondary lobe. Semidetached systems with orbital periods of less than one day and with a large filling factor primary star are described as near-contact binaries (NCB) (Yakut and Eggleton 2005). Figure 10 shows a mass luminosity diagram (M-L) of the components of 25 NCBs with well determined parameters (Yakut and Eggleton 2005). Included in this diagram are the components of BO Lep, the zero-age main sequence line (ZAMS), and the terminal-age main sequence line (TAMS). The NCB primary stars are mostly located along the ZAMS, which supports the assignment of this classification to the primary component of BO Lep. The secondaries are mostly close to or above the TAMS, which means these stars have evolved. The secondary of BO Lep is larger and more luminous than main sequence stars of the same mass, and its location above the TAMS indicates it is also an evolved star.

In the current epoch, BO Lep consists of a less massive but more evolved secondary star, and a more massive but less evolved primary. Theoretical modeling indicates NCBs and contact binaries (CB) form from detached young cool stars with initial orbital periods of about two days (Stepień and Kiraga 2013; Stepień 2011). As the primary star begins to evolve near the end of its main sequence lifetime, combined with mass and angular momentum loss over that same period, Roche lobe overflow will eventually occur. Mass transfer will then cause a reversal in the mass ratio, forming either a CB or NCB. BO Lep is currently at the NCB stage of its evolution. From the period analysis, the downward parabolic trend in the O−C diagram indicates a decreasing orbital period, which implies a nonconservative mass-loss process. For low mass stars this process could result from magnetic braking which is caused by a coupling between the magnetic field and the stellar winds. Magnetic braking will cause a loss of mass and angular momentum that would decrease the orbital period and shrink the orbit. The spot modeled on the secondary star supports current magnetic activity. Conservative mass transfer from the less massive star to the more massive component will have the opposite effect, causing a continuously increasing orbital period and an expanding orbit. The Mode-2 photometric solution indicates the secondary may only be marginally in contact with the Roche surface, thus limiting significant matter transfer through the L_1 point. Due to the proximity of the two stars, a significant mass transfer rate would cause the matter stream to directly impact the primary star, forming a hot spot. The excess light from this spot would form a noticeable hump in the light curves. This asymmetry is not seen and is another indication that mass transfer is presently not active or is occurring at a low rate. It is also possible the decreasing period results from

a combination of mass transfer and wind-driven mass loss. In semidetached systems, these two mechanisms may be strongly competitive (Nanouris *et al.* 2011, 2015; Erdem and Öztürk 2014). Whether BO Lep evolves into a contact binary or an Algol binary will depend on which one of these two mechanisms dominates.

6. Conclusions

The acquisition of precision photometric observations for the eclipsing binary BO Lep resulted in complete light curves in the V, g', r', and i' bands and six new minimum timings. The light curves displayed deep primary and shallow secondary eclipses. Photometric light curve solutions using the WD program found a semidetached configuration with a lower mass secondary star filling its Roche lobe, a mass ratio of q = 0.510, and an orbital inclination of i = 86.6°. The primary component is a main sequence star with a spectral type of F2 and an evolved K3 secondary star. A cool spot on the secondary was included in the final Roche model to address an asymmetry in the light curves. Provisional stellar properties were computed based on the assumption that the primary star has a "normal" main sequence mass for its spectral type. A period analysis resulted in updated ephemerides and revealed an orbital period that is decreasing. This period change results from magnetic braking or a combination of magnetic braking and mass transfer. This NCB will eventually evolve into a contact or an Algol-type binary. A spectroscopic study of this system is required to confirm and update the stellar masses presented in this study and to provide a revised spectral type for the primary star.

7. Acknowledgements

This research was made possible through use of the AAVSO Photometric All-Sky Survey (APASS), funded by the Robert Martin Ayers Sciences Fund. This research has made use of the SIMBAD database and the VizieR catalog access tool, operated at CDS, Strasbourg, France. This work has made use of data from the European Space Agency (ESA) mission Gaia (https://www.cosmos.esa.int/gaia), processed by the Gaia Data Processing and Analysis Consortium (DPAC). Funding for DPAC has been provided by national institutions, in particular the institutions participating in the Gaia Multilateral Agreement (DPAC, https://www.cosmos.esa.int/web/gaia/dpac/consortium).

References

Anders, F., *et al.* 2022, *Astron. Astrophys.*, **658A**, 91.
Bailer-Jones, C. A. L., Rybizki, J., Fouesneau, M., Demleitner, M., and Andrae, R. 2021, *Astron. J.*, **161**, 147.
Bradstreet, D., and Steelman, D. 2002, *Bull. Amer. Astron. Soc.*, **34**, 1224.
Diethelm, R. 2009, *Inf. Bull. Var. Stars*, No. 5894, 1.
Diethelm, R. 2011, *Inf. Bull. Var. Stars*, No. 5960, 1.
Diethelm, R. 2012, *Inf. Bull. Var. Stars*, No. 6029, 1.
Diethelm, R. 2013, *Inf. Bull. Var. Stars*, No. 6042, 1.
Drake, A., *et al.* 2014, *Astrophys. J., Suppl. Ser.*, **213**, 9.
Eggleton, P. P. 1983, *Astrophys. J.*, **268**, 368.
Erdem, A., and Öztürk, O. 2014, *Mon. Not. Roy. Astron. Soc.*, **441**, 1166.
Gaia Collaboration, *et al.* 2016, *Astron. Astrophys.*, **595A**, 1.
Gaia Collaboration, *et al.* 2018, *Astron. Astrophys.*, **616A**, 1.
Gaia Collaboration, *et al.* 2021, *Astron. Astrophys.*, **649A**, 1.
Green, G. M., *et al.* 2018, *Mon. Not. Roy. Astron. Soc.*, **478**, 651.
Henden, A. A., *et al.* 2015, AAVSO Photometric All-Sky Survey, data release 9, (https://www.aavso.org/apass).
Kafka, S. 2017, Variable star observations from the AAVSO International Database (https://www.aavso.org/aavso-international-database).
Kurucz, R. L. 2002, *Baltic Astron.*, **11**, 101.
Kwee, K. K., and van Woerden, H. 1956, *Bull. Astron. Inst. Netherlands*, **12**, 327.
Lucy, L. B. 1968, *Astrophys. J.*, **151**, 1123.
Mirametrics. 2015, Image processing, visualization, data analysis (https://www.mirametrics.com).
Nanouris, N., Kalimeris, A., Antonopoulou, E., and Rovithis-Livaniou, H. 2011, *Astron. Astrophys.*, **535A**, 126.
Nanouris, N., Kalimeris, A., Antonopoulou, E., and Rovithis-Livaniou, H. 2015, *Astron. Astrophys.*, **575A**, 64.
Papageorgiou, Athanasios, Catelan, Márcio, Christopoulou, Panagiota-Eleftheria, Drake, Andrew J., and Djorgovski, S. G. 2018, *Astrophys. J., Suppl. Ser.*, **238**, 4.
Pojmański, G. 2002, *Acta Astron.*, **52**, 397.
Pecaut, M. J., and Mamajek, E. E. 2013, *Astrophys. J., Suppl. Ser.*, **208**, 9. (http://www.pas.rochester.edu/~emamajek/EEM_dwarf_UBVIJHK_colors_Teff.txt).
Ruciński, S. M. 1969, *Acta Astron.*, **19**, 245.
Stępień, K., 2011, in *Magnetic Stars*, eds. I. I. Romanyuk, D. O. Kudryatsev, Special Astrophys. Obs., Nizhny Arkhyz, 86.
Stępień, K., and Kiraga, M. 2013, *Acta Astron.*, **63**, 239.
Strohmeier, W. 1967, *Inf. Bull. Var. Stars*, No. 195, 1.
Terrell, D., and Wilson, R. E. 2005, *Astrophys. Space Sci.,* **296**, 221.
Tout, C. A., Pols, O. R., Eggleton, P. P., and Han, Z. 1996, *Mon. Not. Roy. Astron. Soc.*, **281**, 257.
van Hamme, W. 1993, *Astron. J.*, **106**, 2096.
van Hamme, W., and Wilson, R. 1998, *Bull. Amer. Astron. Soc.*, **30**, 1402.
Watson, C., Henden, A. A., and Price, C. A. 2014, AAVSO International Variable Star Index VSX (Watson+, 2006–2014, https://www.aavso.org/vsx).
Woźniak, P. R., *et al.* 2004, *Astron. J.*, **127**, 2436.
Wilson, R. E. 1978, *Astrophys. J.*, **224**, 885.
Wilson, R. E., and Devinney, E. J. 1971, *Astrophys. J.*, **166**, 605.
Yakut, K., and Eggleton, P. P. 2005, *Astrophys. J.*, **629**, 1055.
Zasche, P., Uhlar, R., Kucakova, H., Svoboda, P., and Masek, M. 2014, *Inf. Bull. Var. Stars*, No. 6114, 1.

Visual and Near-Infrared Photometric Observations of Betelgeuse

Rick Wasatonic
Department of Astrophysics and Planetary Science, Villanova University, Villanova, PA 19085; richard.wasatonic@villanova.edu

Received June 17, 2022; revised August 5, 12, 16, 2022; accepted August 22, 2022

Abstract From 1996 to 2021 time-series photoelectric photometry of the M1-M2Ia-Iab red supergiant Betelgeuse was conducted using a wide-band V-filter centered on λ555 nm and narrow to intermediate-band Wing near infrared (NIR) titanium oxide (TiO) filters centered on λ719 nm, λ754 nm, and λ1024 nm. The observations were made to continually monitor magnitude variations for periodicities and variable amplitudes, calculate seasonal changes of effective temperatures, size, and luminosities, and subsequently examine the interrelationships among these physical properties. Using the V-band observations, short- and long-term dominant periods of 439 ± 5 and 2209 ± 183 days, respectively, were found. Effective temperatures varied from 3528 K to 3731 K, and using an adopted distance of 197 PC, luminosities varied from 70564 $L_{\odot}$ to 114204 $L_{\odot}$. Using these estimated values of effective temperature and luminosity, calculated radii, assuming spherical symmetry, varied from 710 $R_{\odot}$ to 847 $R_{\odot}$. NIR to V-band flux ratios indicate that Betelgeuse radiates, on the average, ~10 to ~20 times more in the NIR bands than the visual band. After NIR magnitude conversions from λ1024 nm to λ1040 nm, a surprising result was that the λ754-nm / λ1040-nm flux ratio was nearly 1.0, indicating the bolometric magnitude can be approximated at the shorter wavelength (λ754 nm) magnitude in addition to the theoretically-thought longer (λ1040 nm) wavelength magnitude.

1. Introduction

Betelgeuse (HD 39801, HR 6201) is one of the best known and most observed stars. It is a bright (nominal V ~0.3 to V ~0.9) semiregular pulsating red (B–V ~1.85) supergiant of spectral type M1-M2Ia-Iab, belonging to the Orion OB1 association (Kaler 2001). Petit (1987) classifies it as an SRc variable; these stars are all extremely bright M-type supergiants with semiregular periods and variable amplitudes. The unpredictable nature of the star became most apparent during the 2019/2020 observing season when its V-band magnitude dropped to an unprecedented value of V ~1.6 at minimum; this unusual occurrence became known as the Great Dimming Event (GDE). This relatively deep minimum occurred after 23 years of prior observations recorded some seasonal minima only near V = ~0.9. The GDE was noticed by both professional and amateur astronomical alike (e.g. Guinan *et al.* 2019a, 2019b) with various theoretical explanations such as reinforcement of multi-periodic minima occurring simultaneously (Guinan *et al.* 2019b) or the development of a dust cloud formed by condensing hot chromospheric material (Dupree *et al.* 2020). Related to this current study, there are many literature references that describe specific aspects of the variability nature of the star; Dupree *et al.* (1987) describe both photometric and spectroscopic variations from which a periodicity of 1.15 years (420 days) was detected; O'Gorman *et al.* (2015) report size and temperature relationships in the outer atmosphere of the star with the mean gas temperature dropping from 3000 K at $2R_{\star}$ to 1800 K at $6R_{\star}$. O'Gorman *et al.* also adopt a photospheric angular diameter of 42.45 milliarcseconds (mas), which, using Harper *et al.*'s (2008) estimated distance of 197 PC, reveals an actual photospheric size of 886 $R_{\odot}$. Townes *et al.* (2009) also report on a continual decrease in the size of Betelgeuse from 57 mas to 48 mas over 15 years using infrared spatial interferometric techniques at λ11.15 μm; again, using the estimated distance of 197 PC the change in size would be from 1190 $R_{\odot}$ to 1002 $R_{\odot}$, further implying that estimates of the linear size are dependent on the wavelength used to conduct the observations. However, despite its relative proximity to Earth, apparent brightness, and large size, there are significant degrees of uncertainties regarding the measures of its physical properties and other parameters such as distance and periodicities.

Dolan *et al.* (2016) neatly summarize a wealth of data on Betelgeuse from prior observations and analyses. This information is given in Tables 1, 2, and 3 of that paper, which includes various distance and radial velocity estimates, estimates of variable V-band magnitudes, luminosities, effective temperatures, and angular diameters that are again wavelength-dependent. Table 1 lists the adopted values of Dolan *et al.*'s V-band magnitude, $L/L_{\odot}$, T_{eff}, and $R/R_{\odot}$ averages; it will be seen in the following sub-sections and further subsequent papers that the photometric observations and resultant calculated parameters compare well with Dolan *et al.*'s adopted values.

Note that Dolan *et al.*'s adopted value of 887 $R_{\odot}$ was calculated by using the estimation of 197 PC as the distance to Betelgeuse (Harper *et al.* 2008) and an adopted value of 41.9 ± 0.06 mas based on Perrin *et al.*'s (2004) uniform disk diameter corrections.

2. Instrumentation and calibrations

The photoelectric observations were conducted using f/10 20-cm (8-inch) and f/10 27.5-cm (11-inch) Schmidt-Cassegrain telescopes at the Wasatonic Observatory near Allentown, Pennsylvania. An uncooled Optec SSP-3 photometer was

Table 1. Betelgeuse values adopted from Dolan (2016).

Parameter	*Adopted Value*
V-band (Å 555 nm)	0.51 mag
T_{eff} (K)	3500 ± 200
Log ($L_{\star}/L_{\odot}$)	5.10
$R_{\star}/R_{\odot}$	887 ± 203

Table 2. Characteristics of the four wavelength-band filters.

Filter	*Spectral Region*	*Central Wavelength (nm)*	*Bandpass (nm-FWHM)*
V	—	555	240
A	TiO (δ; 0,0)	719	11
B	continuum	754	11
C	continuum	1024	42

mated to the telescopes; the SSP-3 has a silicon red-sensitive PIN-photodiode detector that has a broad spectral range from λ300 nm to λ1100 nm. The detector aperture size was 1.0 mm, which converts to a FOV aperture angular size of 74 arcseconds. Integration times for accumulating raw photometer counts were generally 30 to 50 seconds, depending on the variations of the counts themselves. Four-filter photometry was conducted; specific characteristics of the four filters are given in Table 2, where the features for the near-IR filters are adapted from Wing (1992).

The Wing A-band filter measures the TiO λ719-nm (δ; 0,0) band, while the central wavelengths of the B- and C-band filters are located in NIR continuum regions that are relatively free from strong absorption lines. A molecular TiO index was calculated from the reduced Wing A-, B- and C-filter magnitudes via Equation 1 below, which is adopted from Wing (1992):

$$\text{TiO Index} = A - B - [0.13 \star (B - C)] \quad (1)$$

The TiO index variations occur because the strengths of the TiO bands respond to changes in temperature (Wasatonic *et al.* 2015). Coupled with suitable TiO/effective temperature calibrations using known standard stars, changing effective temperatures can then be estimated as the TiO indices vary.

The spectral features of M-giants and supergiants display increasing strengths of TiO molecular lines as the effective temperature decreases and as the spectral sub-types progress from M0 to M8. The TiO/T_{eff} and TiO/M-Spectral Type calibrations that were used to compute the changing effective temperatures and spectral types are given in Equations 2a and 2b and are graphically displayed in the upper and lower panels of Figure 1, respectively.

$$T_{eff}\,(K) = 63.931 * (\text{TiO Index})^2 - 421.620 * (\text{TiO Index}) + 3902.4 \quad (2a)$$

$$\text{M-Spec Type} = -1.0944 * (\text{TiO Index})^2 + 6.1537 * (\text{TiO Index}) - 1.3947 \quad (2b)$$

Note that Equations 2a and 2b are slightly different than the original calibration (Equations A2 and A3) as given in the Appendix in Wasatonic *et al.* (2015); the current calibration was derived using updated atmospheric extinction and transformation coefficients and by re-combining some observed TiO-index calibration results as given in Tables 6 and 7 of the Appendix in Wasatonic *et al.* (2015). The effective temperatures were computed using the red supergiant spectral type/effective temperature scale from Table 5 of Levesque *et al.* (2005), and the M-spectral subtypes were obtained from Wing (1978) calibration stars. Further calibration details are given in section A1 of the Appendix in Wasatonic *et al.* (2015).

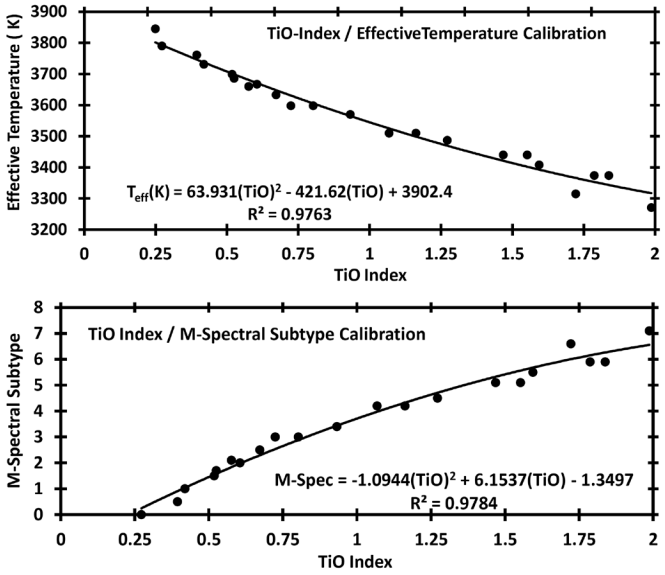

Figure 1. TiO/T_{eff} and TiO/M spectral sub-type calibrations used to compute changing Betelgeuse effective temperatures and M-spectral subtypes. Note that the determination coefficients (R^2) are both near 1.0, indicating high fit reliabilities.

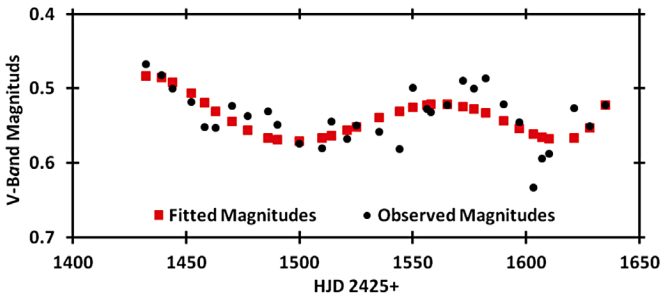

Figure 2. Example of fifth-degree polynomial fit (red squares) overlayed on actual V-band magnitudes (black dots) from the 1999/2000 observations.

For each of the four filters the raw photometer counts were reduced by FORTRAN programs that took into account conversions to Heliocentric Julian Day (HJD), atmospheric extinction, V-band color corrections, C-band λ1024-nm color and mbol corrections, and UT, SSP-3 counts, and air mass interpolations. Using the reduced NIR magnitudes, TiO indicies, effective temperatures, luminosities, and radii were calculated.

All reduced magnitudes and calculated TiO indicies, effective temperatures, radii, and luminosities were then fitted with fifth-degree polynomials on a seasonal basis to generate smooth variations, and the fitted data were then used for final analyses. An example of fitted magnitudes overlayed on actual observations is given in Figure 2.

Betelgeuse was observed differentially over 981 nights in the NIR bands and 997 nights in the V-band from 1996 to 2021. The comparison star was HD 37160 (V = 4.09, B–V = 0.95, G9.5IIIb). Since the comparison star was considerably fainter than Betelgeuse, different SSP-3 amplifier gains had to be used during the observations, that is, when observing Betelgeuse itself the gain had to be reduced to avoid SSP-3 detector saturation. This gain difference was compensated for during the reduction process. Additionally, since the comparison star and Betelgeuse were separated by 4.14 degrees, atmospheric extinction effects

were minimized using photometric reduction techniques as described in Hall and Genet (1982) and Wing (1995). To insure the non-variability of the comparison star, the check star γ Orionis (HD 35468, V = 1.64, B–V = –0.22, B2 V) was observed differentially with respect to the comparison star on 389 nights in the V-band over the entire 25-year observational period. Discounting random observational noise, no variability > 0.025 magnitude was observed between these two stars.

To generate the NIR magnitudes of Betelgeuse itself, the NIR magnitudes of the comparison star itself had to be computed. In order to generate these magnitudes the comparison star was observed differentially with the check star, whose NIR magnitudes are given by Wing and Ridgway (1979). Over the course of the 25-year observational period, differential observations were conducted on 65, 66, and 69 separate nights using the A-band, B-band, and C-band filters, respectively, with the final calculated magnitudes being: A = 0.135 ± 0.002, B = 0.192 ± 0.003, and C = 0.689 ± 0.003.

The reduced magnitude of the C-band filter was used as an estimate of the apparent bolometric magnitude (mbol) as theorized by Wing (1992). This was done after transforming the reduced C-filter magnitude to an effective wavelength of λ1040 nm via a color term and applying a small magnitude adjustment. In using an adopted distance to Betelgeuse of 197 PC the absolute bolometric magnitude (M_{bol}), or intrinsic luminosity with respect to the sun ($L_\star / L_\odot$), could then be calculated. Details of C-filter magnitude corrections are given in section 2 of the Appendix in Wasatonic *et al.* (2015). Finally, knowing the calculated effective temperatures and intrinsic luminosities, radii were calculated from:

$$L = 4\pi\sigma(R)^2(T_{eff})^4 \quad (3)$$

where $\sigma = 5.67 \times 10^{-8}$ joule/s/m^2/K^4 (the Stefan-Boltzmann Constant).

3. Observations and analyses[1]

3.1. Magnitude variations and flux ratios

Figure 3 displays the 25-year V-band fitted magnitude variations in the upper panel and the calculated fitted TiO indices in the lower panel. The semiregular variability nature of Betelgeuse is apparent in examining the magnitude variations. That is, on a season-by-season basis, the magnitude fluctuations do not repeat in a consistent manner. The overall 25-year average V-band magnitude was V = +0.56 ± 0.03, which is near Dolan *et al.*'s (2016) adopted value of V = +0.51 as given in Table 1.

Note the inverse correlation between the V-band magnitude variations and the calculated TiO indices. This inverse correlation was expected, as the magnitude variations are due, in part, to molecular TiO dissociation that results in decreased absorption at λ719 nm, leading to V-band brightening. Subsequent molecular TiO formation results in increased absorption at λ719 nm, leading to V-band dimming. The TiO dissociation

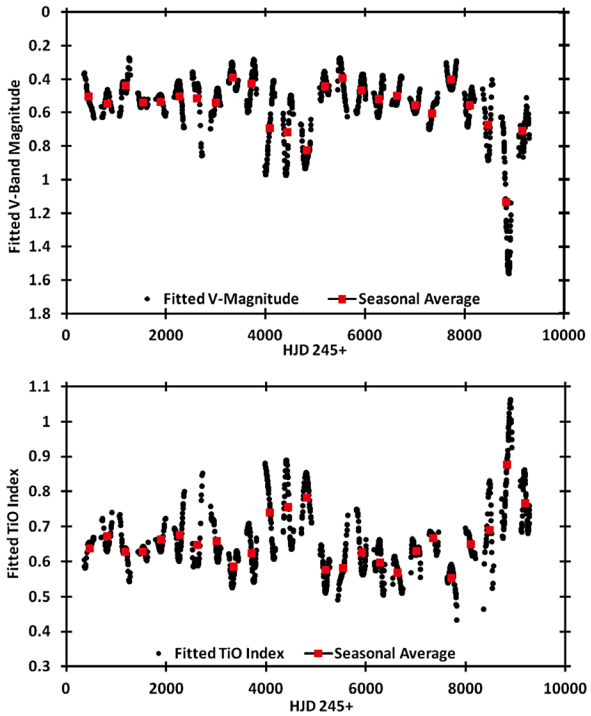

Figure 3. Upper panel: V-band magnitude variations; Lower panel: TiO index variations. Note the expected inverse correlation between these two quantities. The black dots represent the fitted magnitudes and TiO indices and the red squares represent seasonal averages.

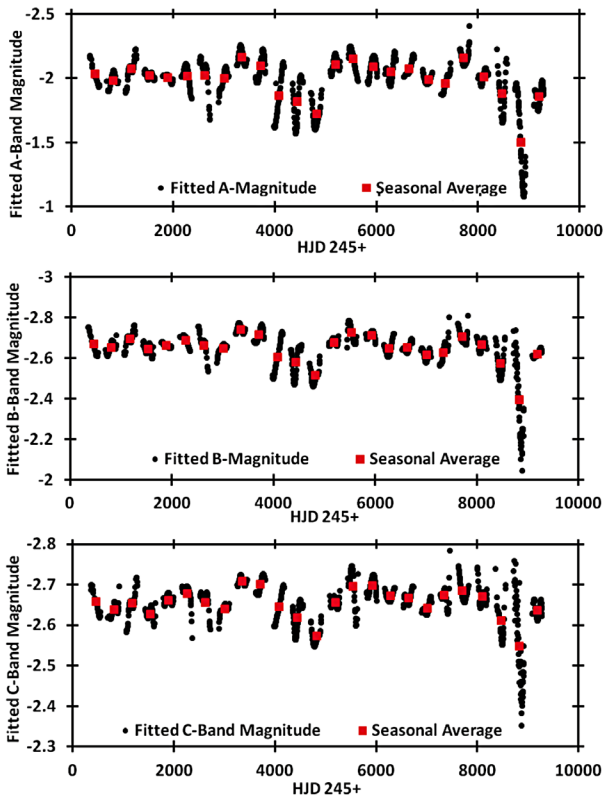

Figure 4. NIR magnitude variations; note the decreasing amplitudes between the A-band variations (~1.4 magnitudes) and the B- and C-band variations (~0.8 and ~0.4 magnitude, respectively). The black dots represent the individual fitted magnitudes, and the red squares represent seasonal averages.

[1] The full dataset is available through the AAVSO ftp site at ftp://ftp.aavso.org/public/datasets/3843-Wasatonic-502-alphaori.txt (if necessary, copy and paste link into the address bar of a web browser).

and formation events are themselves due to increasing and decreasing effective temperatures, respectively, which will be discussed in section 3.4 below.

Figure 4 displays the 25-year NIR magnitude variations. Note that the overall magnitudes are brighter with decreasing wavelength as progression is made from the λ719-nm A-band (upper panel) to the λ754-nm and λ1024-nm B- and C-bands (middle and lower panels). This effect was expected, as Betelgeuse radiates at a peak wavelength of λ793 nm, based on the 25-year overall average effective temperature of 3652 K. The peak wavelength was calculated using Wien's Law, which is:

$$\lambda_{max} = 2.898 \times 10^6 / T(K), \quad (4)$$

where λ_{max} is expressed in nanometers. Additionally, it can be seen from the B- and C-band light curves that the magnitudes in these two bandpasses are nearly identical. Recall that from Table 2 the FWHM of the narrow-band B-filter is only 11 nm, while the FWHM of the intermediate-band C-filter is 42 nm, and that, as mentioned in section 2, after suitable conversions were done the C-filter magnitudes could be considered bolometric in nature. However, because of the similarities of the B- and C-band magnitudes, the B-band magnitudes may also be considered bolometric since the averaged 25-year flux ratio of the B- to the C-band magnitudes (f_b / f_c, as given in Equation 5b below) was 0.995. Therefore, the bolometric magnitude of Betelgeuse possibly can be measured at shorter wavelengths near λ754 nm than originally thought at λ1040 nm. This would mean that the total energy output of Betelgeuse can be measured from deeper atmospheric levels (at λ754 nm) rather than from the outer atmospheric energy levels of the entire star at λ1040 nm.

In Figure 3 note that during the GDE the V-band fitted minimum magnitude dropped to V = +1.56; comparing this minimum with its average V-band magnitude of +0.56 indicates the star appeared fainter by a factor of 2.5. However, in the C- (or bolometric) band (Figure 4) the star appeared fainter by a factor of only 1.355 (in comparing the GDE C-band minimum magnitude of –2.35 to the average C-band magnitude of –2.65). Thus during the GDE itself there was speculation that the star might soon become a supernova event due to its visual decrease in light by a factor of 2.5; however, this thought should have been tempered by the overall (bolometric) loss of only ~1.3 times its pre-GDE value, implying that the overall energy output dropped relatively little compared to the visual energy output, thereby rendering a supernova event as probably non-imminent.

NIR to V-band flux ratios were calculated using Equation 5a:

$$f_{ir} / f_v = 10^{-0.4 * (ir - v)} \quad (5a),$$

where the quantity (ir – v) represents the difference in the seasonal magnitude averages (red squares in Figures 3 and 4) between the NIR bands and the V-band. Additionally, the flux ratios between the B-filter and C-filter seasonal average magnitudes were calculated from Equation 5b as given below:

$$f_b / f_c = 10^{-0.4 * (b - c)}, \quad (5b)$$

where the quantity (b – c) is the difference between the B- and C-band average magnitudes in a given season. Over the course of the 25-year observational time frame, the average observed flux at λ719 nm was ~10.5 times the observed flux at λ550 nm ($f_a / f_v = 10.494$), and the averaged observed flux at λ754 nm and λ1024 nm was ~19.5 times the observed flux at λ550 nm ($f_b / f_v = 19.308$ and $f_c / f_v = 19.562$). These calculated ratios quantify the amounts of observed near-IR flux compared to the observed V-band flux. Additionally, it was seen that the f_b / f_c ratio remained fairly steady near unity over the 25-year observational time frame, implying bolometric magnitudes may be measured by either the narrow B-band filter or the intermediate C-band filter as discussed earlier.

It should be noted that during the GDE of 2019/2020 the NIR to V-band ratios were considerably higher than the above mentioned averages. Specifically, f_a / f_v was 11.35, f_b / f_v was 25.89, and f_c / f_v was 29.73; these higher flux ratios were due to the V-band flux at λ550 nm falling more steeply than the NIR fluxes, giving rise to the higher ratios, again indicative that what was observed was mainly a loss in visual light compared to loss of light in the NIR.

3.2. Amplitudes

While the Figure 3 and Figure 4 light curves themselves look quite similar, note that the amplitudes steadily decrease as progression is made from the V-band filter (upper panel, Figure 3) to the A-band filter (upper panel, Figure 4) to the B- and C-band filters (middle and lower panels, Figure 4).

The maximum total amplitudes over the entire 25-year time frame (excluding the GDE) are 0.701, 0.709, 0.311, and 0.212 magnitude in the V-, A-, B-, and C-bands, respectively. Table 3 lists the 25-year maximum and minimum magnitudes, the HJD of each occurrence for each filter, and the resulting total amplitude for each filter. It was a mild surprise that the A-band total amplitude was virtually identical to the V-band total amplitude. The A-band filter is specifically designed to measure the λ719-nm flux variations that are caused by TiO dissociations (less absorption) and formations (more absorption); to some extent these absorption variations could have affected the perceived flux through the wide-band V-filter, giving rise to near identical amplitudes. The central wavelengths of the B- and C-filters are located in relatively clear spectral regions and are thus not readily affected by changing TiO amounts, thus accounting for the lower overall total amplitudes.

The seasonal total amplitudes, however, are less than the overall 25-year total amplitudes in all four wavelength bands. Seasonal total amplitudes in each wavelength band were computed for those particular seasons with well defined local maxima and minima. The averaged seasonal total

Table 3. Amplitudes over 25 years.

Filter	*Maximum*	*HJD (245+)*	*Minimum*	*HJD (245+)*	*Total Amplitude*
V	0.274	5492	0.975	4412	0.701
A	–2.281	7817	–1.572	4409	0.709
B	–2.772	7633	–2.461	4781	0.311
C	–2.759	8729	–2.547	4781	0.212

amplitudes were 0.263±0.041, 0.250±0.041, 0.100±0.016, and 0.061±0.011 magnitude in the V-, A-, B-, and C-bands, respectively. It is important to realize, however, that seasonal total amplitudes are quite variable, but that a particular seasonal total amplitude will, as a rule, be less that any long-term observed total amplitude.

3.3. Periodicities

Despite the current SRc classification, both short- and long-term period searches using the V-band fitted magnitude variations were attempted by using the Data Compensated Discrete Fourier Transform (DCDFT) that is in the CLEANest routine of the Period Analysis Software (Peranso) package provided by Vanmunster (2021). To this end, the upper and lower panels of Figure 5 display the power spectra of the calculated V-band short- and long-term periods, respectively. The upper panel displays a dominant short-term period of 439±5 days and a secondary period of 405±4 days; these periods generally correspond with previously published results from Dupree *et al.* (1987), who reported a period of 420 days, and Karovska (1987), who reported a period (among five) of 383 days. The bottom panel displays a dominant period of 2209±183 days and a secondary period of 4706±884 days; the dominant period agrees somewhat with previously published results of Guinan (1984) and Goldberg (1984), who both report a period of 2109 days, and Stothers and Leung (1971), who reported a period of 2332 days. The long-term periods have larger uncertainties due to more probabilistic non-regular variations because of the longer time frame. It should be noted that these generated periods can be considered valid for only the 25-year observational time frame.

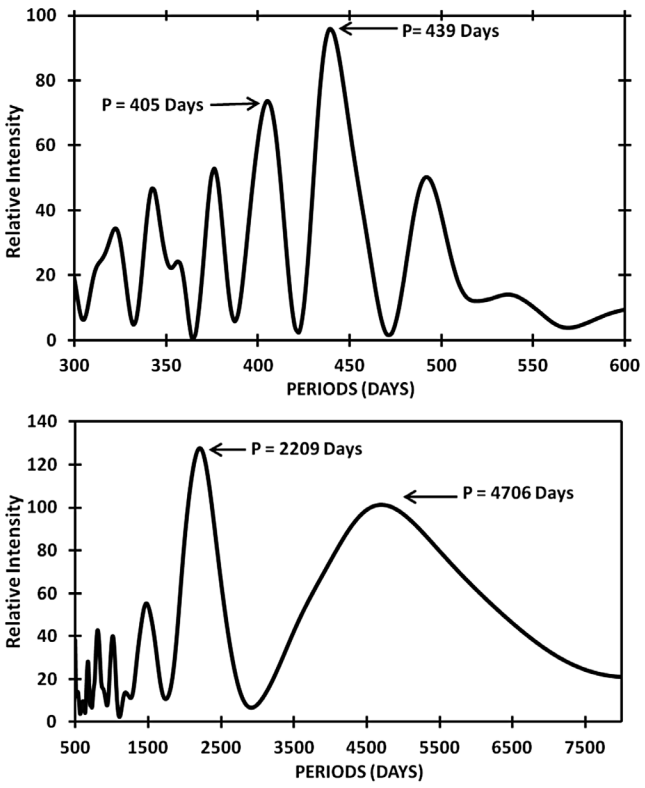

Figure 5. Short-tem (upper panel) and long-term (lower panel) Peranso-generated periods using the V-band fitted observations. The dominant (higher relative intensity) and secondary (lower relative intensity) periods are indicated in days.

3.4. Radius, luminosity, and effective temperature variations

In addition to observing Betelgeuse for magnitude variations and periodicities, radius, luminosity, and effective temperature (hereinafter RLT) estimates were calculated using the NIR variable magnitudes. Effective temperatures were derived from using Equations 1 and 2a, luminosities were determined from the C-filter magnitudes after employing the needed conversions, and radii were the subsequently calculated via Equation 3. Figure 6 displays the RLT variations over the entire 25-year observational time frame; note that the radii and luminosities are given in terms of solar units. The fitted maximum effective temperature of 3731 K was calculated during 2016/2017 and the fitted minimum effective temperature of 3528 K was calculated during the Great Dimming Event of 2019/2020. Similarly the fitted calculated maximum and minimum luminosities were 114204 $L_\odot$ (2015/2016) and 70564 $L_\odot$ (2019/2020), respectively, and the fitted calculated maximum and minimum radii were 847 $R_\odot$ (2015/2016) and 710 $R_\odot$ (2019/2020), respectively.

From Figure 6 note that the effective temperature variations (lower panel) form positive correlations with both the V- and A-band magnitude variations (upper panels, Figures 3 and 4,

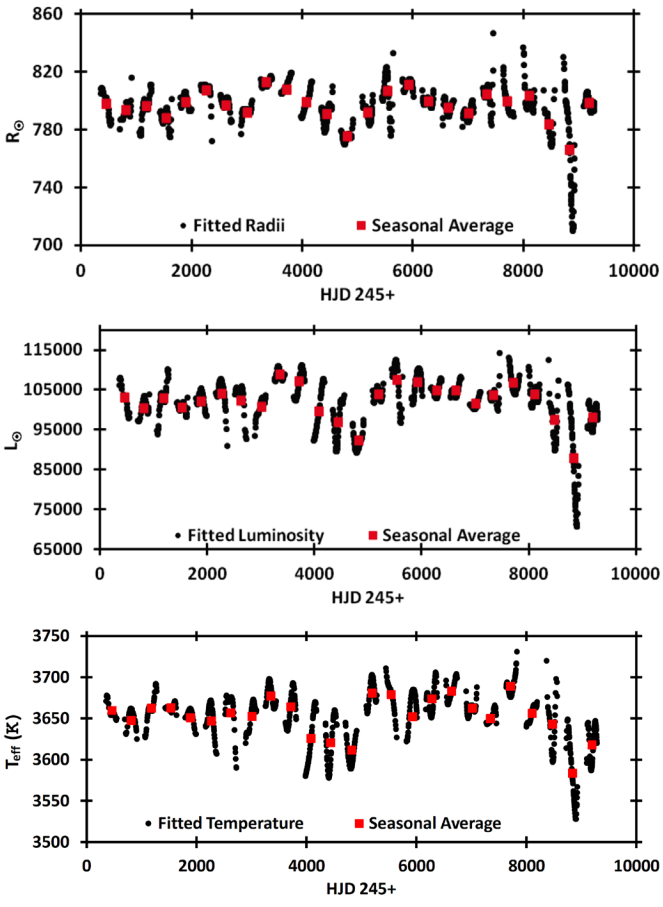

Figure 6. Calculated radius, luminosity, and effective temperature (RLT) variations. The radii and luminosities are given in solar terms. The black dots represent calculated fitted variations, and the red squares represent seasonal averages.

respectively) and form an inverse correlation with the TiO index variations (lower panel, Figure 3). These correlations (both direct and inverse) were expected, since increasing temperatures result in brighter magnitudes due to TiO molecular dissociation and hence less absorption at λ719 nm. Conversely, decreasing temperatures result in fainter magnitudes due to TiO re-formation and hence more absorption at λ719 nm. Despite reported asymmetries from an overall spherical shape of Betelgeuse (e.g. Gilliland and Dupree 1996), Equation 3 was used to calculate radii based on the effective temperature and luminosity observations, and hence the calculated radii should be viewed with caution. From Figure 7 it can be seen that the luminosity and radii variations form an overall positive correlation with respect to the temperature variations, although there is considerable scatter on a season-by-season basis. It is interesting to note that individual seasonal RLT variations at times show positive correlations, yet during other individual seasons the RLT inter-relationships show either negative correlations or no correlations at all. These anomalous RLT inter-relational discrepancies will be discussed in detail in subsequent papers which will also describe unusual relationships among the four-filter magnitude variations on a season-by-season basis. An example of a seasonal magnitude anomaly is given below in section 4.

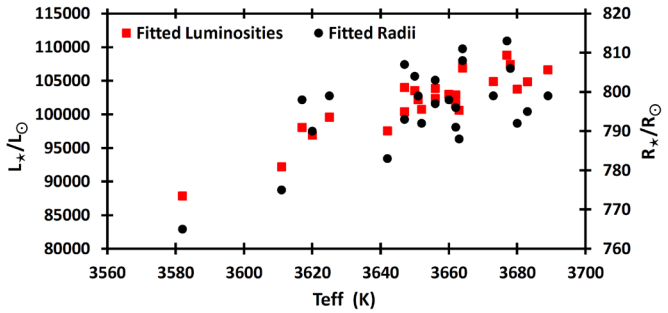

Figure 7. Net positive correlations of luminosity and radius with respect to effective temperature using seasonal averages that were depicted in Figure 6.

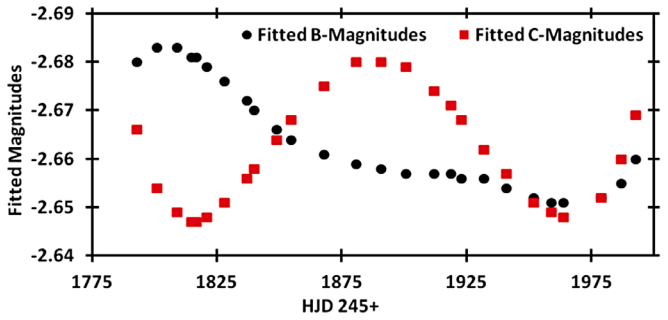

Figure 8. Season 5 (2000/2001) anomalous B-band (black dots) and C-band (red squares) relative magnitude variations. Note the C-band near-sinusoidal magnitude variation while the B-band magnitudes continually decrease throughout the season, contrary to expected uniform magnitude changes (both simultaneously increasing and/or decreasing).

4. Future research

It was stated in section 3.4 that, on a season-by-season basis, the interrelationships among effective temperatures, luminosities, and radii can at times show either a positive or negative correlation, or no correlations at all. Similar anomalies can also be seen in seasonal magnitude variations among the four observed bandwidths. An example of magnitude discrepancies is displayed in Figure 8, which displays the fitted B- and C-band magnitude variations from Season 5 (2000/2001). Note that while the C-band magnitudes (red squares) form an approximate sinusoidal curve, the B-band magnitudes (black dots) consistently decrease throughout most of the season. It is only near the end of the observing season that both the B-band and C-band magnitudes simultaneously increase. Thus, for most of the season these relative variations were unexpected, as both bands lie in relatively clear spectral regions and hence any radiative processes should be nearly identical, leading to approximately uniform magnitude variations. Future planned papers will examine in detail similar unexpected observations that have occurred in specific seasons which will reveal anomalies that are not apparent when examining the entire 25-year observational time frame in singly displayed light curves.

5. Summary

In examining the light curves (Figures 3 and 4) it is apparent that the SRc variable star classification is confirmed for Betelgeuse, as both the magnitude and amplitude variations are semiregular at best. Both V-band dominant long-term (2209 ± 183 days) and short-term (439 ± 5 days) periods were detected, providing astronomers the means to predict with some degree of certainty when the next local maximum or minimum should occur. However, due to the inherent semiregular nature of the star, any predicted times should be taken with caution. The NIR to V-band flux ratios indicate the observed flux from Betelgeuse is ~10 to ~20 times stronger in the NIR than the V-band, which was expected but now has been quantified. The overall 25-year averages of effective temperature at 3652 K, luminosity at ~10^5 $L_\odot$, and radius at 796 $R_\odot$ (based on an adopted distance of 197 PC) are consistent with current literature data. Subsequent papers will investigate in detail unusual four-filter magnitude variations with respect to each other and unusual RLT inter-relationships on a season-by-season basis. Finally, as evidenced by the GDE during the 2019/2020 observing season, continued observations are warranted to monitor the star for any unexpected and anomalous behavior.

6. Acknowledgements

Over the twenty-five years this research has been supported from NASA and NSF grants to Dr. Edward Guinan (Villanova University). Financial support also came from the Department of Astrophysical and Planetary Science, Villanova University. I also thank Dr. Robert Wing (Ohio State University) for his insights in various aspects of the paper through private communications. Finally I would like to thank the referee for strategic and useful comments.

References

Dolan, M. M., Mathews, G. J., Lam, D. D., Quynh Lan, N., Herczeg, G. J., and Dearborn, D. S. P. 2016, *Astrophys. J.*, **819**, 7.

Dupree, A. K., Baliunas, S. L., Guinan, E. F., Hartmann, L., Nassiopoulos, G. E., and Sonneborn, G. 1987, *Astrophys. J., Lett.*, **317**, L85.

Dupree, A. K., et.al. 2020, *Astrophys. J.*, **899**, 68.

Gilliland, R. L., and Dupree, A. K. 1996, *Astrophys. J., Lett.*, **463**, L29.

Goldberg, L. 1984, *Publ. Astron. Soc. Pacific*, **96**, 366.

Guinan, E. F. 1984, in *Cool Stars, Stellar Systems, and the Sun*, ed. S. L. Baliunas, L. Hartmann, Springer-Verlag, New York, 336.

Guinan, E. F., Wasatonic, R. J., and Calderwood, T. J. 2019a, *Astron. Telegram*, No. 13341, 1.

Guinan, E. F., Wasatonic, R. J., and Calderwood, T. J. 2019b, *Astron. Telegram*, No. 13365, 1.

Hall, D. S., and Genet, R. M. 1982, *Photoelectric Photometry of Variable Stars*, International Amateur-Professional Photoelectric Photometry (IAPPP), 13-2, 13-3.

Harper, G. M., Brown, A., and Guinan, E. F. 2008, *Astron. J.*, **135**, 1430.

Kaler, J. 2001, *Extreme Stars: At the Edge of Creation*, Cambridge University Press, New York, 125.

Karovska, M. 1987, in *Stellar Pulsations: A Memorial to John P. Cox*, eds. A. N. Cox, W. M. Sparks, S. G. Starrfield, Springer-Verlag, New York, 260.

Levesque, E. M., Massey, P., Olsen, K. A. G., Plez, B., Josselin, E., Maeder, A., and Meynet, G. 2005, *Astrophys. J.*, **628**, 973.

O'Gorman, E., Harper, G. M., Brown, A., Guinan, E. F., Richards, A. M. S., Vlemmings, W., and Wasatonic, R. 2015, *Astron. Astrophys.*, **580A**, 101.

Perrin, G., Ridgway, S. T., Coudé du Foresto, V., Mennesson, B., Traub, W. A., and Lacasse, M. G. 2004, *Astron. Astrophys.*, **418**, 675.

Petit, M. 1987, *Variable Stars*, Wiley, Chichester, NY, 71.

Stothers, R., and Leung, K. C. 1971, *Astron. Astrophys.*, **10**, 290.

Townes, C. H., Wishnow, E. H., Hale, D. D. S., and Walp, B. 2009, *Astrophys. J., Lett.*, **697**, L127.

Vanmunster, T. 2021, Peranso light curve and period analysis software, version 3.0.2.9 (http://www.peranso.com).

Wasatonic, R. P., Guinan, E. F., and Durbin, A. J. 2015, *Publ. Astron. Soc. Pacific*, **127**, 1010.

Wing, R. F. 1978, *Spectral Classifications and Color Temperatures for 280 Bright Stars in the Range K4–M8*, Ohio State University Press, Columbus, OH, 5–9.

Wing, R. F. 1992, *J. Amer. Assoc. Var. Star Obs.*, **21**, 42.

Wing, R. F. 1995, private communication.

Wing, R. F., and Ridgway, S. T. 1979, *Dudley Obs. Rep.*, No. 14, 253.

New Photometric Observations and the First Wilson Program Analysis of the Totally Eclipsing, Solar Type Binary, UU Camelopardalis

Ronald G. Samec
Pisgah Astronomical Research Institute, 112 Idlewood Acres, Hartwell, GA 30643; ronaldsamec@gmail.com

Daniel Caton
Dark Sky Observatory, Department of Physics and Astronomy, Appalachian State University, 525 Rivers Street, Boone, NC 28608-2106; catondb@appstate.edu

Danny Faulkner
Johnson Observatory, 1414 Bur Oak Court, Hebron, KY 41048; dfaulkner@answersingenesis.org

Received July 1, 2022; revised August 5, 11, 2022; accepted August 12, 2022

Abstract CCD BVRI light curves of UU Cam were taken on 19, 20, 21, 23, 24, and 27 January 2021 by Daniel Caton at the Dark Sky Observatory, North Carolina, with the 0.81-m reflector of Appalachian State University. The variability of UU Cam was discovered by Baker. UU Cam is an eclipsing binary with a totally eclipsing secondary. The eclipse duration is some 54 minutes. The period behavior is quadratic following JD 2454860. Before this, there appears to be a constant period or the scatter is very high. There are 34 timings in the period study covering an interval of ~29.6 years. From our study, the period is found to be increasing. This could be due to mass transfer making the mass ratio decrease. A Wilson-Devinney analysis reveals that the system is an A-type (most massive component is the hottest) W UMa binary with a fairly extreme mass ratio, q = 0.2551 ± 0.0002. Its Roche Lobe fill-out is an extreme ~60%. One cool spot was needed in the solution. The temperature difference of the components is only ~121 K. The inclination is high, 82.04 ± 0.05, resulting in a time of constant light in the primary eclipse.

1. Introduction

The variability of UU Cam was discovered by Baker (1937). He gives a photographic magnitude range of 11.6–12.5. Bond (1978) identified UU Cam spectra as that those of an RR Lyrae variable. Poretti (1986) took the first B, V measures and confirmed substantially that the variable was an RR Lyrae. What we now have identified as the secondary minimum total eclipse was not covered in their light curve. It has been argued that the period changes probably showed long-term light time effects of another body orbiting UU Cam (Liska and Skarka 2015).

A number of IBVS articles contain minima from 2005 on and all refer to UU Cam as an eclipsing binary. This is probably due to the secondary total eclipse as seen in the ASAS-SN curves (Shappee *et al.* 2014; Kochanek *et al.* 2017) seen as Figure 1. This eclipsing binary system was observed by the All-Sky Automated Survey as ASASSN-V J051858.09+365806.2 (Pojmański 2002; Jayasinghe *et al.* 2019). They give a V_{mean} of 11.61, an amplitude of 0.49, an EW designation, and a J–K = 0.205. Their ephemeris is:

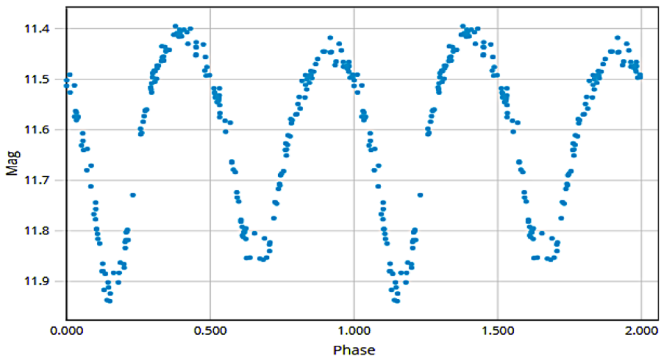

Figure 1. V-ASAS-SN light curves, ASASSN-V J035217.64+743356.8 (Shappee *et al.* 2014).

$$\text{HJD Min I} = 2457769.92503 + 0.6825577\,\text{d} \times \text{E} \quad (1)$$

From the ASAS-SN curves we were able to phase the data with Equation 1 and do parabola fits to the primary and secondary minima to locate seven times of "low light" within 0.001 phase of each minimum (these were weighted 0.1). We also included the ASAS-SN HJD Min I in our period study. This system was observed as a part of our professional collaborative studies of interacting binaries at Pisgah Astronomical Research Institute from data taken from DSO observations. The observations were taken by D. Caton, R. Samec, and D. Faulkner. Reduction and analyses were done by R. Samec.

A sample of the first ten sets of observations is given in Table 1. The complete table is available through the AAVSO ftp site as given in the table.

Our BVRI light curves were taken at Dark Sky Observatory, on 19–21, 23, 24, and 27 January 2021, with a thermoelectrically cooled (–35° C) 1KX1K FLI camera and Bessell filters.

Individual observations included 830 in B, 832 in V, 673 in R, and 666 in I. The probable error of a single observation was 4 mmag in B, V, and R, and 3 mmag in I. The nightly C–K values stayed constant throughout the observing run with a precision of about 1%. Exposure times varied from 45s in B, 20s in V, and 15s in R and I. To produce these images, nightly images were calibrated with 25 bias frames, at least five flat frames in each filter, and ten 300-second dark frames.

Table 1. Sample of first ten UU Cam *B, V, R, I* observations.

Δ*B*	*HJD 2459230+*	Δ*V*	*HJD 2459230+*	Δ*R*	*HJD 2459230+*	Δ*I*	*HJD 2459230+*
–0.1310	3.6189	–0.0450	3.6160	0.0160	3.6205	0.0650	3.6208
–0.0970	3.6243	–0.0310	3.6214	0.0170	3.6216	0.0770	3.6218
–0.1050	3.6254	–0.0250	3.6224	0.0300	3.6227	0.0750	3.6229
–0.0920	3.6264	–0.0230	3.6235	0.0190	3.6237	0.0780	3.6240
–0.0920	3.6275	–0.0220	3.6246	0.0400	3.6248	0.0800	3.6250
–0.0810	3.6286	–0.0190	3.6257	0.0290	3.6259	0.0930	3.6261
–0.0850	3.6297	–0.0160	3.6267	0.0380	3.6270	0.0820	3.6272
–0.0740	3.6308	–0.0150	3.6278	0.0510	3.6280	0.0950	3.6283
–0.0840	3.6318	0.0010	3.6300	0.0450	3.6291	0.0990	3.6294
–0.0710	3.6329	0.0070	3.6311	0.0470	3.6302	0.1070	3.6304

Note: First ten data points of UU Cam B, V, R, I observations. The complete table is available through the AAVSO ftp site at ftp://ftp.aavso.org/public/datasets/3844-Samec-502-uucam.txt (if necessary, copy and paste link into the address bar of a web browser).

Table 2. Photometric targets.

Role	*Label*	*Name*	*V*	*J–K (2MASS)*
Variable	V	UU Cam, GGM2006 6868894	11.45	0.205 ± 0.033, F5V
Comparison	C	GSC 4339 2245	11.79	0.326 ± 0.035, G0V
Check	K	GSC 4339 1108	13.58	0.32 ± 0.04, G0V

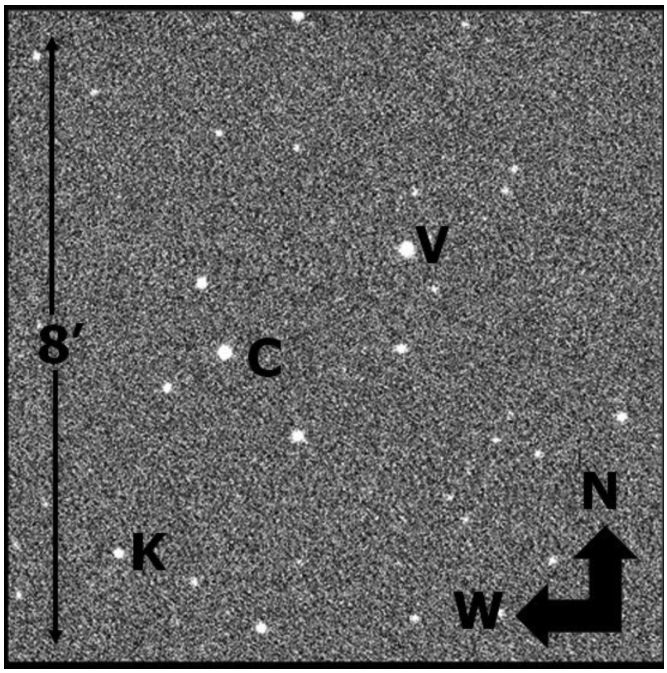

Figure 2. Finding chart of V, the variable star (UU Cam), C, the comparison star (GSC 4339 2245), and K, the check star (GSC 4339 1108).

2. Target stars

The finding chart of the observational field is shown in Figure 2. The target stars are given in Table 2.

3. Period determination

Four mean times (from BVRI data) of minimum light were calculated from our present observations, two primary and two secondary eclipses: the period behavior appears to be quadratic following JD 2448680.67 (Paschke 2020). Before this there appears to be a constant period or the scatter is very high. So, this study is from that of JD 2448680.67 and thereafter (Table 3). The minima mentioned above were weighted as 1.0 in this period study. The single filter minima of multicolor groups were weighted as 0.3. In addition, ten times minima were taken from *IBVS* and two from *BAVM*. Nine times were taken from *MVS*. Seven ASAS-SN times of minimum light were included in the study and weighted as 0.1. This gave us 34 timings in the period study with an interval of ~29.6 years.

From these timings, two ephemerides have been calculated, a linear and a quadratic one:

$$\text{JD Hel Min I} = 2459241.54719 \pm 0\ .00098\,\text{d} + 0.\ 68255861 \pm 0.00000016 \times \text{E} \quad (2)$$

$$\text{JD Hel Min I} = 2459241.55093 \pm 0.00072\text{d} + 0.\ 68256120 \pm 0.00000027\text{E} + 0.000000000212 \pm 0.000000000020 \times \text{E}^2 \quad (3)$$

Equation 3 shows an orbital period that is increasing, as shown in the O–C curve in Figure 3. This might be due to mass transfer to the more massive, primary component, making the mass ratio more extreme. However, this curve could be part of a longer period sinusoid.

The quadratic ephemeris yields a $\dot{\text{P}} = 2.27 \times 10^{-7}$ d/yr or a mass exchange rate of

$$\frac{\text{dM}}{\text{dt}} = \frac{\dot{\text{P}}\,\text{M}_1\,\text{M}_2}{3\text{P}\,(\text{M}_1 - \text{M}_2)} = \frac{5.58 \times 10^{-8}\,\text{M}_\odot}{\text{yr}}. \quad (4)$$

in a conservative scenario (the primary component is the gainer).

Table 3. UU Cam O–C.

Minima 2400000+	*Cycles*	*Linear Residuals*	*Quadratic Residuals*	*Weight*	*Reference*
48680.6700	–15472.5	0.0109	–0.0033	1.0	Schmidt *et al.* (1995)
51349.1290	–11563.0	0.0070	0.0050	1.0	Paschke (2020)
52685.5697	–9605.0	–0.0020	–0.0003	1.0	Hubscher *et al.* (2005)
53450.0349	–8485.0	–0.0025	0.0006	1.0	Kim *et al.* (2006)
54811.7390	–6490.0	–0.0028	0.0014	1.0	Diethelm (2009)
55121.9640	–6035.5	–0.0007	0.0035	1.0	Diethelm (2010)
55125.3768	–6030.5	–0.0007	0.0035	1.0	Hübscher *et al.* (2010)
55566.6466	–5384.0	–0.0050	–0.0009	1.0	Diethelm (2011)
55670.3962	–5232.0	–0.0043	–0.0003	1.0	Hübscher *et al.* (2012)
55849.9057	–4969.0	–0.0078	–0.0038	1.0	Diethelm (2012)
55942.3979	–4833.5	–0.0022	0.0016	1.0	Hübscher and Lehmann (2012)
55969.3566	–4794.0	–0.0046	–0.0008	1.0	Hübscher and Lehmann (2012)
56297.6653	–4313.0	–0.0066	–0.0031	1.0	Diethelm (2013)
57374.7333	–2589.0	–0.0056	–0.0041	0.1	Shappee *et al.* (2014); Kochanek *et al.* (2017)
58322.1247	–2735.0	–0.0161	–0.0143	0.1	Shappee *et al.* (2014); Kochanek *et al.* (2017)
57320.1328	–1347.0	–0.0160	–0.0166	0.1	Shappee *et al.* (2014); Kochanek *et al.* (2017)
58128.9647	–2815.0	–0.0119	–0.0100	0.1	Shappee *et al.* (2014); Kochanek *et al.* (2017)
58018.0506	–1630.0	–0.0120	–0.0120	0.1	Shappee *et al.* (2014); Kochanek *et al.* (2017)
57020.8467	–1792.5	–0.0103	–0.0101	0.1	Shappee *et al.* (2014); Kochanek *et al.* (2017)
57046.7917	–3253.5	0.0039	0.0064	0.1	Shappee *et al.* (2014); Kochanek *et al.* (2017)
57474.3973	–3215.5	0.0117	0.0141	1.0	Hübscher (2017)
57844.3444	–2047.0	–0.0053	–0.0046	1.0	Lehký *et al.* (2021)
58771.2650	–689.0	0.0007	–0.0014	1.0	Pagel (2020)
59061.3499	–264.0	–0.0018	–0.0049	0.3	Auer 2021
59061.3520	–264.0	0.0003	–0.0028	0.3	Auer 2021
59061.3550	–264.0	0.0033	0.0002	0.3	Auer 2021
59062.3801	–262.5	0.0045	0.0015	0.3	Auer 2021
59062.3821	–262.5	0.0065	0.0035	0.3	Auer 2021
59062.3824	–262.5	0.0068	0.0038	0.3	Auer 2021
59233.7062	–11.5	0.0085	0.0048	1.0	Present Observations
59234.7265	–10.0	0.0049	0.0012	1.0	Present Observations
59237.8007	–5.5	0.0076	0.0039	1.0	Present Observations
59241.5511	0.0	0.0039	0.0002	1.0	Present Observations
59489.3212	363.0	0.0052	0.0005	1.0	Pagel (2022)

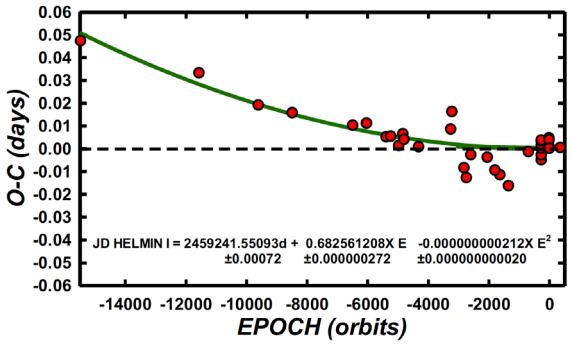

Figure 3. Quadratic O–C residuals.

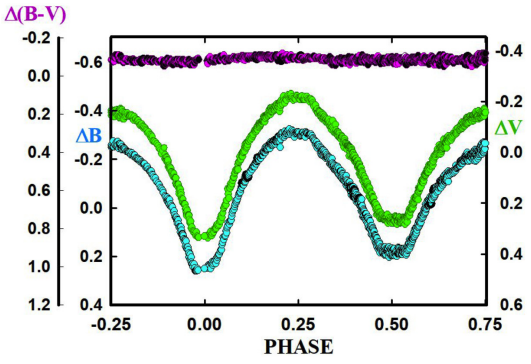

Figure 4. B, V, and B–V magnitude phased plots with the new linear ephemeris, Equation 2.

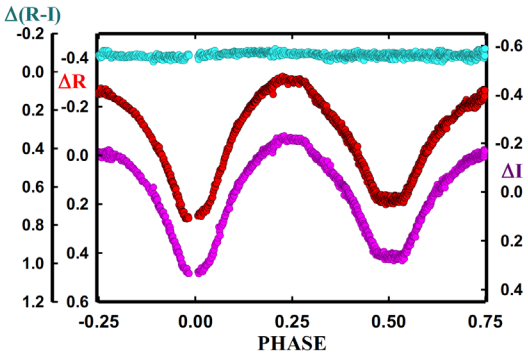

Figure 5. R, I, and R–I magnitude phased plots with the new linear ephemeris, Equation 2.

4. Light curve characteristics

The B, V, B–V, and R, I, and R–I mags were phased with the new linear ephemeris, Equation 2. These phased plots are given in Figures 4 and 5.

The quarter-cycle light curve characteristics of B, V, R, and I plots are given in Table 4.

The curves are of good accuracy, averaging about 2% photometric precision. The noise is probably due to magnetic activity. The amplitude of the light curve varies from 0.507 to 0.551 for I to B magnitudes. The O'Connell effect, an indicator

Table 4. Light curve characteristics.

Filter	*Phase Min I*	*Error*	*Phase Max I*	*Error*		
	0.00	± σ	0.25	± σ		
B	0.243	0.006	–0.308	0.009		
V	0.332	0.004	–0.216	0.008		
R	0.383	0.007	–0.151	0.007		
I	0.420	0.003	–0.087	0.007		
	Min II		Max II			
	0.50	± σ	0.75	± σ		
B	0.183	0.012	–0.257	0.009		
V	0.265	0.009	–0.154	0.008		
R	0.317	0.006	–0.108	0.007		
I	0.372	0.007	–0.058	0.007		
	Min I – Max I	± σ	Max II – Max I	± σ	Min I – Min II	± σ
B	0.551	0.014	0.051	0.017	0.060	0.018
V	0.547	0.012	0.062	0.015	0.066	0.013
R	0.534	0.014	0.043	0.013	0.066	0.014
I	0.507	0.010	0.029	0.013	0.048	0.010
	Min II– Max I	± σ	Min I – Max II	± σ	Min II– Max II	± σ
B	0.491	0.021	0.500	0.014	0.440	0.021
V	0.481	0.016	0.485	0.012	0.419	0.016
R	0.468	0.013	0.491	0.014	0.425	0.013
I	0.459	0.013	0.478	0.010	0.429	0.013

Table 5. B,V,R,I Solution parameters.

Parameters	*Values*
$\lambda_B, \lambda_V, \lambda_R, \lambda_I$ (nm)	440, 550, 640, 790
g_1, g_2	0.32
A_1, A_2	0.50
Inclination (°)	82.040 ± 0.050
T_1, T_2 (K)	6500, 6379 ± 1
$\Omega_1 = \Omega_2$	2.268 ± 0.001
$q(m_1/m_2)$	0.255 ± 0.000
Fill-outs: F(%)	60.1(0.5)
$L_1/(L_1+L_2)_I$	0.771 ± 0.002
$L_1/(L_1+L_2)_R$	0.773 ± 0.002
$L_1/(L_1+L_2)_V$	0.775 ± 0.003
$L_1/(L_1+L_2)_B$	0.779 ± 0.003
JD_o (days)	2459241.5516 ± 0.0001
Period (days)	0.68257 ± 0.00001
Dimensions:	
$r_1/a, r_2/a$ (pole)	0.490 ± 0.001, 0.274 ± 0.001
$r_1/a, r_2/a$ (side)	0.537 ± 0.001, 0.289 ± 0.001
$r_1/a, r_2/a$ (back)	0.616 ± 0.001, 0.351 ± 0.003
Spot, primary component	Cool spot region
Colatitude (°)	71.8 ± 0.5
Longitude (°)	105.6 ± 0.3
Radius (°)	24.71 ± 0.07
T-Factor	0.919 ± 0.0011

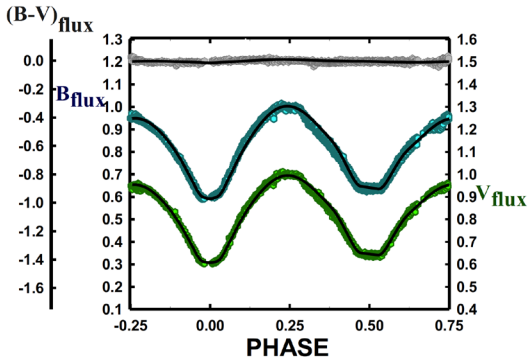

Figure 6. B, V, and B–V normalized fluxes overlaid by the light curve solution.

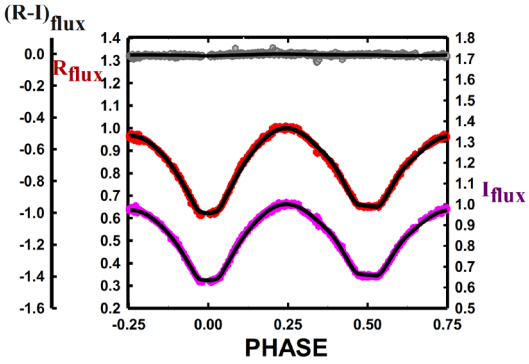

Figure 7. R, I, and R–I normalized fluxes overlaid by the light curve solution.

Table 6. UU Cam system dimensions.

R_1, R_2 (pole, $R_\odot$)	1.89 ± 0.002	0.669 ± 0.0003
R_1, R_2 (side, $R_\odot$)	2.07 ± 0.003	0.700 ± 0.0003
R_1, R_2 (back, $R_\odot$)	2.20 ± 0.003	0.844 ± 0.0004

Table 7. Estimated absolute parameters1.

Parameter	*Star 1*	*Star2*
Mean radius ($R_\odot$)	2.053 ± 0.009	0.738 ± 0.004
Mean density	0.212 ± 0.004	0.303 ± 0.006
Mass ($M_\odot$)	1.35 ± 0.01	0.37 ± 0.01
Log g	3.94	3.86

Note: Using light curve solution units, a = 1, a is calculated for Wilson program, the semi-major axis. Density is in g/cm³, a = 3.8568 $R_\odot$ (Bradstreet and Steelman 2002).

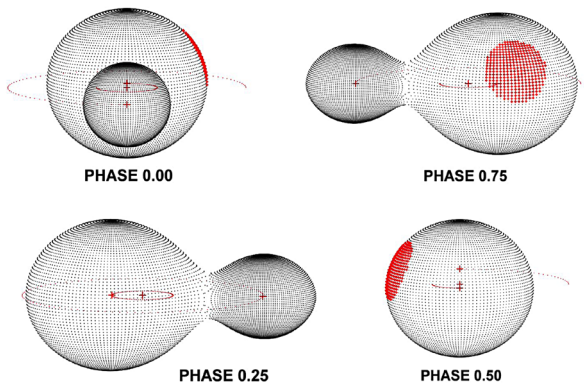

Figure 8. UU CAM, geometrical representation at quarter orbital phases.

of spot activity, was 0.051 to 0.029 magnitude, B to I, indicating magnetic activity. The difference in minima, 0.060 to 0.048 for B to I, indicates over contact light curves that could be in good thermal contact. A time of constant light occurs at our secondary minima and lasts some 54 minutes.

5. Light curve solution

The 2MASS, J–K = 0.205 ± 0.033 for the binary star; this corresponds to ~F5V ± 2.5, which yields a temperature of 6500 ± 200 K. Fast rotating binary stars of this type are noted for having strong magnetic activity, so the binary is of solar type with a convective atmosphere. The B, V, R, and I curves were pre-modeled with Binary Maker 3.0 (Bradstreet and Steelman 2002). Fits were determined in all filter bands which were very stable. The solution was that of an over contact eclipsing binary. The parameters were then averaged (q = 0.24, fill-out = 0.7, i = 81.5°, T_2 = 6394 K, with one 17° cool spot, T-FACT = 0.785) and input into a four-color simultaneous light curve calculation using the Wilson-Devinney Program (Wilson and Devinney 1971; Wilson 1990, 1994, 2004; van Hamme and Wilson 1998). The solution (Table 4) was computed in Mode 3 and converged to a solution. Convective parameters, g = 0.32, A = 0.5 were used. An eclipse duration of ~54 minutes was determined for our secondary eclipse and the light curve solution. Due to the total eclipses, the mass ratio, q, is well determined. The more massive component is the hottest one, making the system a A-type W UMa over contact binary. Third light was tried but ended with negative brightness values. The solution follows as Table 5. The normalized fluxes overlaid by our solution of UU Cam in B,V,R,I are shown in Figures 6 and 7, and the Roche Lobe representation at quarter orbital phases is shown in Figure 8. System dimensions (Tables 6 and 7) were calculated from the value of the semimajor axis, required by the Wilson program determined from Kepler's Law (with the mass ratio, period, and the estimated primary mass from the primary temperature), the stellar densities are found exactly from the orbital period and Binary Maker (contact mode from Roche Lobe equations), and radius values from the Wilson program. The volumes (from the average radius) and the densities give the mass of the two components. The log g values follow from GM/r^2.

6. Discussion

UU Cam is a A-type, W UMa binary. Since the eclipses were total, the mass ratio, q = 0.255, is well determined with a fill-out of 60%. The system has a component temperature difference of ~121 K, so it is in good thermal contact. One spot was needed in the final modeling. The inclination of ~82 degrees resulted in a ~50-minute time of constant light in the secondary eclipse. Its photometric spectral type indicates a surface temperature of ~6500 K for the primary component, making it a solar type binary. The calculated masses (see Table 7) are very near the main sequence star mass of ~1.33 $M_\odot$ (F5V) and the secondary (from the mass ratio) mass of ~0.34 $M_\odot$, making it very much undersized. The temperature of the secondary component (~6379 K) of a main sequence star would make it of type F6V instead of M3V as indicated by its mass.

7. Conclusion

The period of this binary indicates that it is increasing. This could be due to mass exchange with the flow toward the more massive component,

$$\frac{dM}{dt} = \frac{5.58 \times 10^{-8}\, M_\odot}{yr}, \qquad (5)$$

making the mass ratio more extreme (M_1/M_2 smaller). The mass ratio is approaching that of an extreme mass ratio binary as noted in many other of the authors' papers (Caton *et al.* 2019; Samec *et al.* 2017, 2015, 2012, and earlier). This means the two components may coalesce in time, making it, presently, a red novae progenitor. Combined with the high fill-out, this system is approaching the characteristics of Deep Low-Mass Ratio (DLMR) systems (Qian *et al.* 2005).

8. Future work

Radial velocity curves are needed to obtain absolute (not relative) system parameters.

References

Auer, R. F. 2021, *Open Eur. J. Var. Stars*, **210**, 1.
Baker, E. A. 1937, *Mon. Not. Roy. Astron. Soc.*, **98**, 65.
Bond, H. E. 1978, *Publ. Astron. Soc. Pacific*, **90**, 526.
Bradstreet, D. H., and Steelman, D. P. 2002, *Bull. Amer. Astron. Soc.*, **34**, 1224.
Caton, D., Gentry, D. R., Samec, R. G., Chamberlain, H., Robb, R., Faulkner, D. R., and Hill, R. 2019, *Publ. Astron. Soc. Pacific*, **131**, 054203.
Diethelm, R. 2009, *Inf. Bull. Var. Stars*, No. 5871, 1.
Diethelm, R. 2010, *Inf. Bull. Var. Stars*, No. 5920, 1.
Diethelm, R. 2011, *Inf. Bull. Var. Stars*, No. 5992, 1.
Diethelm, R. 2012, *Inf. Bull. Var. Stars*, No. 6011, 1.
Diethelm, R. 2013, *Inf. Bull. Var. Stars*, No. 6063, 1.
Hübscher, J. 2017, *Inf. Bull. Var. Stars*, No. 6196, 1.
Hübscher, J. and Lehmann, P. B. 2012, *Inf. Bull. Var. Stars*, No. 6026, 1.
Hübscher, J. Lehmann, P. B., Monninger, G., Steinbach, H. M., and Walter, F. 2010, *Inf. Bull. Var. Stars*, No. 5941, 1.
Hübscher, J. Lehmann, P. B., and Walter, F. 2012, *Inf. Bull. Var. Stars*, No. 6010, 1.
Hübscher, J. Paschke, A., and Walter, F. 2005, *Inf. Bull. Var. Stars*, No. 5657, 1.
Jayasinghe, T., *et al.* 2019, *Mon. Not. Roy. Astron. Soc.*, **486**, 1907.
Kim, C.-H., Lee, C.-U., Yoon, Y.-N., Park, S.-S., Kim, D.-H., Cha, S.-M., and Won, J.-H. 2006, *Inf. Bull. Var. Stars*, No. 5694, 1.
Kochanek, C. S., *et al.* 2017, *Publ. Astron. Soc. Pacific*, **129**, 104502.
Lehký, M., *et al.* 2021, *Open Eur. J. Var. Stars*, **211**, 1.
Liška,, J., and Skarka, M. 2015, *Open Eur. J. Var. Stars*, **169**, 38.
Pagel, L. 2020, *BAV J.*, No. 33, 1.
Pagel, L. 2022, *BAV J.*, No. 60, 1.
Paschke, A. 2020, O–C Gateway (http://var.astro.cz/ocgate/).

Pojmański, G. 2002, *Acta Astron.*, **52**, 397.
Poretti E. 1986, *Astrophys. Space Sci.*, **126**, 329.
Qian, S.-B., Yang, Y.-G., Soonthornthum, B., Zhu, L.-Y., He, J.-J., and Yuan, J.-Z. 2005, *Astron. J.*, **130**, 224.
Samec, R. G., Benkendorf, B., Dignan, J. B., Robb, R., Kring, J., and Faulkner, D. R. 2015, *Astron. J.*, **149**,146.
Samec, R. G., Figg, E. R., Labadorf, C. M., Faulkner, D. R., and van Hamme, W. 2012, *Observatory*, **132**, 98.
Samec, R. G., Gray, C. R., Caton, D., Faulkner, D. R., Hill, R., and van Hamme, W. 2017, *J. Amer. Assoc. Var. Star Obs.*, **45**, 140.
Schmidt, E. G., Chab, J. R, and Reiswig, D. E. 1995, *Astron. J.*, **109**, 1239.
Shappee, B. J., *et al.* 2014, *Astrophys. J.*, **788**, 48.
van Hamme, W. V., and Wilson, R. E. 1998, *Bull. Amer. Astron. Soc.*, **30**, 1402.
Wilson, R. E. 1990, *Astroophys. J.*, **356**, 613.
Wilson, R. E. 1994, *Publ. Astron. Soc. Pacific*, **106**, 921.
Wilson, R. E. 2004, *New Astron. Rev.*, **48**, 695.
Wilson, R. E., and Devinney, E. J. 1971, *Astrophys. J.*, **166**, 605.

Photometry, Period Study, and Light Curve Modeling of the HADS Variables BN Trianguli and V488 Geminorum

Kevin B. Alton
UnderOak Observatory, 70 Summit Avenue, Cedar Knolls, NJ 07927; kbalton@optonline.net

Received August 30, 2022; revised November 25, 2022; accepted December 2, 2022

Abstract Multi-bandpass (BVI_c) CCD-derived photometric data were acquired from BN Tri and V488 Gem (ATO J106.2184+10.4567) at Desert Blooms Observatory (DBO). Both of these pulsating variables are classified as high amplitude δ Scuti-type systems. Analysis of precise time-series light curve data from each target was accomplished using discrete Fourier transformation (DFT) which in both cases revealed a dominant fundamental mode (f_0) of oscillation along with associated harmonics. Furthermore, BN Tri exhibited two other statistically meaningful but low amplitude independent pulsation modes, while V488 Gem may possess up to four other independent oscillations. New times of maximum (ToMax) produced from both targets were combined with other ToMax timings mined from other sources (SuperWASP, TESS, and AAVSO-VSX) in order to update their corresponding linear ephemerides. Preliminary evidence suggests a secular increase in the fundamental oscillation period of BN Tri between 1999 and 2021. In contrast, secular analysis of the fundamental pulsation period for V488 Gem (ATO J106.2184+10.4567) revealed a sinusoidal-like variation in the pulse timing differences. These residuals, believed to result from a light-travel time effect (LiTE), were fit using simplex optimization. The resulting LiTE simulation suggested that V488 Gem is a binary system with a stellar-sized object in an eccentric orbit (7.91 ± 0.09 y). The evolutionary status, age, and physical nature of both HADS variables were investigated using the PAdova and TRieste Stellar Evolution Code for generating stellar tracks and isochrones. The totality of results including residence in the Galactic thin disk, near solar metallicity, mass predictions, and effective temperature estimates firmly support classification for both stars as high amplitude \delta Scuti-type variables.

1. Introduction

High amplitude δ Scuti stars, hereafter HADS, represent a very small percentage (<1%) of all δ Sct variables (Lee *et al.* 2008). They commonly oscillate (ΔV > 0.1 mag) via low-order single or double radial pulsation modes (Poretti 2003a; Poretti 2003b; Niu *et al.* 2013; Niu *et al.* 2017) driven by the κ-mechanism (opacity bump) resulting from partial ionization of He II (Pamyatnykh 1999). Many (~40%) are double mode pulsators exhibiting simultaneous pulsations in the fundamental and the first overtone mode with amplitudes generally higher in the fundamental mode (McNamara 2000). HADS variables have traditionally been divided according to metallicity relative to the Sun where [Fe/H] is defined as zero. The metal-poor ([Fe/H] << 0) group is classified as SX Phe-like stars, based on the prototype SX Phoenicis. Ostensibly they have shorter periods (0.02 < P < 0.125 d) and lower masses (~1.0–1.3 $M_\odot$) than related HADS variables possessing near solar metal abundance (McNamara 2011). SX Phe stars frequently reside in globular clusters (GC), which are ancient collections of Population II stars. The majority of these pulsators are classified as blue straggler stars, paradoxically appearing much younger than their GC cohorts. Balona and Nemec (2012) proposed that it is not possible to differentiate between δ Sct and field SX Phe variables based on pulsation amplitude, the number of pulsation modes, period, or even metallicity (Garg *et al.* 2010). Much more sensitive space instruments like the National Aeronautics and Space Administration's (NASA) Kepler Mission (Gilliland *et al*. 2010; Guzik 2021), the European Space Agency's (ESA) Convection, Rotation and planetary Transits (CoRoT) Mission (Baglin 2003), and the Canadian Microvariability and Oscillations of STars (MOST) Mission (Walker *et al.* 2003) have found many examples that violate the traditional differentiation between HADS and SX Phe pulsators. Balona and Nemec (2012) further contend that the evolutionary status of each star is the only way to distinguish between these two classes.

An additional classification scheme for δ Scuti stars was proposed by Qian *et al.* (2018) wherein two distinct groups of δ Scuti stars that fundamentally differed in effective temperature were uncovered from the Large Sky Area Multi-Object Fiber Spectroscopic Telescope (LAMOST) survey (Zhao *et al.* 2012). One group was identified as normal δ Scuti stars (NDSTs) when T_{eff} ranged between 6700–8500 K, while the other was defined as unusual and cool variable stars (UCVs) with T_{eff} values less than 6700 K. A more narrow fundamental pulsation period range (0.09–0.22 d) coupled with being slightly metal poor (–0.25 ≤ [Fe/H] ≤ 0.0) further differentiates the UCVs from the NDST group. Furthermore, once UCV stars were removed from the analyses, empirically based temperature-period, log g-period, and metallicity-period relationships could be derived for NDSTs.

Herein, a photometric investigation of BN Tri and V488 Gem (ATO J106.2184+10.4567) is described which includes Fourier deconvolution of their light curves to derive significant pulsation mode(s) along with an evolutionary analysis using PARSEC models (Bressan *et al.* 2012). CCD-derived photometric data for BN Tri (GSC 1763-0477) were first acquired from the ROTSE-I survey between 1999 and 2000 (Akerlof *et al.* 2000; Woźniak *et al.* 2004; Gettel *et al.* 2006) and later from the Catalina Sky (Drake *et al.* 2014) and SuperWASP (Pollacco *et al.* 2006) surveys. Khruslov (2007) initially identified this pulsating variable as a δ Scuti-type system based on data from the ROTSE-I survey. Later on (2019) light curves for BN Tri derived from time-series exposures (120 s) were produced by the TESS Science Processing Operations Center (TESS-SPOC) (Jenkins *et al.* 2016).

Evidence for the variability of V488 Gem can be found in light curve data (2002–2009) from the sparsely-sampled All Sky Automated Survey (ASAS) (Pojmański 2000; Pojmański *et al.* 2005) and the ASAS-SN (2014–2018) survey (Jayasinghe *et al.* 2018). Time-series light curve measurements from V488 Gem were also mined from the AAVSO International Database (Kafka 2021) and TESS-SPOC archives (Jenkins *et al.* 2016).

No reported times of maximum (ToMax) for BN Tri and only four for V488 Gem (Wils *et al.* 2013; Wils *et al.* 2014) have been found in the literature. This paper marks the first detailed multi-bandpass, secular, and evolutionary study for both HADS variables.

2. Observations and data reduction

Precise time-series images were acquired at Desert Blooms Observatory (DBO, USA, 31.941 N, 110.257 W) using a QSI 683 wsg-8 CCD camera mounted at the Cassegrain focus of a 0.4-m Schmidt-Cassegrain telescope. A Taurus 400 (Software Bisque) equatorial fork mount allowed continuous operation without the need to perform a meridian flip. The image (science, darks, and flats) acquisition software (TheSkyX Pro Edition 10.5.0; Software Bisque 2019) controlled the main and integrated guide cameras.

This focal-reduced (f/7.2) instrument produces an image scale of 0.76 arcsec/pixel (bin =2 × 2) and a field-of-view (FOV) of 15.9 × 21.1 arcmin. The CCD camera is equipped with B, V, and I_c filters manufactured to match the Johnson-Cousins Bessell prescription. Computer time was updated immediately prior to each session. Dark subtraction, flat correction, and registration of all images collected at DBO were performed using AIP4Win v2.4.1 (Berry and Burnell 2005). Instrumental readings were reduced to catalog-based magnitudes using the AAVSO Photometric All-Sky Survey (APASS) star fields (Henden *et al.* 2009; Henden *et al.* 2010; Henden *et al.* 2011; Smith *et al.* 2011) built into MPO Canopus v10.7.1.3 (Minor Planet Observer 2010). When necessary, I_c values were estimated from B, V, r', and i'-mag values according to Jester *et al.* 2005. The identities (HST Guide Star Catalog, Version GSC-ACT), Gaia DR2 J2000 coordinates and APASS color indices (B–V) for each ensemble of comparison stars used for differential aperture photometry are provided in Table 1. Since all program stars share a relatively small FOV, differential atmospheric extinction was ignored, while data from images taken below 30° altitude (airmass > 2.0) were excluded. All photometric data acquired from BN Tri and V488 Gem at DBO can be retrieved from the AAVSO International Database (Kafka 2021).

Uncertainty in comparison star measurements, calculated according to the so-called "CCD Equation" (Mortara and Fowler 1981), typically stayed within ±0.007 mag for V- and I_c- and ±0.010 mag for B-passbands. The identity, J2000 coordinates, and color indices (B–V) for these stars are provided in Table 1. AAVSO finder charts for BN Tri (Figure 1) and V488 Gem (Figure 2) are centered around each target along with a corresponding ensemble of comparison stars used for differential aperture photometry.

Time-of-Maximum (ToMax) light values and associated uncertainties from data acquired at DBO and those mined from AAVSO-VSX, TESS, and SuperWASP were calculated according to Andrych and Andronov (2019) and Andrych *et al.* (2020) using the "Polynomial Fit" routine in the program MAVKA (https://uavso.org.ua/mavka/). Simulation of extrema was automatically optimized by finding the most precise degree (α) and best fit algebraic polynomial expression.

Long-term or secular changes in the fundamental pulsation period can sometimes be revealed by plotting the difference between the observed maximum light times and those predicted by a reference epoch against cycle number. These pulsation timing differences (PTD) vs. epoch were fit using scaled Levenberg-Marquardt algorithms (QtiPlot 0.9.9-rc9; https://www.qtiplot.com/). Results from these analyses are separately discussed for each HADS variable in the subsections (3.1 and 3.2) below.

No medium-to-high resolution classification spectra were found in the literature for either variable. As such, the effective temperature (T_{eff}) of each star has been estimated using color index (B–V) data acquired at DBO and from the 2MASS survey. 2MASS J and K values were transformed to (B–V) (http://brucegary.net/dummies/method0.html). In both cases, interstellar extinction (A_V) was calculated (E(B–V) × 3.1) using the reddening values (E(B–V)) estimated from Galactic dust map models reported by Schlafly and Finkbeiner (2011). Additional effective temperature values were mined from the Gaia DR2 (http://vizier.u-strasbg.fr/viz-bin/VizieR?-source=I/345/gaia2), LAMOST DR5 (http://dr5.lamost.org/search), and TESS (https://exofop.ipac.caltech.edu/tess/) websites. The mean T_{eff} value derived from all sources (Table 2) indicates an effective temperature (7371 ± 186 K) for BN Tri that probably ranges in spectral class between A8V and F0V. The reader should be aware of dangers associated with adopting a single T_{eff} value for a pulsating variable. With the exception of light curves acquired at DBO it is not known when T_{eff} measurements were made during each pulsation cycle. For example, with BN Tri (Figure 3) the largest difference between maximum and minimum light is observed in the blue passband (ΔB = 0.24 mag), followed by V (ΔV = 0.18 mag) and finally the smallest difference detected in infrared (ΔI_c = 0.11 mag). Plotting (B–V) against phase (Figure 4) shows significant color index change (Δ = 0.07 mag) going from maximum ((B–V)≃0.21 mag) to minimum light ((B-V)≃0.28 mag). This corresponds to a T_{eff} which ranges between 7650 and 7363 K.

Similarly, dereddened color indices ($(B–V)_0$) for V488 Gem gathered from different sources are also listed in Table 2. The mean value (7129 ± 202 K) corresponds to a star that likely ranges in spectral class between A9V and F1V. An examination of the light curves acquired at DBO reveals that the largest difference between maximum and minimum light is observed in the blue passband (ΔB = 0.64 mag), followed by V (ΔV = 0.48 mag) and finally the smallest difference detected in infrared (ΔI_c = 0.29 mag). Plotting (B–V) against phase (Figure 5) shows significant color index change (Δ = 0.21 mag) going from maximum ((B–V)≃0.15) to minimum light ((B–V)≃0.36) where V488 Gem is least bright. These values correspond to an effective temperature which ranges between 7893 and 7023 K.

Table 1. Astrometric coordinates (J2000), V-mags and color indices (B–V) for BN Tri, V488 Gem and their corresponding stars used for ensemble aperture photometry.

Star Identification	*R.A. (J2000) h m s*	*Dec. (J2000) ° ′ ″*	*V-mag*[a]	*(B–V)*[a]
BN Tri	01 54 58.043	+29 47 37.06	12.010	0.302
GSC 1763-0205	01 55 26.596	+29 51 53.40	12.395	0.553
GSC 1763-0151	01 55 44.066	+29 54 05.17	11.524	0.563
GSC 1763-1011	01 55 07.094	+29 54 44.61	12.172	0.684
GSC 1763-0859	01 55 45.534	+29 43 45.11	11.518	0.509
V488 Gem	07 04 52.410	+10 27 24.20	12.596	0.533
GSC 7530-1915	07 04 29.567	+10 20 43.61	10.838	0.397
GSC 7530-1677	07 04 25.243	+10 17 55.43	12.378	0.417
GSC 7530-1473	07 05 21.822	+10 18 48.90	10.869	0.483
GSC 7530-2574	07 05 28.505	+10 25 32.52	12.183	0.407
GSC 7530-1301	07 05 06.695	+10 25 53.10	11.776	0.634

[a] *V-mag and (B–V) for comparison stars derived from APASS database described by Henden* et al. *(2009, 2010, 2011) and Smith* et al. *(2011).*

3. Results and discussion

Results and detailed discussion about the determination of ephemerides are individually provided for BN Tri and V488 Gem in this section. Thereafter, deconvolution of pulsation period(s) using a Discrete Fourier Transform (DFT) routine featured in Period04 (Lenz and Breger 2005) are separately examined. Finally, preliminary estimates for mass ($M_\odot$) and radius ($R_\odot$), along with corresponding calculations for luminosity ($L_\odot$), surface gravity (log (g)), and bolometric magnitude (M_{bol}), are derived from study observations and predictions based upon evolutionary modeling.

3.1. BN Tri

3.1.1. Photometry and ephemerides

Photometric values in B (n = 290), V (n = 289), and I_c (n = 278) acquired between 2020 December 1 and 2021 November 29 were each period-folded producing light curves in three passbands (Figure 3). Included in these determinations were 45 new ToMax values which are summarized in Table 3. BN Tri was also imaged during the SuperWASP survey (Pollacco *et al.* 2006), which provided a rich source of photometric data taken (30-s exposures) at modest cadence that repeats every 9 to 12 min. In some cases (n = 69) these measurements taken between 2004 and 2006 were amenable to extrema estimation using MAVKA.

Although primarily designed to capture very small host star brightness changes during an exoplanet transit, the TESS Mission (Ricker *et al.* 2015; Caldwell *et al.* 2020) also provides a wealth of light curve data for many variable stars. The four TESS cameras produce a combined FOV of 24° × 96°. Each ecliptic hemisphere is divided into 13 partially overlapping sectors (24° × 96°) that extend from 6° latitude to the ecliptic pole. Each sector is then continuously observed for 27.4 days (two spaceship orbits), with the camera boresight pointing at ± 54° latitude or approximately antisolar. To observe the next sector, the FOV is shifted eastward in ecliptic longitude by about 27°. Each hemisphere takes one year to image with the all-sky survey completed in ~2 y. A pre-selected number of dwarf

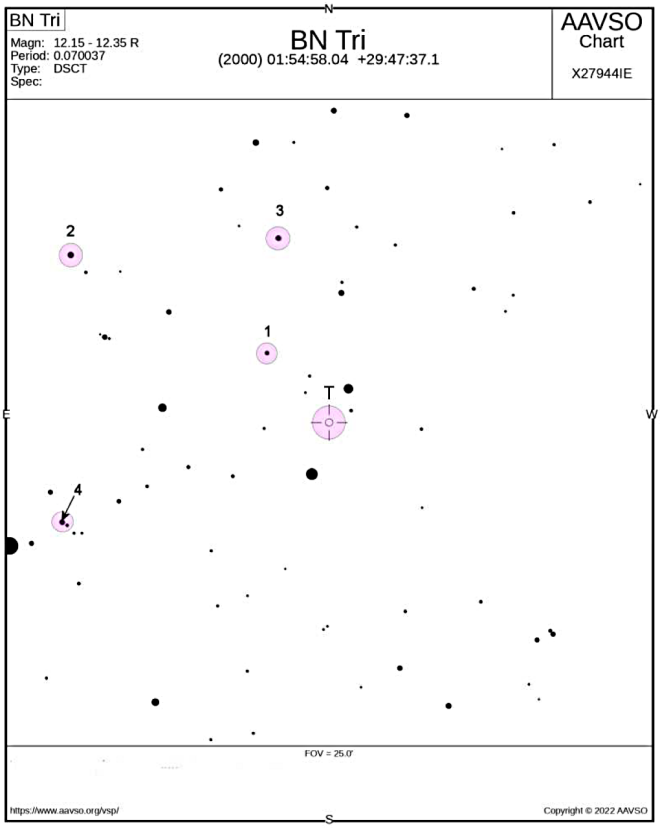

Figure 1. Finder chart for target (T) variable BN Tri (center) also showing the comparison stars (1–4) used for aperture-derived ensemble photometry.

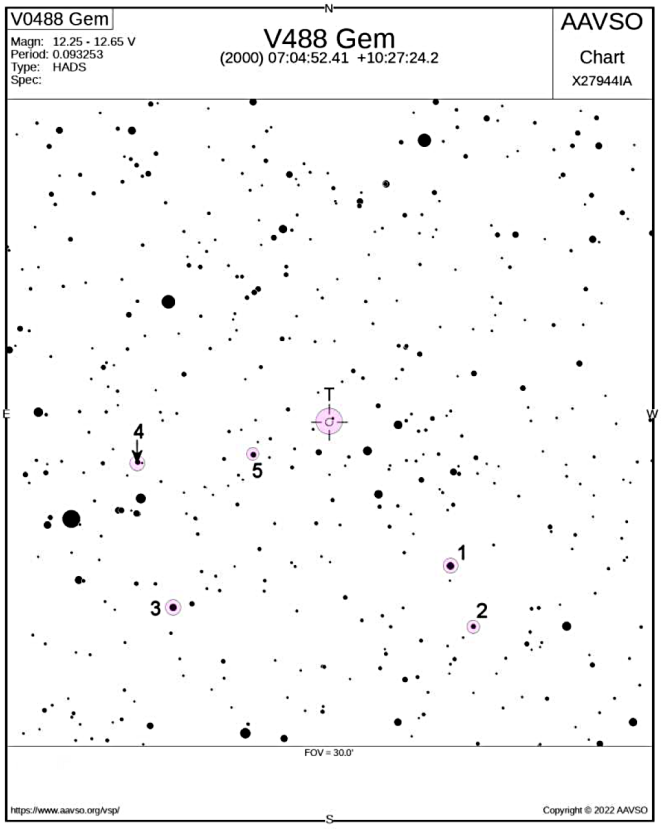

Figure 2. Finder chart for target (T) variable V488 Gem (center) also showing the comparison stars (1–5) used for aperture-derived ensemble photometry.

Table 2. Derivation of the eective temperature (T_{eff}) of BN Tri and V488 Gem based upon estimates from multiple sources.

	2MASS	*DBO*	*Gaia DR2*[a]	*LAMOST DR5*[b]	*TESS*[c]	*Mean*
BN Tri						
$(B–V)_0$[d]	0.307 (44)	0.246 (20)	—	—	—	—
T_{eff}[e] (K)	7181 (225)	7504 (110)	7556 -204+203	-	7243 (152)	7371 (186)
Spectral Class[f]	A9V-F1V	A7V-A9V	A7V-A9V	—	A9V-F0V	A8V-F0V
V488 Gem						
$(B–V)_0$[d]	0.356 (48)	0.259 (39)	—	—	—	—
T_{eff}[e] (K)	6935 (309)	7434 (213)	7216 -122+149	7085 (58)	6977 (166)	7129 (202)
Spectral Class[f]	F0V-F4V	A8V-F0V	A9V-F1V	F0V-F2V	F0V-F4V	A9V-F1V

[a] *Gaia Collab. (2016, 2018).* [b] *Zhao* et al. *(2012).* [c] *https://exofop.ipac.caltech.edu/tess/ .* [d] *Intrinsic $(B–V)_0$ determined using E(B–V) reddening value (BN Tri = 0.0762 ± 0.0017 and V488 Gem = 0.0828 ± 0.0019); T_{eff} interpolated from Pecaut and Mamajek (2013).* [e] *Mean T_{eff} values adopted for evolutionary modeling.* [f] *Spectral class range estimated from Pecaut and Mamajek (2013).*

Table 3. Sample table for BN Tri times-of-maximum (November 15, 1999–November 29, 2021), cycle number and fundamental pulsation timing difference (PTD) between observed and predicted times derived from the updated linear ephemeris (Equation 1).

HJD 2400000+	*HJD Error*	*Cycle No.*	*PTD*	*Ref.*
51497.8616	0.0010	–114942	0.00386	1
53200.6897	0.0006	–90628	0.00073	2
53203.7040	0.0007	–90585	0.00350	2
58767.7723	0.0002	–11138	0.00023	4
58767.8422	0.0002	–11137	0.00010	4
58767.9119	0.0002	–11136	–0.00026	4

References: (1) NSVS (Akerlof et al. *2000; Wozniak* et al. *2004; Gettel* et al. *2006); (2) SuperWASP (Polacco* et al. *2006); (4) TESS-SPOC (Jenkins* et al. *2016). Full table available at: ftp://ftp.aavso.org/public/datasets/3852-Alton-bntri.txt. All references relevant to the fulltable that appears on the AAVSO ftp site are included in the References section of this article and in the full ftp table.*

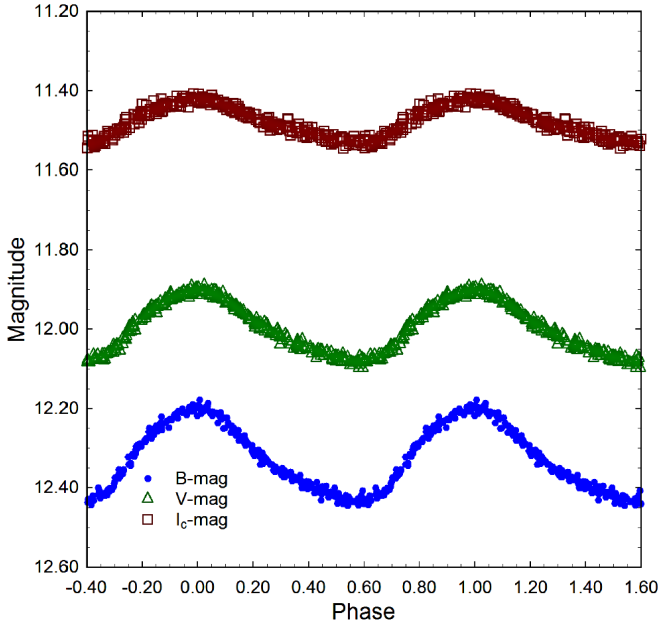

Figure 3. Period (0.070035 ± 0.000002 d) folded CCD light curves for BN Tri produced from photometric data obtained between 2020 December 1 and 2021 November 29 at DBO. The top (I_c), middle (V), and bottom curve (B) shown above were reduced to APASS-based catalog magnitudes using MPO Canopus.

Table 4. Fundamental frequency with corresponding harmonics and independent oscillations detected following DFT analysis of time-series photometric data from BN Tri acquired during the TESS Mission (October 8 through October 30, 2019).

	Freq. (c · d^{-1})	*Freq. Err.*	*Amp. (flux)*	*Amp. Err.*	*Phase Err.*	*Phase S/N*	*Amp.*
f_0	14.2789	0.0002	0.0538	0.0043	0.1776	0.0067	767
$2f_0$	28.5578	0.0001	0.0098	0.0001	0.2844	0.0008	128
$3f_0$	42.8367	0.0004	0.0032	0.0001	0.7797	0.0029	58
$4f_0$	57.1156	0.0006	0.0018	0.0001	0.8903	0.0063	32
$5f_0$	71.3922	0.0395	0.0008	0.0002	0.9874	0.1056	14
f_1	14.2502	0.0027	0.0008	0.0038	0.3790	0.0822	11
f_2	25.9221	0.0019	0.0006	0.0001	0.2509	0.0113	10

main-sequence stars were initially targeted for photometric study using two-minute exposures. The TESS CCD detector bandpass ranges between 600 and 1000 nm and is centered near the Cousins I band (I_c). One such BN Tri imaging campaign started on 2019 October 8 and ran every two min through 2019 November 2 but only produced evaluable light curve data during two time segments (2019 October 8–October 15 and 2019 October 21–October 30). Raw flux readings were processed by the TESS Science Processing Operations Center (TESS-SPOC) to remove long term trends using so-called Co-trending Basis Vectors (CBVs). These results identified as "Pre-search Data Conditioning Simple Aperture Photometry" (PDCSAP) flux are usually cleaner data than the SAP flux. A large number (n = 101) of maximum light timings were generated (MAVKA) from the TESS observations. These, along with three more ToMax values interpolated from sparse-sampling surveys (NSVS and ASAS-SN), were used to determine whether any secular changes in the fundamental pulsation period could be detected from the PTD residuals (Table 3).

Since there appeared to be a curvilinear relationship between the ToMax residuals and epoch (Figure 6), near term values (2015–2021) were used to establish an up-to-date linear ephemeris (Equation 1):

$$\text{Max (HJD)} = 2459547.8220(2) + 0{:}0700350(1)\ E. \quad (1)$$

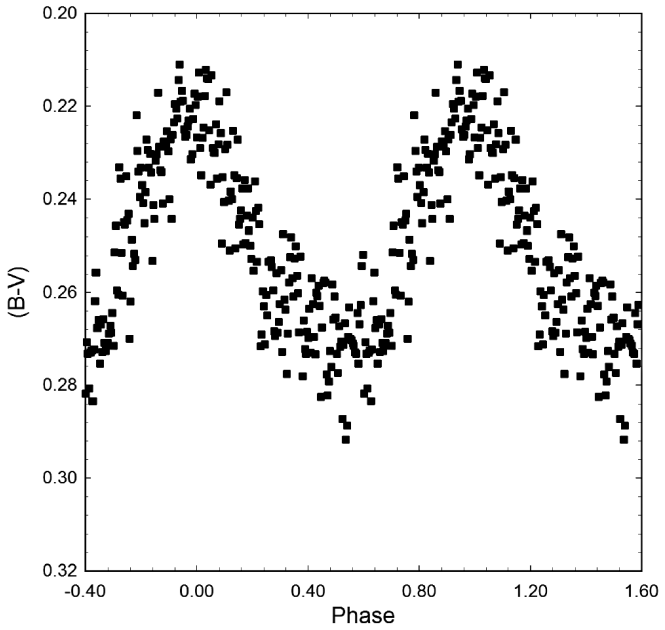

Figure 4. Color curve from BN Tri illustrating significant color change as maximum light B–V≃ 0.22 mag.) descends to minimum light B–V ≃ 0.28 mag, where this variable is least bright.

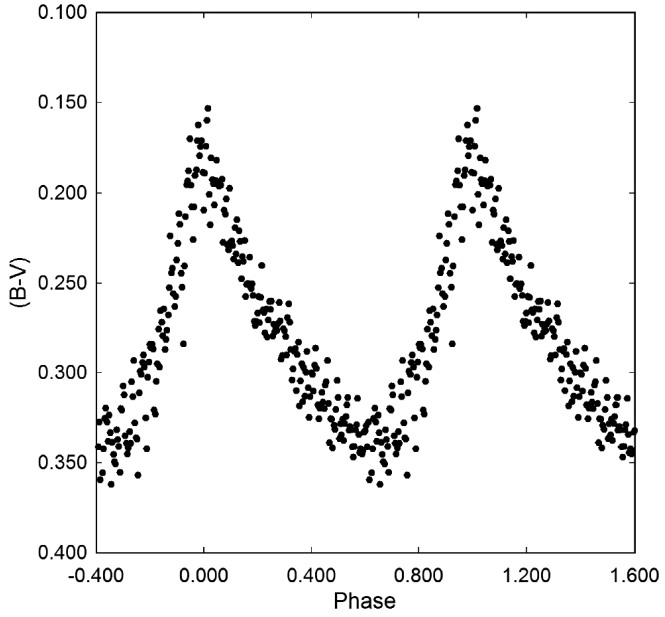

Figure 5. Color curve from V488 Gem illustrating significant color change as maximum light B–V≃ 0.21 mag.) slowly descends to minimum light B–V≃ 0.36 mag.).

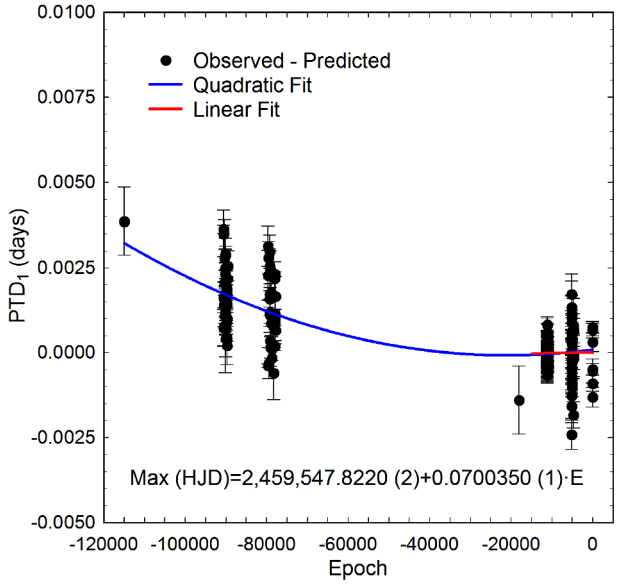

Figure 6. The upwardly directed quadratic fit (Equation 2) to the PTD vs. epoch (cycle number) data is shown with a solid blue line and suggests the pulsation period of BN Tri is increasing with time. The linear ephemeris (Equation 1) was determined from near-term data acquired between 2019 and 2021 (solid red line).

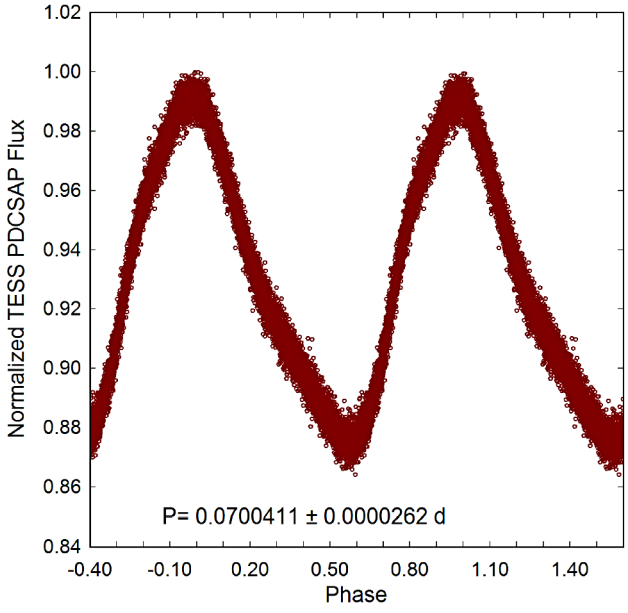

Figure 7. Period (0.0700411 ± 0.0000262 d) folded light curve for BN Tri produced from the TESS Mission between 2019 October 8 and October 30. Data were normalized to maximum light using PDCSAP flux values.

The difference between the observed ToMax times and those predicted by the linear ephemeris (Equation 1) plotted against epoch (cycle number) was best fit by a quadratic relationship (Equation 2) where:

$$\text{Max(HJD)} = 8.8983 \cdot 10^{-5} + 1.5826 \cdot 10^{-8}\,\text{E} + 3.7481 \cdot 10^{-13}\,\text{E}^2. \quad (2)$$

Since the quadratic term coefficient ($+3.7481 \cdot 10^{-13}$) is positive, this result would suggest that the fundamental pulsation period has been slowly increasing with a (1/P) dP/dt value of 5.6 (1.8) $\cdot$ 10^{-8} y^{-1}, a result consistent with observations for Population I radial pulsators (Breger and Pamyanykh 1998). Evolutionary models predict the overwhelming majority should experience increasing periods (Breger and Pamyanykh 1998). In reality there appears to be an equal distribution between period increases and decreases. Pulsation period changes of δ Scuti variables can occur from a variety of evolutionary and non-evolutionary causes (Templeton 2005). These could include undiscovered light-time effects due to binarity, non-linear interactions between pulsation modes, or secular changes in the chemical nature of the star (Neilson *et al.* 2016). Many period changes in δ Scuti systems greatly exceed the rates

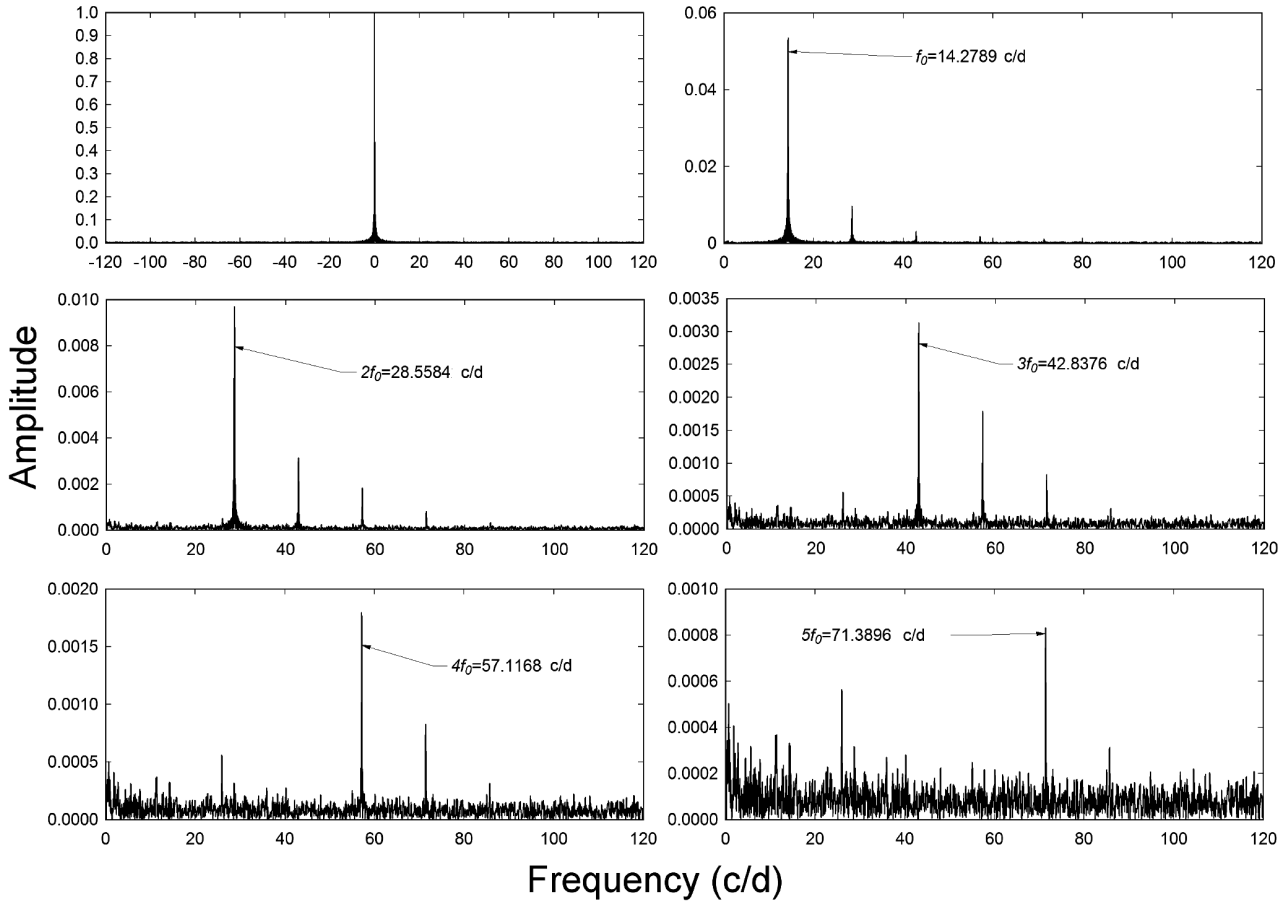

Figure 8. DFT spectral window (top left panel) and amplitude spectra showing the fundamental oscillation frequency (f_0), corresponding harmonics ($2f_0$, $3f_0$, $4f_0$, and $5f_0$), and other independent oscillations (f_1 and f_2) which describe the BN Tri light curves acquired from 2019 October 8 to October 30 during the TESS Mission.

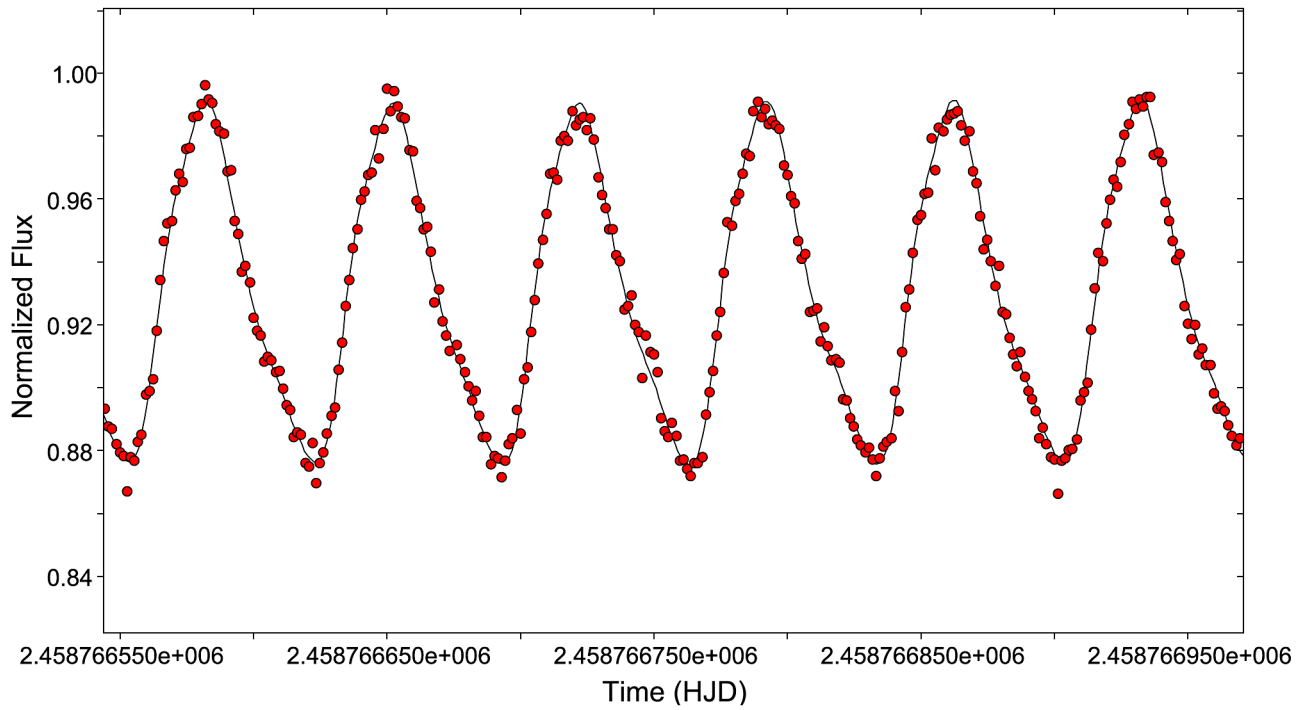

Figure 9. Representative DFT model fit from BN Tri light curve data acquired during TESS Mission (2019 October 10, 01:12 to 10:48 UTC). Observed data are shown as red circles while the DFT-derived simulation is represented with a black line.

Table 5. Global stellar parameters for BN Tri using values reported from observations at DBO and those predicted from evolutionary modelling.

Parameter	*Observed*	*PARSEC (Z = 0.020)*
Mean T_{eff} [K]	7371 ± 186	—[a]
Mass [$M_\odot$]	1.808 ± 0.033	1.759 ± 0.014
Radius [$R_\odot$]	2.185 ± 0.136	2.120 ± 0.021
Luminosity [$L_\odot$]	12.692 ± 0.92	—[a]
rho [g/cm^3]	0.245 ± 0.027	0.260 ± 0.008
log g [cgs]	4.017 ± 0.032	4.031 ± 0.016
Q [d]	0.0292 ± 0.0014	0.0297 ± 0.0011

[a] *T_{eff} and luminosity fixed according to the observed values.*

expected from theoretical models of stellar evolution (Handler 2000; Breger and Pamyatnykh 1998). When the evolutionary model includes the effect from convection core overshoot, improvement between observed rates and model predicted rates was obtained for some but not all stars. The bottom line is that based on current models, evolution alone cannot account for the period changes observed in δ Scuti stars. There may be unknown physical processes at work that the models do not address.

Light curves from BN Tri, and in general other HADS variables, are asymmetrical, characterized by a rapid increase in brightness producing a sharply defined maximum peak. Thereafter a slower decline in magnitude results in a broad minimum. This behavior is commonly observed with pulsating F- to A-type stars. The highly precise flux measurements (PDCSAP $< \pm 0.0038$ $e^- \cdot s^{-1}$) from the TESS satellite revealed very little change in amplitude or light curve morphology (Figure 7) over time.

3.1.2. Discrete Fourier transformation

Discrete Fourier transformation (DFT) was applied using Period04 (Lenz and Breger 2005) to extract statistically significant pulsation frequencies (frequency range = 0–120 $c \cdot d^{-1}$) which best describe the BN Tri light curves. Pre-whitening steps which successively remove the previous most intense signals were employed to draw out other potential oscillations from the residuals. Results derived from BN Tri observations conducted during the TESS Mission (2019 October 8–October 30) are presented in Table 4. A detection limit (S/N ≥ 6) was adopted based on a time-series study with TESS data (Baran and Koen 2021). Uncertainties in frequency, amplitude, and phase were estimated by the Monte Carlo simulation (n = 400) routine featured in Period04. As described above, amplitude-frequency spectra from the TESS Mission (2019 October 8–October 30) are shown in Figure 8, while DFT-derived modelling results indicate a very good fit for the TESS light curve data (Figure 9). Overall, these results are consistent with a HADS variable dominated by a fundamental radial pulsation at $14.2789 \pm 0.0001\ c \cdot d^{-1}$ with potentially two other independent low amplitude pulsations ($f_1 = 14.2502 \pm 0.0001$ and $f_2 = 25.9221 \pm 0.0001\ c \cdot d^{-1}$). The shape of the TESS light curve is best described by harmonics of the fundamental which are detectable up to 5 orders ($2f_0$–$5f_0$). Stellingwerf (1979) defined pulsation modes for δ Scuti stars by calculating the period ratios expected from the first four radial modes. Accordingly the first overtone exists when P_1/P_0 falls between 0.756 and 0.787, the second overtone when P_2/P_0 is between 0.611 and 0.632, and finally the third overtone when P_3/P_0 is between 0.500 and 0.525. Neither f_1 nor f_2 meets the period ratio criteria expected from the first, second, or third radial overtones. They may be artefacts or potentially non-radial modes of oscillation that are becoming increasingly more evident with highly precise photometric measurements of HADS variables taken from space telescopes (Poretti *et al.* 2011).

Fourier deconvolution of light curves (BVI_c) acquired at DBO produced nearly the same fundamental pulsation frequency ($\overline{X} = 14.2786 \pm 0.0001\ c \cdot d^{-1}$) but only revealed statistically significant harmonics at $2f_0$ and $3f_0$. This is testimony to the very high quality of the photometric data acquired by the TESS satellite compared to those produced from ground-based observations.

3.1.3. Global parameters

The Gaia EDR3 parallax-derived distance reported for this variable is 957 ± 16 pc. Since a parallax-derived value is considered the gold-standard for measuring distances, hereafter all calculations dependent on d (pc) use the Gaia EDR3 (Gaia Collab. 2021) value. Absolute V-mag ($M_V = 1.947 \pm 0.078$ mag) was calculated from:

$$M_V = -5 \cdot \log(d) + m - A_V + 5. \quad (3)$$

when $A_V = 0.2567 \pm 0.0059$ mag and $V_{avg} = 12.527 \pm 0.027$ mag. The average V-mag was adopted as a compromise value due to the significant differences between maximum and minimum light.

Luminosity ($12.68 \pm 0.92\ L_\odot$) was determined from:

$$L_* / L_\odot = 10^{((M_{bol\odot} - M_{bol*}) / 2.5)}, \quad (4)$$

When $M_{bol\odot} = 4.74$ mag, $M_V = 1.947 \pm 0.078$ mag, and BC = 0.0338 mag (Flower 1996), then $M_{bol*} = 1.981 \pm 0.078$ mag.

Photometric and spectroscopic observations of eclipsing binary stars are commonly used to determine component mass by applying the laws of gravity and motion derived by Isaac Newton and Johannes Keppler. In contrast, the mass of an isolated field star like BN Tri or V488 Gem is very difficult to determine by direct measurement. However, it is possible under certain conditions to estimate mass according to Eker *et al.* (2018), who empirically derived a mass-luminosity relationship from main sequence (MS) stars in detached binary systems when $1.05 < M_\odot \leq 2.40$. This expression:

$$\log(L) = 4.329(\pm 0.087) \cdot \log(M) - 0.010(\pm 0.019), \quad (5)$$

leads to a mass of $1.808 \pm 0.033\ M_\odot$ for BN Tri. This result, summarized in Table 5 along with others derived from DBO data, is fairly typical for a HADS variable. Finally, the radius ($R_* = 2.185 \pm 0.136\ R_\odot$) was estimated using the well-known relationship where:

$$L_* / L_\odot = (R_* / R_\odot)^2\ (T_* / T_\odot)^4, \quad (6)$$

Values derived for density ($\rho_\odot$), surface gravity (log g), and pulsation constant (Q are also included in Table 5. Stellar density (ρ_*) in g/cm^3 was calculated according to:

$$\rho_* = 3 \cdot M_* \cdot m_\odot / 4\pi (R_* \cdot r_\odot)^3, \quad (7)$$

where $m_\odot$ = solar mass (g), $r_\odot$ = solar radius (cm), M_* is the mass, and R_* the radius of BN Tri in solar units. Using the same algebraic assignments, surface gravity (log g) was determined by the following expression:

$$\log g = \log (M_* \cdot m_\odot \cdot G / (R_* \cdot r_\odot)^2, \quad (8)$$

The dynamical time that it takes a p-mode acoustic wave to internally traverse a star is strongly correlated with the stellar mean density, which can be expressed in terms of other measurable stellar parameters where:

$$\log(Q) = -6.545 + \log(P) + 0.5\log(g) + 0.1M_{bol} + \log(T_{eff}). \quad (9)$$

The full derivation of this expression can be found in Breger (1990). The resulting Q values provided in Table 5 are within the range (Q = 0.025–0.049 d) observed from other δ Sct variables (Breger 1979; Breger and Bregman 1975; North *et al.* 1997; Joshi and Joshi 2015; Antonello and Pastori 1981; Poro *et al.* 2021), where all radial pulsations are derived from the fundamental.

3.1.4. Evolutionary status of BN Tri

The evolutionary status of BN Tri was evaluated (Figure 10) using the PAdova and TRieste Stellar Evolution Code (PARSEC) for stellar tracks and isochrones (Bressan *et al.* 2012) and then plotted (log T_{eff} vs. log($L/L_\odot$)) in a theoretical Hertzsprung-Russell diagram (HRD). The thick solid maroon-colored line defines the zero-age main sequence (ZAMS) position for stars with metallicity Z = 0.020. The two broken lines nearly perpendicular to the ZAMS delimit the blue (left) and red (right) edges of the theoretical instability strip for radial low-p modes (Xiong *et al.* 2016). Also included are the positions of several known HADS and SX Phe-type variables (Balona 2018).

The solid black circle with error bars indicates the fixed position for observed T_{eff} and $L_\odot$ values (Table 5) used to ultimately estimate mass, radius, and age from the PARSEC model when Z = 0.020 or Z = 0.004.

Ironically a single undisputed value for metallicity from the star closest to us remains elusive. Over the last few decades, the reference metallicity values used by several authors for computing stellar models have ranged between Z =0 .012 and 0.020 (Amard *et al.* 2019). Serenelli *et al.* (2016) took great exception to a high solar metallicity value (Z = 0.0196 ± 0.0014) based on in situ measurements of the solar wind (von Steiger and Zurbuchen 2016; Vagnozzi *et al.* 2017) rather than abundance traditionally determined by spectroscopic analysis. Despite the uncertainty in defining an absolute value for $Z_\odot$, an estimate for metal abundance is still required in order to predict the mass, radius, and age of BN Tri from theoretical evolutionary tracks. A Z-value can be estimated indirectly from its location in the Milky Way. According to the following expression:

$$z = d \ \sin(b), \quad (10)$$

the distance in parsecs (z) below or above the Galactic plane can be calculated where d = 957.12 ± 15.76 pc and b is the Galactic latitude (–31.084265°). In this case its position ~500 pc below the Galactic plane suggests residence in the thin disk (Li and Zhao 2017) rather than the halo where many metal poor ([Fe/H] < –1.6) stars like SX Phe-type variables reside (Carollo *et al.* 2010). Furthermore, Qian *et al.* (2018) report an empirical relationship between metallicity ([Fe/H]) and the fundamental pulsation period P) for an NDST star according to the following:

$$[Fe / H] = -0.121(0.026) + 0.92(0.25) \times P. \quad (11)$$

As expected for a thin disk resident, the predicted value ([Fe/H] = –0.056 ± 0.031) suggests that BN Tri approaches solar metallicity, or at most a few times lower.

Two separate PARSEC evolutionary models (Bressan *et al.* 2012) ranging in age between 1×10^8 and 2.21×10^9 y are illustrated in Figure 10. The red solid lines show the model tracks (M_* = 1.70, 1.75, and 1.80 $M_\odot$) over time when Z = 0.020, while the solid blue lines define the metal-poor models (M_* =1.40, 1.45, and 1.50 $M_\odot$) where Z = 0.004. The latter simulations correspond to a decrease in metallicity by a factor of 3 to 5, depending on the reference solar metallicity. Assuming Z =0.020, it can be shown by linear extrapolation that BN Tri would have a mass of 1.759 ± 0.014 $M_\odot$ and a radius of 2.12 ± 0.02 $R_\odot$. The position of this intrinsic variable near the $M_\odot$ = 1.75 evolutionary track extrapolates to an age of 0.996 ± 0.147 Gyr, suggesting it is a moderately evolved MS object lying amongst other HADS variables closer to the blue edge of the instability strip.

By comparison, if BN Tri is more metal deficient (Z = 0.004), then it would have a somewhat greater radius (2.26 ± 0.12 $R_\odot$), but would be less massive (1.44 ± 0.026 $M_\odot$). Its position closest to the 1.45 $M_\odot$ track lies prior to the HRD region where evolutionary tracks of low metallicity stars begin stellar contraction near the end of core hydrogen burning. This star would still be a MS object but with an age approaching 1.96 ± 05 Gyr.

It should be noted that the theoretical mass (1.759 $M_\odot$) where Z = 0.020 is much closer to results (1.773 ± 0.032 $M_\odot$) independently determined using an empirical mass-luminosity relationship. If or when high resolution spectroscopic data become available in the future, uncertainty about the mass and metallicity of BN Tri will likely improve.

3.2. V488 Gem

A total of 330 photometric values in B-, 323 in V-, and 320 in I_c-passbands were acquired at DBO for V488 Gem between 2019 December 21 and 2020 January 18 (Figure 11). Included in these determinations were 25 new ToMax values which are listed in Table 6. ToMax values (n = 79) were determined (MAVKA) from the TESS-SPOC survey (2020 December 31 through 2021 January 13) along with 26 other ToMax values using data mined from the AAVSO VSX archives. An updated linear ephemeris (Figure 12) based on near-term PTD values (2019 December 21–2022 February 7) was derived as follows:

$$\text{Max(HJD)} = 2459618.3444(1) + 0.0932493(1)\ E. \quad (12)$$

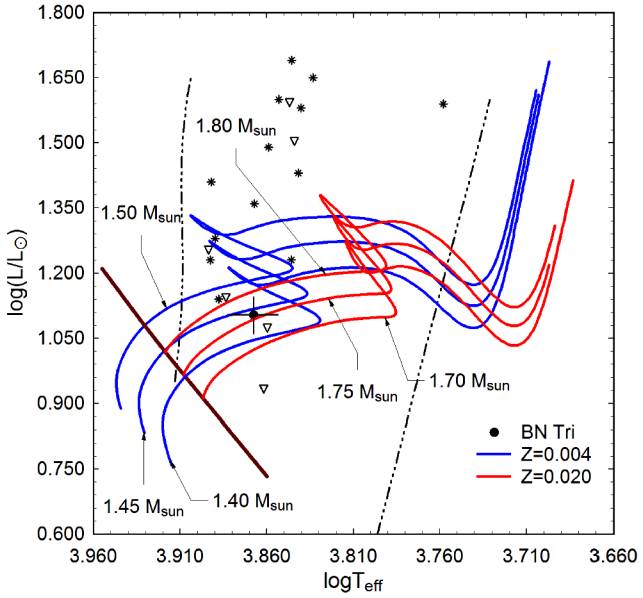

Figure 10. Evolutionary tracks (red lines, Z = 0.020, and blue lines, Z = 0.004) derived from PARSEC models (Bressan *et al.* 2012) showing the position of BN Tri (black filled circle) relative to ZAMS (thick maroon line) and within the theoretical instability strip (black dashed lines) for low-order radial mode δ Scuti pulsators. The position of other HADS (*) and SX Phe (open triangle) variables reported by Balona (2018) are included for comparison.

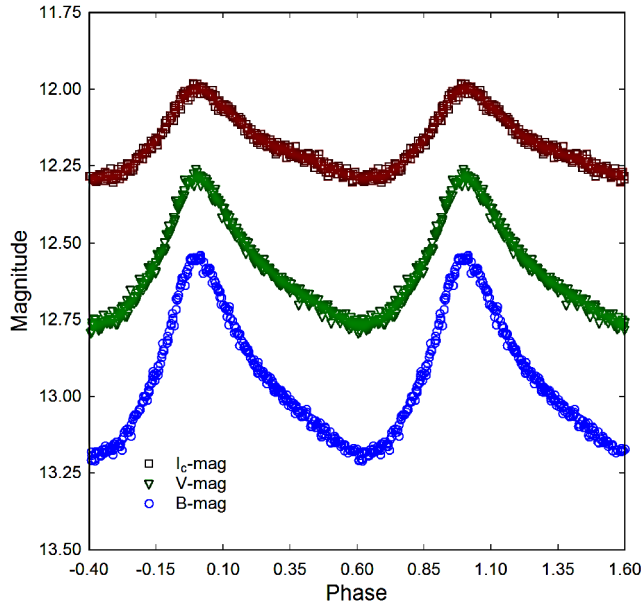

Figure 11. Period (0.093258 ± 0.000001 d) folded CCD light curves for V488 Gem produced from photometric data obtained at DBO between 2019 December 21 and 2020 January 18. The top (I_c), middle (V), and bottom curve (B) shown above were reduced to APASS-based catalog magnitudes using MPO Canopus.

Table 6. Sample table of V488 Gem times-of-maximum (January 31, 2012–February 7, 2022), cycle number and fundamental pulsation timing difference (PTD) between observed and predicted times derived from the updated linear ephemeris (Equation 12).

HJD 2400000+	*HJD Error*	*Cycle No.*	*PTD*	*Ref.*
55958.4130	0.0033	–39249	0.00994	1
56341.3893	0.0015	–35142	0.01141	2
56637.4594	0.0008	–31967	0.01502	2
56656.3897	0.0005	–31764	0.01572	2
59217.4658	0.0001	–4299	0.00010	5
59217.5587	0.0002	–4298	–0.00025	5
59217.6519	0.0002	–4297	–0.00030	5
59217.7463	0.0002	–4296	0.00090	5

References: (1) Wils et al. *(2013); (2) Wils* et al. *(2014); (5) TESS-SPOC (Jenkins* et al. *2016). Full table available at: ftp://ftp.aavso.org/public/datasets/3852-Alton-v488gem.txt. All references relevant to the full table that appears on the AAVSO ftp site are included in the References section of this article and in the full ftp table.*

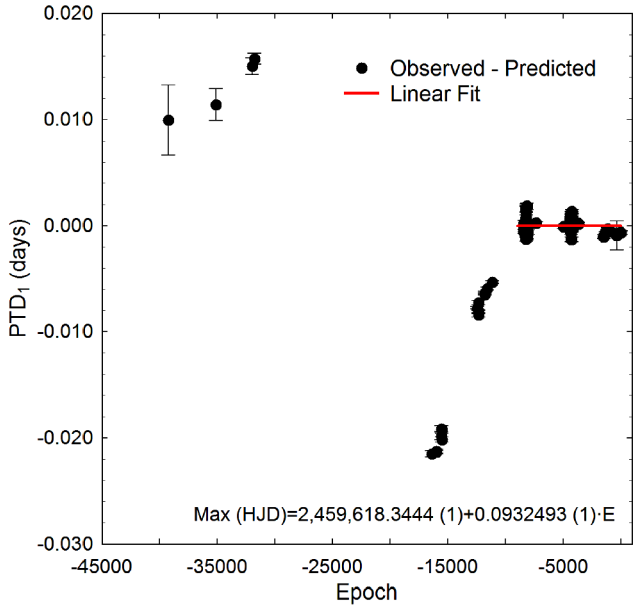

Figure 12. Plot of pulsation timing differences (PTD) vs epoch (cycle number). A linear ephemeris (Equation 12) represented by a solid red line) was determined from near-term (2019–2022) ToMax data.

Table 7. Solution to the putative light-time effect (LiTE) observed from sinusoidal-like changes in V488 Gem fundamental pulsation timings.

Parameter	*Units*	*LiTE values*
HJD0 – 2400000	—	58125.7815 ± 0.0007
P_{orb}	(y)	7.911 ± 0.093
ω	(°)	12.57 ± 1.89
A (semi-ampl.)	(d)	0.0076 ± 0.0001
e	—	0.561 ± 0.027
f(M_2)(mass func.)	($M_\odot$)	0.0612 ± 0.0003
M_2 (i = 90°)	($M_\odot$)	0.811 ± 0.002
M_2 (i = 60°)	($M_\odot$)	0.970 ± 0.002
M_2 (i = 30°)	($M_\odot$)	2.048 ± 0.005
Sum of squared residuals	0.000428	

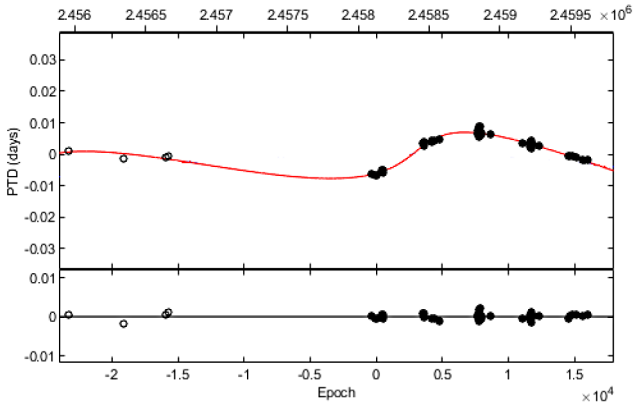

Figure 13. LiTE fit summarized in Table 7 using fundamental pulsation timing differences (PTD) determined for V488 Gem between 2012 January 31 and 2021 February 7. The solid red line in the top panel describes the fit for an elliptical (e = 0.561) orbit (P = 7.911 ± 0.093 y) of a putative binary partner. Solid circles (•) represent the observed times at maximum light. The bottom panel illustrates the PTD residuals remaining after LiTE analysis.

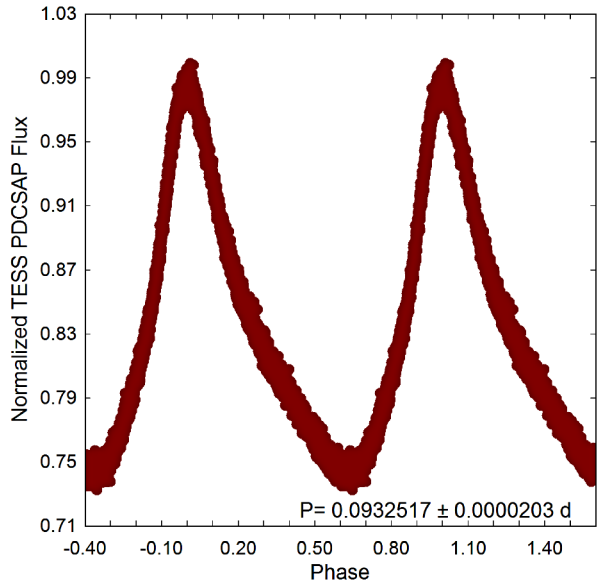

Figure 14. Period (0.0932517 ± 0.0000203 d) folded light curve for V488 Gem produced from the TESS Mission between 2020 December 18 and 2021 January 13. Data were normalized to maximum light using PDCSAP flux values.

Collectively the data suggest complex changes in the apparent fundamental pulsation rate of V488 Gem. One solution posits that cyclic changes in timings for maximum light can result from the gravitational influence of an unseen companion, the so-called light-travel time effect (LiTE). To address this possibility LiTE analyses were performed using an adaptation of the simplex code for third light reported by Zasche *et al.* (2009). Accordingly, the associated parameters in the LiTE equation (Irwin 1959):

$$\rho = \frac{a_{12}\sin i}{c}\left[(1-e^2)\frac{\sin(\nu+\omega)}{1+e\cdot\cos\nu}+\sin\omega\right] \qquad (13)$$

were derived which and include parameter values for P (orbital period of the theoretical binary pair about the barycenter), orbital eccentricity e, argument of periapsis ω, true anomaly

Table 8. Fundamental frequency, corresponding harmonics, and independent oscillations detected following DFT analysis of time-series photometric data from V488 Gem acquired during the TESS Mission (December 18, 2020–January 13, 2021).

	Freq. ($c \cdot d^{-1}$)	*Freq. Err.*	*Amp. (flux)*	*Amp. Err.*	*Phase*	*Phase Err.*	*Amp. S/N*
f_0	10.7233	0.0003	0.09980	0.00324	0.251	0.005	1060
$2f_0$	21.4485	0.0003	0.03456	0.00266	0.828	0.003	629
$3f_0$	32.1717	0.0001	0.01275	0.00004	0.863	0.001	244
$4f_0$	42.8950	0.0001	0.00664	0.00004	0.947	0.001	121
$5f_0$	53.6202	0.0003	0.00335	0.00004	0.510	0.002	67
f_1	10.7506	0.0055	0.00301	0.00307	0.469	0.017	31
$6f_0$	64.3434	0.0005	0.00169	0.00004	0.658	0.004	36
f_2	10.6921	0.0037	0.00137	0.00298	0.709	0.130	14
f_3	10.7837	0.0208	0.00097	0.00007	0.480	0.068	8
$7f_0$	75.0686	0.0009	0.00090	0.00004	0.239	0.007	20
f_0+f_2	21.4212	0.0025	0.00088	0.00266	0.592	0.032	14
f_4	13.3480	0.0012	0.00070	0.00004	0.055	0.009	14

Table 9. Global stellar parameters for V488 Gem using values reported from observations at DBO and those predicted from evolutionary modelling.

Parameter	*Observed*	*PARSEC (Z = 0.020)*
Mean T_{eff} [K]	7129 ± 202	—[a]
Mass [$M_\odot$]	2.152 ± 0.042	2.038 ± 0.036
Radius [$R_\odot$]	3.404 ± 0.232	3.459 ± 0.127
Luminosity [$L_\odot$]	26.97 ± 2.05	—[a]
rho [g/cm^3]	0.077 ± 0.016	0.069 ± 0.008
log g [cgs]	3.707 ± 0.060	3.669 ± 0.033
Q [d]	0.0218 ± 0.0017	0.0209 ± 0.0011

[a] *T_{eff} and luminosity fixed according to the observed values.*

ν, time of periastron passage T_0, and amplitude $A = a_{12} \sin i_2$. Despite a five-year gap in ToMax timings between 2013 and 2018, an eccentric (e = 0.561 ± 0.027) sinusoidal-like fit to these data with very low sum of squared residuals (0.000428) was obtained (Figure 13). The results predict a binary system with an unseen stellar object in an eccentric orbit (7.911 ± 0.093 y) that is located at least 2.97 ± 0.14 AU distant.

The angular resolution of the Gaia photometric detector is limited to 0.18 arcsec (Gaia Collab. 2021). Since the putative secondary is only separated by 2.97 AU (3.36 milli-arcsec), any apparent magnitude determination will be a composite of both stars. The LiTE solution (Table 7) provides three predictions for mass ($M_\odot$), depending on the orbital inclination (90, 60, and 30°). Assuming this nearby star is on the main sequence (MS), then the radius ($R_\odot$) and effective temperature (T_{eff}) can be estimated (Pecaut and Mamajeck 2013). Since the distance is known, the apparent magnitude (V_{mag}) can be calculated. When i = 30°, a secondary with $M_\odot$ = 2.048 would have an apparent V_{mag} of 12.43. Combining the magnitudes from both stars according to:

$$m = m_1 - 2.5\log(1+10^{-0.4(m_2-m_1)}), \qquad (14)$$

reveals that the companion star would brighten the observed V_{mag} (11.60) considerably; therefore, this LiTE prediction when i = 30° is untenable. A less massive companion (0.970 $M_\odot$), such as when the orbital inclination is 60°, is predicted to be

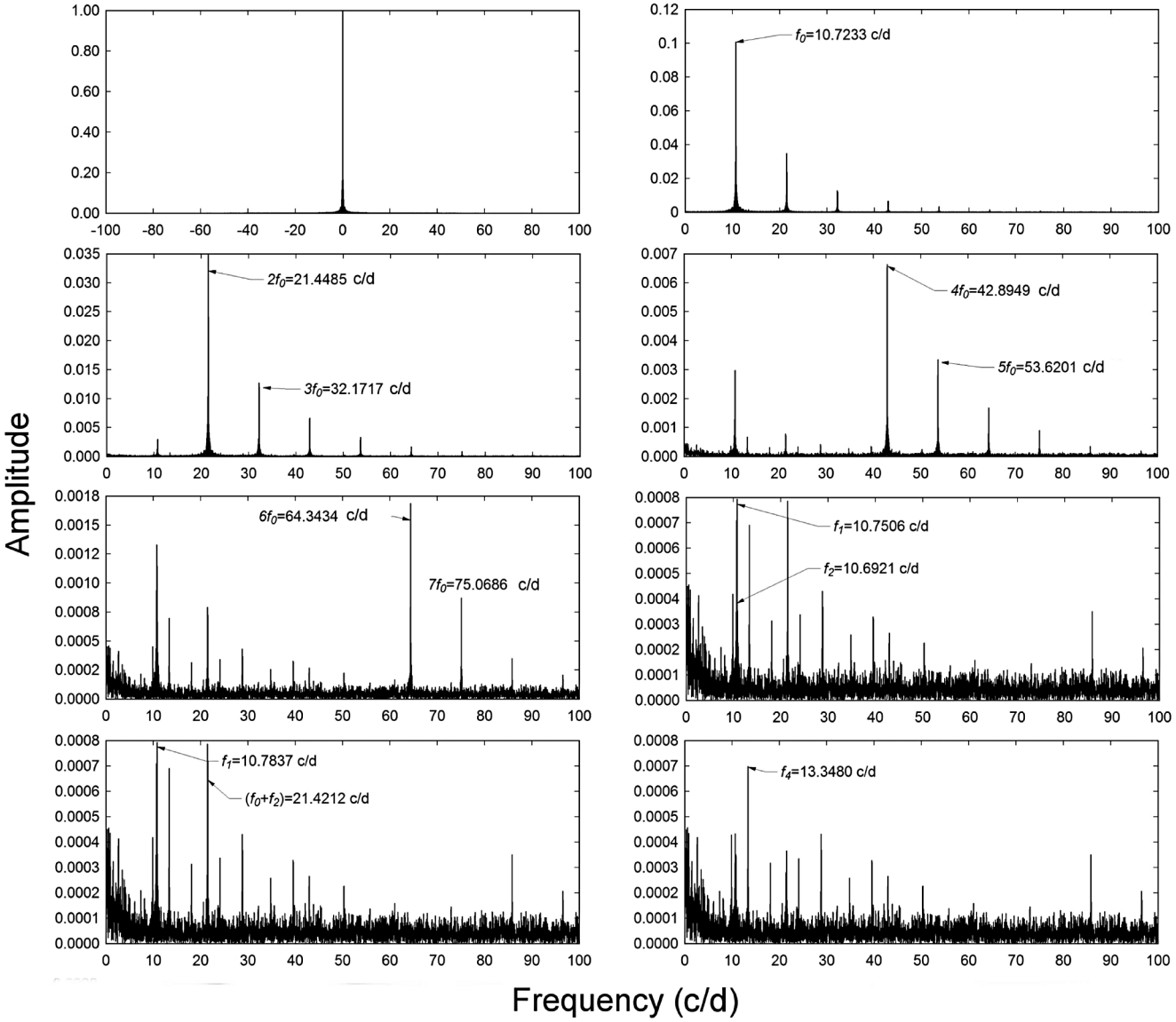

Figure 15. DFT spectral window (top left panel) and amplitude spectra from V488 Gem showing the fundamental pulsation frequency (f_0), its harmonics ($2f_0$–$7f_0$), and independent oscillations (f_i–f_4) from light curves acquired during the TESS Mission (2020 December 18–2021 January 13).

much dimmer (V≃16.02 mag). In this case, the combination of a V≃16.02 mag star with an unresolved V_{avg}≃12.53 mag star would only be slightly brighter (V≃12.48 mag) than the observed value. Said another way, any MS star with an apparent magnitude dimmer than V≃16.02 mag would not meaningfully affect measuring the apparent magnitude of V488 Gem. This analysis constrains the orbital inclination of a putative MS binary partner ($M_\odot$ = 0.811–0.970) to be somewhere between 60 and 90°.

3.2.1 Discrete Fourier transformation

Light curves were mined from the TESS Mission (Ricker *et al.* 2015; Caldwell *et al.* 2020) during an imaging campaign started on 2020 December 18 which ran continuously every two minutes through 2021 January 13. These highly precise flux measurements (PDCSAP < ± 0.0044 $e^- \cdot s^{-1}$) did not reveal any meaningful change over time in amplitude or light curve morphology (Figure 14). As previously described for BN Tri, Period04 (Lenz and Breger 2005) was used to extract prominent frequencies when the frequency range = 0–100 $c \cdot d^{-1}$ (Table 8). Representative amplitude-frequency spectra from the TESS Mission are provided in Figure 15, while DFT-derived modelling results indicate an excellent fit for the TESS light curve data (Figure 16). For the most part, these results suggest that V488 Gem is dominated by a fundamental pulsation at (f_0 = 10.7233 ± 0.0003 $c \cdot d^{-1}$) with a light curve shape that can be best described with harmonics of the fundamental that are detectable up to 7 orders ($7f_0$). In addition, four weak but statistically significant independent oscillations were observed at 10.7506 ± 0.0055 (f_1), 10.6921 ± 0.0037 (f_2), 10.7837 ± 0.0208 (f_3) and 13.3480 ± 0.0012 (f_4) $c \cdot d^{-1}$. One additional pulsation was detected at 21.4212 ± 0.0025 $c \cdot d^{-1}$, which probably represents a combination of f_0 and f_2. It is unlikely that any of these independent oscillations (P_i) correspond to radial overtones based on the calculation of period ratios (P_i / P_0), which did not fit predictions (Stellingwerf 1979). As mentioned

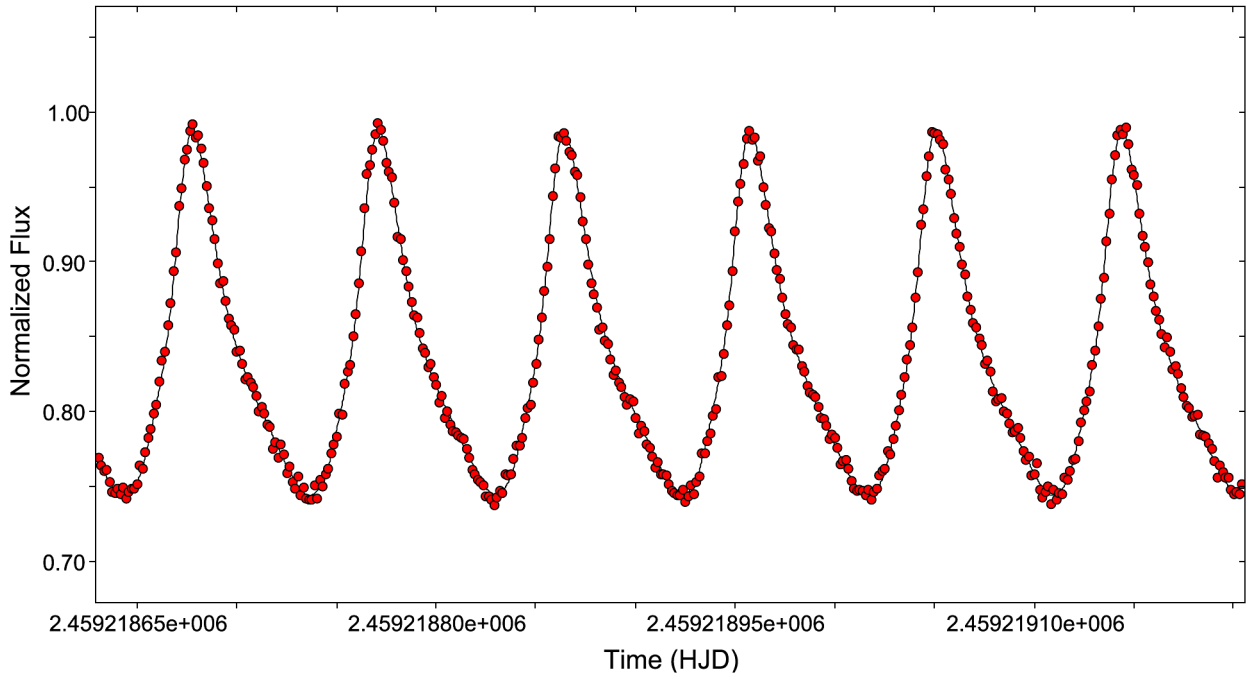

Figure 16. Representative DFT model fit from V488 Gem light curve data acquired during TESS Mission (2021 January 4, 03:06–16:54 UTC). Observed data are shown as red circles while the DFT-derived simulation is represented with a black line.

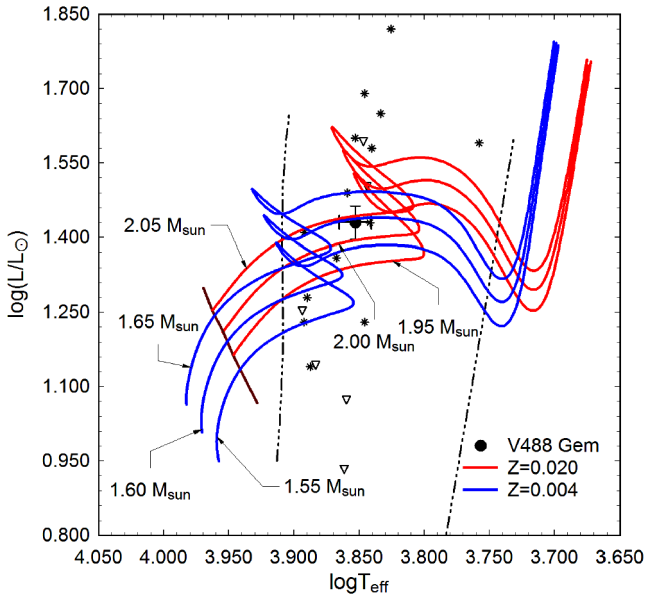

Figure 17. Evolutionary tracks (red lines, Z = 0.020, and blue lines, Z = 0.004) derived from PARSEC models (Bressan *et al.* 2012) showing position of V488 Gem (black filled circle) relative to ZAMS (thick maroon line) and within the theoretical instability strip (black dashed lines) for low-order radial mode δ Scuti pulsators. The position of other HADS (*) and SX Phe (open triangle) variables reported by Balona (2018) are included for comparison.

earlier (section 3.1.2) heretofore undetected pulsation modes continue to be uncovered from the highly precise photometric measurements produced by space telescopes. By comparison, Fourier deconvolution of light curves (BVI_c) acquired at DBO produced nearly the same fundamental pulsation period ($\bar{X}$ = 10.7238 ± 0.0001 c · d^{-1}) and harmonics (2–6f_0) but with no detectable independent modes of oscillation which were probably buried in the periodogram noise.

3.2.2. Global parameters

Estimates for V488 Gem mass, radius, and luminosity in solar units along with density, log g, and Q were derived (Table 9) by applying the same relationships (Equations 3–9) described for BN Tri. Hereafter all calculations dependent on d (pc) use the value reported (1691 ± 61 pc) in Gaia EDR3 (Gaia Collab. 2021). Absolute V-mag (M_V = 1.129 ± 0.083 mag) was calculated from Equation 3 when V_{avg} = 12.527 ± 0.027 mag and A_V =0.2567 ± 0.0059 mag.

As with BN Tri, a mean effective temperature (7129 ± 202 K) for V488 Gem was derived from observations made during this study along with others from various surveys (Table 3). Luminosity (26.97 ± 2.05 $L_\odot$) was determined from Equation 4; when $M_{bol\odot}$ = 4.74 mag, M_V = 1.129 ± 0.083 mag and BC = 0.0334 mag (Flower 1996) then M_{bol*} = 1.163 ± 0.083 mag. Mass (2.152 ± 0.042 $M_\odot$) was estimated from a mass-luminosity relationship (Equation 5) derived from main sequence (MS) stars in detached binary systems (Eker *et al.* 2018). Finally, the radius in solar units (R_* = 3.404 ± 0.232) was estimated using Equation 6. Derived values for density ($\rho_\odot$), surface gravity (log g), and pulsation constant (Q) are also included in Table 9. The resulting Q values provided in Table 9 are lower than the expected (Q = 0.029–0.049 d) value from other δ Sct variables (Breger and Bregman 1975; Breger 1979; Antonello and Pastori 1981; North *et al.* 1997; Joshi and Joshi 2015; Poro *et al.* 2021) known as pure p-mode radial oscillators. This may suggest that one or more of the independent oscillations (f_1–f_4) have affected the pulsation constant. Furthermore, since V488 Gem may have a close binary partner it is uncertain what effect this may have on the determination of Q.

3.2.3. Evolutionary status of V488 Gem

As with BN Tri, the evolutionary status of V488 Gem was evaluated (Figure 17) using the PAdova and TRieste Stellar Evolution Code (PARSEC) for stellar tracks and isochrones (Bressan *et al.* 2012). According to Equation 10, its position ≃230 pc above the Galactic plane suggests residence in the thin disk (Li and Zhao 2017) rather than the halo where many metal-poor ([Fe/H] <–1.6) stars reside (Carollo *et al.* 2010). As expected for a thin disk denizen, the LAMOST spectroscopic value ([Fe/H] = –0.237 ± 0.056) suggests that V488 Gem approaches (~58%) solar metallicity.

Separate PARSEC evolutionary models (Bressan *et al.* 2012) ranging in age between 1.013×10^8 and 1.63×10^9 y are illustrated in Figure 17. The solid black circle with error bars indicates the HRD position when fixed by the observed T_{eff} and $L_{\odot}$ values (Table 9). If Z = 0.020, then by linear extrapolation V488 Gem would have a mass of 2.038 ± 0.036 $M_{\odot}$ and a radius of 3.459 ± 0.127 $R_{\odot}$. The position of this intrinsic variable closest to the $M_{\odot}$ = 2.05 evolutionary track extrapolates to an age of 1.013 ± 0.020 Gyr, suggesting it is a moderately evolved MS object lying amongst other HADS variables closer to the blue edge of the instability strip.

By comparison, a metal-deficient (Z = 0.004) V488 Gem would have a slightly smaller radius (3.425 ± 0.148 $R_{\odot}$), but would be considerably less massive (1.593 ± 0.030 $M_{\odot}$). Its position near the 1.60 $M_{\odot}$ track lies after the HRD region where evolutionary tracks of low metallicity stars begin stellar contraction near the end of core hydrogen burning. This star would still be a MS object but with an age approaching 1.613 ± 0.001 Gyr. It should be noted that the theoretical mass (2.038 $M_{\odot}$) where Z = 0.020 favors the higher metallicity of V488 Gem is also in general agreement with results (2.152 ± 0.042 $M_{\odot}$) independently determined using an empirical mass-luminosity relationship (Equation 5). Uncertainty about the mass and metallicity of V488 Gem will likely improve should high resolution spectroscopic data become available in the future.

4. Conclusions

New times of maximum were determined for both BN Tri and V488 Gem based on precise time-series CCD-derived light curve data acquired at DBO. These along with other published values and those extracted from the SuperWASP (Pollacco *et al.* 2006) and TESS (Ricker *et al.* 2015; Caldwell *et al.* 2020) surveys led to an updated linear ephemeris for each system. Potential changes in the fundamental pulsation period were assessed using differences between observed and predicted timings for maximum light. A quadratic relationship was established between the residuals and epoch for BN Tri, suggesting that the pulsation period appears to be very slowly increasing (0.0003 ± 0.0001 s · y^{-1}). Secular analysis of the fundamental pulsation period for V488 Gem revealed a sinusoidal-like variation in the pulse timing differences over a nine year period. These residuals, believed to result from a light-travel time effect, were fit using simplex optimization and subsequently suggest that V488 Gem is a binary system with a stellar-sized companion in an eccentric orbit (7.91 y). Continued observation of both systems for at least a decade could prove highly useful in affirming their secular behavior. The adopted effective temperatures (T_{eff}) for BN Tri (7371 ± 186 K) and V488 Gem (7129 ± 202 K) most likely correspond to spectral class A8V-F0V for the former and A9V-F1V for the latter variable. The totality of results, including residence in the Galactic thin disk, near solar metallicity, mass predictions, and effective temperature estimates, firmly support classification for both stars as HADS-type variables. Nonetheless, high resolution UV-vis spectra would be necessary to unequivocally confirm the spectral type, metallicity, and effective temperature of both systems.

5. Acknowledgements

This research has made use of the SIMBAD database operated at Centre de Données astronomiques de Strasbourg, France. In addition, the Northern Sky Variability Survey previously hosted by the Los Alamos National Laboratory, and the ASAS-SN Variable Stars Database (https://asas-sn.osu.edu/variables) were mined for essential information. This work also presents results from the European Space Agency (ESA) space mission Gaia (DR2 and EDR3). Gaia data are processed by the Gaia Data Processing and Analysis Consortium (DPAC). Funding for the DPAC is provided by national institutions, in particular those participating in the Gaia MultiLateral Agreement (MLA). The Gaia mission website is https://www.cosmos.esa.int/gaia. The Gaia archive website is https://archives.esac.esa.int/gaia. This paper makes use of data from the first public release of the WASP data as provided by the WASP consortium and services at the National Aeronautics and Space Administration (NASA) Exoplanet Archive, which is operated by the California Institute of Technology, under contract with NASA under the Exoplanet Exploration Program. The use of public data from the Large Sky Area Multi-Object Fiber Spectroscopic Telescope (LAMOST) is also acknowledged. Guoshoujing Telescope is a National Major Scientific Project built by the Chinese Academy of Sciences. Funding for the project has been provided by the National Development and Reform Commission. LAMOST is operated and managed by the National Astronomical Observatories, Chinese Academy of Sciences. Some of the data presented in this paper were obtained from the Mikulski Archive for Space Telescopes (MAST) at the Space Telescope Science Institute. Support to MAST for these data is provided by the NASA Office of Space Science via grant NAG57584 and by other grants and contracts. This paper also includes data collected with the TESS mission, obtained from the MAST data archive at the Space Telescope Science Institute (STScI). Funding for the TESS mission is provided by the NASA Explorer Program. STScI is operated by the Association of Universities for Research in Astronomy, Inc., under NASA contract NAS 526555. Many thanks to the anonymous referee whose valuable commentary and corrections led to significant improvement of this paper. This research was made possible through use of the AAVSO Photometric All-Sky Survey (APASS), funded by the Robert Martin Ayers Sciences Fund.

References

Akerlof, C., *et al.* 2000, *Astron. J.*, **119**, 1901.

Amard, L., Palacios, A., Charbonnel, C., Gallet, F., Georgy, C., Lagarde, N., and Siess, L. 2019, *Astron. Astrophys.*, **631A**, 77.

Andrych, K. D., and Andronov, I. L. 2019, *Open Eur. J. Var. Stars*, **197**, 65.

Andrych, K. D., Andronov, I. L., and Chinarova, L. L. 2020, *J. Phys. Stud.*, **24**, 1902.

Antonello, E., and Pastori, L. 1981, *Publ. Astron. Soc. Pacific*, **93**, 237.

Baglin, A. 2003, *Adv. Space Res.*, **31**, 345.

Balona, L. A. 2018, *Mon. Not. Roy. Astron. Soc.*, **479**, 183.

Balona, L. A., and Nemec, J .M. 2012, *Mon. Not. Roy. Astron. Soc.*, **426**, 2413.

Baran, A. S., and Koen, C. 2021, *Acta Astron.*, **71**, 113.

Berry, R. and Burnell, J. 2005, *The Handbook of Astronomical Image Processing*, 2nd ed., Willmann-Bell, Richmond VA.

Breger, M. 1979, *Publ. Astron. Soc. Pacific*, **91**, 5.

Breger, M. 1990, *Delta Scuti Star Newsl.*, **2**, 13.

Breger, M., and Bregman, J. N. 1975, *Astrophys. J.*, **200**, 343.

Breger, M., and Pamyatnykh, A. A. 1998, *Astron. Astrophys.*, **332**, 958.

Bressan, A., Marigo, P., Girardi, L., Salasnich, B., Dal Cero, C., Rubele, S., and Nanni, A. 2012, *Mon. Not. Roy. Astron. Soc.*, **427**, 127.

Caldwell, D. A. 2020, *Res. Notes Amer. Astron. Soc.*, **4**, 201.

Carollo, D., *et al.* 2010, *Astrophys. J.*, **712**, 692.

Drake, A. J., *et al.* 2014, *Astrophys. J., Suppl. Ser.*, **213**, 9.

Eker, Z., *et al.* 2018, *Mon. Not. Roy. Astron. Soc.*, **479**, 5491.

Flower, P. J. 1996, *Astrophys. J.*, **469**, 355.

Gaia Collaboration, *et al.* 2016, *Astron. Astrophys.*, **595A**, 1.

Gaia Collaboration, *et al.* 2018, *Astron. Astrophys.*, **616A**, 1.

Gaia Collaboration, *et al.* 2021, *Astron. Astrophys.*, **649A**, 1.

Garg, A., *et al.* 2010, *Astron. J.*, **140**, 328.

Gettel, S. J., Geske, M. T., and McKay, T. A. 2006, *Astron. J.*, **131**, 621.

Gilliland, R. L., *et al.* 2010, *Publ. Astron. Soc. Pacific*, **122**, 131.

Guzik, J. A. 2021, *Frontiers Astron. Space Sci.*, **8**, 1.

Handler, G. 2000, in *The Impact of Large-Scale Surveys on Pulsating Star Research*, eds. L. Szabados, D. Kurtz, ASP Conf. Ser. 203, Astronomical Society of the Pacific, San Francisco, 408.

Henden, A. A., Levine, S. E., Terrell, D., Smith, T. C., and Welch, D. L. 2011, *Bull. Amer. Astron. Soc.*, **43**.

Henden, A. A., Terrell, D., Welch, D., and Smith, T. C. 2010, *Bull. Amer. Astron. Soc.*, **42**, 515.

Henden, A. A., Welch, D. L., Terrell, D., and Levine, S. E. 2009, *Bull. Amer. Astron. Soc.*, **41**, 669.

Irwin, J. B. 1959, *Astron. J.*, **64**, 149.

Jayasinghe, T., *et al.* 2018, *Mon. Not. Roy. Astron. Soc.*, **477**, 3145.

Jenkins, J. M., *et al.* 2016, *Proc. SPIE*, **9913**, id. 99133E.

Jester, S., *et al.* 2005, *Astron. J.*, **130**, 873.

Joshi, S., and Joshi, Y. C. 2015, *J. Astrophys, Astron.*, **36**, 33.

Kafka, S. 2021, Observations from the AAVSO International Database (https://www.aavso.org/data-download).

Khruslov, A.V. 2007, *Perem. Zvezdy Prilozh.*, **7**, 25.

Lee, Y.-H, Kim, S. S., Shin, J., Lee, J., and Jin, H. 2008, *Publ. Astron. Soc. Japan*, **60**, 551.

Lenz, P., and Breger, M. 2005, *Commun. Asteroseismology*, **146**, 53.

Li, C., and Zhao, G. 2017, *Astrophys. J.*, **850**, 25.

McNamara, D. H. 2000, in *Delta Scuti and Related Stars, Reference Handbook and Proceedings of the 6th Vienna Workshop in Astrophysics*, eds. M. Breger, M. Montgomery, ASP Conf. Ser. 210, Astronomical Society of the Pacific, San Francisco, 373.

McNamara, D. H. 2011, *Astron. J.*, **142**, 110.

Minor Planet Observer. 2010, MPO Software Suite (http://www.minorplanetobserver.com), BDW Publishing, Colorado Springs.

Mortara, L., and Fowler, A. 1981, in *Solid State Images for Astronomy*, SPIE Conf. Proc. 290, 28, Society for Photo-Optical Instrumentation Engineers, Bellingham, WA, 28.

Neilson, H. R., Percy, J. R., and Smith, H. A. 2016, *J. Amer. Assoc. Var. Star Obs.*, **44**, 179.

Niu, J.-S, Fu, J.-N., and Zong, W.-K. 2013, *Res. Astron. Astrophys.*, **13**, 1181.

Niu, J.-S, *et al.* 2017, *Mon. Not. Roy. Astron. Soc.*, **467**, 3122.

North, P., Jaschek, C., and Egret, D. 1997, *Proceedings of the ESA Symposium "Hipparcos-Venice '97,"* ESA SP-402, ESA Publications Division, Noordwijk, The Netherlands, 367.

Pamyatnykh, A. A. 1999, *Acta Astron.*, **49**, 119.

Pecaut, M. J., and Mamajek, E. E. 2013, *Astrophys. J., Suppl. Ser.*, **208**, 9.

Pojmański, G. 2000, *Acta Astron.*, **50**, 177.

Pojmański, G., Pilecki, B., and Szczygiel, D. 2005, *Acta Astron.*, **55**, 275.

Pollacco, D. L., *et al.* 2006, *Publ. Astron. Soc. Pacific*, **118**, 1407.

Poretti, E. 2003a, *Astron. Asstrophys.*, **409**, 1031.

Poretti, E. 2003b, in *Interplay of Periodic, Cyclic and Stochastic Variability in Selected Areas of the H-R Diagram*, ed. C. Sterken, ASP Conf. Ser. 292, Astronomical Society of the Pacific, San Francisco, 145.

Poretti, E., *et al.* 2011, *Astron. Astrophys.*, **528A**, 147.

Poro, A., *et al.* 2021, *Publ. Astron. Soc. Pacific*, **133**, 084201.

Qian, S.-B., Li, L.-J., He, J.-J., Zhang, J., Zhu, L.-Y., and Han, Z.-T. 2018, *Mon. Not. Roy. Astron. Soc.*, **475**, 478.

Ricker, G., *et al.* 2015, *J. Astron. Telesc. Instrum. Syst.*, **1**, 014003.

Schlafly, E. F., and Finkbeiner, D. P. 2011, *Astrophys. J.*, **737**, 103.

Serenelli, A., Scott, P., Villante, F. L., Vincent, A. C., Asplund, M., Basu, S., Grevesse, N., and Peña-Garay, C. 2016, *Mon. Not. Roy. Astron. Soc.*, **463**, 2.

Smith, T. C., Henden, A. A., and Starkey, D. R. 2011, in *The Society for Astronomical Sciences 30th Annual Symposium on Telescope Science*, Society for Astronomical Sciences, Rancho Cucamonga, CA, 121.

Software Bisque. 2019, TheSkyX Professional Edition 10.5.0 (https://www.bisque.com).

Stellingwerf, R. F. 1979, *Astrophys. J.*, **227**, 935.
Templeton, M. R. 2005, *J. Amer. Assoc. Var. Star Obs.*, **34**, 1.
Vagnozzi, S., Freese, K, and Zurbuchen, T. H. 2017, *Astrophys. J.*, **839**, 55.
von Steiger, R., and Zurbuchen, T. H. 2016, *Astrophys. J.*, **816**, 13.
Walker, G., *et al.* 2003, *Publ. Astron. Soc. Pacific*, **115**, 1023.
Wils, P., *et al.* 2013, *Inf. Bull. Var. Stars*, No. 6049, 1.
Wils, P., *et al.* 2014, *Inf. Bull. Var. Stars*, No. 6122, 1.
Woźniak, P. R., *et al.* 2004, *Astron. J.*, **127**, 2436.
Xiong, D. R., Deng, L., Zhang, C., and Wang, K. 2016, *Mon. Not. Roy. Astron. Soc.*, **457**, 3163.
Zasche, P., Liakos, A., Niarchos, P., Wolf, M., Manimanis, V., and Gazeas, K. 2009, *New Astron.*, **14**, 121.
Zhao, G., Zhao, Y.-H., Chu, Y.-Q., Jing, Y.-P., and Deng, L.-C. 2012, *Res. Astron. Astrophys.*, **12**, 723.

MOTESS-GNAT Sky Survey: MG1 Long Period Variable Stars Re-Visited After 10 Years

Brian L. Craine
Western Research Company, Inc. and GNAT, Inc., 3275 W. Ina Road, Suite 221-A1, Tucson, AZ 85741; send email correspondence to blcraine@wrc-inc.com

Andrew S. Kulessa
Colin Gum Observatory, Greenhill, SA, Australia; GNAT, Inc., 3275 W. Ina Road, Suite 221-A1, Tucson, AZ 85745; andskul@gmail.com

Eric R. Craine
Western Research Company, Inc. and GNAT, Inc., 3275 W. Ina Road, Suite 221-A1, Tucson, AZ 85741; ercraine@wrc-inc.com

Roger B. Culver
GNAT, Inc., 3275 W. Ina Road, Suite 221-A1, Tucson, AZ 85741; Professor Emeritus of Astronomy, Colorado State University, Fort Collins, CO 80523; Roger.Culver@coloradostate.edu

Adam L. Kraus
Department of Astronomy, University of Texas, Austin, TX 78712; alk@astro.as.utexas.edu

Roy A. Tucker
Tucson, AZ (deceased)

Douglas K. Walker
Prime Solutions Group, Inc and GNAT, Inc., 3275 W. Ina Road, Suite 221-A1, Tucson, AZ 85741; dougwalker@psg-inc.net

Received August 9, 2022; revised November 25, 2022; accepted December 6, 2022

Abstract The MG6 survey is a 10-year follow-up to the MG1 survey. A new reduction of these surveys has been performed and screened for candidate long period variable stars (LPVs). In combination with the original 47 LPVs found in the MG1 variable star candidate catalog a total of 138 LPVs have been identified in the MG1 48.3'-wide equatorial strip. The additional data have allowed for refinement of the period determinations for most of the LPVs. Some of the biases of the selected population with respect to period length and color distribution are examined. This study has newly identified 9 unique LPVs, bringing the total number of new LPV identifications from the MOTESS-GNAT survey to 56. The number of LPVs in this list exhibiting hump characteristics has been expanded to at least 15.

1. Introduction

Since 2001 the Moving Object and Transient Event Search System (MOTESS) (Tucker 2007) and the Global Network of Astronomical Telescopes (GNAT) have collaborated to produce equatorial sky surveys and data reduction pipelines useful for the discovery and characterization of variable stars. The first MG1 data pipeline (Kraus *et al.* 2007) produced a subset of candidate variable stars numbering about 26,000 out of the nearly two million stars detected. This work is referred to as the "MG1 Variable Star Catalog" (MG1-VSC).

Among the variable stars characterized are the long period variables (LPVs) detected in MG1-VSC (Craine *et al.*, 2015). Since publication of those observations a second survey (MG6) has been completed; this survey was conducted for the same survey strip that was observed for MG1 but 10 years later, hence adding additional temporally distributed observations of this set of LPVs. Further, the MG1 observations have been re-reduced using a newly developed pipeline which generates a comprehensive database of light curves of all the stars detected in the survey images (Craine *et al.* 2021). The MG6 survey data have been reduced using the same protocols.

Reported here are the results of the additional observations of LPVs resulting from re-evaluation of the MG1 and MG6 databases.

2. Methods

The MG1 and MG6 survey images (section 2.1) were reduced to produce the MG1A and MG6A databases of unsaturated objects and associated screening parameters (section 2.2). Some of those parameters were used as selection criteria for potential LPVs (section 2.3). The original images containing the potential LPVs were then subjected to more stringent photometry (section 2.4) and these data were used to determine an estimate of the period (section 2.5). This section provides more detail on these steps and other methodology.

2.1. Observations

The MG1 and MG6 surveys consisted of scan mode images centered at a declination of +03° 18' 20" with a width of 48.3' in declination obtained between 2001–2003 (282 nights observing) and 2011–2013 (232 nights observing), respectively, with each object typically observed three times per night at 20-minute intervals by the MOTESS system (Tucker 2007; Kraus *et al.* 2007). The image scale for the scan mode images was 2.83 arcsec/pixel. Unfiltered observations with an integration time of 192 seconds yielded a practical detection range of 12.6 to 17.4 in Gaia R band magnitude.

2.2. Data reduction

The MG1 and MG6 survey images were processed, analyzed, and the data organized into SQL databases for each survey using dedicated Python scripts that relied upon the Astropy library as described (Craine *et al.* 2021). These databases were designated MG1A and MG6A. The light curve data saved to the MG1A and MG6A databases were obtained using an unsupervised pipeline that employed a high image stringency that rejected many images that contained usable data for some objects in the image. In addition, the data were obtained from only two of the three telescopes (A and B) in the MOTESS system (Tucker 2007). Single aperture photometry with an ensemble comparison was used to determine the screening light curves (see Craine *et al.* 2021 for details).

Parameters calculated for each object included the Lomb-Scargle false alarm probability (FAP) (Press 1996; Scargle 1982), the inverse of the Von Neuman ratio (1/η) index (Von Neumann 1941), Equation (1), and the short-term slope (μ), Equation (2).

The inverse Von Neuman index is calculated as:

$$1/\eta = \frac{(N-1)\,\sigma^2}{\sum_{i=1}^{N-1}(m_{i+1}-m_i)^2}, \qquad (1)$$

where N is the number of observations, m is the magnitude of the observations in order of observation time, and σ is the standard deviation of the magnitudes. The Von Neuman statistic, η, is the mean square successive difference of the time series divided by the sample variance, which is small when there is strong positive serial correlation between successive data points. This is a statistical test for the serial dependence of a time series of data (i.e., H_0:; there is no serial correlation of successive magnitudes). The inverse Von Neuman index is a convenient metric which increases in value for variable objects. The observed range of 1/η for survey objects was 0.27 to 21.9.

A new metric specifically tailored for the detection of long period variables, the short-term slope (μ), is introduced. This metric calculates the average absolute value of the slope of sub-intervals of a light curve. It is calculated as:

$$\mu = \frac{\sum_{n=1}^{n=\left|\frac{\Delta t}{\delta}\right|}\left|\frac{\sum_{i=1}^{kn}(t_i-\bar{t})(m_i-\bar{m})}{\sum_{i=1}^{k_n}(t_i-\bar{t})^2}\right|}{\left|\frac{\Delta t}{\delta}\right|}, \qquad (2)$$

where t_i is the time of ith observation in the nth interval, m_i is the differential magnitude at t_i, t-bar is the average time of observations in the nth interval, m-bar is the average magnitude of observations in the nth interval, Δt is the total time of the survey, δ is a selected time sub-interval (which was 60 days for the LPV search), and k_n is the number of observations in the nth interval. This parameter is sensitive to increasing or decreasing trends in magnitude over times scales of multiples of δ. For convenience the μ metric was scaled to a slope per ~5.184 days (10^6 seconds). The theoretical range of μ is 0 to undefined. In practice, the survey objects had an observed range of 0.0 to 3.2.

2.3. LPV selection

The selection of the potential LPV objects was a two-step procedure. First, objects in the databases were selected by the union of objects with an FAP < 0.00001, μ > 0.09, and 1/η >5.0. These cutoffs were selected as values that maximized the enrichment of LPVs in the selected objects. This enrichment averaged about 10^4-fold (detailed in section 3.1, Table 1). Secondly, the light curves from these objects were screened visually and obvious erroneous assignments, typically due to outlier points from a small number of bad images that survived initial quality checks, were rejected.

2.4. Photometry

To provide a more robust data set, selected potential LPV objects were re-analyzed employing the annular photometry routine from Astropy (Astropy Collab. 2018, ; Bradley *et al.*, 2019). All images containing the object, including those from the third telescope, were measured. This made maximum use of images available for each LPV candidate. Two nearby reference and check stars (typically within a 5' radius) were selected for least crowded backgrounds. Since the images are obtained in scan mode the reference and check stars may unpredictably fall out of some frames. Consequently, the combination of reference and check stars producing the greatest number of measurements was finally used. The aperture radius was 4px and the annulus had an inner radius of 6px and an outer radius of 10px for all objects. The target measurements were rejected when the corresponding check star magnitude exceeded ±2 standard deviations of the average for the check star. These are the light curves described below (see Appendix B).

2.5. Period determination

The light curves from the annular photometry were analyzed to determine a period for the objects using a Generalized Lomb-Scargle periodogram (GLS) algorithm (Zechmeister and Kürster 2009; VanderPlas 2018).

The GLS algorithm solves for the coefficients Aω, Bω, and Cω in a model describing magnitude as a function of time (M(t)), given by equation (3):

$$M(t) = A\omega \sin(\omega t) + B\omega \cos(\omega t) + C\omega, \qquad (3)$$

by least squares over a frequency grid, ω. The frequency corresponding to the maximum in the periodogram is chosen as the optimum frequency and the corresponding coefficients define the light curve model. Often there can be ambiguity

Table 1. Results of screening MG1 and MG6 for LPVs.

Database	*Pre-Screen*	*Post-Screen*	*Visual Accepted*
MG1A	936,764	73	43
MG6A	1,046,732	111	95

between periodogram peaks and in these cases a method based on statistical inference employing the Vuong statistic as outlined in (Baluev 2012) is used to distinguish the preferred light curve model.

The Vuong statistic is computed for pairs of rival models, corresponding to peaks in the periodogram. This statistic tests the null hypothesis that the difference between models is consistent with random noise, while applying a significance level of 0.05.

Aliasing was resolved by inspection of time series light curves (when available) from higher cadence observations from the Zwicky Transient Facility (Bellm *et al.* 2019) or ASAS-SN observations (Kochanek *et al.* 2017; Shappee *et al.* 2014).

The GLS algorithm was implemented in the Python class Gls.py (Zechmeister 2019) for all LPV candidates. A large subset of the data was also analyzed using GNAT software developed by one of the authors (A. Kulessa). Period determinations between the two codes agreed to within one day. The amplitude of objects was determined from the best light curve model according to Equation (4). This approach allows for the amplitude determination even in the case where the maximum or minimum is not observed.

$$\text{full amplitude} = 2\left(\sqrt{(A_\omega^2 + B_\omega^2)}\right), \quad (4)$$

2.6. LPV hump measurement

LPV hump structure was identified by visual examination of light curves. A fourth order polynomial fit to the data points surrounding the hump was determined, as illustrated in Figure 1A. This section of the light curve was detrended using the determined fit yielding the recognizable hump structure as in Figure 1B. The magnitude of the hump, Δm, is measured as the magnitude at the peak time. The duration is measured as the time from the rise to the fall of the curve from 0. The phase position of the hump is calculated from the peak time and the determined period and zero time for the LPV.

2.7. Statistics

Distributions were tested for similarity using the nonparametric Kolmogorov–Smirnov two-sample test H_0:; the two populations from which our samples were drawn have the same distribution function, critical p-value of 0.05). The difference between sample means was tested with the two-sample t-test (H_0: sample means are the same, critical p-value of 0.05). Calculations were performed using the Python scipy.stats library (Virtanen *et al.* 2020).

3. Results

3.1. Screening for LPVs

The completion of the MG6A database and the MG1A database together with the original MG1-VSC provides three

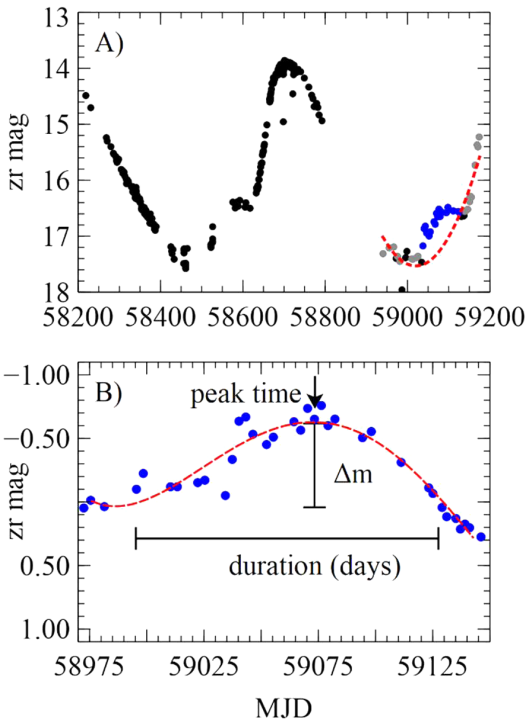

Figure 1. Measuring an LPV hump. (A) is the light curve for a LPV with an identified hump marked as blue dots and the nearby surrounding points marked as gray dots. The red dashed line is a polynomial fit to the surrounding gray dots. (B) is the detrended hump points as blue dots obtained by subtracting the fitted line from panel A from the light curve. The red dashed line is a polynomial fit to the hump.

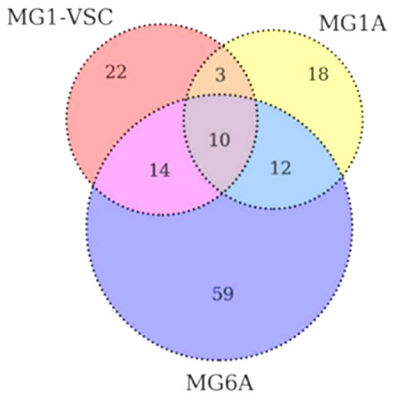

Figure 2. Venn diagram showing the distribution of LPV candidates identified by the three different surveys of a 48' declination strip centered at +03° 18′ 20″.

different approaches to recover LPVs from the +03° 18' 20" survey strip. The primary differences in the surveys are the data reduction methods (MG1A and MG6A versus MG1-VSC) or survey epoch (MG1-VSC and MG1A versus MG6A). These differences manifested in identification of overlapping and unique LPVs between the surveys as summarized in the Venn diagram shown in Figure 2.

The LPV candidates were selected from the MG1A and MG6A databases by applying cutoff values for three key parameters—Lomb-Scargle false alarm probability, inverse Von Neuman index, and the short-term slope value—to the entire collection of detected survey objects. This resulted in a small number of objects highly enriched for LPVs (see Table 1).

The post-screen objects were then manually examined for final verification as an LPV.

The MG1-VSC identified variable stars using the Welch-Stetson index (Welch and Stetson 1993) to create a database of 26,042 variable star candidates. The light curves of objects from this database were manually searched multiple times by at least two separate investigators, resulting in the discovery of 47 LPV candidate stars (Craine *et al.* 2007).

Each of the three surveys provides a unique, but related, window on the identification of LPV candidates. These relationships can be viewed in more detail in the Venn diagram shown in Figure 2. As expected, many of the objects are observed in more than one survey. Each survey also has uniquely detected objects. MG1A and MG6A, which share methodology, have 22 candidates in common, while MG1-VSC and MG1A, which share epochs, have 13 candidates in common. MG1-VSC and MG6A, which only share the same declination strip, have 24 candidates in common. A total of 138 candidates were found. The diagram graphically shows the large contribution that the MG6 survey has added to the discovery of LPV candidates, suggesting that the key survey parameter is not the data processing methodology but factors affecting the image collection.

3.2. Characterization of LPV candidates

3.2.1. Observed periods

The screened objects were selected, in part, for having a high probability of being periodic based upon a Lomb-Scargle analysis (Press 1996; Scargle 1982). However, the period obtained during screening is not a reliable period due to aliasing, sampling cadences, and sample size. Therefore, the LPV candidates were re-examined using all the survey images, which included images from all three telescopes of the MOTESS system. The photometry was performed using a local background estimation by the annular photometry method with two check stars and two comparison stars. This allowed for the recovery of usable data that had been discarded in a conservative unsupervised manner in the original screen. The enlarged pool of measurements was then smoothed with a five-day recursive median filter for period analysis.

The period was determined as described in the methods (section 2.5). The distribution of periods for the candidates is shown in Figure 3. LPVs are often characterized as having periods between 80 and 1,000 days (Percy 2007). The observed distribution from the MG survey is not normally distributed and is primarily in the 200–400-day range with an apparent under-representation of longer periods. This relatively narrow distribution could result from the actual range of LPV periods or a consequence of the inherent observing cadence of the survey. The black-dotted line in Figure 3 is the distribution fit to the periods for LPVs in the GaiaDR2 survey (Mowlavi 2018), which is different from the MG period distribution (Kolmogorov-Smirnov statistic = 0.31, $P < 1.4 \times 10^{-5}$). The mean periods of the MG data are different from the mean of the GaiaDR2 (275 d versus 341 d, respectively, $P_{(same)} < 1.4 \times 10^{-7}$), supporting the conclusion that the MG survey may be under-represented in longer period variables due to systematic limitations. The distribution of LPVs (Miras) from the ASAS-SN sky survey (Kochanek *et al.* 2017; Shappee *et al.* 2014) was not significantly different from the MG survey (P = 0.147) and the mean periods (275 d versus 288 d, $P_{(same)} = 0.174$) were not significantly different.

The Gaia DR2 survey (Mowlavi 2018) LPVs included 55 of the MG candidates and a comparison of the periods determined between the two surveys is presented in Figure 4. The agreement is quite good despite the lack of overlap in the actual timing of the surveys. LPVs are known to change their periods over time, and this may account for the small number of stars showing greater divergence from the expected value and may be good candidates for the study of more rapidly evolving stars. One of the divergent periods appears consistent with being a harmonic error in Gaia period determination (MG6A 10639637).

A similar comparison with 24 MG candidates overlapping with GCVS catalog (Samus *et al.* 2017) LPVs revealed a particularly good agreement for 20 of the stars (see Figure 5). Two of the stars (MG1 1388633 and MG6A 10854654) appeared to be significantly different. Despite being suspicious multiples of the GCVS period, a review of the MG data did not justify a period change.

The periods determined for the enlarged dataset, MG1A and MG6A, were also compared with the periods initially published using only the data from the original MG1-VSC (Craine *et al.* 2015). The results confirmed earlier expressed concerns about data aliasing in the MG survey data with significant changes in period assignment for 6 of the LPVs (see Figure 6).

3.2.2. Color relationship

The LPV stars are red giants occupying a characteristic position on the Hertzsprung–Russell diagram. Ninety-three of the MG candidates could be found in the Gaia DR2 source database, providing the absolute G, B, and R band magnitudes allowing for the evaluation of the color characteristics for 82 of them. Figure 7 shows their placement on a Color Absolute Magnitude Diagram (CMD) and comparison with the characteristics of the LPVs identified by the Gaia DR2 survey (Mowlavi 2018). The MG candidates that could be evaluated appear as might be expected for a collection of LPV stars except for three to four objects that were not as red as might be expected.

Closer inspection of the CMD suggests that the MG candidates are more concentrated in the redder region of the diagram than the average LPV. This is verified in Figure 8, which shows a detailed comparison of the distribution of MG candidates and the larger collection of Gaia DR2 LPVs. The color distributions are significantly different ($P < 0.00001$, KS two-sample test) with the average MG candidate having a B–R of about 5.2 compared to the Gaia DR2 collection of about 3.0 (significance $p < 0.00001$, t-test for equal means). Comparing the MG survey to the ASAS-SN survey also shows a significantly different color distribution (P = 0.003) but the mean B–R is not significantly different (P = 0.226). Figure 8 strongly suggests that the MG survey is missing a significant number of LPVs with B–R color indices in the 1.5–4.5 range, perhaps for reasons discussed below.

Characterizing the Gaia DR2 LPVs by amplitude in period-color space shows a strong clustering of the higher amplitude

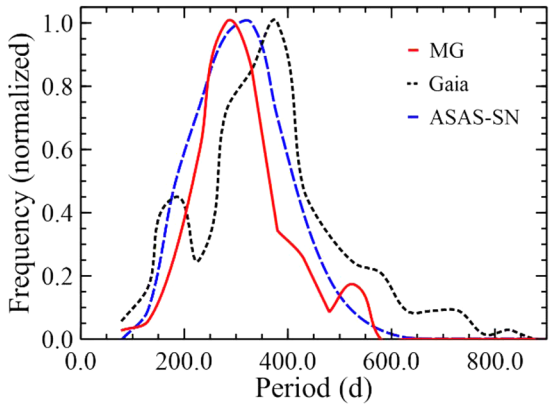

Figure 3. Distribution of observed periods in sky surveys.

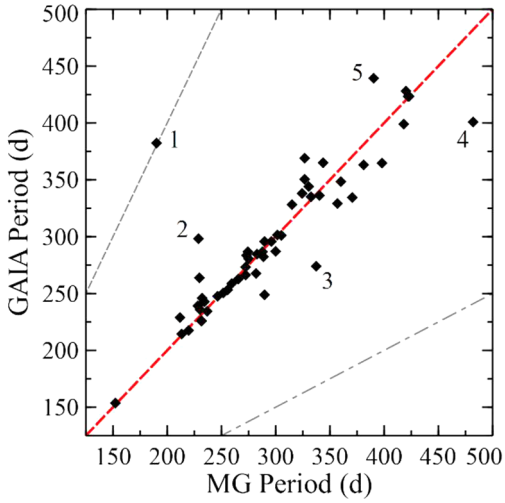

Figure 4. Comparison of determined periods for screened objects with those from GaiaDR2 survey (Mowlavi 2018). The labeled outliers are (1) MG6A 10639637, (2) MG6A 10722590, (3) MG6A 10637601, (4) MG1A 10696051, and (5) MG6A 10644124. Gray dashed line is second harmonic for MG period and gray dot-dash line is second harmonic for Gaia period.

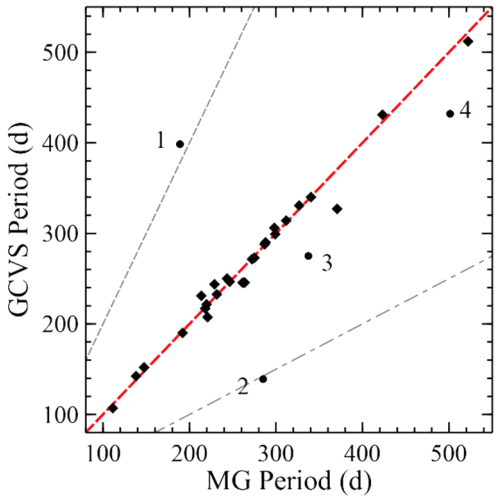

Figure 5. Correlation of MG periods with published GSVS periods. The labeled outlier objects are (1) MG1-1388633, (2) MG6A 10854654, (3) MG6A 10637601, and (4) MG1A 10624436. Gray dashed line is second harmonic for MG period and gray dot-dash line is second harmonic for Gaia period.

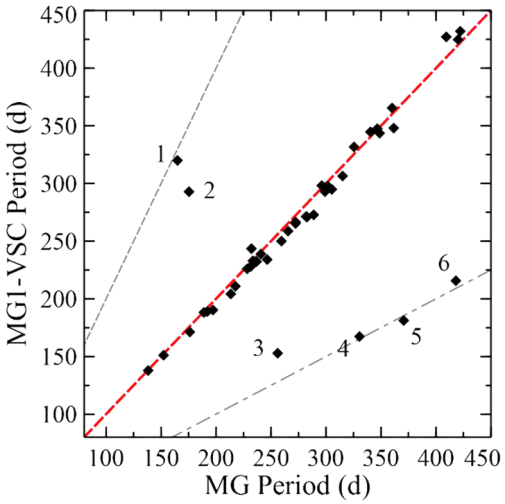

Figure 6. Correlation of originally reported periods with those determined using combined data from MG1 and MG6 surveys. The labeled outliers are (1) MG1-1376419, (2) MG6A 10660631, (3) MG6A 10620863, (4) MG1-1468465, (5) MG6A 10566412, and (6) MG1A 10658602. Gray dashed line is second harmonic for MG period and gray dot-dash line is second harmonic for MG1-VSC period.

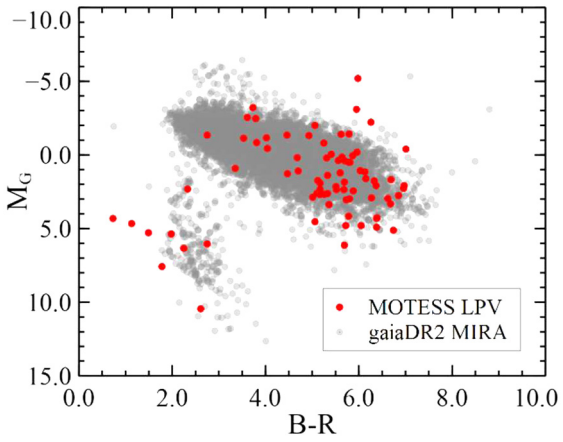

Figure 7. Color magnitude diagram (MG, is the absolute Gaia G magnitude; B–R, is the Gaia B minus R band color index). All color data are from the Gaia database (Gaia Collab., *et al.* 2018).

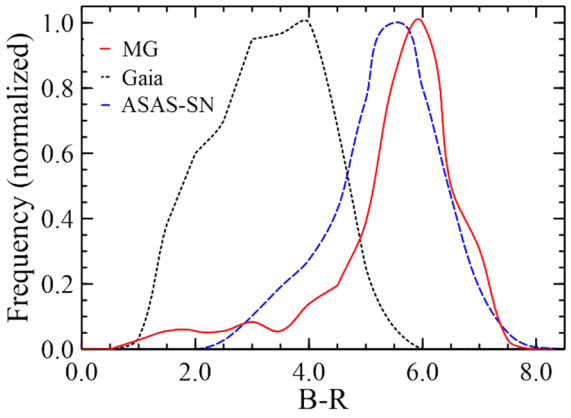

Figure 8. Comparison of redness distribution of MG objects with Gaia DR2 and ASAS-SN survey objects. All color data are from the Gaia database (Gaia Collab. *et al.* 2018).

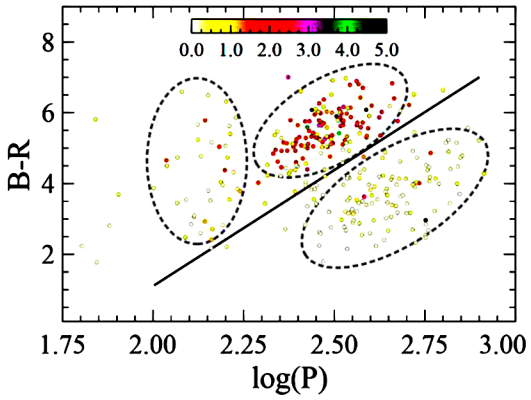

Figure 9. Period color diagram for the Gaia DR2 LPV in the MG1 survey strip. The color map indicates the amplitude of the object. Three visual clusters are demarcated by the dashed gray line. The line is drawn to separate the two main clusters in color, period space.

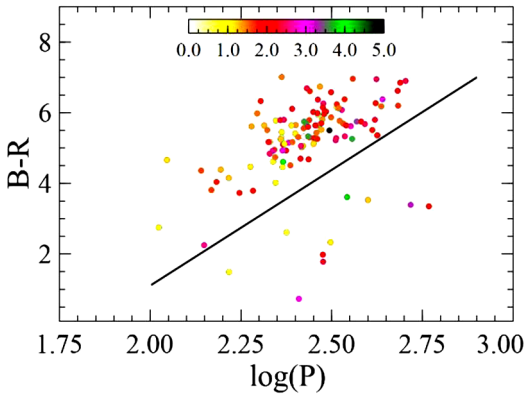

Figure 10. Period color diagram for the MOTESS LPV in the MG1 survey strip. The B–R color index is plotted as a function of the log of the period. The color map indicates the amplitude of the object. The line separating period, color space is from Equation (5).

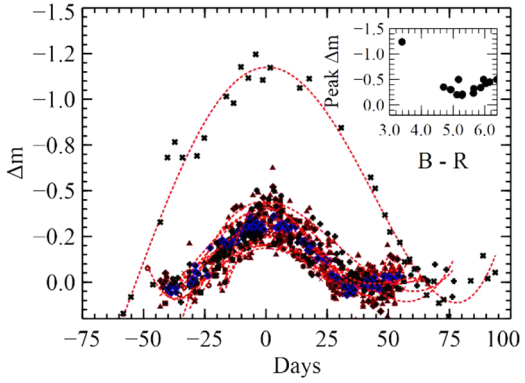

Figure 11. Humps (change in magnitude, Δm, of detrended light curve segment) from 15 LPVs with the peaks centered at 0 days. The inset shows the Δm at the peak value for each LPV as a function of color (the B–R bandpasses from Gaia measurements).

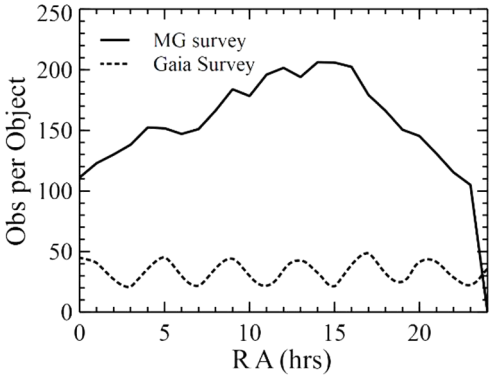

Figure 12. Mean number of observations per object as a function of RA for the MG and Gaia surveys.

Table 2. Comparison of object mean amplitudes(A) in magnitude and frequency (%) above and below the period color line (PCL) from Figure 9 between MG and Gaia DR2 surveys.

	Above PCL		*Below PCL*		
Source	*%*	*A*	*%*	*A*	*P*†
MG	80.6	2.03	19.4	2.15	0.71
Gaia DR2	61.2	1.31	38.8	0.36	$<10^{-5}$
P		$<10^{-4}$		$<10^{-4}$	

†*P, probability amplitudes are the same by student t-test.*

Table 3. MG LPVs that exhibit "Humps."

Source	*Identifier*	*Δm*	*Days*	*Phase*
†MG6A	10282350	–0.45	51	0.80
*MG1	1098444	–0.35	47	0.73
MG6A	10624347	–0.21	45	0.71
†MG6A	10634536	–0.50	69	0.62
MG6A	10641834	–0.32	55	0.70
†MG6A	10654089	–0.50	61	0.74
*MG1	1334111	–0.42	50	0.79
*MG1	1339600	–0.19	45	0.78
*MG1	1341934	–0.30	34	0.70
†MG6A	10680158	–0.20	49	0.65
†MG1A	10619638	–1.24	107	0.71
†MG6A	10731840	–0.50	65	0.75
MG1A	10647664	–0.23	55	0.74
*†MG1	1414532	–0.34	64	0.71
†MG6A	10767909	–0.30	46	0.79

**Previously noted (Craine* et al. *2015).* †*LPVs with humps in multiple cycles.*

objects in a redder region compared to the low amplitude objects. A period color line (PCL) can be drawn to separate the two main clusters shown in Figure 9 defined as:

$$B–R = 6.55 \log P – 12.0, \quad (5)$$

where P is the period in days and B–R is the color index. There is a third apparent cluster of low period objects that also tend to have low amplitude but on the redder side of the line.

Characterizing the MG survey LPVs in a similar manner, as shown in Figure 10, reveals that the low amplitude bluer cluster is only about half as abundant (19.4% of objects) compared to the Gaia DR2 survey (38.8% of objects), Table 2. The small number of objects in the region of the bluer cluster are mostly high amplitude and not different from the redder cluster (2.15 compared to 2.03, $P_{same} = 0.71$). The MG survey objects in the bluer cluster, however, do have a significantly higher amplitude than those from the Gaia DR2 survey (2.15 compared to 0.36, $P_{same} = 4.2 \times 10^{-5}$). The redder cluster has the characteristics of typical MIRA Mira type stars while the bluer cluster may represent the abundant Optical Gravitational Lensing Experiment (OGLE) Small Amplitude Red Giants (OSARGs) (Gaia Collab. *et al.* 2019).

3.2.3. LPVs with humps

The LPVs identified by screening the MG1 and MG6 surveys were examined to determine which might exhibit recognizable "hump" structures. The humps were best recognized in the Zwicky Transient Facility light curves of the identified LPVs (Bellm *et al.* 2019). Humps were found in 15 of the sample LPVs (see Table 3). Eight of the LPVs were observed to have humps in multiple cycles and are identified in Table 3 with a dagger. The best delineated hump from each of the LPVs was selected for further characterization. The region of the light curve with the hump was analyzed by fitting a high order polynomial to the points surrounding the hump to establish a baseline for detrending the data (see section 2.6 for details). The detrended data can be seen in the graphs in Appendix C. The maximum difference of the hump from the baseline is presented in the Table 3 as Δm (change in magnitude in the R band). The duration of the hump is reported as "days." The phase at which the hump peak occurred is listed as "phase" in the table. The asterisk denotes an LPV that was noted to have a hump in the original MG1 study (Craine *et al.*, 2015).

To facilitate the comparison of the population of humps they are plotted together in Figure 11, with the hump peaks normalized to day 0. Most of the humps are very similar in shape and magnitudes. However, the hump observed for MG1A 1785161 was noticeably brighter in magnitude (Δm = –1.24 versus an average of –0.40) and duration (107 d versus an average of 56.2 d). It is intriguing that this LPV was the least red of the group (B–R = 3.39 versus and average of 5.37).

4. Discussion

The new reduction of the MG1 and MG6 surveys has resulted in the expanded identification of LPV stars in the MG1 strip with approximated R magnitudes between ~12.6 and ~17.4 from the initial 47 (Kraus, *et al.* 2007) to the current 138. Review of the compilation catalogs of the GCVS (Samus *et al.* 2017) and AAVSO (International Variable Star Index; VSX), in addition to the large collection of automated identification of LPV candidates from the Gaia survey (Gaia Collab. *et al.* 2018, 2019) and the ASAS-SN survey (Kochanek *et al.* 2017; Shappee *et al.* 2014), revealed that this study has newly identified nine unique LPVs (marked with an asterisk in Appendix A Tables A1 and A2). This brings the total number of new LPV identifications from the MOTESS-GNAT survey to 56 (including those reported in (Kraus *et al.* 2007)).

The surveys referenced in this study each have unique characteristics which are based upon the observing strategy, equipment, and whether ground-based, or space-based. These characteristics manifest themselves in the number of observations per object and the cadence of these observations, which in turn impacts the ability to define a period. For example, comparing the MG survey with the Gaia survey shows that the MG survey has accumulated a greater number of observations per object and that the number of observations per object is a function of the RA, with the most productive period around 14 to 15 hours. The pattern of observation for the space-based Gaia satellite however is quite different (see Figure 12).

The number of observations obtained by the MG survey is an advantage although it may be offset by seasonal gaps in observing. The Gaia survey observes objects more regularly, which more closely satisfies some of the basic assumptions of key frequency analysis methods. In addition, the Gaia survey has superior precision, with typical normalized errors of about 0.1%, compared to the MG errors of about 1%. The result is, as shown in Figure 4, the general agreement in period determinations. However, there are several objects where even the Gaia data benefits from the complementary data from ground-based surveys.

The MG survey collects unfiltered imaging. The impact on color properties of identified LPVs can be observed in Figures 8–10. These results revealed a bias in color of identified LPVs from the MG survey compared to those reported for the Gaia survey (Gaia Collab. *et al.* 2019). First, this bias is due to the bluer population of stars included in the Gaia LPVs (e.g., OSARGs) being fainter in the red magnitude. This results in a decreased signal signal-to to-noise ratio, increasing the variance in the MG survey photometry (which is already greater than that of the Gaia survey) and contributing to underrepresentation of some Gaia objects in the MG survey. Second, the bluer Gaia population of LPVs displays smaller amplitudes than the redder MIRA type stars, limiting their survival of the screening method employed (i.e., μ and 1/η).

The differences in the various surveys provide a strong argument for using the data in a complementary fashion to compensate for the shortcomings of each survey. Notable among surveys areis the data produced by the Zwicky Transient Facility (Bellm *et al.* 2019) that combines precision and large sample sizes which can be highly synergistic. The current trend of providing the ability to cross-reference the different surveys (such as at the Vizier (https://vizier.u-strasbg.fr/viz-bin/VizieR) or Gaia (https://gea.esac.esa.int/archive/) web portals) is important for both the amateur and professional astronomer and needs to be expanded.

5. Acknowledgements

This research has made use of the International Variable Star Index (VSX) database, operated at AAVSO, Cambridge, Massachusetts, USA.

References

Astropy Collaboration. 2018, *Astron. J.*, **156**, 123.

Baluev, R. V. 2012, *Mon. Not. Roy. Astron. Soc.*, **422**, 2372.

Bellm E. C., *et al*. 2019, *Publ. Astron. Soc. Pacific*, **131**, 18002.

Bradley, L., *et al.* 2019, astropy/photutils: v0.6 (https://doi.org/10.5281/ZENODO.2533376).

Craine, B. L., Craine, E. R., Tucker, T. A., Culver, R. B., and Anderson, R. 2021, in *Proceedings for the 40th Annual Symposium of the Society for Astronomical Sciences SAS-2021*, eds. J. C. Martin, R. K. Buchheim, R. M. Gill, W. Green, R. Stephens, Society for Astronomical Sciences, Rancho Cucamonga, CA, 31.

Craine, E. R., Culver, R. B., Eykholt, R., Flurchick, K. M., Kraus, A. L., Tucker, R. A., and Walker, D. K. 2015, *J. Amer. Assoc. Var. Star Obs.*, **43**, 131.

Craine, E. R., Culver, R. B., Kraus, A. L., Tucker, R. A., Walker, D., and Wing, R. F. 2007, in *The Society for Astronomical Sciences 26th Annual Symposium on Telescope Science*, Society for Astronomical Sciences, Rancho Cucamonga, CA, 45.

Gaia Collaboration, Brown, A. G. A., *et al.* 2018, *Astron. Astrophys.*, **616A**, 1.

Gaia Collaboration, Eyer, L., *et al.* 2019, *Astron. Astrophys.*, **623A**, 110.

Kochanek, C. S., *et al.* 2017, *Publ. Astron. Soc. Pacific*, **129**, 104502.

Kraus, A. L., Tucker, R. A., Thompson, M. I., Craine, E. R., and Hillenbrand, L. A. 2011, *Astrophys. J.*, **728**, 48.

Kraus, Adam L., Craine, Eric R., Giampapa, Mark S., Scharlach, W. W. G., and Tucker, Roy A. 2007, *Astron. J.*, **134**, 1488.

Mowlavi, N. 2018, *Astron. Astrophys.*, **618A**, 58.

Percy, J. R. 2007, *Understanding Variable Sstars*, Cambridge Univ. Press., Cambridge, 209.

Press, W. H., Teukolsky, S. A., Vetterling, W. T., and Flannery, B. P. 1996, *Numerical Recipes in Fortran 90*, Cambridge Univ. Press, Cambridge.

Samus, N. N., Kazarovets, E. V., Durlevich, O. V., Kireeva, N. N., and Pastukhova, E. N. 2017, *Astron. Rep.*, **61**, 80.

Scargle, J. D. 1982, *Astrophys. J.*, **263**, 835.

Shappee, B. J., *et al.* 2014, *Astrophys. J.*, **788**, 48.

Tucker, R. A. 2007, *Astron. J.*, **134**, 1483.

VanderPlas, J. T. 2018, *Astrophys. J., Suppl. Ser.*, **236**, 16.

Virtanen, P., *et al.* 2020, *Nat. Methods*, **17**, 261.

Von Neumann, J. 1941, *Ann. Math. Statistics*, **12**, 367.

Welch, D. L., and Stetson, P. B. 1993, *Astron. J.*, **105**, 1813.

Zechmeister, M. 2019, "GLS/Python at Master-Mzechmeister/GLS," (github.com/mzechmeister/GLS/tree/master/python) accessed 12 Dec. 2022.

Zechmeister, M., and Kürster, M. 2009, *Astron. Astrophys.*, **496**, 577.

Appendix A: Tables of LPVs

Table A1. Long period variable stars with high confidence periods. Objects identified as new LPVs in this study are marked with an asterisk.

Database ID								
MG1-VSC	*MG1A*	*MG6A*	*R.A. (2000) h*	*Dec. (2000) °*	*mMG*[1]	*Amplitude (mag)*	*Period (d)*	*Epoch*[2] *(MJD)*
—	—	10125719	6.27973	3.48849	12.74	1.56	333	52018.7
—	—	10157151	6.66172	3.41147	12.55	2.47	344	52200.1
—	—	10245630	7.39174	3.16072	13.02	0.98	106	52224.6
—	—	10282350	7.86004	3.48481	11.87	1.05	327	51923.4
—	—	10313628	8.58345	2.99139	12.99	2.91	257	52219.8
—	—	10318510	8.75614	3.45367	13.67	1.24	398	52208.8
—	10412126	—	17.44638	3.46843	11.44	1.38	261	51899.2
—	10420454	10492206	17.56957	3.05137	11.84	0.90	218	52023.6
—	10424503	10496867	17.62531	3.45457	12.51	1.71	275	52356.4
—	—	10514819	17.83027	3.28816	11.99	1.70	220	51852.9
—	—	10525998	17.92806	3.03218	12.98	2.26	416	51968.1
—	—	10538157	18.01871	3.55115	12.61	1.65	147	52041.0
1098444	—	10541529	18.04222	3.08712	14.30	2.12	259	51805.2
1117392	—	10549004	18.08990	2.94400	13.00	1.97	192	51898.2
1155788	—	10566412	18.17950	2.95202	14.29	3.35	371	51827.2
—	—	10577762	18.24071	3.10995	12.44	1.30	156	51987.2
—	—	10589271	18.29673	3.66614	12.20	1.60	243	51991.4
—	—	10595142	18.32747	3.21517	13.26	1.66	274	51858.8
—	—	10596880	18.33669	3.54930	14.14	2.04	273	51943.6
—	—	10597482	18.33939	3.43108	12.59	0.97	221	52036.2
1248064	10521961	10608672	18.39271	3.41298	13.77	1.83	283	51830.3
—	—	10610820	18.40066	3.18591	13.31	1.53	210	51966.4
1258871	—	10614674	18.42071	3.67411	13.33	1.87	232	51815.5
—	—	10615458	18.42484	3.04575	14.30	1.03	230	51875.6
—	10528529	10616558	18.43054	3.21746	11.78	1.21	264	51891.3
1270097	—	—	18.44853	2.91056	13.70	2.42	234	52068.7
1270289	—	10620863	18.44899	3.22180	13.70	1.84	265	51938.1
—	—	10623473	18.45900	3.23070	13.87	1.25	165	52001.4
—	—	10624347	18.46358	3.17335	12.63	0.72	230	51915.6
1287551	—	—	18.49306	3.47056	13.53	2.45	420	51821.8
1291327	—	—	18.50289	3.39167	13.40	2.84	241	51855.4
—	—	10634536	18.51324	3.68385	13.88	1.25	214	52004.8
—	—	10637601	18.53199	3.03832	13.13	2.58	337	51903.6
—	—	10638266	18.53610	3.54179	14.25	2.51	300	52010.2
—	—	10638788	18.53956	3.68264	14.21	2.10	212	51842.1
—	—	10639637	18.54536	3.59500	14.66	1.35	190	52009.6
—	10549295	—	18.55313	2.91184	13.25	1.63	265	52000.8
—	—	10641834	18.56043	3.34669	13.00	1.40	252	51809.1
—	—	10643445	18.57031	3.41909	14.25	2.47	456	52082.5
—	—	10644124	18.57412	3.00430	14.33	2.45	390	52034.0
—	—	10646120	18.58583	3.39812	14.52	0.78	237	51885.4
1315064	10554843	10646737	18.58913	3.64086	14.56	2.00	299	51801.2
—	—	10650043*	18.60816	3.62960	13.59	2.08	481	51917.2
1326286	—	10654089	18.62912	3.65812	15.21	1.82	302	52020.4
—	—	10656955	18.64352	3.12275	12.93	2.18	381	51947.3
—	—	10658268	18.65026	3.57515	14.15	1.77	327	52044.1
—	—	10658466	18.65129	3.69543	14.66	2.49	324	51896.1
1334111	—	10659344	18.65542	3.05212	14.71	1.96	305	52040.0

Table continued on following pages

Table A1. Long period variable stars with high confidence periods (cont.).

Database ID								
MG1-VSC	*MG1A*	*MG6A*	*R.A. (2000) h*	*Dec. (2000) °*	*mMG*[1]	*Amplitude (mag)*	*Period (d)*	*Epoch*[2] *(MJD)*
—	10566760	10659797	18.65731	3.28148	13.59	2.24	290	51772.5
1336304	—	—	18.66331	3.08861	13.96	1.70	362	51971.4
—	—	10663230	18.67001	3.64038	14.42	1.32	296	51866.2
—	—	10664502	18.67500	3.60400	12.81	1.09	251	51979.6
1339600	—	10664704	18.67601	3.42910	14.89	2.44	325	51902.2
1341934	10572125	10666775	18.68734	3.33558	14.77	2.18	237	52032.8
—	—	10666916	18.68815	3.47474	13.87	1.13	245	51912.8
—	10573832	—	18.69702	2.91197	15.37	2.74	357	51808.8
1344747	10574581	—	18.70092	3.09939	14.79	1.51	197	51863.4
—	10575668	10670584	18.70721	2.96925	15.43	2.59	141	52037.8
—	—	10671162	18.71028	3.65455	15.55	4.09	232	51931.4
—	10581264	10676905	18.74174	3.36799	15.38	0.58	292	51820.2
—	10583328	—	18.76376	2.97547	15.74	1.29	206	52023.8
—	—	10679837*	18.77205	3.47107	15.43	1.94	303	51822.6
—	10583952	—	18.77278	2.99682	14.77	2.08	315	51843.3
—	—	10679937	18.77355	3.56562	13.41	0.88	234	51854.0
—	—	10680158	18.77661	3.62856	15.84	1.59	205	51920.1
—	—	10680181*	18.77706	3.24949	15.81	1.35	218	51981.6
—	—	10681094	18.79188	2.94482	16.36	1.87	202	51877.4
—	10585083	10681185	18.79312	3.31842	15.06	1.77	275	52003.7
—	—	10682562	18.81648	3.41414	15.28	1.77	343	51891.9
—	10586841	10683307	18.82688	3.02730	16.22	2.47	260	51793.1
—	—	10683894*	18.83644	3.48245	15.25	2.40	506	51956.7
—	10589889*	—	18.88252	3.03746	14.95	1.94	586	51903.5
—	10592725	10690206	18.93340	2.99415	11.79	1.48	230	51828.9
—	10593262*	10690831*	18.94750	2.91795	13.21	2.32	270	52024.9
—	—	10691652	18.96674	3.47641	15.78	1.54	433	51727.2
—	10595225	—	18.98945	3.11190	15.67	1.36	294	51954.8
—	—	10699251	19.04595	3.44845	12.77	2.07	489	52067.5
—	—	10703054*	19.05968	3.46663	15.50	3.62	269	51834.5
1372707	—	—	19.07372	3.42139	15.51	4.17	349	52222.6
—	—	10707886	19.07564	3.36433	14.87	1.07	222	51831.0
1376419	—	—	19.08364	3.17194	15.22	0.80	165	51910.6
1379672	—	10713590	19.09167	3.55671	13.75	1.83	152	52041.5
—	10619638	—	19.09897	2.94856	14.01	3.24	522	51528.3
—	—	10717332	19.09977	3.57870	13.39	1.10	290	51893.5
—	10623199	—	19.10785	3.17282	13.73	1.54	221	51831.3
—	10624436	—	19.11093	3.44052	13.19	3.25	501	51979.7
1388413	—	10721993	19.11139	3.03939	13.34	1.57	246	51824.1
1388633	—	—	19.11197	3.28667	13.65	1.12	189	52035.4
—	10625131	10722447	19.11257	3.27738	13.77	4.97	312	51748.3
—	—	10722590	19.11300	3.42302	12.40	1.22	229	51890.8
—	10626627	—	19.11614	2.98712	14.32	2.12	423	51831.7
1391053	—	—	19.11625	2.98722	14.11	1.91	422	51838.6
—	—	10725247	19.12023	3.35178	13.09	1.36	298	51752.6
1393846	—	—	19.12111	2.95944	13.67	3.71	360	51739.5
—	10634557	—	19.13294	3.30466	15.28	2.08	246	51997.1

Table continued on next page

Table A1. Long period variable stars with high confidence periods (cont.).

Database ID								
MG1-VSC	*MG1A*	*MG6A*	*R.A. (2000) h*	*Dec. (2000) °*	*mMG*[1]	*Amplitude (mag)*	*Period (d)*	*Epoch*[2] *(MJD)*
—	—	10731840	19.14089	3.26123	15.21	3.10	437	51777.9
1406788	10642204	—	19.15478	2.91548	13.31	2.07	299	51757.6
1410977	—	—	19.16472	2.90583	13.40	1.61	340	52001.4
1413873	10647664	10742975	19.17113	3.03156	15.13	2.09	347	52012.4
1414532	—	—	19.17256	2.96806	13.39	1.59	315	51849.6
1428501	10658602	—	19.20193	3.05442	13.29	1.92	418	51714.5
—	—	10759858	19.22240	3.30691	13.17	1.09	314	51946.7
1440964	—	—	19.23317	3.12889	13.70	1.88	409	51918.1
1444065	10670343	10764936	19.24078	3.18946	13.46	3.66	266	51908.1
—	—	10765454	19.24268	3.21684	12.72	2.08	281	51896.5
1448319	10673873	10767909	19.25080	2.91731	13.43	2.67	218	51929.0
1457857	—	—	19.27147	3.61722	13.07	1.16	282	51896.1
—	—	10776316	19.27731	3.42775	12.58	1.77	289	52008.5
1466778	10685409	10780200	19.29204	3.38649	14.25	2.00	296	51796.3
1468465	—	—	19.29603	2.92750	14.80	1.51	330	52007.2
1477416	—	10786863	19.31665	3.51341	13.35	1.63	138	52008.3
—	10696051	—	19.33167	3.37791	13.38	1.71	482	51713.4
1492532	—	—	19.35258	3.53500	14.14	2.49	213	51940.3
1496600	10704133	10798486	19.36387	3.51821	12.70	2.06	289	51843.2
—	10706234	—	19.37303	3.31331	12.60	1.55	288	51787.4
—	—	10805023	19.39115	3.32842	12.37	1.16	111	52005.2
—	10710722	10805298	19.39227	3.15070	11.99	1.56	256	51834.8
1518640	—	—	19.41364	3.62250	13.06	2.32	228	51944.0
1523972	—	—	19.42514	3.30889	13.86	2.21	272	52045.2
1540903	—	—	19.46025	3.38639	13.69	3.65	272	51902.5
—	10737124	10832301	19.49149	3.50998	13.79	2.28	300	51942.3
—	—	10854654	19.58874	3.65374	12.92	2.04	285	51775.7
—	—	10864634	19.63745	3.52213	12.37	1.94	214	52049.6
—	10777381	—	19.67851	3.20240	11.26	0.91	232	51918.7
1653368	10781632	10877309	19.70695	3.53429	13.02	3.08	232	51961.8
—	—	10897045	19.83316	3.15389	11.54	1.50	287	51848.8
1877036	—	—	20.47967	2.98500	14.15	1.87	176	51985.1

[1] *mMG, differential magnitude unfiltered.*

[2] *Epoch, establishes a zero-time at one period before the first maxima in the observed data.*

Table A2. Long period variables with ambiguous periods. The period candidates have been evaluated by determining the Vuong statistic (Baluev 2012) and found to have p-values > 0.05 indicating that one of the periods could not be favored. Objects identified as new LPVs in this study are marked with an asterisk.

Database (ID)						
MG1-VSC	*MG1A*	*MG6A*	*R.A. (2000) h*	*Dec. (2000) °*	*mMG*[1]	*Period (d)*
1334664	—	10660631	18.66048	2.28784	14.10	119,175
		10691329*	18.95937	3.45862	15.39	199, 390
—	10595620*	—	18.99722	3.64549	14.49	521, 456
—	—	10693742	19.00426	2.98192	14.69	598, 516
1375418	—	—	19.08108	2.90444	15.12	149, 540
165463	10629210	—	19.12164	2.99446	13.29	73,120
—	10632033	10727558	19.12709	3.49154	13.79	152, 146, 263
1410394	—	—	19.16333	3.57500	13.73	71, 88, 90, 121
—	10671116	—	19.24264	3.50580	14.92	526, 244
1478012	—	—	19.31811	3.40917	16.44	168, 338
1545107	10731356	10826002	19.46893	3.00822	14.37	170, 302

[1] *mMG, differential magnitude unfiltered.*

Appendix B: Light curves for LPV stars

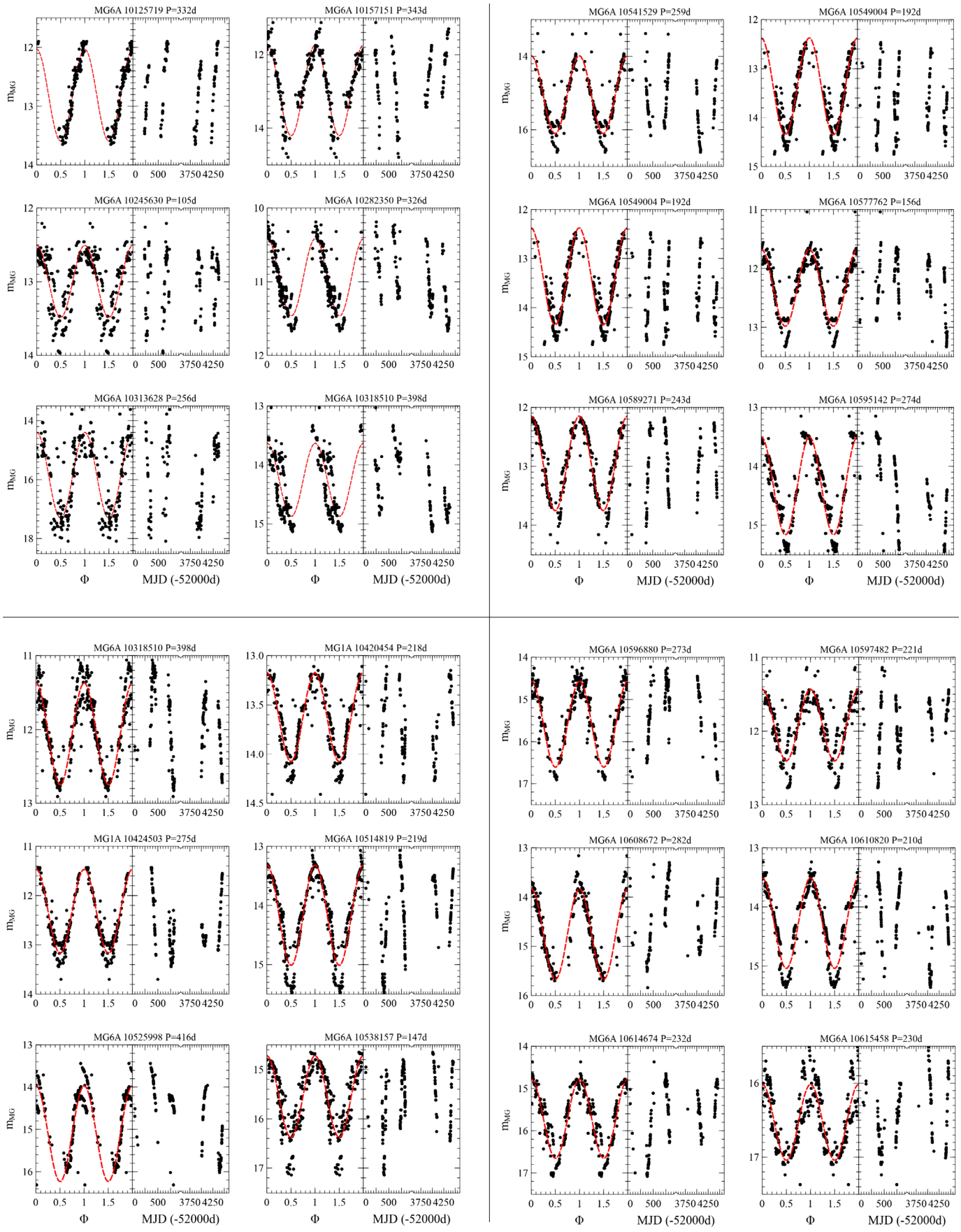

Figure B1. Light curves and folded phase light curves for LPVs with high confidence periods. Red dashed line is the least squares sinusoidal fit to the data. P is the period determined using the Lomb-Scargle GLS method. (Figure continued on following pages.)

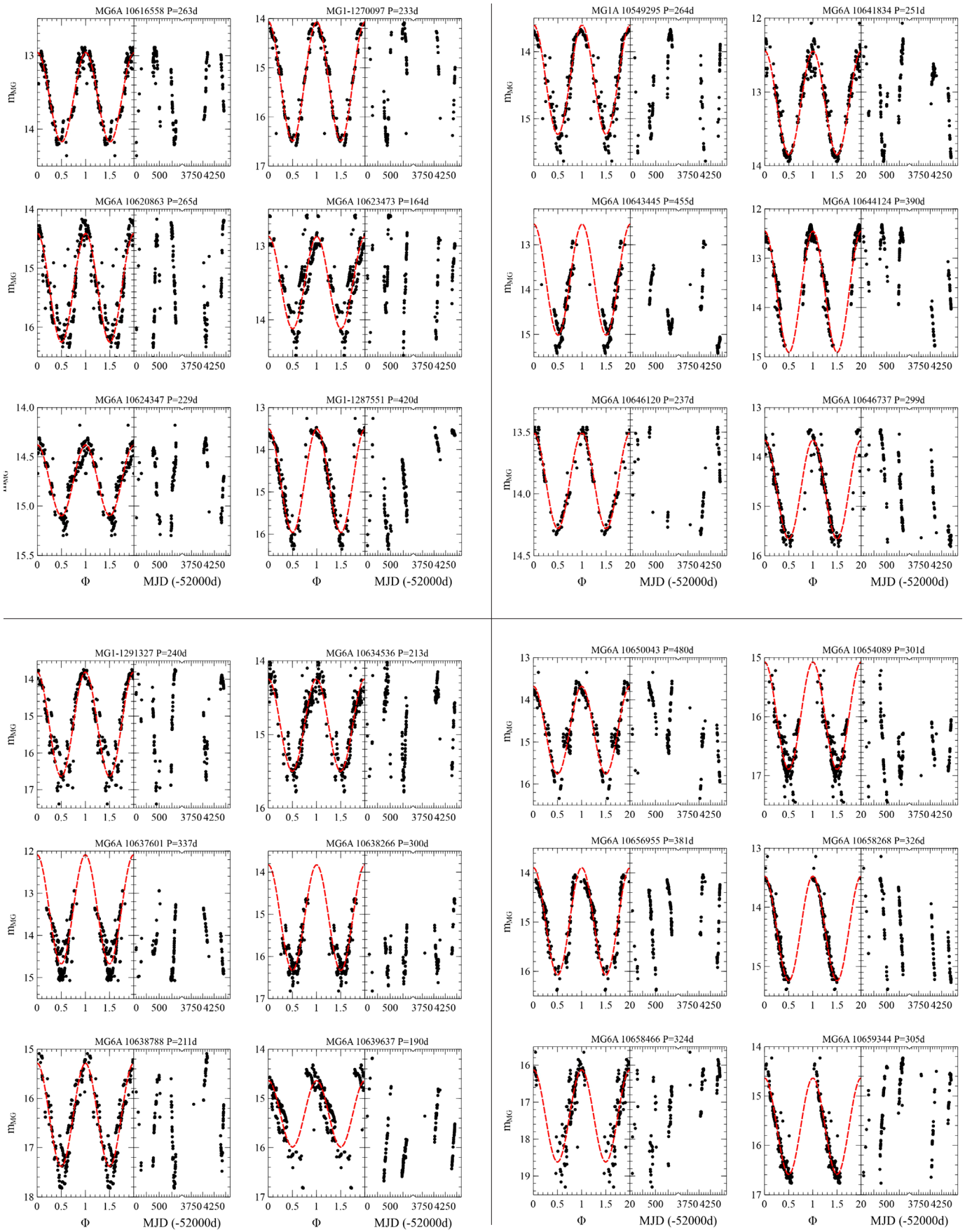

Figure B1. Light curves and folded phase light curves for LPVs with high confidence periods. Red dashed line is the least squares sinusoidal fit to the data. P is the period determined using the Lomb-Scargle GLS method (cont.). (Figure continued on following pages.)

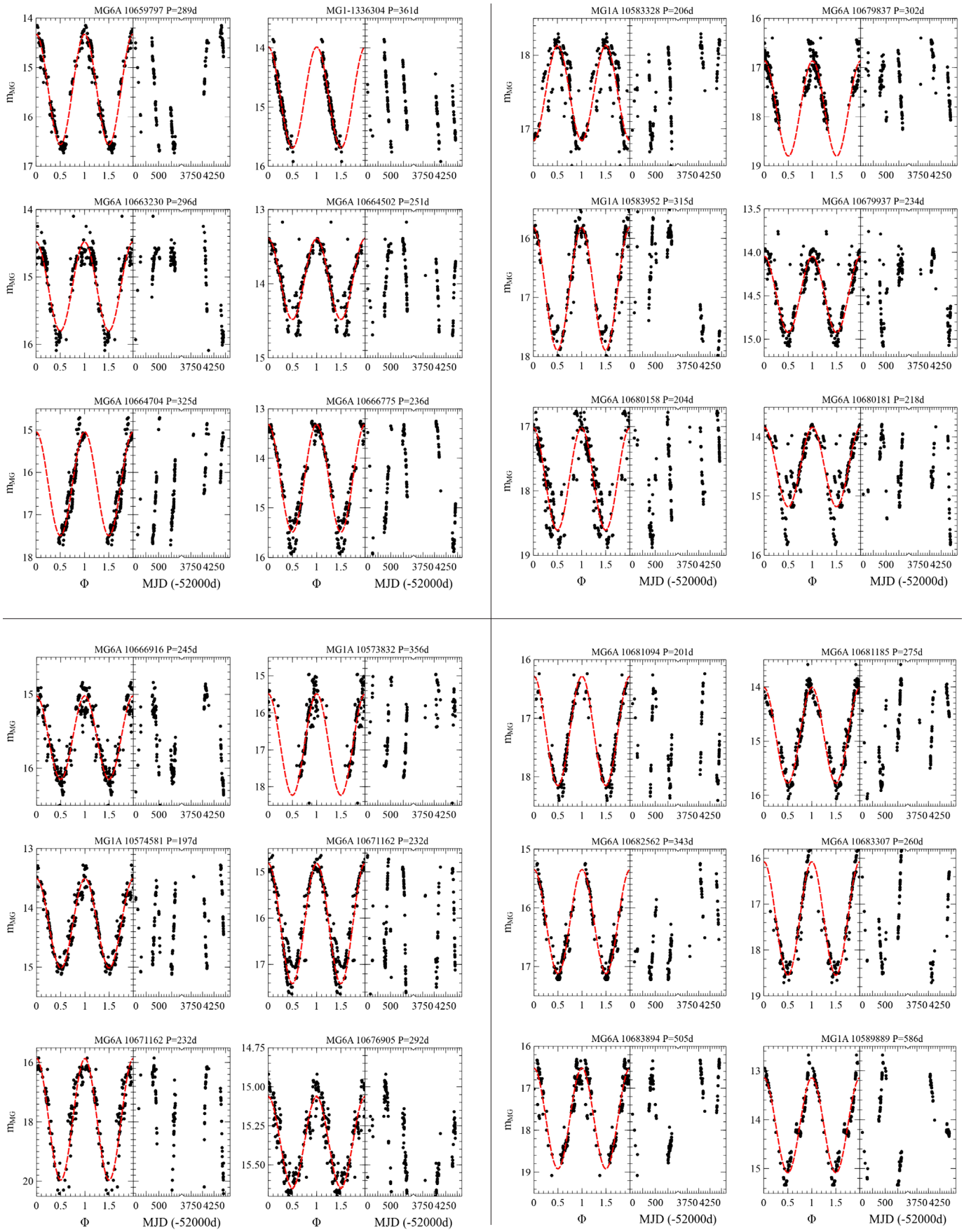

Figure B1. Light curves and folded phase light curves for LPVs with high confidence periods. Red dashed line is the least squares sinusoidal fit to the data. P is the period determined using the Lomb-Scargle GLS method (cont.). (Figure continued on following pages.)

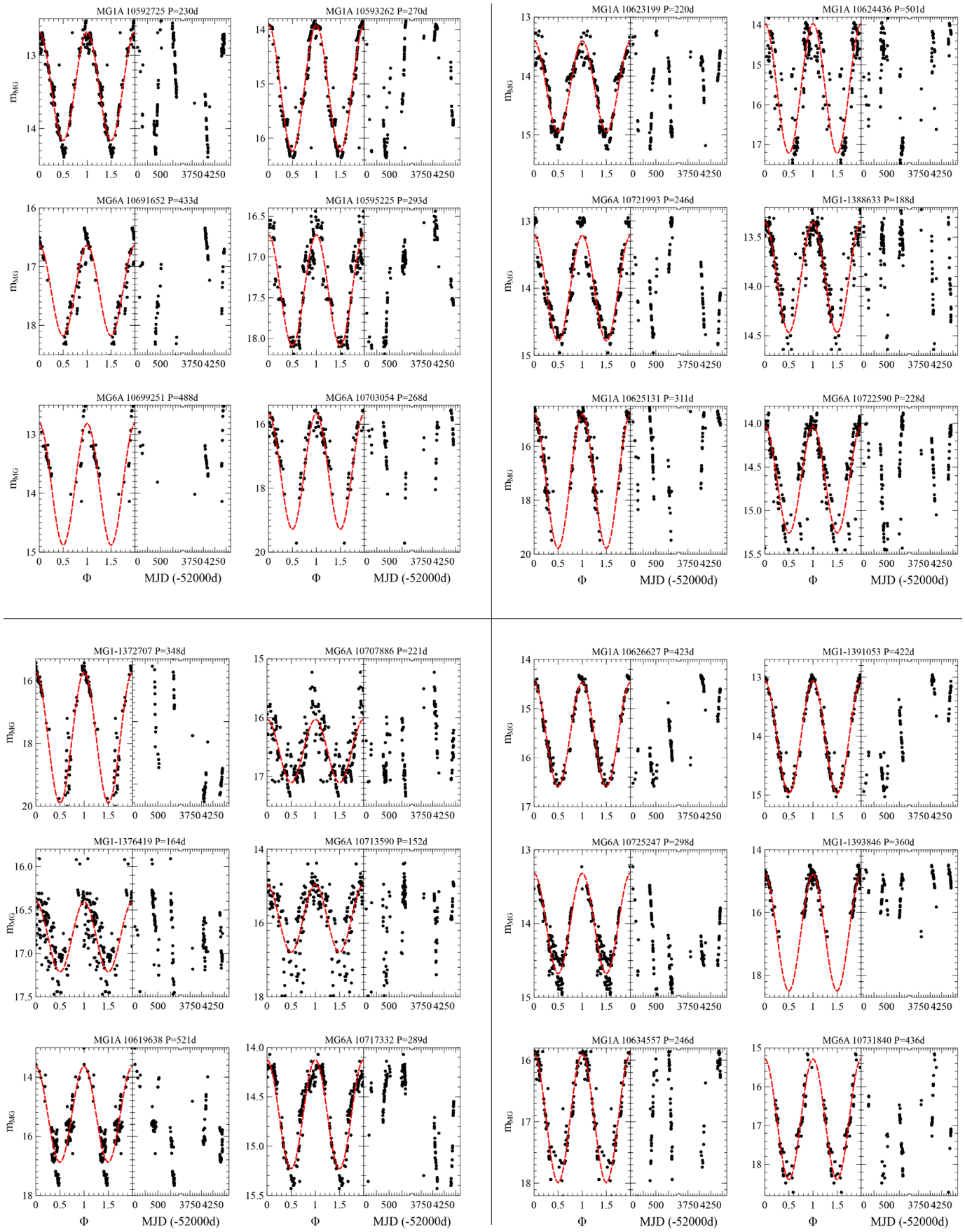

Figure B1. Light curves and folded phase light curves for LPVs with high confidence periods. Red dashed line is the least squares sinusoidal fit to the data. P is the period determined using the Lomb-Scargle GLS method (cont.). (Figure continued on following pages.)

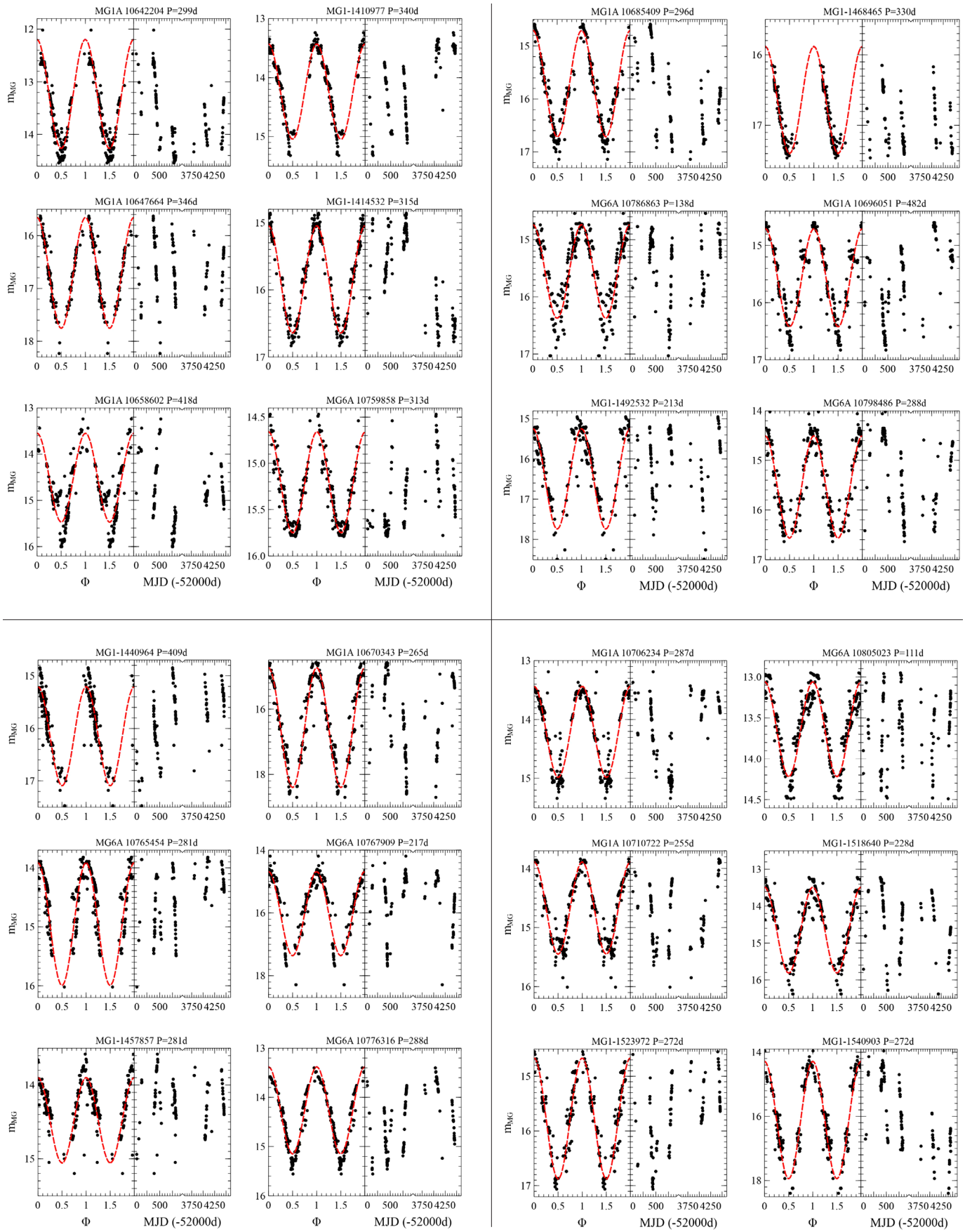

Figure B1. Light curves and folded phase light curves for LPVs with high confidence periods. Red dashed line is the least squares sinusoidal fit to the data. P is the period determined using the Lomb-Scargle GLS method (cont.). (Figure continued on next page.)

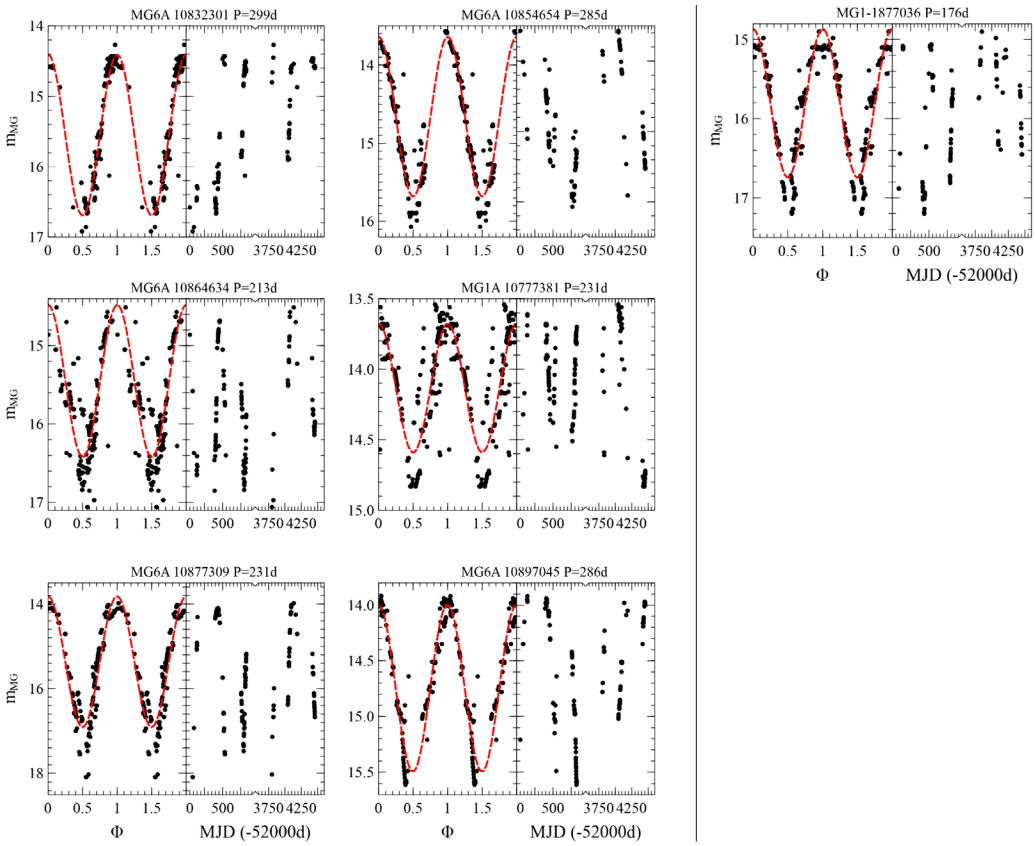

Figure B1. Light curves and folded phase light curves for LPVs with high confidence periods. Red dashed line is the least squares sinusoidal fit to the data. P is the period determined using the Lomb-Scargle GLS method (cont.).

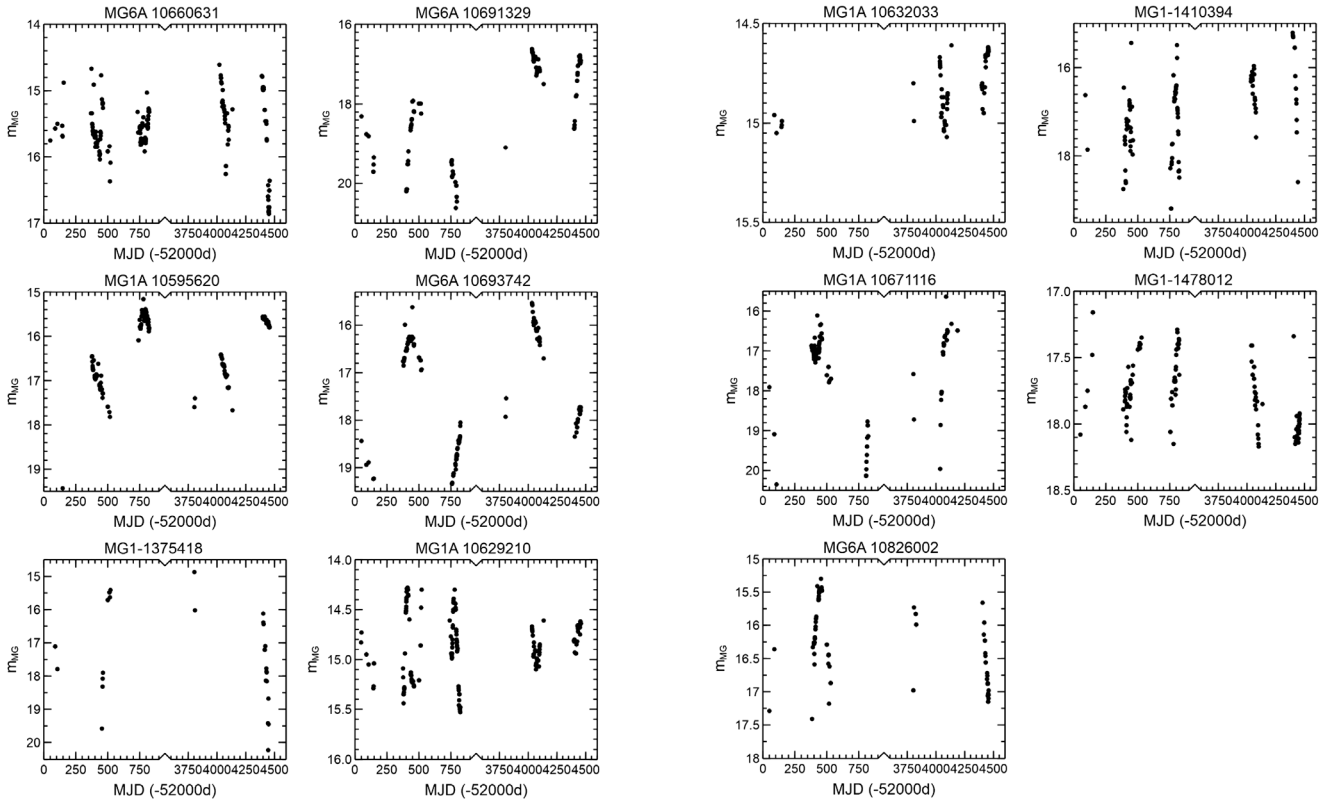

Figure B2. Light curves for LPVs with ambiguous periods. Data point before 52900 MJD are from the MG1 survey and those after 55750 MJD are from the MG6 survey.

Appendix C: Light curves for hump feature

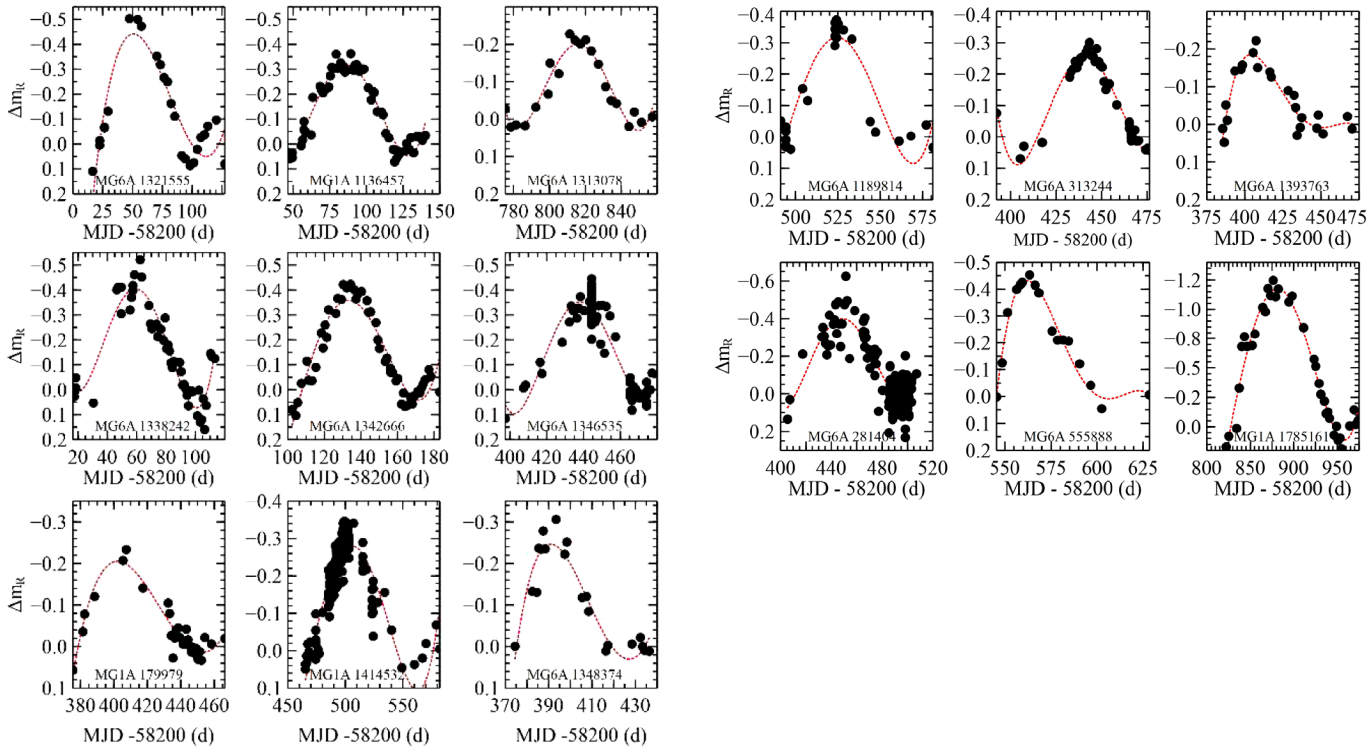

Figure C1. The region around the "hump" of an ascending or descending arm of the periodic light curves were detrended prior to plotting to facilitate the visualization of the hump. The data are from the ZTF survey R band (Bellm *et al.* 2019). The red dotted line is a fourth order polynomial fit to the hump.

Solar Coronal Flattening during the Total Solar Eclipse of August 2017 from CATE Data

Jennifer Birriel
Joseph Teitloff
Department of Physics, Earth Science, and Space Systems Engineering, Morehead State University, 150 University Boulevard, Morehead, KY 40351; j.birriel@moreheadstate.edu

Received June 14, 2022; revised July 5, 2022; accepted July 8, 2022

Abstract The Continental-America Telescopic Eclipse (CATE) Experiment used a fleet of 68 identical telescopes spread along the line of totality to acquire images of the total solar eclipse on August 21, 2017. The original science goal was to construct a 90-minute, high-definition movie of the eclipse to examine the dynamics of the magnetic fields and plasmas in the solar corona. We used processed white light images from three CATE sites to examine the solar coronal flattening parameter, ε. The flattening parameters from sites 000 and 002, near the start of the eclipse, are the same as that measured for site 044b, the mid-point of the eclipse. Our average flattening parameter, $\varepsilon = 0.24 \pm 0.09$, is consistent with values obtained by other observers for the 2017 solar eclipse. Furthermore, it is consistent with values obtained during other eclipses at the same solar phase as the 2017 eclipse, $\Phi = 0.789$. These results represent yet another useful scientific result from the CATE Experiment.

1. Introduction

Solar magnetic variability is most readily observed by variations in sunspot number. Sunspot observations date back nearly 2,000 years, but the sunspot cycle was not discovered until 1844 by Heinrich Schwabe (Hathaway 2015). Other indicators of solar activity include changes in emission lines such as Fe XIV (530.3 nm) and Ca II K (396.85 nm) and disk radio emissions at 10.7 cm. Total eclipse observations since the mid-nineteenth have revealed changes in the shape of the solar white light corona; these changes also vary cyclically with solar activity (e.g., Pishkalo 2011; Rušin 2017; Pasachoff and Rušin 2022).

The white light solar corona is essentially created by the presence of helmet streamers around the circumference of the photosphere. During solar minimum these are limited to the equatorial regions of the solar disk, while during solar maximum helmet streamers are uniformly distributed around the solar disk. Since solar coronal structures such as helmet streamers and coronal holes are produced by the solar magnetic field extending above the photosphere, variations in the shape of the white light corona (WLC) makes them a useful indicator of solar activity.

In the early part of the 20th century, Hans Ludendorff developed a "flattening" coefficient to describe shape of the solar corona (Pishkalo 2011 and references therein). The so-called Ludendorff-index, ε, is defined as:

$$\varepsilon = \frac{d_e - d_p}{d_p} \quad (1)$$

where d_e is the average equatorial diameter of the WLC and the d_p the average polar diameter. The average equatorial diameter, d_e, is determined by measuring the diameter of an isophote at the equator and the diameter of this same isophote at angles +22.5° and –22.5° from the equator. The average polar diameter is similarly defined. The solar flattening index increases in a linear fashion out to a distance of two solar radii and then rapidly falls off. The accepted methodology to determine $\varepsilon(2R_\odot)$ involves plotting measured values of ε for various isophotes as a function of $R/R_\odot$ and determining a linear fit to the data (e.g. Rušin 2017; Pishkalo 2011; Imaduddin *et al.* 2016).

2. Observations and analysis

The Citizen CATE experiment is described in detail elsewhere (Penn *et al.* 2020); here we provide a brief overview of the essential instrumental components. Each site on the line of totality consisted of identical equipment which included an 80-mm diameter, 500-mm focal length APO refractor from Daystar fitted with a Thousand Oaks white light solar filter, #S4250. The mount was a Celestron Omni CG4, #915 with Celestron motor drive CG4, #93522. Images were acquired by a 5-Mpix CMOS camera, Pt Grey GS3-U3-51S5M-C which was controlled by an Arduino Uno. CATE data consist of white light images taken through a solar filter. Each site collected data for dark- and flat-field correcting. All sites collected a sequence of eight distinct exposures during totality: this resulted in hundreds of images from each site over the course of totality.

We used data from three CATE sites: two near the start of the eclipse—Site 000 in Weiser, Idaho, and Site 002 in Salem, Oregon—and one from the middle of the eclipse and the location with the longest duration of totality, Site 044 in Hopkinsville, Kentucky (Figure 1). These are the best images obtained at each site and are dark-corrected and flat field-processed. The CATE coronal isophotes agree in the overall shape found by Pasachoff and Rušin (2022) and Tsvetkov *et al.* (2019).

We used ImageJ software (Collins *et al.* 2017) to produce isophote images for each site, shown in Figure 2. Each isophote image was printed on paper: a protractor was used to measure angles and a ruler was used to measure isophote diameters. This method was suggested to us by Pishkalo (2021).

The measured radii for each image were used to compute flattening parameters which were then plotted as a function

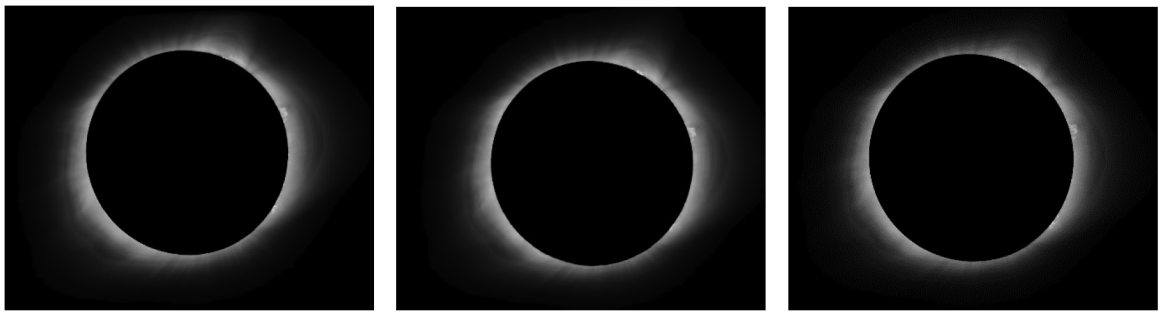

Figure 1. White light images of totality from Sites (a) 000 Weiser, Idaho; (b) 002 Salem, Oregon; and (c) 044b Hopkinsville, Kentucky. Images are dark- and flat-field corrected. Note that the image for site 000 is slightly shifted and this results in a slight "clipping" in its outermost isophote as seen in Figure 2.

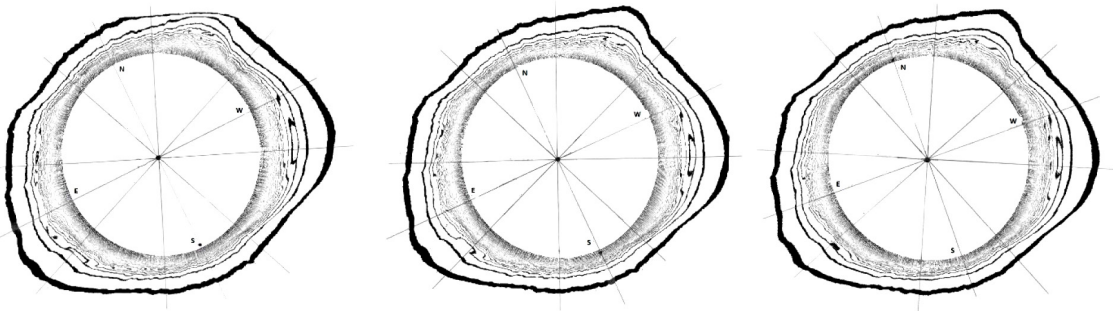

Figure 2. Isophotes for each site produced using ImageJ software (Collins *et al.* 2017): (a) 000 Weiser, Idaho; (b) 002 Salem, Oregon; and (c) 044b Hopkinsville, Kentucky. The solar orientation is indicated in each image as are the lines used to measure individual isophotes. The outermost isophote of site 000 is "clipped" at the northwest location due to a misalignment of the image on the camera chip.

of solar radius. The data are fit with a linear trendline and the resulting equation is used to calculate the solar flattening parameter $\varepsilon(2R_{\odot})$ for each site. Figure 3 shows the plots of data for each site.

3. Results and conclusion

Our results are summarized in Table 1. The average solar flattening parameter for the total solar eclipse of August 21, 2017, derived from CATE data is 0.24 ± 0.09. This result is in agreement with the value of 0.24 found by Pasachoff and Rušin (2022); it is also consistent with the results of Tsvetkov *et al.* (2019), who found a flattening parameter of 0.220 ± 0.002. (Our uncertainty is larger than Tsvetkov *et al.* for two reasons: our resolution is apparently lower and our isophotes do not extend out as far.)

As mentioned in the introduction, the flattening index varies with solar activity. The phase of the solar cycle is defined as from a historical perspective; the CATE data are consistent with historical measurements over the last century, as shown in Figure 4. The phase of the solar cycle is defined by:

$$\Phi = \frac{T - m_1}{m_2 - m_1} \qquad (2)$$

where T is the time of observation, m_1 is the preceding minimum, and m_2 is the subsequent maximum (Rušin 2017); all of these values are in years and Φ ranges in value from 0 to +1. For the August 21, 2017, eclipse the solar phase was $\Phi = 0.789$. A historical plot of ε versus Φ (Figure 4) demonstrates that our value of $\varepsilon = 0.24$ is consistent with historical data at the same solar activity phase.

Citizen CATE participants consisted of both amateurs and professional scientists. As discussed by Stoev and Stoeva (2008), amateur observations of solar eclipses can provide useful scientific data regarding the structure of the solar corona in the form of solar flattening indices. Our results represent another useful contribution to solar eclipse science resulting from data derived largely by amateurs and students from the 2017 Citizen CATE project.

4. Acknowledgements

The authors wish to thank Matt Penn and Mike Conley for the use of CATE data from their sites. We are especially grateful to Matt Penn for processing all of the CATE data specifically used in this study. We thank Mykola Pishkalo for his advice and assistance in understanding how to make solar flattening parameter measurements. Finally, we thank Jay M. Paschoff and Vojtech Rušin for feedback that improved the quality of this paper.

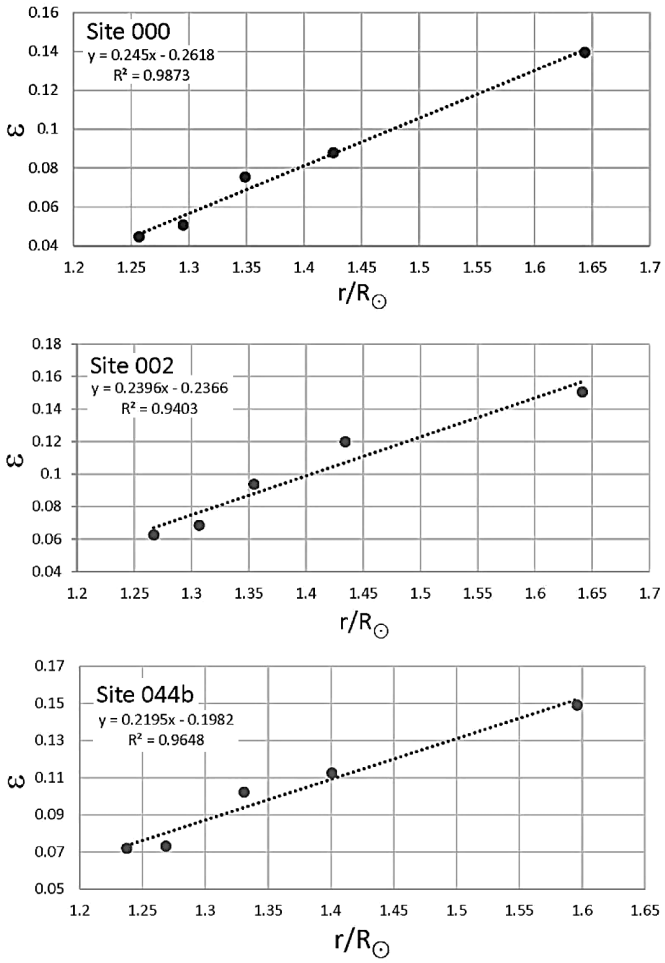

Figure 3. Plots of Ludendorff flattening parameter, ε, as a function of heliocentric radial distance.

Table 1. Solar Flattening Parameters Derived from selected CATE data.

Site No. (Location)	*Observer*	*ε (2R⊙)*
000 (Idaho)	Matthew Penn	0.23 ± 0.04
002 (Oregon)	Mike Conley	0.24 ± 0.09
044b (Kentucky)	Birriel, Birriel, Yess	0.24 ± 0.06

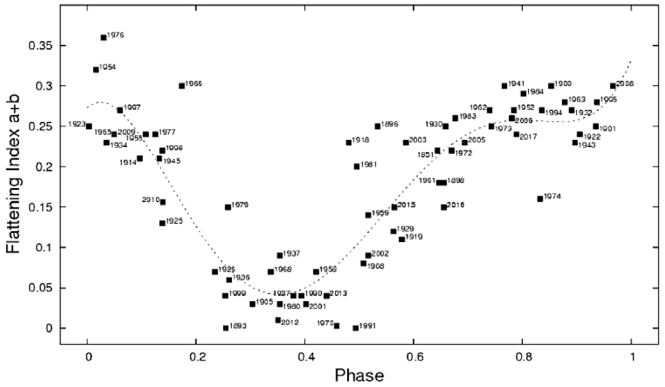

Figure 4. A plot of historical values of solar flattening, ε, versus solar activity phase, Φ. The red squares indicate flattening parameters for Cycle 24. (Reprinted by permission from Springer Nature, *Solar Physics*, "The Flattening Index of the Eclipse White-Light Corona and Magnetic Fields," J. M. Pasachoff and V. Rušin, 2022.)

References

Collins, K. A., Kielkopf, J. F., Stassun1, K. G., and Hessman, F. V. 2017, *Astron. J.*, **153**, 77 (https://www.astro.louisville.edu/software/astroimagej).

Hathaway, D. H., 2015, *Living Rev. Sol. Phys.*, **12**, 4.

Imaduddin, I., Akbar, E. I., and Putri, G. P. 2016, *J. Phys. Conf. Ser.*, **771**, 012008.

Pasachoff, J. M., and Rušin, V. 2022, *Sol. Phys.*, **297**, 28.

Penn, Matthew, *et al.* 2020, *Publ. Astron. Soc. Pacific*, **132**, 014201.

Pishkalo, M. I. 2011, *Sol. Phys.*, **270**, 347.

Pishkalo, M. I. 2021, private communication (October 10, 2021).

Rušin, V. 2017, *Sol. Phys.*, **292**, 24.

Stoev, A. D., and Stoeva, P. V. 2008, *Adv. Space Res.*, **42**, 1806.

Tsvetkov, T., Miteva, R., Ivanov, E., Popov, V., Nakeva, Y., Bojevski, L., Damm, T., and Petrov, N. 2019, in *Space, Ecology, Safety—SES 2019*, eds. P. Getsov, G. Mardirossian, Ts. Srebrova, Space Research and Technology Institute, Bulgarian Academy of Sciences, Sofia, 52.

Recent Minima of 234 Eclipsing Binary Stars

Gerard Samolyk
P.O. Box 20677, Greenfield, WI 53220; gsamolyk@wi.rr.com

Received August 23, 2022; accepted August 23, 2022

Abstract This paper continues the publication of times of minima for eclipsing binary stars. Times of minima determined from observations received by the AAVSO Eclipsing Binaries Section from February 2022 through July 2022 are presented.

1. Recent observations

The accompanying list (Table 1) contains times of minima calculated for 234 variables calculated from recent CCD observations made by participants in the AAVSO's eclipsing binary program. These observations were reduced by the observers or the writer using the method of Kwee and van Woerden (1956).

The linear elements in the *General Catalogue of Variable Stars* (GCVS; Kholopov *et al.* 1985) were used to compute the O–C values for most stars. For a few exceptions where the GCVS elements are missing or are in significant error, light elements from another source are used: DV Cep (Frank and Lichtenknecker 1987), Z Dra (Danielkiewicz-Krosniak *et al.* 1996), DF Hya (Samolyk 1992), EF Ori (Baldwin and Samolyk 2005), GU Ori (Samolyk 1985).

The light elements used for HV Aqr, CV Boo, LM Boo, EH Cnc, IU Cnc, CZ CMi, AS CrB, V2197 Cyg, V2239 Cyg, LS Del, MR Del, BC Her, IT Her, V728 Her, WZ Leo, XY LMi, DZ Lyn, V404 Lyr, V592 Lyr, V2612 Oph, DK Sct, BS UMa, HX UMa, KM UMa, and CG Vir are from (Kreiner 2004).

The light elements used for V641 Aur, XY Boo, QV Cnc, AW CrB, BD CrB, V2240 Cyg, V2552 Cyg, MY Eri, V1044 Her, V1057 Her, CE Leo, GU Leo, GV Leo, HI Leo, VW LMi, AG LMi, EL Lyn, FI Lyn, KS Lyn, V2610 Oph, V1851 Ori, EQ UMa, QT UMa, and IR Vir are from (Paschke 2014).

The light elements used for V428 Gem, V658 Lyr, and HO Psc are from (Nelson 2014).

The light elements used for PQ Eri, V740 Lyr, V958 Mon, V970 Mon, V723 Per, VY UMi, and V715 Vir are from (Watson *et al.* 2014).

The standard error is included when available. Column F indicates the filter used. A "C" indicates a clear filter.

This list will be web-archived and made available through the AAVSO ftp site at:

ftp://ftp.aavso.org/public/datasets/gsamj234.txt.

This list, along with the eclipsing binary data from earlier AAVSO publications, is also included in the Lichtenknecker Database administrated by the Bundesdeutsche Arbeitsgemeinschaft für Veranderliche Sterne e.V. (BAV) at:

http://www.bav-astro.de/LkDB/index.php?lang=en.

References

Baldwin, M. E., and Samolyk, G. 2005, *Observed Minima Timings of Eclipsing Binaries No. 10*, AAVSO, Cambridge, MA.

Danielkiewicz-Krosniak, E, Kurpińska-Winiarska, M., eds. 1996, *Rocznik Astron.* (SAC 68), **68**, 1.

Frank, P., and Lichtenknecker, D. 1987, *BAV Mitt.*, No. 47, 1.

Kholopov, P. N., *et al.* 1985, *General Catalogue of Variable Stars*, 4th ed., Moscow.

Kreiner, J. M. 2004, *Acta Astron.*, **54**, 207 (http://www.as.up.krakow.pl/ephem/).

Kwee, K. K., and van Woerden, H. 1956, *Bull. Astron. Inst. Netherlands*, **12**, 327.

Nelson, R. 2014, Eclipsing Binary O–C Files (http://www.aavso.org/bob-nelsons-o-c-files).

Paschke, A. 2014, "O–C Gateway" (http://var.astro.cz/ocgate/).

Samolyk, G. 1985, *J. Amer. Assoc. Var. Star Obs.*, **14**, 12.

Samolyk, G. 1992, *J. Amer. Assoc. Var. Star Obs.*, **21**, 111.

Watson, C., Henden, A. A., and Price, C. A. 2014, AAVSO International Variable Star Index VSX (Watson+, 2006–2014; http://www.aavso.org/vsx).

Table 1. Recent times of minima of stars in the AAVSO eclipsing binary program.

Star	JD (min) Hel. 2400000 +	Cycle	O–C (day)	F	Observer	Standard Error (day)	Star	JD (min) Hel. 2400000 +	Cycle	O–C (day)	F	Observer	Standard Error (day)
AB And	59803.4723	71390.5	–0.0535	V	L. Corp	0.0004	QV Cnc	59647.8631	15917	0.0293	V	K. Alton	0.0004
HV Aqr	59791.4441	19471.5	–0.0010	V	L. Corp	0.0006	QV Cnc	59648.6764	15919.5	0.0293	B	K. Alton	0.0004
FK Aql	59777.6806	2767	–0.0813	V	L. Hazel	0.0006	QV Cnc	59648.6766	15919.5	0.0295	V	K. Alton	0.0002
KO Aql	59770.7363	6244	0.1045	V	G. Samolyk	0.0001	QV Cnc	59648.6767	15919.5	0.0296	R	K. Alton	0.0003
KO Aql	59776.4652	6246	0.1053	V	T. Arranz	0.0002	QV Cnc	59648.8387	15920	0.0290	V	K. Alton	0.0003
KP Aql	59762.8401	5751	–0.0262	V	G. Samolyk	0.0001	QV Cnc	59648.8390	15920	0.0293	B	K. Alton	0.0003
OO Aql	59757.7873	41722.5	0.0827	V	G. Samolyk	0.0001	QV Cnc	59648.8391	15920	0.0294	R	K. Alton	0.0002
OO Aql	59769.4432	41745.5	0.0825	V	L. Corp	0.0003	XZ CMi	59674.4105	29768	0.0076	V	T. Arranz	0.0001
OO Aql	59791.4902	41789	0.0842	R	L. Corp	0.0003	AK CMi	59666.5974	29272	–0.0262	V	G. Samolyk	0.0001
OO Aql	59791.4905	41789	0.0845	V	T. Arranz	0.0001	AK CMi	59677.3496	29291	–0.0261	V	T. Arranz	0.0001
V343 Aql	59727.8343	16960	–0.0496	V	G. Samolyk	0.0001	CZ CMi	59679.3872	16837	–0.0185	V	T. Arranz	0.0001
V343 Aql	59790.5514	16994	–0.0490	V	T. Arranz	0.0001	AB Cas	59771.8332	12479	0.1523	V	L. Hazel	0.0003
V346 Aql	59740.7698	16109	–0.0158	V	L. Hazel	0.0003	BH Cas	59784.7311	8719	0.0236	V	L. Hazel	0.0006
V346 Aql	59751.8336	16119	–0.0156	V	G. Samolyk	0.0001	V523 Cas	59791.6078	79469	0.1396	V	L. Hazel	0.0003
SS Ari	59789.8372	51138.5	–0.4615	V	G. Samolyk	0.0002	SU Cep	59754.8337	37086	0.0075	V	G. Samolyk	0.0001
SX Aur	59620.4507	16080	0.0256	V	T. Arranz	0.0001	WW Cep	59779.7069	22659	0.3695	V	G. Samolyk	0.0001
EP Aur	59633.3886	56385	0.0205	V	T. Arranz	0.0001	WZ Cep	59755.6508	75974.5	–0.2399	V	G. Samolyk	0.0002
KU Aur	58138.6546	4273	0.0293	V	K. Alton	0.0001	XX Cep	59749.6489	6379	0.0403	V	L. Hazel	0.0006
KU Aur	58138.6547	4273	0.0294	I	K. Alton	0.0001	DK Cep	59734.8550	26518	0.0261	V	G. Samolyk	0.0002
KU Aur	58138.6548	4273	0.0295	B	K. Alton	0.0001	DL Cep	59789.8026	15850	0.0708	V	G. Samolyk	0.0004
V641 Aur	59630.4181	16550	–0.0038	V	T. Arranz	0.0002	DV Cep	59679.8593	11116	–0.0056	V	G. Samolyk	0.0002
V641 Aur	59642.5349	16574	–0.0041	V	K. Menzies	0.0002	DV Cep	59772.8161	11196	–0.0068	V	G. Samolyk	0.0003
TU Boo	59665.8572	82025	–0.1716	V	G. Samolyk	0.0001	EG Cep	59771.7598	31540	0.0048	V	L. Hazel	0.0003
TU Boo	59707.6907	82154	–0.1711	V	L. Hazel	0.0003	EG Cep	59788.6432	31571	0.0049	V	G. Samolyk	0.0001
TU Boo	59727.6336	82215.5	–0.1718	V	G. Samolyk	0.0003	GW Cep	59749.7158	67009.5	0.0257	V	L. Hazel	0.0006
TU Boo	59729.4174	82221	–0.1716	CV	M. Castets	0.0002	RW Com	59637.8887	82645	0.0205	V	G. Samolyk	0.0002
TU Boo	59736.5516	82243	–0.1717	V	T. Arranz	0.0001	RW Com	59710.6351	82951.5	0.0204	V	K. Menzies	0.0001
TY Boo	59691.6603	79493.5	0.0546	V	G. Samolyk	0.0003	RW Com	59717.4002	82980	0.0211	V	T. Arranz	0.0001
TY Boo	59707.6752	79544	0.0536	V	G. Samolyk	0.0001	RW Com	59717.5174	82980.5	0.0196	V	T. Arranz	0.0001
TY Boo	59707.8346	79544.5	0.0544	V	G. Samolyk	0.0002	RW Com	59745.6449	83099	0.0217	V	G. Samolyk	0.0002
TY Boo	59709.5784	79550	0.0539	V	K. Menzies	0.0001	RZ Com	59665.8840	73347	0.0617	V	G. Samolyk	0.0001
TY Boo	59758.4221	79704	0.0568	CV	M. Castets	0.0003	SS Com	59686.7337	84021	1.0355	V	G. Samolyk	0.0003
TY Boo	59758.4221	79704	0.0568	V	T. Arranz	0.0001	SS Com	59727.3966	84119.5	1.0384	V	T. Arranz	0.0001
TZ Boo	59686.7249	67484.5	0.0541	V	G. Samolyk	0.0003	CC Com	59611.9113	90981.5	–0.0405	V	K. Menzies	0.0001
TZ Boo	59755.5170	67716	0.0532	V	T. Arranz	0.0001	CC Com	59658.8056	91194	–0.0420	V	G. Samolyk	0.0001
TZ Boo	59755.6656	67716.5	0.0532	V	G. Samolyk	0.0002	CC Com	59704.4868	91401	–0.0429	V	T. Arranz	0.0001
UW Boo	59681.7151	17196	–0.0048	V	G. Samolyk	0.0002	U CrB	59748.7469	12456	0.1553	V	G. Samolyk	0.0002
VW Boo	59691.6872	83308.5	–0.3261	V	G. Samolyk	0.0001	RW CrB	59703.8073	26090	0.0037	V	G. Samolyk	0.0001
VW Boo	59700.7603	83335	–0.3246	V	K. Menzies	0.0002	RW CrB	59784.4371	26201	0.0018	V	T. Arranz	0.0001
VW Boo	59727.6297	83413.5	–0.3277	V	G. Samolyk	0.0001	TW CrB	59712.6520	37044	0.0625	V	G. Samolyk	0.0001
VW Boo	59736.5300	83439.5	–0.3279	V	T. Arranz	0.0001	TW CrB	59784.4946	37166	0.0625	V	T. Arranz	0.0001
XY Boo	59716.4278	53330.5	0.0524	V	T. Arranz	0.0001	AS CrB	59763.4678	19081	0.0226	V	T. Arranz	0.0004
AC Boo	59761.4948	96429.5	0.4701	V	T. Arranz	0.0001	AW CrB	59764.3999	23169.5	–0.0188	V	T. Arranz	0.0003
AD Boo	59691.6728	17650	0.0401	V	G. Samolyk	0.0002	AW CrB	59764.5813	23170	–0.0178	V	T. Arranz	0.0003
AQ Boo	59719.4827	21670.5	–0.0165	V	T. Arranz	0.0003	BD CrB	59762.4453	23939	0.0209	V	T. Arranz	0.0003
CV Boo	59758.4463	8569	–0.0030	V	T. Arranz	0.0001	BD CrB	59775.4699	23975.5	0.0197	V	T. Arranz	0.0006
EQ Boo	59726.5124	2170	–0.0128	V	T. Arranz	0.0001	BD CrB	59780.4668	23989.5	0.0205	V	T. Arranz	0.0006
ET Boo	59755.4228	7399.5	–0.0156	V	T. Arranz	0.0001	BD CrB	59785.4624	24003.5	0.0198	V	T. Arranz	0.0005
LM Boo	59727.5016	22039.5	0.0022	V	T. Arranz	0.0001	W Crv	59709.4278	51694.5	0.0173	V	T. Arranz	0.0001
SV Cam	59710.6770	28860	0.0631	V	L. Hazel	0.0003	RV Crv	59696.7469	24981.5	–0.1154	V	G. Samolyk	0.0003
SV Cam	59713.6418	28865	0.0625	V	L. Hazel	0.0006	SX Crv	59696.6474	58995.5	–1.0608	V	G. Samolyk	0.0002
AL Cam	59611.8638	24994	–0.0229	V	K. Menzies	0.0001	V Crt	59665.7179	26022	0.0022	V	G. Samolyk	0.0002
WW Cnc	59679.4150	3347	0.0510	V	T. Arranz	0.0001	Y Cyg	59734.7861	16781	–0.0938	V	G. Samolyk	0.0005
EH Cnc	59684.3883	17185.5	–0.0121	V	T. Arranz	0.0002	SW Cyg	59743.8007	3909	–0.3978	V	G. Samolyk	0.0001
IU Cnc	59621.6906	16890	0.0355	V	K. Menzies	0.0001	WW Cyg	59753.8208	5840	0.1638	V	G. Samolyk	0.0001
QV Cnc	59643.6339	15904	0.0292	V	K. Alton	0.0002	WW Cyg	59763.7725	5843	0.1623	V	L. Hazel	0.0006
QV Cnc	59643.6339	15904	0.0292	R	K. Alton	0.0003	ZZ Cyg	59733.7844	23438	–0.0847	V	G. Samolyk	0.0001
QV Cnc	59643.6340	15904	0.0293	B	K. Alton	0.0003	ZZ Cyg	59735.6706	23441	–0.0844	V	L. Hazel	0.0006
QV Cnc	59643.7967	15904.5	0.0294	B	K. Alton	0.0004	BO Cyg	59767.7815	13279	0.0748	V	L. Hazel	0.0006
QV Cnc	59643.7967	15904.5	0.0294	V	K. Alton	0.0003	BR Cyg	59747.6228	13664	0.0009	V	L. Hazel	0.0006
QV Cnc	59643.7968	15904.5	0.0295	R	K. Alton	0.0002	BR Cyg	59787.6005	13694	0.0016	V	T. Arranz	0.0001
QV Cnc	59647.7004	15916.5	0.0293	B	K. Alton	0.0005	DO Cyg	59733.7536	8916	–0.0645	V	L. Hazel	0.0006
QV Cnc	59647.7007	15916.5	0.0296	V	K. Alton	0.0004	DO Cyg	59745.7285	8923	–0.0597	V	L. Hazel	0.0006
QV Cnc	59647.7007	15916.5	0.0296	R	K. Alton	0.0003	DO Cyg	59786.7636	8947	–0.0648	V	L. Hazel	0.0006
QV Cnc	59647.8627	15917	0.0289	R	K. Alton	0.0004	KR Cyg	59789.6736	36305	0.0281	V	G. Samolyk	0.0001
QV Cnc	59647.8630	15917	0.0292	B	K. Alton	0.0004	KV Cyg	59774.7083	10675	0.0626	V	G. Samolyk	0.0004

Table continued on following pages

Table 1. Recent times of minima of stars in the AAVSO eclipsing binary program (cont.).

Star	*JD (min) Hel. 2400000 +*	*Cycle*	*O–C (day)*	*F*	*Observer*	*Standard Error (day)*
V346 Cyg	59786.6860	8785	0.2036	V	L. Hazel	0.0006
V387 Cyg	59748.8102	49584	0.0173	V	G. Samolyk	0.0001
V387 Cyg	59791.7303	49651	0.0174	V	L. Hazel	0.0006
V401 Cyg	59758.8234	27326	0.1030	V	G. Samolyk	0.0002
V401 Cyg	59788.5409	27377	0.1017	V	T. Arranz	0.0001
V445 Cyg	59710.8316	10044	0.3371	V	L. Hazel	0.0006
V456 Cyg	59758.6694	16660	0.0543	V	G. Samolyk	0.0002
V466 Cyg	59706.8283	22228.5	0.0080	V	G. Samolyk	0.0002
V477 Cyg	59731.6924	6622.5	–0.5168	V	L. Hazel	0.0006
V477 Cyg	59745.7745	6628.5	–0.5166	V	G. Samolyk	0.0002
V477 Cyg	59789.6627	6647	–0.0477	V	G. Samolyk	0.0001
V704 Cyg	59791.7072	38290	0.0420	V	G. Samolyk	0.0003
V836 Cyg	59729.7514	22767	0.0256	V	L. Hazel	0.0006
V2197 Cyg	59782.6489	15636	–0.0009	V	L. Hazel	0.0003
V2239 Cyg	59710.7567	11809	0.0026	V	L. Hazel	0.0006
V2240 Cyg	59717.6956	20763.5	–0.0775	V	L. Hazel	0.0009
V2552 Cyg	59713.8192	29676	0.0012	V	L. Hazel	0.0006
W Del	59789.4415	3425	–0.0005	V	T. Arranz	0.0006
TT Del	59791.7191	5071	–0.1443	V	G. Samolyk	0.0004
YY Del	59754.8401	21177	0.0146	V	G. Samolyk	0.0001
YY Del	59770.7022	21197	0.0148	V	L. Hazel	0.0006
FZ Del	59747.8684	36291	–0.0291	V	G. Samolyk	0.0001
FZ Del	59784.6781	36338	–0.0304	V	L. Hazel	0.0003
LS Del	59784.4652	20020	–0.0047	V	L. Corp	0.0009
MR Del	59769.5280	13934	–0.0148	V	L. Corp	0.0002
Z Dra	59666.8028	7236	–0.0029	V	G. Samolyk	0.0001
Z Dra	59734.6748	7286	–0.0027	V	G. Samolyk	0.0001
RZ Dra	59754.6900	28277	0.0761	V	G. Samolyk	0.0001
RZ Dra	59779.4795	28322	0.0762	V	T. Arranz	0.0001
UZ Dra	59735.7393	5570	0.0019	V	L. Hazel	0.0009
UZ Dra	59753.6771	5575.5	0.0026	V	G. Samolyk	0.0001
AI Dra	59747.7986	13727	0.0436	V	G. Samolyk	0.0001
BW Dra	59743.4905	58771.5	–0.1462	V	T. Arranz	0.0001
BW Dra	59745.388	58778	–0.1480	V	T. Arranz	0.0001
MY Eri	58854.6096	19398.5	0.0058	B	K. Alton	0.0004
MY Eri	58854.6096	19398.5	0.0058	I	K. Alton	0.0006
MY Eri	58854.6098	19398.5	0.0060	V	K. Alton	0.0003
MY Eri	58855.6898	19401.5	0.0056	B	K. Alton	0.0004
MY Eri	58855.6899	19401.5	0.0057	I	K. Alton	0.0006
MY Eri	58855.6902	19401.5	0.0060	V	K. Alton	0.0003
MY Eri	58856.5896	19404	0.0052	V	K. Alton	0.0005
MY Eri	58856.5898	19404	0.0054	B	K. Alton	0.0005
MY Eri	58856.5904	19404	0.0060	I	K. Alton	0.0002
MY Eri	58857.6701	19407	0.0053	V	K. Alton	0.0005
MY Eri	58857.6706	19407	0.0058	I	K. Alton	0.0003
MY Eri	58857.6713	19407	0.0065	B	K. Alton	0.0002
MY Eri	58859.6507	19412.5	0.0053	B	K. Alton	0.0006
MY Eri	58859.6516	19412.5	0.0062	V	K. Alton	0.0002
MY Eri	58859.6516	19412.5	0.0062	I	K. Alton	0.0004
PQ Eri	59210.7609	23429	0.0223	I	K. Alton	0.0005
PQ Eri	59210.7615	23429	0.0229	B	K. Alton	0.0003
PQ Eri	59210.7620	23429	0.0234	V	K. Alton	0.0002
PQ Eri	59241.6274	23527.5	0.0224	I	K. Alton	0.0009
PQ Eri	59241.6282	23527.5	0.0232	V	K. Alton	0.0009
PQ Eri	59241.6292	23527.5	0.0242	B	K. Alton	0.0009
RW Gem	59654.6474	14431	0.0023	V	G. Samolyk	0.0002
SX Gem	59516.7480	29619	–0.0519	V	L. Hazel	0.0006
SX Gem	59638.3960	29708	–0.0559	V	T. Arranz	0.0001
TX Gem	59639.3678	14211	–0.0432	V	T. Arranz	0.0001
WW Gem	59666.3721	27211	0.0400	V	T. Arranz	0.0002
AF Gem	59616.4370	26099	–0.0698	CV	M. Castets	0.0001
AF Gem	59631.3592	26111	–0.0697	V	T. Arranz	0.0001
AL Gem	59630.4197	23938	0.1120	V	T. Arranz	0.0001
AZ Gem	59647.4227	33440	0.0992	CV	M. Castets	0.0001
CX Gem	59628.4053	14533	–0.0451	V	T. Arranz	0.0002
V428 Gem	59616.6845	5207.5	–0.0008	V	K. Menzies	0.0001
SZ Her	59712.7175	21817	–0.0378	V	G. Samolyk	0.0001
SZ Her	59717.6263	21823	–0.0376	V	L. Hazel	0.0003
SZ Her	59772.4384	21890	–0.0381	V	T. Arranz	0.0001
TT Her	59727.7921	21634	0.0436	V	G. Samolyk	0.0002
TT Her	59783.4279	21695	0.0428	V	T. Arranz	0.0001
TU Her	59730.6889	6912	–0.2805	V	L. Hazel	0.0003
TU Her	59730.6900	6912	–0.2795	V	G. Samolyk	0.0002
TU Her	59771.4963	6930	–0.2792	V	T. Arranz	0.0001
UX Her	59734.7878	12953	0.1824	V	G. Samolyk	0.0001
UX Her	59745.6304	12960	0.1831	V	L. Hazel	0.0006
UX Her	59762.6680	12971	0.1834	V	G. Samolyk	0.0001
UX Her	59773.5105	12978	0.1839	V	T. Arranz	0.0001
AK Her	59727.4896	41613.5	0.0235	V	L. Corp	0.0003
BC Her	59446.6631	2250	0.0526	V	L. Hazel	0.0006
BC Her	59733.7962	2343	0.0707	V	L. Hazel	0.0003
CC Her	59727.7035	11568	0.3824	V	G. Samolyk	0.0001
CC Her	59774.5234	11595	0.3841	V	T. Arranz	0.0001
CT Her	59734.6649	9635	0.0117	V	G. Samolyk	0.0001
CT Her	59786.4692	9664	0.0111	V	T. Arranz	0.0001
IT Her	59763.4684	21401	–0.0189	V	L. Corp	0.0002
LT Her	59730.7320	17504	–0.1651	V	G. Samolyk	0.0003
LT Her	59755.6637	17527	–0.1664	V	G. Samolyk	0.0004
V728 Her	59733.6566	15348	0.0329	V	G. Samolyk	0.0004
V728 Her	59768.5332	15422	0.0338	V	T. Arranz	0.0001
V1044 Her	57944.5926	24431	0.0040	V	K. Alton	0.0004
V1044 Her	57944.5929	24431	0.0043	I	K. Alton	0.0009
V1044 Her	57944.5943	24431	0.0057	B	K. Alton	0.0009
V1044 Her	57950.7287	24456.5	0.0038	B	K. Alton	0.0003
V1044 Her	57950.7287	24456.5	0.0038	V	K. Alton	0.0004
V1044 Her	57950.7290	24456.5	0.0041	I	K. Alton	0.0003
V1044 Her	57953.7371	24469	0.0042	I	K. Alton	0.0003
V1044 Her	57953.7379	24469	0.0050	V	K. Alton	0.0002
V1057 Her	59772.4723	8984	–0.0123	V	T. Arranz	0.0003
AV Hya	59677.3890	33661	–0.1231	V	T. Arranz	0.0001
DF Hya	59637.5933	50966.5	0.0258	V	G. Samolyk	0.0003
DF Hya	59637.7593	50967	0.0265	V	G. Samolyk	0.0001
DF Hya	59671.6468	51069.5	0.0270	V	G. Samolyk	0.0002
SW Lac	59789.8052	45256	–0.0876	V	G. Samolyk	0.0002
TW Lac	59740.7466	6005	0.5229	V	L. Hazel	0.0006
CO Lac	59747.7172	20888	0.0141	V	L. Hazel	0.0006
RT Leo	59683.3588	4812	–0.0019	V	T. Arranz	0.0002
UU Leo	59658.7018	8490	0.2456	V	G. Samolyk	0.0003
UU Leo	59707.4152	8519	0.2465	V	T. Arranz	0.0001
UV Leo	59611.7671	35280	0.0497	V	K. Menzies	0.0003
UV Leo	59665.4747	35369.5	0.0497	V	L. Corp	0.0001
UV Leo	59675.3761	35386	0.0497	CV	M. Castets	0.0001
UV Leo	59705.3814	35436	0.0508	V	T. Arranz	0.0001
VZ Leo	59690.3887	26173	–0.0370	V	T. Arranz	0.0001
WZ Leo	59710.4396	5120	–0.0001	V	T. Arranz	0.0002
XY Leo	59639.4800	51267	0.1936	V	L. Corp	0.0002
XZ Leo	59639.4550	29963	0.0902	V	L. Corp	0.0003
AM Leo	59639.4238	46873	0.0133	V	L. Corp	0.0002
AP Leo	59637.5093	46707.5	0.0397	V	L. Corp	0.0005
AP Leo	59707.4439	46870	0.0412	V	T. Arranz	0.0001
CE Leo	59665.4118	39501	–0.0108	CV	M. Castets	0.0006
CE Leo	59705.4621	39633	–0.0132	V	T. Arranz	0.0001
GU Leo	58198.6301	16418	0.0005	V	K. Alton	0.0001
GU Leo	58198.6306	16418	0.0010	B	K. Alton	0.0004
GU Leo	58198.6313	16418	0.0017	I	K. Alton	0.0005
GU Leo	58211.7323	16455	0.0015	V	K. Alton	0.0002
GU Leo	58211.7324	16455	0.0016	B	K. Alton	0.0004
GU Leo	58211.7326	16455	0.0018	I	K. Alton	0.0003
GU Leo	58213.6798	16460.5	0.0016	B	K. Alton	0.0005
GU Leo	58213.6798	16460.5	0.0016	I	K. Alton	0.0002
GU Leo	58213.6801	16460.5	0.0019	V	K. Alton	0.0001
GU Leo	58217.7519	16472	0.0017	I	K. Alton	0.0006

Table continued on following pages

Table 1. Recent times of minima of stars in the AAVSO eclipsing binary program (cont.).

Star	JD (min) Hel. 2400000 +	Cycle	O–C (day)	F	Observer	Standard Error (day)
GU Leo	58217.7525	16472	0.0023	V	K. Alton	0.0003
GU Leo	58217.7528	16472	0.0026	B	K. Alton	0.0004
GU Leo	58219.7011	16477.5	0.0034	I	K. Alton	0.0004
GU Leo	58219.7020	16477.5	0.0043	V	K. Alton	0.0003
GU Leo	58219.7021	16477.5	0.0044	B	K. Alton	0.0006
GU Leo	59710.4027	20687.5	0.0072	V	T. Arranz	0.0001
GV Leo	59695.3877	26022.5	–0.0857	V	T. Arranz	0.0001
HI Leo	59699.4391	22333	0.0420	V	T. Arranz	0.0001
T LMi	59699.4077	4736	–0.1357	V	T. Arranz	0.0001
VW LMi	59706.4396	23466	0.0468	V	T. Arranz	0.0001
XY LMi	59698.4931	16476.5	–0.0105	V	T. Arranz	0.0003
AG LMi	59621.8519	11913	–0.0019	V	K. Menzies	0.0001
Z Lep	59639.3523	32419	–0.2053	V	T. Arranz	0.0001
SS Lib	59747.7317	12929	0.1917	V	G. Samolyk	0.0002
SS Lib	59766.4260	12942	0.1920	V	T. Arranz	0.0001
RY Lyn	59672.4693	11697	–0.0283	V	T. Arranz	0.0001
SW Lyn	59687.4043	24395	0.0877	V	T. Arranz	0.0001
UU Lyn	59672.4919	32016.5	–0.0109	V	T. Arranz	0.0003
UV Lyn	59666.3812	46736.5	0.1241	V	T. Arranz	0.0002
DZ Lyn	59687.4466	18425	–0.0084	V	T. Arranz	0.0001
EL Lyn	59637.6561	12452	–0.0166	V	K. Menzies	0.0004
FI Lyn	59677.4493	21697	–0.0066	V	T. Arranz	0.0001
KS Lyn	59629.7984	13340	–0.0074	V	K. Menzies	0.0004
RV Lyr	59738.7776	3949	–0.3022	V	L. Hazel	0.0006
RV Lyr	59792.7342	3964	–0.3314	V	L. Hazel	0.0009
RV Lyr	59803.5655	3967	–0.2972	V	L. Corp	0.0001
UZ Lyr	59763.8101	8499	–0.0581	V	G. Samolyk	0.0002
BV Lyr	59738.6769	14679	0.0432	V	L. Hazel	0.0006
EW Lyr	59762.7677	17069	0.3178	V	G. Samolyk	0.0001
EW Lyr	59776.4089	17076	0.3180	V	T. Arranz	0.0001
FL Lyr	59787.4566	9901	–0.0026	V	T. Arranz	0.0001
FL Lyr	59791.8131	9903	–0.0024	V	K. Menzies	0.0001
V404 Lyr	59717.8199	9874	0.0017	V	L. Hazel	0.0009
V592 Lyr	59713.7425	20281	0.0132	V	L. Hazel	0.0006
V658 Lyr	59729.6769	13055	–0.0854	V	L. Hazel	0.0006
V740 Lyr	59776.5551	21060.5	0.0258	V	T. Arranz	0.0001
V740 Lyr	59787.4031	21093.5	0.0262	V	T. Arranz	0.0002
V740 Lyr	59787.5663	21094	0.0250	V	T. Arranz	0.0001
V740 Lyr	59792.4983	21109	0.0262	V	T. Arranz	0.0001
RW Mon	59639.4493	13619	–0.0946	V	T. Arranz	0.0001
BO Mon	59671.5920	7264	0.0020	V	G. Samolyk	0.0001
V958 Mon	59633.3807	27178.5	0.0526	V	T. Arranz	0.0001
V970 Mon	59269.6160	11498.5	–0.0096	I	K. Alton	0.0002
V970 Mon	59269.6178	11498.5	–0.0078	V	K. Alton	0.0008
V970 Mon	59269.6188	11498.5	–0.0068	B	K. Alton	0.0009
V970 Mon	59272.6231	11506.5	–0.0075	V	K. Alton	0.0011
V970 Mon	59272.6232	11506.5	–0.0074	I	K. Alton	0.0007
V970 Mon	59272.6236	11506.5	–0.0070	B	K. Alton	0.0013
V970 Mon	59537.9992	12213	–0.0097	B	K. Alton	0.0007
V970 Mon	59537.9993	12213	–0.0096	I	K. Alton	0.0006
V970 Mon	59547.9542	12239.5	–0.0087	I	K. Alton	0.0009
V970 Mon	59547.9559	12239.5	–0.0070	B	K. Alton	0.0011
V970 Mon	59549.8314	12244.5	–0.0097	V	K. Alton	0.0009
V970 Mon	59549.8319	12244.5	–0.0092	B	K. Alton	0.0002
U Oph	59755.7192	9145	0.0021	V	G. Samolyk	0.0005
SX Oph	59770.6432	12781	0.0003	V	G. Samolyk	0.0004
V501 Oph	59772.7625	29817	–0.0096	V	G. Samolyk	0.0001
V501 Oph	59781.4741	29826	–0.0095	V	T. Arranz	0.0001
V508 Oph	59734.8039	42496	–0.0254	V	G. Samolyk	0.0001
V508 Oph	59763.4213	42579	–0.0258	V	T. Arranz	0.0005
V508 Oph	59763.5929	42579.5	–0.0266	V	T. Arranz	0.0001
V508 Oph	59782.3845	42634	–0.0261	V	T. Arranz	0.0001
V508 Oph	59784.4531	42640	–0.0263	V	L. Corp	0.0002
V566 Oph	59785.3941	43816.5	0.2920	V	T. Arranz	0.0001
V566 Oph	59785.5984	43817	0.2915	V	T. Arranz	0.0002
V839 Oph	59712.8556	47101	0.3541	V	G. Samolyk	0.0001
V839 Oph	59777.4780	47259	0.3553	V	T. Arranz	0.0001
V1010 Oph	59727.8147	31432.5	–0.2311	V	G. Samolyk	0.0003
V1010 Oph	59728.8050	31434	–0.2330	V	G. Samolyk	0.0002
V2610 Oph	59741.4986	17283.5	–0.0716	V	L. Corp	0.0007
V2612 Oph	59741.4468	19294.5	–0.0095	V	L. Corp	0.0004
EF Ori	59628.3996	4494	0.0110	V	T. Arranz	0.0001
ER Ori	59620.3865	42498.5	0.1618	V	T. Arranz	0.0001
ET Ori	59612.3251	34627	–0.0049	V	T. Arranz	0.0001
FL Ori	59613.3372	9198	0.0419	V	T. Arranz	0.0001
FT Ori	59630.5667	5803	0.0255	V	G. Samolyk	0.0001
FZ Ori	59616.3142	38981	–0.0218	V	T. Arranz	0.0002
FZ Ori	59616.5160	38981.5	–0.0199	V	T. Arranz	0.0002
GU Ori	59604.3852	35129	–0.0706	CV	M. Castets	0.0004
GU Ori	59628.3864	35180	–0.0742	V	T. Arranz	0.0001
V648 Ori	59625.4171	20675.5	0.0679	V	T. Arranz	0.0002
V1851 Ori	59582.6904	24994.5	–0.0014	V	K. Alton	0.0002
V1851 Ori	59582.6907	24994.5	–0.0011	B	K. Alton	0.0005
V1851 Ori	59582.6907	24994.5	–0.0011	I	K. Alton	0.0004
V1851 Ori	59582.8284	24995	–0.0019	V	K. Alton	0.0002
V1851 Ori	59582.8287	24995	–0.0016	I	K. Alton	0.0002
V1851 Ori	59582.8288	24995	–0.0015	B	K. Alton	0.0001
U Peg	59770.7985	62061	–0.1806	V	G. Samolyk	0.0001
BB Peg	59769.7999	44275	–0.0390	V	L. Hazel	0.0003
BB Peg	59774.8615	44289	–0.0384	V	G. Samolyk	0.0002
BB Peg	59787.6947	44324.5	–0.0385	V	L. Hazel	0.0006
BN Peg	59792.6483	36305	–0.0016	V	L. Hazel	0.0003
WY Per	59613.4112	4091	–0.3665	V	T. Arranz	0.0001
AY Per	59620.3171	2757	–0.1293	V	T. Arranz	0.0004
V723 Per	59618.3864	10253.5	0.3314	V	T. Arranz	0.0001
HO Psc	58755.9620	4420	–0.0030	I	K. Alton	0.0005
HO Psc	58755.9627	4420	–0.0023	V	K. Alton	0.0003
HO Psc	58755.9633	4420	–0.0017	B	K. Alton	0.0005
HO Psc	58759.8610	4432	–0.0010	I	K. Alton	0.0001
HO Psc	58759.8611	4432	–0.0009	V	K. Alton	0.0005
HO Psc	58759.8613	4432	–0.0007	B	K. Alton	0.0005
UZ Pup	59658.6286	18928	–0.0132	V	G. Samolyk	0.0001
AV Pup	53799.5681	40661	0.1411	V	G. Samolyk	0.0002
AV Pup	54215.6542	41409	0.0857	V	J. Bialozynski	0.0002
AV Pup	59676.3862	51224	0.3514	V	T. Arranz	0.0001
U Sge	59790.4818	12619	0.0351	V	T. Arranz	0.0001
V1968 Sgr	59789.6494	39004	–0.0187	V	G. Samolyk	0.0004
DK Sct	59789.5049	5986	0.0177	V	T. Arranz	0.0005
AO Ser	58306.7112	27490	–0.0142	V	K. Alton	0.0001
AO Ser	58306.7112	27490	–0.0142	I	K. Alton	0.0001
AO Ser	58306.7114	27490	–0.0140	B	K. Alton	0.0001
AO Ser	58307.5904	27491	–0.0143	I	K. Alton	0.0009
AO Ser	58307.5906	27491	–0.0141	V	K. Alton	0.0009
AO Ser	58307.5911	27491	–0.0136	B	K. Alton	0.0006
AO Ser	59757.6410	29140	–0.0077	V	G. Samolyk	0.0001
AO Ser	59766.4341	29150	–0.0081	V	T. Arranz	0.0001
CC Ser	59681.8836	43021	1.2109	V	G. Samolyk	0.0003
CC Ser	59754.6447	43162	1.2151	V	G. Samolyk	0.0002
RW Tau	59619.4396	5033	–0.3140	V	T. Arranz	0.0001
RZ Tau	59616.3981	52781	0.1048	V	T. Arranz	0.0001
RZ Tau	59631.3625	52817	0.1049	V	T. Arranz	0.0001
AC Tau	59617.4512	6842	0.2194	V	T. Arranz	0.0001
AH Tau	59603.3958	85792	–0.0002	CV	M. Castets	0.0001
AH Tau	59617.3679	85834	–0.0005	V	T. Arranz	0.0001
V781 Tau	59619.3581	45648	–0.0476	V	L. Corp	0.0002
RV Tri	59617.3410	18024	–0.0516	V	T. Arranz	0.0001
W UMa	59679.6248	41704	–0.1316	V	G. Samolyk	0.0003
TY UMa	59654.6379	56754.5	0.4804	V	G. Samolyk	0.0003
TY UMa	59706.4035	56900.5	0.4834	V	T. Arranz	0.0001
UX UMa	59703.6780	113239	–0.0015	V	G. Samolyk	0.0001
UX UMa	59703.8743	113240	–0.0018	V	G. Samolyk	0.0002
UX UMa	59732.3915	113385	–0.0020	V	T. Arranz	0.0001

Table continued on next page

Table 1. Recent times of minima of stars in the AAVSO eclipsing binary program (cont.).

Star	*JD (min) Hel. 2400000 +*	*Cycle*	*O–C (day)*	*F*	*Observer*	*Standard Error (day)*	*Star*	*JD (min) Hel. 2400000 +*	*Cycle*	*O–C (day)*	*F*	*Observer*	*Standard Error (day)*
UX UMa	59740.6524	113427	–0.0013	V	K. Menzies	0.0004	BH Vir	59722.4139	20189	–0.0160	V	T. Arranz	0.0001
UX UMa	59753.6324	113493	–0.0016	V	G. Samolyk	0.0001	BH Vir	59734.6673	20204	–0.0157	V	G. Samolyk	0.0001
VV UMa	59666.6313	20151	–0.0996	V	G. Samolyk	0.0001	CG Vir	59708.3861	7707	0.0098	CV	M. Castets	0.0004
VV UMa	59704.4365	20206	–0.1003	V	T. Arranz	0.0001	IR Vir	59737.4333	26833.5	–0.0189	V	T. Arranz	0.0001
XZ UMa	59683.4531	11057	–0.1651	V	T. Arranz	0.0001	V715 Vir	59327.8619	19372.5	–0.0016	B	K. Alton	0.0006
BS UMa	59736.4339	16558	–0.0247	V	T. Arranz	0.0004	V715 Vir	59327.8645	19372.5	0.0010	I	K. Alton	0.0013
EQ UMa	59676.3951	30628.5	–0.0285	V	T. Arranz	0.0004	V715 Vir	59327.8649	19372.5	0.0014	V	K. Alton	0.0013
HX UMa	59737.4158	19088	–0.0396	V	T. Arranz	0.0003	V715 Vir	59339.7316	19409.5	–0.0025	V	K. Alton	0.0007
KM UMa	59715.4260	20506	–0.0247	V	T. Arranz	0.0001	V715 Vir	59339.7329	19409.5	–0.0012	I	K. Alton	0.0007
QT UMa	59685.3843	17150	0.0140	V	T. Arranz	0.0002	V715 Vir	59339.7333	19409.5	–0.0008	B	K. Alton	0.0002
W UMi	59658.7676	15270	–0.2320	V	G. Samolyk	0.0005	V715 Vir	59341.8180	19416	–0.0015	B	K. Alton	0.0003
RU UMi	59686.8519	34463	–0.0155	V	G. Samolyk	0.0003	V715 Vir	59341.8180	19416	–0.0015	V	K. Alton	0.0006
VY UMi	59629.7879	25675.5	0.0672	V	K. Menzies	0.0002	V715 Vir	59341.8199	19416	0.0004	I	K. Alton	0.0003
VV Vir	59636.8927	63693	–0.0509	V	G. Samolyk	0.0002	V715 Vir	59343.7436	19422	–0.0008	V	K. Alton	0.0005
VV Vir	59708.7199	63854	–0.0516	V	L. Hazel	0.0003	V715 Vir	59343.7437	19422	–0.0007	I	K. Alton	0.0002
VV Vir	59727.4573	63896	–0.0519	V	T. Arranz	0.0001	V715 Vir	59343.7438	19422	–0.0006	B	K. Alton	0.0004
AG Vir	59704.3759	22208	–0.0266	CV	M. Castets	0.0007	AW Vul	59758.8063	16707	–0.0424	V	G. Samolyk	0.0001
AH Vir	59650.8523	33952	0.3143	V	G. Samolyk	0.0001	AW Vul	59767.6769	16718	–0.0428	V	L. Hazel	0.0003
AH Vir	59747.6420	34189.5	0.3178	V	G. Samolyk	0.0003	AX Vul	59723.7587	7344	–0.0460	V	L. Hazel	0.0006
AK Vir	59748.6568	14387	–0.0471	V	G. Samolyk	0.0001	AX Vul	59788.5562	7376	–0.0433	V	T. Arranz	0.0001
AW Vir	59666.8247	41368	0.0339	V	G. Samolyk	0.0001	AY Vul	59779.7636	7086	–0.2114	V	G. Samolyk	0.0002
AW Vir	59745.4116	41590	0.0334	V	T. Arranz	0.0001	BE Vul	59772.7744	12668	0.1000	V	G. Samolyk	0.0001
AX Vir	59654.8473	45670	0.0317	V	G. Samolyk	0.0001	BO Vul	59775.7363	12224	0.0026	V	L. Hazel	0.0003
AX Vir	59738.4486	45789	0.0324	V	T. Arranz	0.0002	BS Vul	59779.6571	34683	–0.0394	V	G. Samolyk	0.0001
AZ Vir	59703.7604	44978	–0.0169	V	G. Samolyk	0.0001	BU Vul	59747.7705	46071	0.0110	V	L. Hazel	0.0006
AZ Vir	59733.6572	45063.5	–0.0165	V	G. Samolyk	0.0001	CD Vul	59734.7747	19651	–0.0033	V	L. Hazel	0.0003
BH Vir	59707.7109	20171	–0.0153	V	G. Samolyk	0.0001	FR Vul	59745.6760	26293	–0.0118	V	L. Hazel	0.0006

The Photometric Period of PGIR22akgylf (Nova Cygni 2022)

Richard E. Schmidt
1810 35th Street NW, Washington, DC 20007; schmidt.rich@gmail.com

Received October 13, 2022; revised November 29, 2022; accepted November 30, 2022

Abstract A photometric study of the galactic nova PGIR22akgylf (Nova Cygni 2022) was undertaken at the Burleith Observatory in Washington, DC. A total of 1,075 CCD observations were obtained over a time span of 32.1 days, yielding an observed period 4.140 h ± 0.003 h, of amplitude 0.008 magnitude I_C. The epoch (HJD) of minimum light was 2459838.54041 (2022 September 16.0404 UT). A suspected ZTF variable in the field of the nova, GSC 02678-01797, was found to be multi-periodic.

1. Introduction

This is the seventh in a series of reports on the discovery of photometric periods of recent classical novae (Schmidt 2021). These *JAAVSO* reports serve a dual purpose: adding to the relatively few known orbital periods of novae, and hopefully inspiring urban astronomers to participate in nova research. The reddened color of galactic novae and their typically long period of outbursts lend them well to CCD observation—even in heavily light-polluted cities—when observing in the near infrared, as with the Cousins I_C filter and a monochromatic camera with sensitivity in the 700–900 nm region.

The year 2022 has brought the fewest number of galactic novae discoveries in eight years, as seen in Figure 1 (Mukai 2022). Thus, the discovery of PGIR22akgylf (Nova Cygni 2022, AT 2022sfe, ZTF22abazrjk), R.A. = $20^h\,00^m\,29.25^s$, Dec. = +34° 44' 49.8" (J2000), by the Palomar Gattini-IR survey on 2022 August 16 (De *et al.* 2022) was welcome news. Its spectroscopic identification as a slow nova, highly reddened by extinction at galactic latitude 2.5°, was made by its discoverers on 2022 August 29. The nova's position, about 53 arc-minutes southeast of η Cygni, was ideal for observing at low airmass from my Washington, DC, site in early evening.

As of 2022 October 12, nearly 60 days post-discovery, PGIR22akgylf had yet to begin its final decline in brightness. The 20 arc-minute field of PGIR22akgylf (I_C image) is shown in Figure 2.

2. Observations

At Burleith Observatory a total of 1,075 CCD observations of PGIR22akgylf were obtained between 2022 September 10.1 and October 12.0 UT with a 0.32-m PlaneWave CDK astrograph and SBIG STL-1001E CCD camera with an Astrodon I_C filter. Pixel size was 1.95 arc-seconds, yielding on average 2-pixel FWHM, and the field of view was 33 arc-minutes square. The observatory computer was synchronized to USNO NTP before each observing session. Images were de-darked and flat-fielded in real time. Exposure times ranged from 30 to 90 seconds.

3. Reductions

Cousins I-band differential ensemble photometry was performed using the comparison stars in Table 1, which are labeled in Figure 2. Synthetic aperture photometry was performed using C-Munipack 2.1.29 (Motl 2021). Heliocentric corrections were applied to dates of observation. Data from poor nights and large outliers were filtered out, leaving 1,075 images for analysis.

Table 2 and Figure 3 provide nightly mean times of observation in HJD and UT, observed nightly mean magnitudes I_C, standard error of the mean magnitudes, duration of nightly observing sessions, and mean air mass. Figure 4 shows a histogram of the distribution of air masses. A sample night's observation from 2022 September 28 is shown in Figure 5.

Table 1. Photometry comparison stars from AAVSO chart sequence X28196I.

No.	*AUID*	*R.A. (J2000) h m s*	*Dec. (J2000) ° ′ ″*	*Mag. I_C*	*Mag. Err.*	*(B–V)*
114	000-BPL-180	20 00 42.09	+34 46 44.0	10.548	0.085	0.719
116	000-BPL-181	20 01 01.38	+34 44 23.8	10.895	0.021	0.609
120	000-BPL-182	20 00 36.19	+34 53 37.0	11.196	0.024	0.604
124	000-BPL-183	20 00 30.69	+34 56 02.7	11.503	0.032	0.759
128	000-BPL-184	20 00 35.55	+34 56 57.9	12.056	0.037	0.638
132*	000-BPL-132	20 00 23.89	+34 56 48.3	12.376	0.049	0.646

** Check star.*

Table 2. Nightly mean magnitudes I_C.

HJD	*UT*	*Mag. I_C*	*Stderr of Mean*	*Duration (hours)*	*Mean Airmass*
2459832.590511	Sep. 10.090	12.593	0.001	3.18	1.023
2459837.589513	Sep. 15.089	12.269	0.001	4.20	1.047
2459838.579091	Sep. 16.079	12.228	0.001	3.73	1.033
2459839.565689	Sep. 17.066	12.182	0.001	3.06	1.021
2459841.524425	Sep. 19.024	12.153	0.001	1.05	1.018
2459842.573287	Sep. 20.073	12.109	0.001	3.17	1.027
2459843.594962	Sep. 21.095	12.084	0.001	2.39	1.043
2459844.568964	Sep. 22.069	12.080	0.001	2.30	1.019
2459845.565741	Sep. 23.066	12.042	0.001	1.69	1.013
2459846.572885	Sep. 24.073	12.005	0.001	2.14	1.024
2459847.545851	Sep. 25.046	11.790	0.001	1.80	1.009
2459850.576200	Sep. 28.076	11.729	0.001	1.70	1.035
2459862.567876	Oct. 10.068	11.567	0.001	3.20	1.095
2459863.563666	Oct. 11.064	11.593	0.001	1.87	1.074
2459864.549373	Oct. 12.049	11.591	0.001	2.90	1.065

Table 3. Observation summary PGIR22akgylf (Nova Cygni 2022).

Period (d)	0.1725 (0.0001)
Period (h)	4.140 (0.003)
Amplitude (mean curve) (mag. I_C)	0.008
Number of observations used	1075
Time span (d)	32.1
Epoch of minimum	2459838.54041 (Sep. 16.0404, 2022)

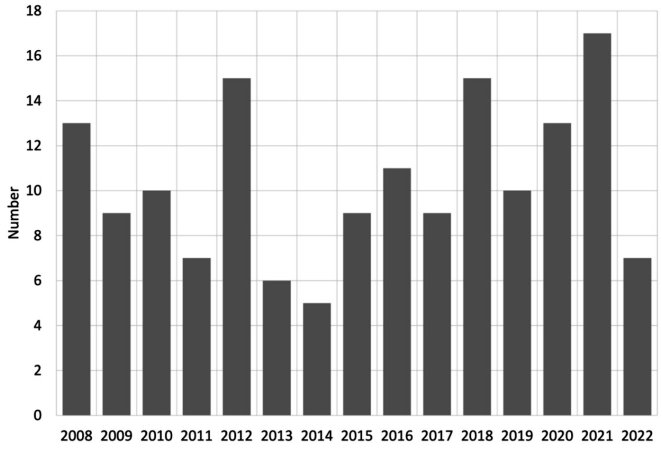

Figure 1. Annual numbers of galactic nova discoveries (Mukai 2022).

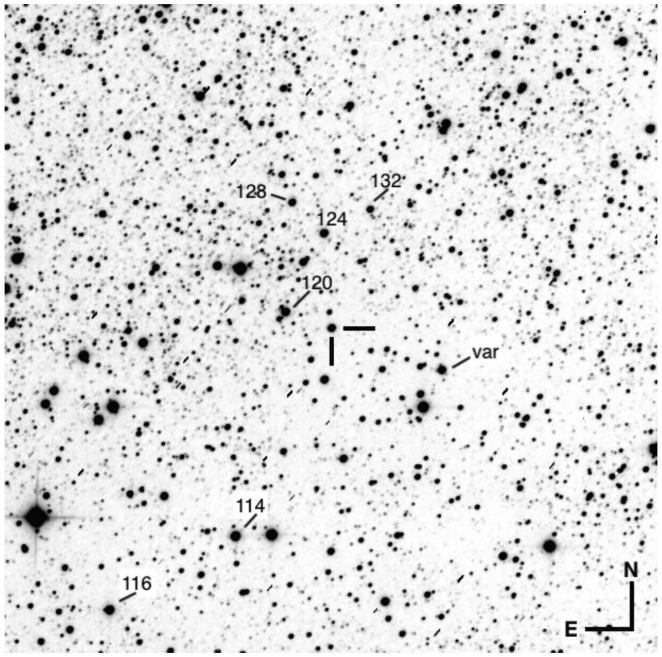

Figure 2. 20 arc-min field of PGIR22akgylf (center) and variable ("var") in I_C.

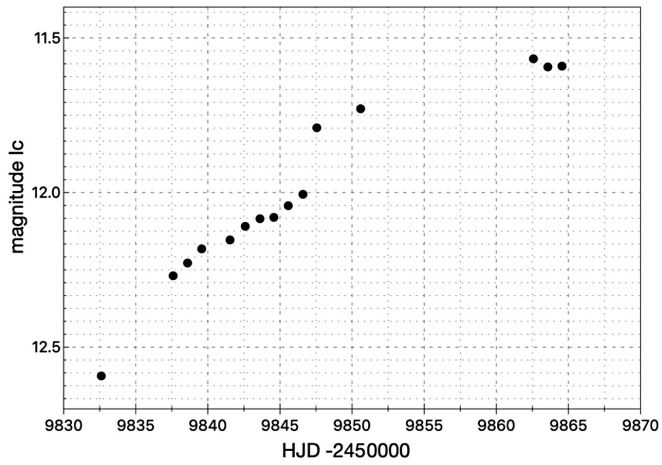

Figure 3. PGIR22akgylf nightly mean I_C magnitudes.

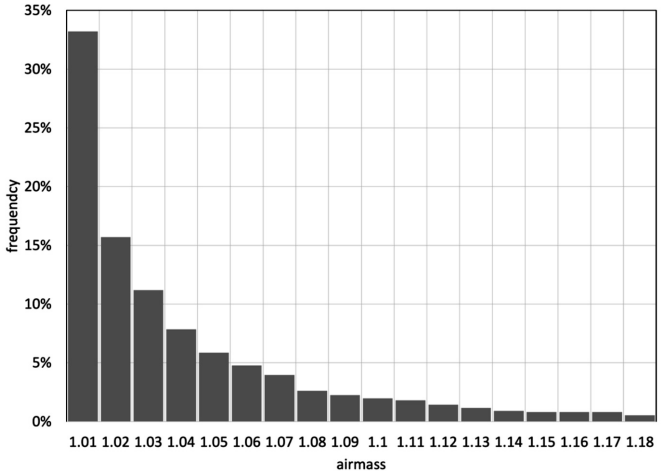

Figure 4. Histogram of airmass values.

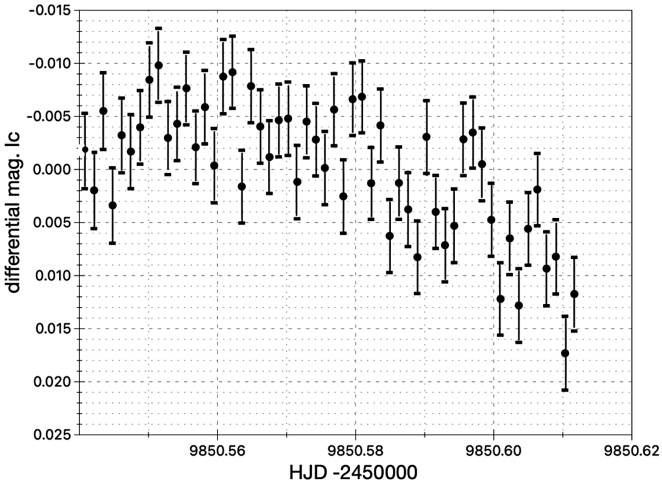

Figure 5. Example observations, 2022 September 28.

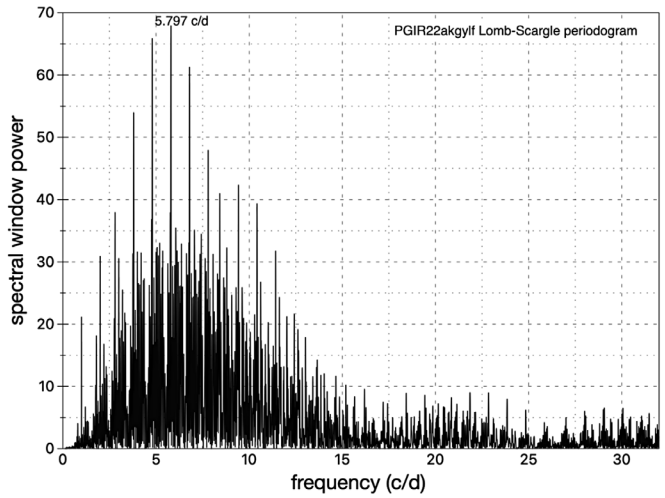

Figure 6. Wide Lomb-Scargle periodogram.

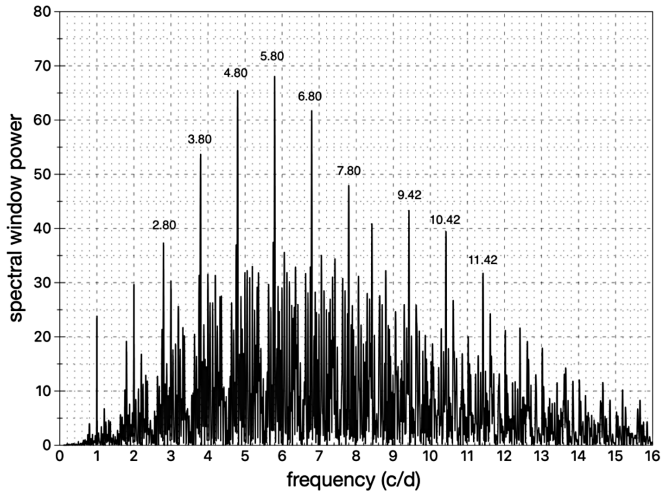

Figure 7. Detail, periodogram of PGIR22akgylf.

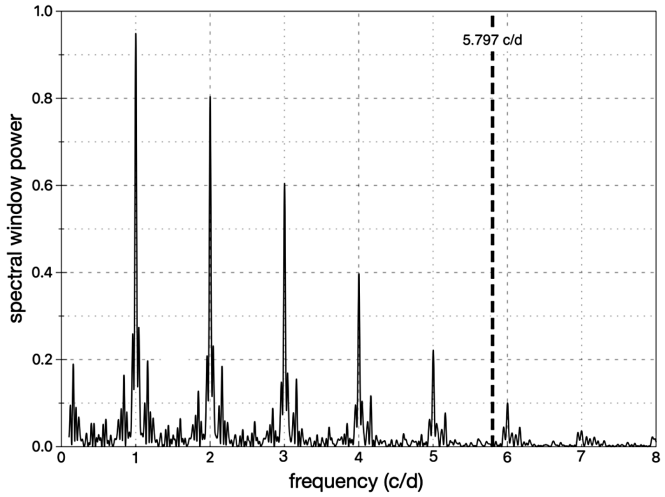

Figure 8. Spectral window of observations.

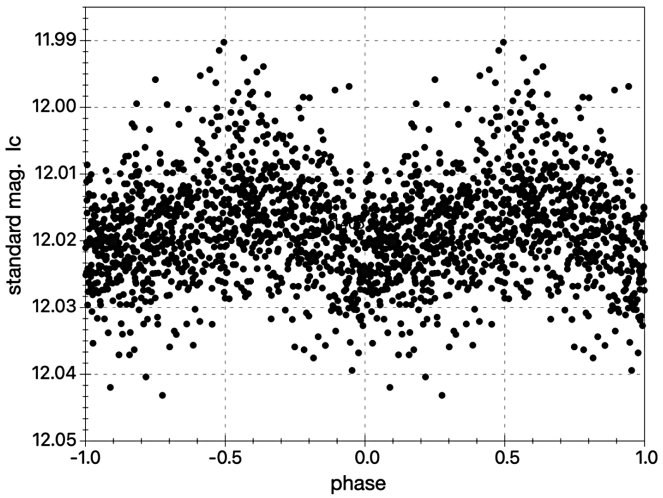

Figure 9. PGIR22akgylf, double-phase plot.

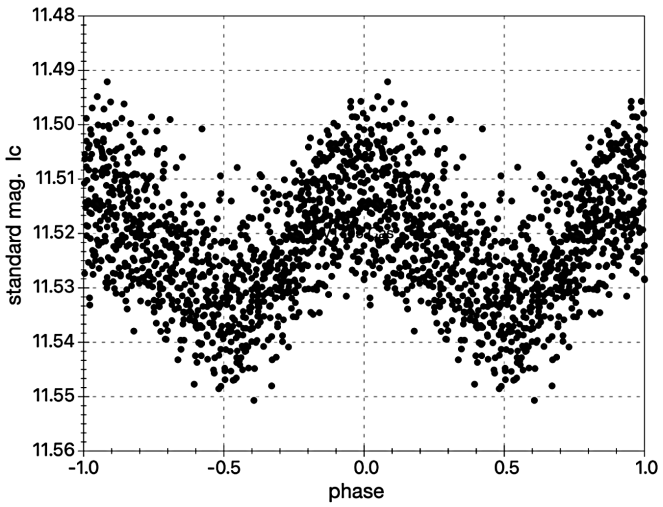

Figure 10. Phase plot of GSC 02678-01797, primary period = 1.4576 h.

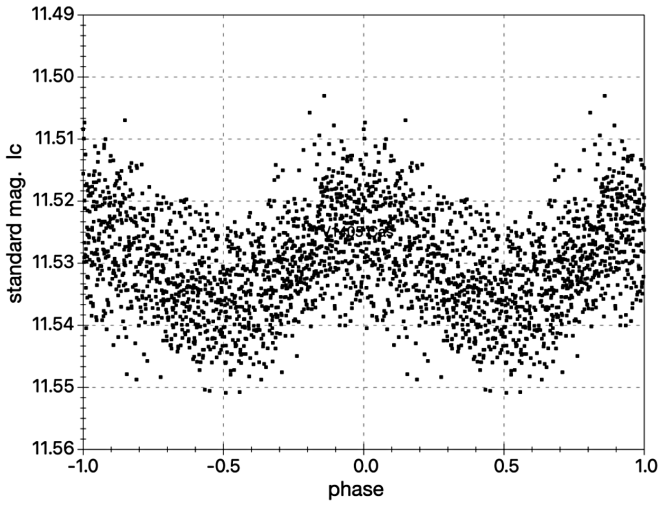

Figure 11. Phase plot of GSC 02678-01797, pre-whitened period = 1.859 h.

4. Analysis

Prior to Fourier analysis, each nightly observation set was pre-processed by subtracting the nightly average brightness. Period analysis was performed using Peranso 3.0.3 software (Paunzen and Vanmunster 2016), computing a Lomb-Scargle spectra of the observations. Because of the low signal-to-noise ratio of the nova light curve, solutions of 52,000 steps were computed.

Figure 6 shows a Lomb-Scargle periodogram over the frequency range 0–32 cycles / day, which peaks at 5.7973 cycles / day (4.139834 hours). This wide view shows the absence of strong signals at high frequencies. Figure 7 shows detail in the range 0–16 cycles/day. Note the labelled period aliases which appear at 0.5-day and 1-day intervals due to the diurnal nature of night observing. The observations were also analyzed using Peranso's phase binned Analysis of Variance (AoV) method (Schwarzenberg-Czerny 1989), which is ideal for period finding in non-sinusoidal signals. This method returned the same period, 4.140 h (± 0.003).

Figure 8 shows the spectral window for these observations, which displays artifacts caused by the cadence of observations. The absence of a peak at the observed frequency 5.80 cycles / day shows that this frequency is not an artifact of the observing window.

A folded double-phase plot of the most prominent period is shown in Figure 9.

Table 3 summarizes observed data for PGIR22akgylf with errors in parentheses. The period error estimate was computed by Peranso as the 1-sigma confidence level on the period P which equals the line width of its Mean Noise Power Level, using the method in section 4.4 of (Schwarzenberg-Czerny 1991). The two False Alarm Probabilities (FAPs) computed by Peranso were below 0.01 (1%), indicating strong confidence in the computed period. The epoch of extremum is found from a 7-degree polynomial fit to the observations using the Peranso software.

5. "Discovery" of a dual-period δ Scuti variable

Tens of thousands of stars appear in each 33 × 33 arc-minute field taken with this telescope and CCD. Photometry reduction programs such as C-Muniwin can generate plots of magnitude vs. standard deviation for each field object. Each object with heightened magnitude standard deviation is checked for possible periodicity. Examination of the field of PGIR22akgylf resulted in the "independent discovery" of a variable star, which was subsequently found by Sebastián Otero in Table 3, "unclassified suspected variables" of the "Zwicky Transient Facility Catalog of Periodic Variable Stars" (Chen *et al.* 2020). The variable ZTFJ200012.67+345156.7 (GSC 02678-01797) has ZTF period 1.45752 h and amplitude in g-band 0.045, from 145 ZTF observations. This variable has been assigned AAVSO AUID 000-BPL-178. Its position is R.A. = $20^h\,00^m\,12.68^s$, Dec. = +34° 43' 38.4" (J2000) (marked "var" in Figure 2). From 1,413 observations over 60.0 days I found the prominent period 1.4576 h ± 0.0007 h, with amplitude 0.019 magnitude I_C. The fast period and low amplitude is typical of δ Scuti variables. A double phase plot is shown below (Figure 10). As many δ Scuti variables are multi-periodic (with radial and non-radial pulsations), I performed pre-whitening of this period, revealing a second prominent period of 1.859 h ± 0.001 h, amplitude 0.011 magnitude (Figure 11).

6. Conclusion

The photometric variability of PGIR22akgylf, though of low amplitude, (0.008 magnitude I_C), is detected with a Lomb-Scargle spectral analysis based on a large number of observations. The four-hour period falls within the strong maximum at 3 to 4 hours which encompasses one-third of known novae orbital periods (Özdönmez *et al.* 2018; Fuente-Morales *et al.* 2021). In spite of its location in a heavily light-polluted city (Washington, DC), the modest telescope of Burleith Observatory produces Cousins I-band photometric measurements with a mean error of 0.005, and standard error 0.001 magnitude. The serendipitous "independent discovery" of a multi-periodic δ Scuti variable further adds to the enjoyment of CCD field photometry.

7. Acknowledgements

Schmidt wishes to thank Sebastián Otero, AAVSO, and James A. DeYoung, NRL/USNO (ret.) for helpful comments. Special thanks to the AAVSO for providing photometric standards from the AAVSO Comparison Star Database via its Variable Star Plotter utility.

References

Chen, X., Wang, S., Deng, L, de Grijis, R., Yang, M., and Tian, H. 2020, *Astrophys. J., Suppl. Ser.*, **249**, 18.

De, K., *et al.* 2022, *Astron. Telegram*, No. 15587, 1.

Fuente-Morales, I., Tappert, C., Zorotovic, M., Vogt, N., Puebla, E. C., Schreiber, M. R., Ederoclite, A., and Schmidtobreick, L. 2021, *Mon. Not. Roy. Astron. Soc.*, **501**, 6083.

Motl, D., 2021, C-Munipack software utilities (http://c-munipack.sourceforge.net).

Mukai, K. 2022, "Koji's List of Recent Galactic Novae," NASA, Goddard Space Flight Center, 22 Sep. 2022 (https://asd.gsfc.nasa.gov/Koji.Mukai/novae/novae.html).

Özdönmez, A., Ege, E., Güver, T., and Ak, T. 2018, *Mon. Not. Roy. Astron. Soc.*, **476**, 4162.

Paunzen, E., and Vanmunster, T. 2016, *Astron. Nachr.*, **337**, 239.

Schmidt, R. E. 2021, *J. Amer. Assoc. Var. Star Obs.*, **49**, 261.

Schwarzenberg-Czerny, A. 1989, *Mon. Not. Roy. Astron. Soc.*, **241**, 153.

Schwarzenberg-Czerny, A. 1991, *Mon. Not. Roy. Astron. Soc.*, **253**, 198.

Supplementary Intermediate Report (July 2022) to the Spectroscopic Monitoring of the 2017–2019 Eclipse of VV Cephei

Ernst Pollmann
International Working Group Active Spectroscopy in Astronomy (ASPA), Emil-Nolde-Str. 12, 51375 Leverkusen, Germany; ernst-pollmann@t-online.de

Received July 6, 2022; revised July 18, 2022; accepted July 18, 2022

Abstract In a report that we previously published on spectroscopic monitoring of VV Cephei, time-series analysis yielded a different period (52 d) for the radial velocity of the violet (V) emission lobe of Hα than for the other features of Hα (42 d). Here, an analysis incorporating extensive new data resolves this discrepancy, giving an improved period of 43.8 ± 0.1 d for all Hα features.

1. Results

Based on the already published campaign results (Pollmann and Bennett 2020), a new geometric structure of the emission sources was developed in collaboration with Phil Bennett. Among other things, it was found that the gravitational force of the M star in VV Cep exerts an enforced angular momentum on the orbital companion star of spectral class B and its accretion disk, which results in a 43-day precession period of the disk rotation axis as well as the axis-oriented upper V emission lobe and the lower R Emission lobe. This periodic precession of the disk rotation axis would inevitably lead to a simultaneous periodic variation of the radial velocity (RV), at least the V-line flow (upper emission lobe of Figure 10 in Pollmann and Bennett 2020). However, in the *JAAVSO* publication we found within the time period JD 2457873–2458911 a 52-day period for the V emission lobe instead, with the ca. 10-day period difference not being resolved at the time of publication. A now expanded data set of RV measurements from JD 2458951 to JD 2459777 of the V emission lobe up to July 2022 (Figure 1) allowed a new period analysis to clarify this discrepancy.

Figures 3 and 4 show the period analysis of the trend-adjusted RV data (detrended by fitting a 6th order polynomial) in Figure 2, now from 415 spectra obtained up to July 2022, giving a significantly improved period of 43.8 days (± 0.1). This result now very well confirms the expected 43-day periodic precession movement of the disk rotation axis of the B star, including its accretion disk. The causes of the slow RV variation in Figure 1 are still unclear to this day, which is why further, longer phase sections are awaited to clarify them. However, it should be mentioned again that this RV has been evaluated as a relative RV with respect to the resting M supergiant (cf. the description in the *JAAVSO* paper mentioned above).

The companion star is currently in the orbital phase 0.87, which is why it will be interesting to see to what extent the precession period of 43 days persists (or not) after the periastron passage March 2025 to the orbital phase 0.5 (apastron).

The new results presented here will soon be included in a comprehensive description of this theoretical work.

Reference

Pollmann, E., and Bennett, P. D. 2020, *J. Amer. Assoc. Var. Stars*, **48**, 118.

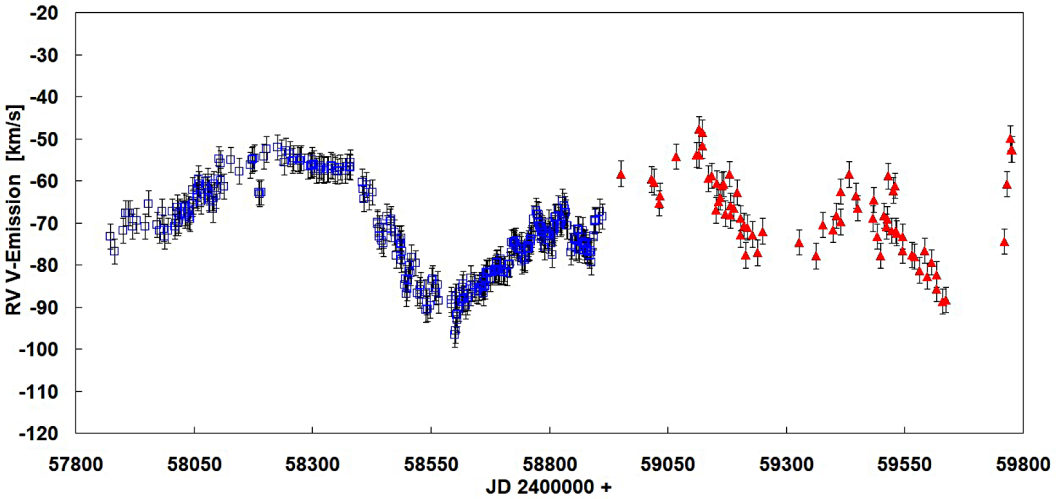

Figure 1. Extended data (red triangles, JD 2458951–2459777) from RV measurements of the maximum line flux of the V emission lobe from spectra of the ARAS spectroscopy group; blue squares are from the 2017–2019 monitoring, published already in Pollmann and Bennett (2020).

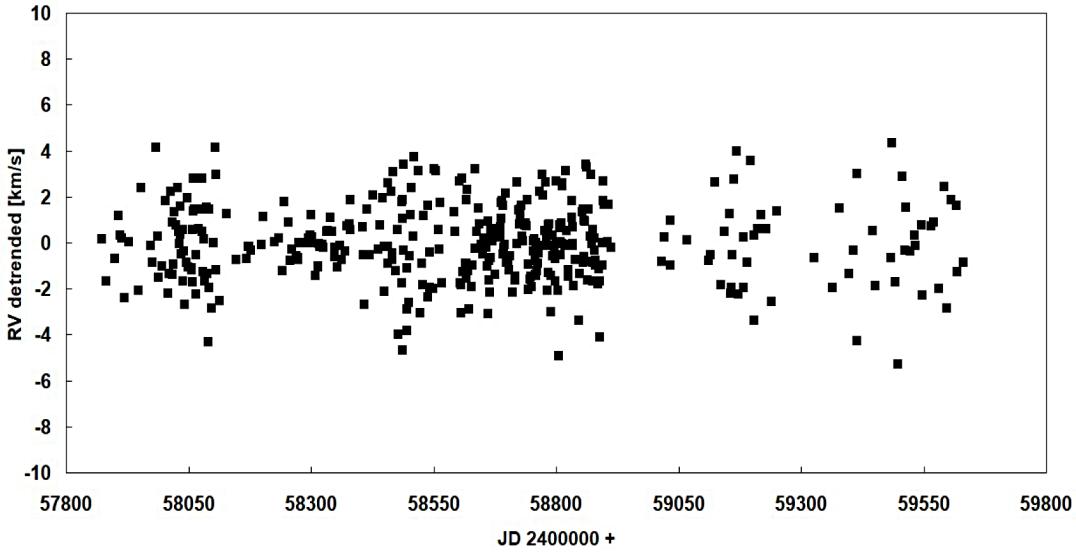

Figure 2. Trend-adjusted RV from Figure 1.

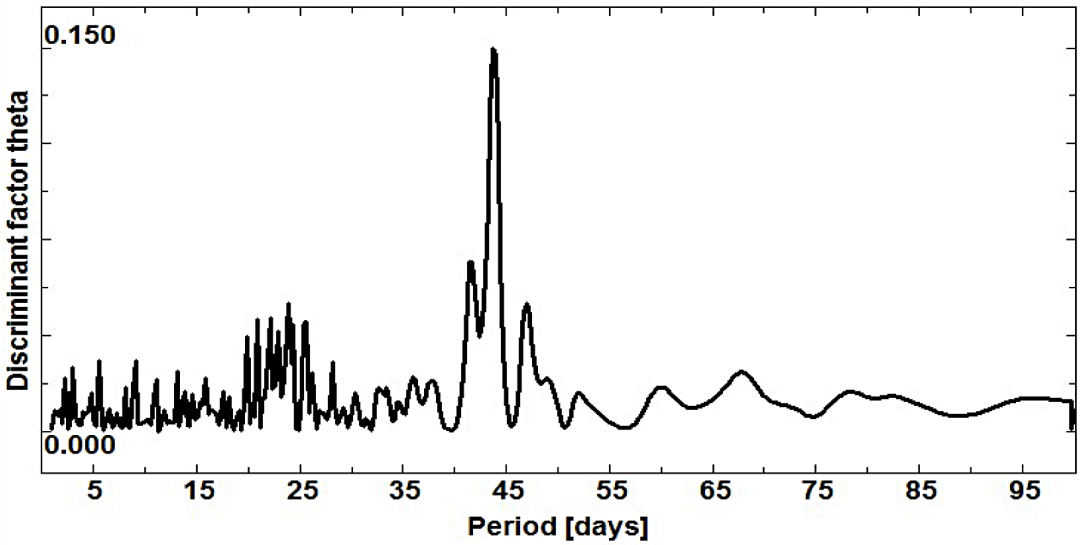

Figure 3. Scargle Period Analysis; P = 43.8 d (± 0.1).

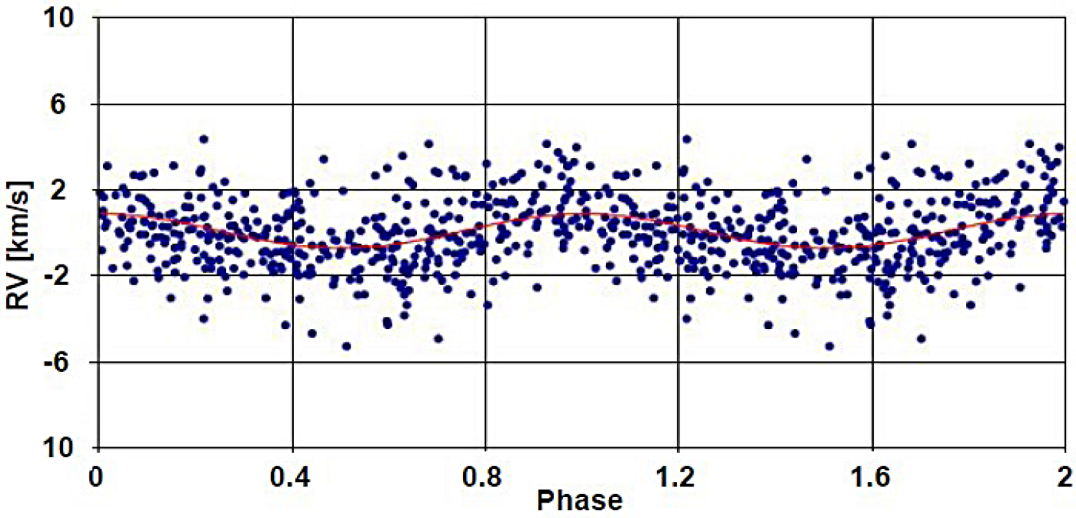

Figure 4. Phase diagram from Figure 3.

Errata: Light Curve Analysis of Eclipsing Binary Stars LX Leo, V345 UMa, and MU Leo

Lauren Hoffman
Vince Mazzola
Vayujeet Gokhale
Truman State University, 100 E. Normal Street, Kirksville, MO, 63501; gokhale@truman.edu

In the article "Light Curve Analysis of Eclipsing Binary Stars LX Leo, V345 UMa, and MU Leo" (*JAAVSO*, 2022, **50**, 3–7), the numerals in the star name "V354 UMa" were transposed in four places in the text. The corrections are noted here below with reference to the original article's pages.

1) Page 3: title, "Light Curve Analysis of Eclipsing Binary Stars LX Leo, V345 UMa, and MU Leo" should read "Light Curve Analysis of Eclipsing Binary Stars LX Leo, V354 UMa, and MU Leo."

2) Page 3: abstract, first sentence, "We present light curve analysis of three eclipsing binary stars, LX Leo, V345 UMa, and MU Leo..." should read "We present light curve analysis of three eclipsing binary stars, LX Leo, V354 UMa, and MU Leo...."

3) Page 3, left column: introduction, second sentence, "In this paper, we extend these analyses to three additional EB systems: LX Leo (P = 0.235247 d), V345 UMa (P = 0.293825 d), and MU Leo (P = 0.388442d)" should read "In this paper, we extend these analyses to three additional EB systems: LX Leo (P = 0.235247 d), V354 UMa (P = 0.293825 d), and MU Leo (P = 0.388442d)."

4) Page 6, left column: discussion, first sentence, "We have quantified the asymmetries in three short period eclipsing binary systems: LX Leo (P = 0.235247 d), V345 UMa (P = 0.293825 d), and MU Leo (P = 0.388442 d)." should read "We have quantified the asymmetries in three short period eclipsing binary systems: LX Leo (P = 0.235247 d), V354 UMa (P = 0.293825 d), and MU Leo (P = 0.388442 d)."

Index to Volume 50

Author

Subject

MULTIPLE STAR SYSTEMS

NOVAE; RECURRENT NOVAE; NOVA-LIKE [See also CATACLYSMIC VARIABLES]

PERIOD ANALYSIS; PERIOD CHANGES

PHOTOMETRY, CCD

PHOTOMETRY, CMOS

PHOTOMETRY, PHOTOGRAPHIC

PHOTOMETRY, VISUAL

PLANETS, EXTRASOLAR (EXOPLANETS)

PULSATING VARIABLES

NOTES